DIMENSION REDUCTION OF NEURAL MODELS ACROSS MULTIPLE SPATIO-TEMPORAL SCALES

by

Youngmin Park

BS Applied Mathematics, Case Western Reserve University, 2013

MS Applied Mathematics, Case Western Reserve University, 2013

Submitted to the Graduate Faculty of

the Kenneth P. Dietrich School of Arts and Sciences in partial

fulfillment

of the requirements for the degree of

Doctor of Philosophy

University of Pittsburgh

2018

UNIVERSITY OF PITTSBURGH

KENNETH P. DIETRICH SCHOOL OF ARTS AND SCIENCES

This dissertation was presented

by

Youngmin Park

It was defended on

March 30, 2018

and approved by

G. Bard Ermentrout, Distinguished University Professor, Mathematics

Rob D. Coalson, Professor, Chemistry

Brent Doiron, Professor, Mathematics

Jonathan E. Rubin, Professor, Graduate Director, Mathematics

Dissertation Director: G. Bard Ermentrout, Distinguished University Professor, Mathematics

DIMENSION REDUCTION OF NEURAL MODELS ACROSS MULTIPLE SPATIO-TEMPORAL SCALES

Youngmin Park, PhD

University of Pittsburgh, 2018

In general, reducing the dimensionality of a complex model is a natural first step to gaining insight into the system. In this dissertation, we reduce the dimensions of models at three different scales: first at the scale of microscopic single-neurons, second at the scale of macroscopic infinite neurons, and third at an in-between spatial scale of finite neural populations. Each model also exhibits a separation of timescales, making them amenable to the method of multiple timescales, which is the primary dimension-reduction tool of this dissertation. In the first case, the method of multiple timescales reduces the dynamics of two coupled n-dimensional neurons into one scalar differential equation representing the slow timescale phase-locking properties of the oscillators as a function of an exogenous slowly varying parameter. This result extends the classic theory of weakly coupled oscillators. In the second case, the method reduces the many spatio-temporal dynamics of "bump" solutions of a neural field model into its scalar coordinates, which are much easier to analyze analytically. This result generalizes existing studies on neural field spatio-temporal dynamics to the case of a smooth firing rate function and general even kernel. In the third case, we reduce the dimension of the oscillators at the spiking level – similar to the first case – but with additional slowly varying synaptic variables. This result generalizes existing studies that use scalar oscillators and the Ott-Antonsen ansatz to reduce the dimensionality and determine the synchronization properties of large neural populations.

TABLE OF CONTENTS

LIST OF TABLES

LIST OF FIGURES

PREFACE

On April 30th, 2013, I received the following email from the graduate director at the time: "Dear Mr Park, I realize that at this point you almost certainly have accepted an offer (PhD + TA) from another school. However, we have an unexpected withdrawal and so have one remaining opening on our Phd program (with TA support). If you are still interested please let me know and we will email you a formal offer immediately."

At the time, I had received rejections from every other graduate program and dreaded a rejection from Pitt. To this day I am deeply grateful to the people responsible for the acceptance and I have worked very hard to ensure that they would have no regrets. I can only hope that my research contributions reflect positively on the department of mathematics at Pitt.

I have additional people to thank for helping me along this journey, starting with my undergraduate and masters mentors and colleagues Chris Wilson, Hillel Chiel, Kendrick Shaw, and Peter Thomas: Through your combined mentoring and collaborations I developed a strong work ethic, which I heavily depended on throughout graduate school.

During my PhD, many people continued to push me intellectually. I thank the many professors with whom I have taken classes and their general dedication to helping me succeed as a student. I thank in particular the members of my thesis committee, Rob Coalson, Brent Doiron, Bard Ermentrout, and Jon Rubin.

My intellectual growth extended well beyond Pitt. I had the unique privilege of meeting many amazing people at the computational neuroscience course at Woods Hole. To the class of 2015: Your intelligence and humility is astounding, and through your kindness and gratitude, you restored purpose to my life. In particular I thank Diana Burk whose fortitude and friendship is a continuing source of inspiration, and Gily Ginosar, who spurred me on

the path to further self improvement.

Mental health is not an easy subject to discuss openly, but I feel it is important to accept and acknowledge my clinical depression and treatment through therapy and medication. Over the course of many years I met regularly with therapists Pam, Katy, Susan, and Betsy, and psychiatrists, Dr. Brooks and Dr. Handler. They skillfully helped me overcome countless personal obstacles that otherwise would have halted my productivity. My successful completion of this dissertation is due in large part to their help.

I thank my advisor Bard. You have been a strong positive influence over the years, and I learned so much from just watching you work. I watched you generate elaborate bifurcation diagrams seemingly driven only by pure curiosity, and watched you help me get unstuck on difficult problems, all the while having fun. Watching you fearlessly tackle difficult problems was such a great experience. I can't thank you enough for giving me all the resources I needed to be maximally productive. I hope that when I am one day an independent researcher with my own students, I will be able to give them the same quality, enthusiastic advising that you gave me. Moreover, I arrived at Pitt being socially dysfunctional, and thanks in large part to your kind and friendly interactions with everyone you meet, I will leave being more socially adept.

Finally, I dedicate this dissertation to my father Pilho Park and sister Young-Eun Park. We have all been through so much. I couldn't have gotten to this point without your support.

1.0 INTRODUCTION

All figure generation code in this dissertation is available on GitHub:

https://github.com/youngmp

1.1 NEURAL OSCILLATORS

Neurons have been known to form the primary computational building block of the brain, with some of the earliest computational studies performed by Lapique in 1907 [11]. Using nerve fiber activity in frogs, he reported the first known neural model: a circuit description of the neural membrane in terms of a parallel capacitor and resistor [1]. A brief overview of the method and resulting model is shown in Figure 1.

Lapicque was interested in the relation between the membrane parameters (resistance and capacitance) and its relation to neural excitability. Several decades later, the stage was set for Hodgkin and Huxley to uncover the mechanism of action potential generation as a function of the many transmembrane currents.

As part of their seminal work, Hodgkin and Huxley derived an equivalent circuit representation of the neural membrane. We show an example of the circuit and its relation to the membrane in Figure 2. The conductances (conductance is the reciprocal of the resistance) follow nonlinear voltage-dependent rules, which Hodgkin and Huxley determined through experiments. They derived a system of four ordinary differential equations that accurately

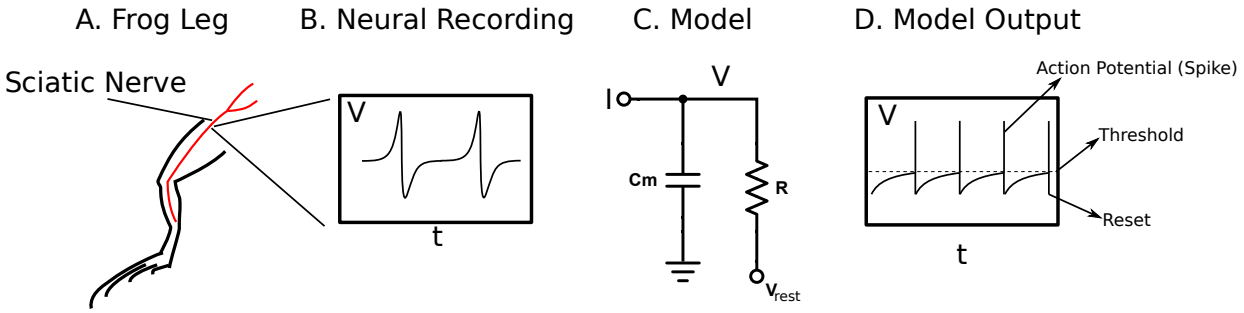

Figure 1: A schematic of Lapicque's experiment. A: Location of the sciatic nerve relative to the frog leg. B: A cartoon of the neural recordings C: Proposed model relating the membrane capacitance and resistance to excitability. D: Model dynamics. As the potential reaches a threshold, the model "spikes" and resets.

captured the nonlinear effects of transmembrane currents:

$$\begin{aligned} C\dot{V} &= I - \bar{g}_{\mathrm{K}} n^4 (V - E_{\mathrm{K}}) - \bar{g}_{\mathrm{Na}} m^3 h (V - E_{\mathrm{Na}}) - g_{\mathrm{L}} (V - E_{\mathrm{L}}) \\ \dot{n} &= \alpha_n(V)(1-n) - \beta_n(V) n \\ \dot{m} &= \alpha_m(V)(1-m) - \beta_m(V) m \\ \dot{h} &= \alpha_h(V)(1-h) - \beta_h(V) h, \end{aligned} \tag{1.1}$$

where

$$\begin{aligned} \alpha_n(V) &= 0.01 \frac{10 - V}{\exp\left(\frac{10-V}{10}\right) - 1}, \quad \beta_n(V) = 0.125 \exp\left(\frac{-V}{80}\right), \\ \alpha_m(V) &= 0.1 \frac{25 - V}{\exp\left(\frac{25-V}{10}\right) - 1}, \quad \beta_m(V) = 4 \exp\left(\frac{-V}{18}\right), \\ \alpha_h(V) &= 0.07 \exp\left(\frac{-V}{20}\right), \quad \beta_h(V) = \frac{1}{\exp\left(\frac{30-V}{10}\right) + 1}. \end{aligned} \tag{1.2}$$

The variables n, m, and h are voltage-dependent gating variables, whose function is well-documented in several texts [44, 25]. These gating variables are active (near 1) or inactive

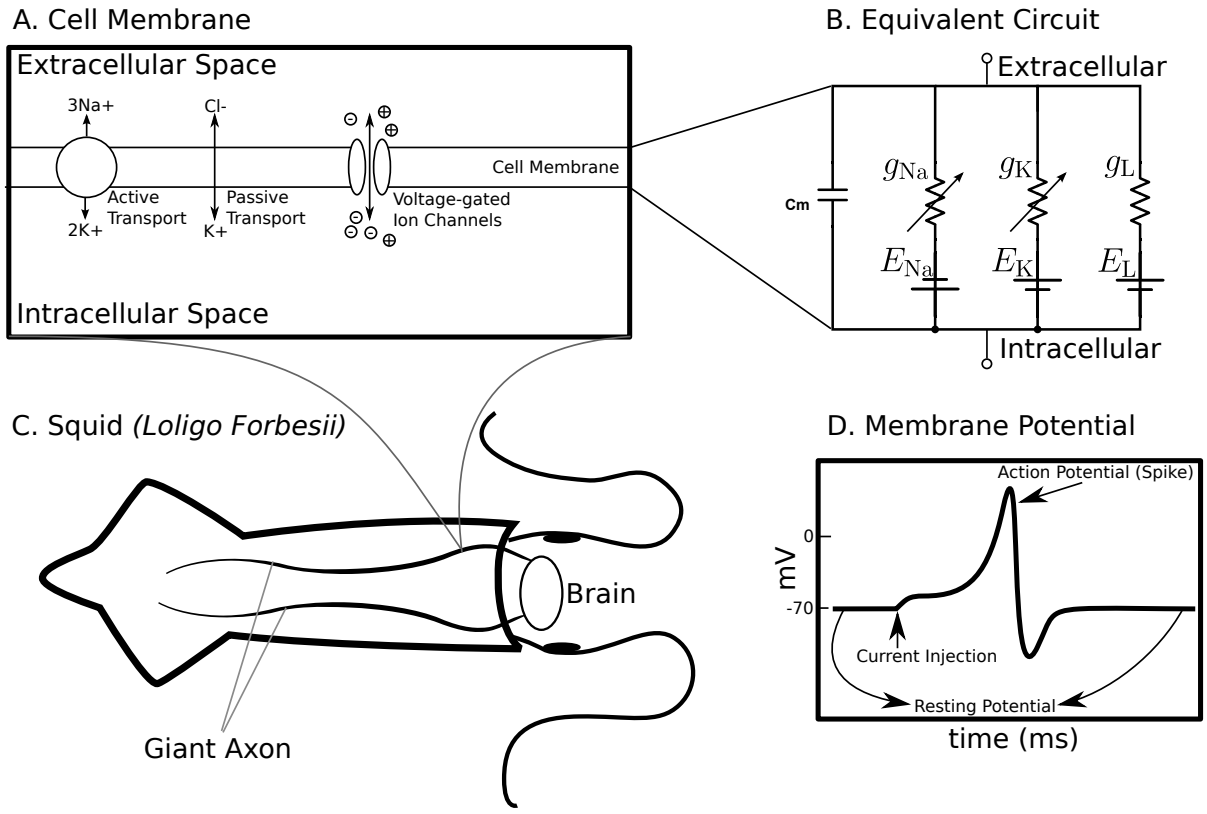

Figure 2: The giant squid axon and equivalent circuit. A: The membrane of the giant axon contains active and passive mechanisms for action potential propagation. B: The membrane can be expressed in terms of an equivalent circuit. C: Schematic of the squid (*loligo forbesii*) used in the original experiments, and the position of the giant axon. D: Sufficient current injection in the giant axon or the equivalent circuit model results in an action potential (spike).

(near 0) depending on the voltage value, and the rate of activation (or inactivation) as a function of voltage is determined by the α and β functions in Equation (1.2). The terms $\bar{g}_{\mathrm{K}}, \bar{g}_{\mathrm{Na}}$, and g_{L} represent maximal conductance values, which for the squid are typically [44]

$$\bar{g}_{\mathrm{K}} = 36\mathrm{mS/cm}^2, \quad \bar{g}_{\mathrm{Na}}120\mathrm{mS/cm}^2, \quad g_{\mathrm{L}}0.3\mathrm{mS/cm}^2. \tag{1.3}$$

The constants E_{K}, E_{Na}, and E_{L} represent reversal potentials for each ion type (the leak current is typically carried by chloride ions). For the squid, these reversal potentials are [44]

$$E_{\mathrm{K}} = -12\mathrm{mV}, \quad E_{\mathrm{Na}} = 120\mathrm{mV}, \quad E_{\mathrm{L}} = 10.6\mathrm{mV}. \tag{1.4}$$

The two remaining constants, C and I represent the membrane capacitance, and input current, respectively. The capacitance C is typically chosen to be $C = 1\mu\mathrm{F/cm}^2$, and the injected current I has units of $\mu\mathrm{A/cm}^2$.

Equation (1.1) describes the voltage potential of the squid giant axon at a single point. Remarkably, this conductance-based description of neurons generalizes to any neuron type where transmembrane currents produce excitability (action potentials or spikes). Thus, with only slight modifications to this model, it is possible to model excitability in mammalian cortical neurons, which are the primary neuron type in this dissertation.

We remark that these equations form a system of ordinary differential equations (ODEs). Hodgkin and Huxley included a spatial component in their original equations thus deriving a system of partial differential equations (PDEs), but single-neuron models in this dissertation will focus solely on this ODE single-point description.

Conductance-based models are capable of producing a great number of dynamics as a function of an input current. In particular, these models may fire repetitive action potentials with sufficient and constant current injection. Similar effects are seen in real neurons, although repetitive spikes are not perfectly periodic due to natural intrinsic and extrinsic effects. However, a rigorous mathematical treatment of spiking neurons requires simplifying assumptions. Of the many approaches one can take to understand single-neuron dynamics, we take a deterministic dynamical systems approach: assume the dynamics at a single point on the cell body is given by the smooth autonomous system,

$$\dot{\mathbf{x}} = \mathbf{F}(\mathbf{x}), \tag{1.5}$$

where $\mathbf{x} \in \mathbb{R}^n$ represents a vector of the membrane potential and gating variables of the neuron. The vector field $\mathbf{F} : \mathbb{R}^n \to \mathbb{R}^n$ contains parameters including the external input current $I \in \mathbb{R}$. When the input current is sufficiently large, we assume there exists a closed, attracting, and isolated T-periodic solution $\gamma(t) \in \mathbb{R}^n$. In dynamical systems theory, $\gamma(t)$

is a stable T-**periodic limit cycle solution** satisfying Equation (1.5). Note that the description in Equation (1.5) is a general framework that includes Hodgkin and Huxley's conductance-based description in Equation (1.1).

Because the solution $\gamma(t)$ is stable and isolated, there exists a set of points in the phase space, $B \subseteq \mathbb{R}^n$, that converge as $t \to \infty$ to the set of points on the limit cycle, $\Gamma := \{\gamma(t) : t \in \mathbb{R}\}$. The set of points B is called the **basin of attraction**. It follows that sufficiently small-magnitude perturbations off the limit cycle γ allow solutions to remain within the basin of attraction B and to converge back towards the limit cycle.

One example of weak perturbations arises in the case of weakly coupled oscillators:

$$\begin{aligned} \dot{\mathbf{x}}_1 &= \mathbf{F}(\mathbf{x}_1) + \varepsilon \mathbf{G}_1(\mathbf{x}_1, \mathbf{x}_2), \\ \dot{\mathbf{x}}_2 &= \mathbf{F}(\mathbf{x}_2) + \varepsilon \mathbf{G}_2(\mathbf{x}_2, \mathbf{x}_1), \end{aligned} \tag{1.6}$$

where $0 < \varepsilon \ll 1$ small, and $\mathbf{G} : \mathbb{R}^n \times \mathbb{R}^n \to \mathbb{R}^n$ is a smooth term describing how the two vector fields influence each other. The physical interpretation of $\mathbf{G}_i$ is rather general, but in this dissertation it typically represents synaptic neural coupling. The weak assumption is justifiable by the fact that postsynaptic potentials in the cortex are generally orders of magnitude smaller than action potentials [42].

In the theory to follow, we write our oscillating solution γ in terms of a phase variable $\theta \in [0, T)$ [71]. When the oscillators are uncoupled ($\varepsilon = 0$), we associate each point $\mathbf{x} \in \Gamma$ with a phase value $\theta(\mathbf{x})$, where

$$\frac{d\theta_i}{dt} = 1, \quad i = 1, 2.$$

In turn, because the limit cycle is a simple closed loop, a given phase value $\theta \pmod T$ uniquely determines a point on the limit cycle. This equivalence allows for an analysis of oscillator phase differences in terms of the phase angle instead of the full n-dimensional dynamics. As the details of the following derivation exist in many sources, we omit many calculations. For a thorough introduction to these topics, we refer the reader to [25, 82, 71].

When the oscillators are weakly coupled ($\varepsilon > 0$, small), an order ε term appears in the phase equation,

$$\frac{d\theta_i}{dt} = 1 + \varepsilon \nabla_{\mathbf{x}} \theta(\gamma(\theta_i)) \cdot \mathbf{G}_i(\gamma(\theta_i), \gamma(\theta_k)), \quad i = 1, 2, k = 3 - i.$$

The new term depends on the spatial gradient of the phase function, $\nabla_{\mathbf{x}}\theta(\gamma(\theta_i))$, and the coupling function $\mathbf{G}_i$ from Equation (1.6). The spatial gradient of θ evaluated along the limit cycle is the **infinitesimal phase response curve** (iPRC), i.e., the response of the neuron to small perturbations. For notational convenience, we denote the iPRC by $\mathbf{z}$.

Subtracting the moving frame and averaging over the timescale of the oscillators allows for the study of slow timescale synchronization properties using the scalar differential equation,

$$\frac{d\phi}{dt} = \varepsilon[H_2(-\phi) - H_1(\phi)], \tag{1.7}$$

where

$$H_i(\phi) = \frac{1}{T}\int_0^T \mathbf{z}(t)\cdot\mathbf{G}_i[\gamma(t),\gamma(t+\phi)]dt,$$

and $\phi = \theta_2 - \theta_1$. The fixed points of Equation (1.7) correspond to phase-locked states of the two oscillators. If, for example, $\phi = 0$ is a stable (unstable) solution to Equation (1.7), then the neural oscillators satisfying Equation (1.6) will tend to synchronize (with some dependence on initial conditions). In summary, predicting the synchronization between two n-dimensional deterministic weakly coupled oscillators reduces to the analysis of one scalar differential equation. Moreover, this technique generalizes to N oscillators, providing a means to analyze the degree of synchronization within a population [25].

The scalar reduction of weakly coupled oscillators and subsequent analysis of synchronization properties form the core ideas of Chapter 2.

1.2 MEAN-FIELD NEURON DYNAMICS

Building up a population-level understanding from the spiking-level is possible using weak coupling theory, and this approach provides a good first approximation to the degree of synchrony within a neural population. However, there exist rich spatio-temporal dynamics of the cortex where the population is asynchronous and individual neurons spike irregularly. We now briefly summarize these dynamics as observed in the cortex.

There exist spatially coherent activity states during normal brain function that correspond to a spectrum of computations. Neurons in the primary visual cortex respond

preferentially to the orientation of edges [5]. In the rat brain, there exists a system of head-direction cells that fire maximally when the rat faces one particular direction [96]. In several model animals, cortical neurons exhibit persistent activity during delayed response tasks [90, 72]. We show a cartoon of cortical circuitry and corresponding modeling approaches in Figure 3.

In each of these examples, elevated firing rates are observed at the population level and the neural populations are entirely asynchronous. Thus, in contrast to the previous section, these population-level dynamics with asynchronous and irregular spiking neurons requires a different mathematical framework.

In Wilson and Cowan's seminal work, they considered two populations of inhibitory and excitatory neurons and used mean-field theory to derive equations for the firing rate of each population (Figure 3C,D). This approach allows for a standard planar dynamical systems analysis, where the results apply to the population level [95]. Extending upon this work, some studies analyze the spatially extended dynamics of a neural network using a single-layer mean field description that combines inhibitory and excitatory connections (Figure 3D, but with both layers compressed into one). The result of this combination is the activity formulation [2, 76]:

$$\frac{\partial u(\mathbf{x},t)}{\partial t} = -u(\mathbf{x},t) + \int_{\Omega} K(\mathbf{x}-\mathbf{y}) f(u(\mathbf{y},t)) d\mathbf{y} + \alpha_1 I(\mathbf{x},t) + \alpha_2 z(\mathbf{x},t) \tag{1.8}$$

$$\frac{\partial z(\mathbf{x},t)}{\partial t} = \beta[-z(\mathbf{x},t) + u(\mathbf{x},t)] \tag{1.9}$$

where $K : \mathbb{R}^n \to \mathbb{R}$ is a Mexican-hat function (Figures 4A and 5A), $f : \mathbb{R} \to \mathbb{R}$ is a sigmoidal function (Figure 4B), $I : \mathbb{R}^n \times \mathbb{R} \to \mathbb{R}$ is the input current to the system, $u : \mathbb{R}^n \times \mathbb{R} \to \mathbb{R}$ is the neural activity at position $\mathbf{x}$ at time t (Figures 4C and 5B), and α_i, β are parameters controlling the strength and timecourse of the input current I and adaptation z. In the literature, the domain Ω is the real line, the ring, the real plane, or the torus. In this dissertation, we choose Ω to be either the ring, $[-\pi, \pi]$, or torus, $[-\pi, \pi] \times [-\pi, \pi]$.

Many studies choose an explicit form for the kernel. One common choice is a difference of Gaussians, defined by

$$\hat{K}(x) = \frac{1}{\sqrt{\pi}\sigma_e} e^{-(x/\sigma_e)^2} - \frac{1}{\sqrt{\pi}\sigma_i} e^{-(x/\sigma_i)^2}.$$

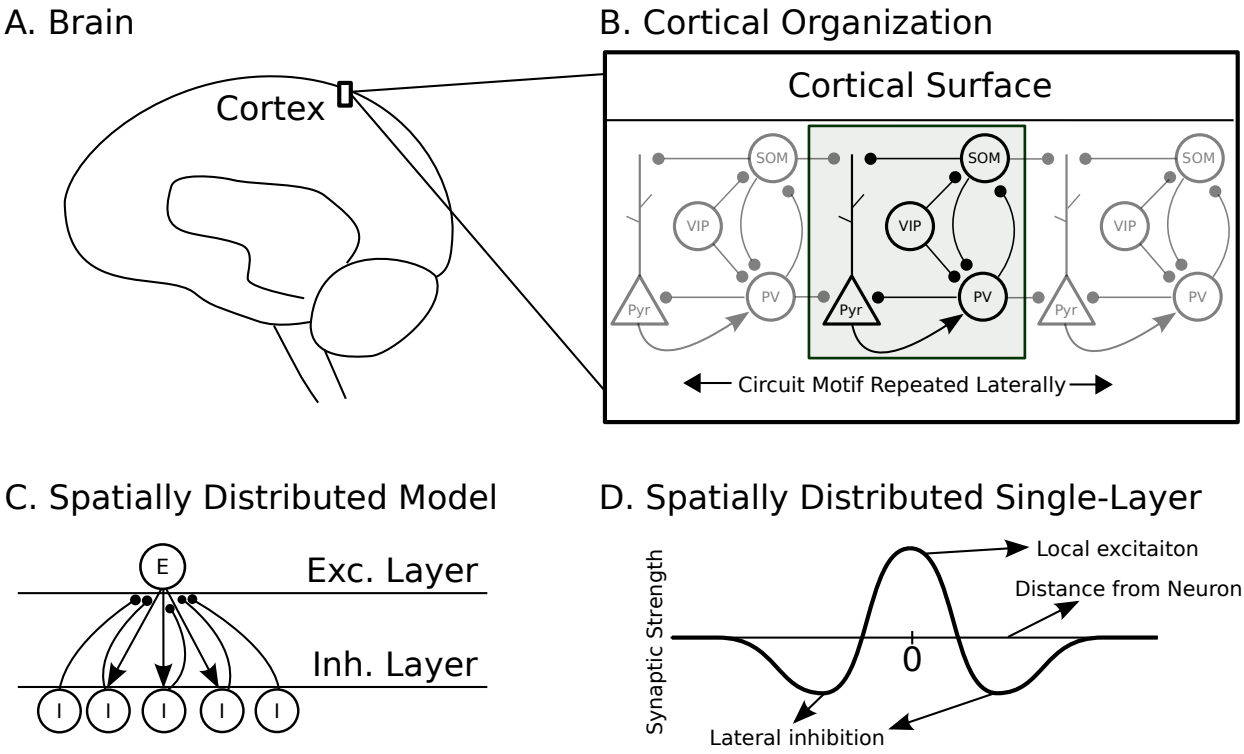

Figure 3: Population-level cortical models. A: The human brain. B: Approximate cortical circuitry. Circles denote inhibitory synapses and arrows denote excitatory synapses. Pyramidal (Pyr) neurons are innervated by multiple inhibitory interneurons types, including somatostatin-positive (SOM), parvalbumin-positive (PV), and vasoactive intestinal peptide (VIP) neurons. PVs exhibit lateral and feedforward inhibition. The green box highlights a single microcircuit motif that is repeated throughout the neocortex. C: Idealized population-level modeling based on cortical connectivity. Arrows indicate excitatory connections. D: The single-layer population-level modeling approach combines the two spatial layers. For a given neuron, the inhibitory or excitatory synaptic strength depends on the distance of neighboring neurons.

This difference of Gaussians results in a function nearly identical to Figure 4A, but defined on the real line. This choice is motivated by observed cortical connections, where given a particular neuron, it is excited by nearby neurons, inhibited by neurons slightly farther away, and receives no influence from neurons much farther away. This type of connectivity structure is often called lateral inhibition, because in addition to the local excitation, neighboring neurons inhibit in lateral directions.

This definition of $\hat{K}$ is sufficient for a domain on the real line, but because our domain is perodic, we periodize the function:

$$K(x) = \sum_{n \in \mathbb{Z}} \hat{K}(x + 2\pi n).$$

We show an example of this function in Figure 4A. Many studies also choose an explicit form for the firing rate function. A common choice is

$$f(x) = \frac{1}{1 + \exp(-r(x - u_{th}))},$$

where r is the gain of the sigmoid and u_{th} is the threshold (Figure 4B). Other examples of the firing rate function include the hyperbolic tangent or arctangent, which are chosen because of their sigmoidal graph. For our numerical simulations, we choose the firing rate function above, and a Mexican hat function defined in terms of a cosine:

$$K(x) = A + B\cos(x).$$

In our theory we use general firing rates and kernels unless otherwise specified. Figure 5A shows the kernel and panel B shows the resulting bump solution.

Both types of single- and double-layer neural field models are capable of producing a vast number of spatio-temporal dynamics including stationary and traveling bump solutions [98, 50, 34, 76, 15, 28], bump solutions that oscillate in width (breathers) [9, 31, 32, 33], pulse-emitting bumps, [50, 49], oscillatory wavefronts [8, 9], and spiral waves [49]. Many of these studies require an additional variable representing spike-frequency adaptation, but the core mechanism (the single-layer neural field in Equation (1.8) or the two-layer Wilson-Cowan model [95]) remains nearly unchanged across studies. In this thesis, we restrict our attention to bump solutions of the form in Figures 4C and 5B.

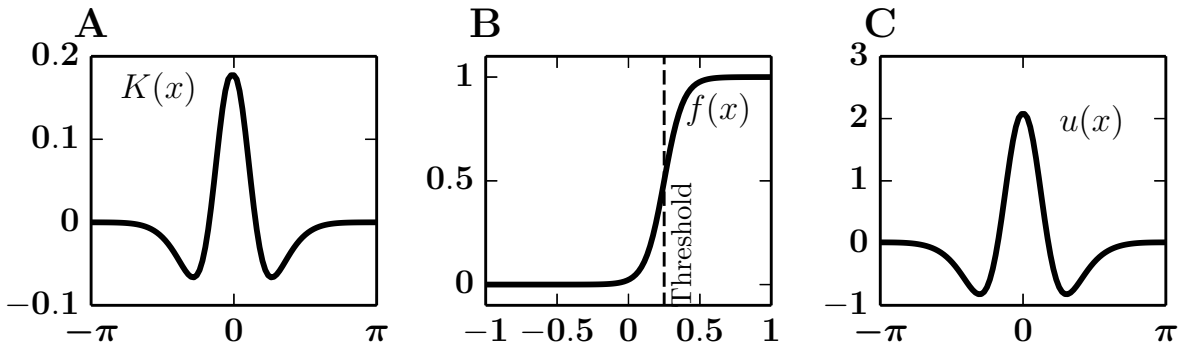

Figure 4: Typical choices of the Mexican hat kernel. (A), firing rate function (B), and the resulting bump solution (C). In this figure, $\sigma_e = 0.5$, $\sigma_i = 1$, $u_{th} = 0.25$, and $r = 15$.

Classic studies on existence, uniqueness, and stability of solutions to Equation (1.8) use the infinite-gain limit of the firing rate function f. This assumption is a natural first step to making Equation (1.8) mathematically tractable. To demonstrate the classic proof techniques, we consider Equation (1.8) in the high gain limit, without adaptation or input current:

$$\frac{\partial u(\mathbf{x},t)}{\partial t} = -u(\mathbf{x},t) + \int_\Omega K(\mathbf{x}-\mathbf{y})H(u(\mathbf{y},t)-\theta)d\mathbf{y},$$

where H is the Heaviside step function, θ is the threshold for firing, and $K(x) = A + B\cos(x)$, where $A = -0.5$ and $B = 3$. The arguments to follow are similar to [25], chapter 12.4.1, but we consider a ring domain instead of the real line.

Suppose the system is at steady-state. Then the system reduces to the integral equation

$$u(\mathbf{x}) = \int_\Omega \cos(\mathbf{x}-\mathbf{y})H(u(\mathbf{y})-\theta)d\mathbf{y}.$$

In this example, our choice of kernel (Figure 5A) leads to a numerically computed bump solution of the form in Figure 5B. Thus, if a bump solution exists, it is reasonable to assume that $u(x) \geq \theta$ on the interval $[-r, r]$, where $2r$ is a constant bounded above by the length of

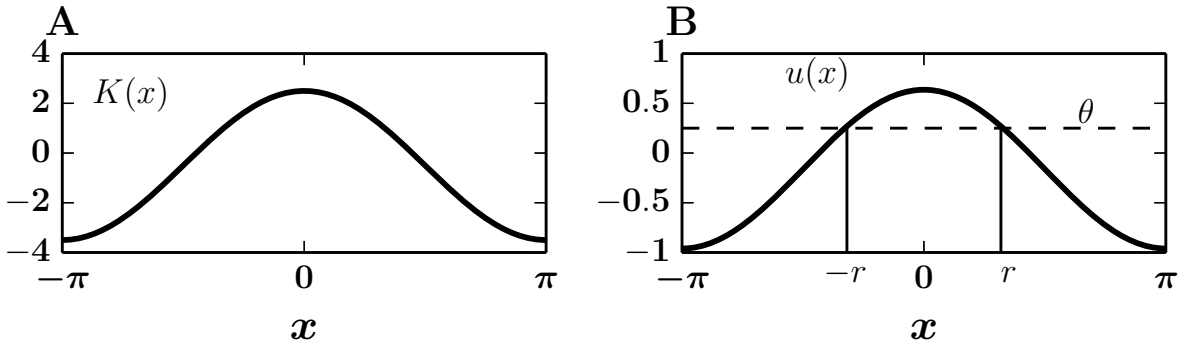

Figure 5: The kernel K and numerically computed steady-state bump solution u. A: The Mexican hat kernel K plotted on the ring domain. B: The bump solution u plotted on the real domain. The horizontal dashed line shows the threshold value. The bump width is shown with the vertical lines which mark the interval $[-r, r]$.

the domain. We simplify the integral further by exploiting the Heaviside function and basic trigonometric identities:

$$\begin{aligned} u(x) &= \int_{-r}^{r} \cos(x-y)dy \\ &= \cos(x)\int_{-r}^{r} \cos(y)dy + \sin(x)\int_{-r}^{r} \sin(y)dy \\ &= 2\sin(r)\cos(x). \end{aligned}$$

Thus, with a cosine kernel, we can expect a sinusoidal bump solution. Moreover, recalling that the bump width r depends on the threshold θ, we conclude that the bump solution has an amplitude that is nonlinearly proportional to the threshold θ.

Numerically, one can show that the bump solution is not always centered at the origin, suggesting that the bump solution is translation invariant. To show translation invariance

on the ring domain, we simply repeat the calculations above on the interval $[\alpha, \beta]$, where $\beta - \alpha = 2r$ and $|\alpha|, |\beta| < \pi$. The resulting bump solution is given by

$$u(x) = 2\sin(r)\cos(x - (\alpha + r)).$$

Given θ, it follows that r is constant, so this solution is unique up to α. In fact, the term $(\alpha + r)$ represents the center of the bump solution, and for any α the shape of the solution remains invariant, thus proving translation invariance. Arguments for determining uniqueness and stability of solutions are found in [2, 25].

These results are useful because they are exact and are qualitatively indistinguishable from numerical results when the gain of the firing rate function is large but finite. Thus, they serve as satisfactory proofs for solutions that depend on large and finite gain. Moreover, the utility of this proof method goes well beyond existence and stability of bump solutions. Proofs of existence and stability of time-dependent solutions like breathers, sloshers, and traveling pulses classically rely on the Heaviside assumption [9, 31, 32, 33, 50, 49, 49].

In this thesis, we side-step the Heaviside assumption by reducing the neural field into scalar differential equations that enable us to analyze the neural field model with a general kernel and smooth firing rate function (high gain is not necessary). The analysis of Equation (1.8) through a dimension reduction, assuming weak input current and an additional weak and slow adaptation variable, forms the primary motivation behind Chapter 3.

1.3 BRIDGING MICROSCOPIC AND MACROSCOPIC DYNAMICS

Despite the success of the Wilson-Cowan model and related activity-based models in modeling cortical activity, several recent studies express concern at the derivation of these mean-field models, which uses strictly population level quantities, e.g., proportion of active cells, distribution of refractory cells, and the proportion of non-refractory cells receiving above-threshold input. Thus, recent studies have shifted focus to a re-derivation of the mean-field starting at the spiking level.

Macroscopic variables and mean field models have been derived when the population is asynchronous [58, 57, 79] and with Poisson statistics [4, 3]. However, the missing piece in the literature, and indeed the goal of this dissertation, is to determine the degree of synchrony of oscillators in a population when they are not constrained to asynchronous activity.

To this end, most current studies use the Kuramoto model [53] and the Ott-Antonsen ansatz to derive a complementary order parameter to the mean-field description. To demonstrate this derivation, we summarize the relevant results of the original Ott and Antonsen paper [66], followed by a summary of the derivation of macroscopic observables (firing rate and mean membrane potential) of the continuum limit of quadratic integrate-and-fire neurons in [63].

Consider a simple case of all-to-all, homogeneously coupled Kuramoto oscillators

$$\frac{d\theta_i}{dt} = \omega_i + \frac{K}{N}\sum_{j=1}^{N}\sin[\theta_j(t) - \theta_i(t)],$$

where θ_i denotes the phase angle of oscillator $i = 1, \ldots, N$, ω_i is the natural frequency of oscillator i, and K is the coupling strength. In the limit as $N \to \infty$, the state of the oscillator system at time t can be described by a continuous distribution function, $f(\omega, \theta, t)$ satisfying

$$\frac{\partial f}{\partial t} + \frac{\partial}{\partial \theta}\left\{\left[\omega + \frac{K}{2i}\left(re^{-i\theta} - r^* e^{i\theta}\right)\right] f\right\},$$

where

$$r(t) = \int_0^{2\pi} d\theta \int_{-\infty}^{\infty} d\omega f(\omega, \theta, t) e^{i\theta}.$$

The partial differential equation is the continuity equation, which is the joint probability distribution function of oscillators θ and frequencies ω, at time t. The function r is the complex order parameter expressed as the total of all oscillator states θ and frequencies ω, and r^* is the complex conjugate.

The key assumption by Ott and Antonson is to take the Fourier series of f as

$$f = \frac{g(\omega)}{2\pi}\left\{1 + \left[\sum_{n=1}^{\infty} f_n(\omega, t)\exp(in\theta) + c.c.\right]\right\},$$

where $f_n(\omega, t) = \alpha(\omega, t)^n$ with $|\alpha| \leq 1$. The term $c.c.$ stands for complex conjugate. For further analysis, they require additional assumptions:

- α can be analytically continued from real ω into the complex ω-plane.
- α has no singularities in the lower half ω-plane.
- $|\alpha(\omega, t)| \to 0$ as $\text{Im}(\omega) \to -\infty$.
- $g(\omega) = \frac{\Delta}{\pi} \frac{1}{(\omega-\omega_0)^2+\Delta^2}$, i.e., the natural frequencies of the oscillators are drawn from a Lorentzian distribution.

These assumptions allow the authors to use the residue theorem, from which they derive a pair of first order differential equations governing the dynamics of the order parameter $r = \rho e^{-i\phi}$, where ρ and ϕ satisfy

$$\frac{d\rho}{dt} + \left(1 - \frac{K}{2}\right)\rho + \frac{K}{2}\rho^3 = 0, \quad \frac{d\phi}{dt} = 0.$$

These equations are significant because they reduce an infinite dimensional problem to one non-trivial dimension. The authors use this approach to reduce the dimension of several related problems, including the case of sinusoidal external drive, and a more general case with coupled populations of Kuramoto oscillators with heterogeneous coupling between populations.

More recent studies also derive macroscopic observables, e.g., the firing rate and mean membrane potential of large populations of quadratic integrate and fire models [63]. We briefly summarize the results. Consider the network of quadratic integrate and fire neurons,

$$\dot{V}_j = V_j^2 + I_j,$$

where $I_j = \eta_j + Js(t) + I(t)$, and $s(t) = r(t)$, the firing rate at time t. J represents the synaptic strength, and η_j add heterogeneity to the connections. In the continuum limit, the conditional distribution of neurons, $\rho(V|\eta, t)$, satisfies the continuity equation

$$\partial_t \rho + \partial_v[(v^2 + \eta + Js + I)\rho] = 0,$$

where the variable η is a random number drawn from the Lorentzian distribution

$$g(\eta) = \frac{1}{\pi} \frac{\Delta}{(\eta - \bar{\eta})^2 + \Delta^2}.$$

Assuming, independent of g and the initial condition, that all solutions of the continuity equation converge to a Lorentzian distribution, we can write

$$\rho(V|\eta,t) = \frac{1}{\pi}\frac{x(\eta,t)}{[V-y(\eta,t)]^2 + x(\eta,t)^2},$$

where x is the half-width of the distribution and y is its center. To determine the conditions on x, y for this ansatz to be a solution, we plug this ansatz into the continuity equation, resulting in the coupled equations,

$$\partial_t w(\eta,t) = i[\eta + Js(t) - w(\eta,t)^2 + I(t)],$$

where $w(\eta,t) \equiv x(\eta,t) + iy(\eta,t)$. From the Lorentzian assumption on η, it follows that the firing rate $r(t)$ and mean membrane potential $v(t)$ depend on w at one point:

$$\pi r(t) + iv(t) = w(\bar{\eta} - i\Delta, t).$$

This property substantially simplifies the equation for w into a system of two ordinary differential equations,

$$\begin{aligned}\dot{r} &= \frac{\Delta}{\pi} + 2rv \\ \dot{v} &= v^2 + \bar{\eta} + Jr + I(t) - \pi^2 r^2.\end{aligned}$$

The authors also show that this system is amenable to the same type of Kuramoto order parameter reduction as summarized earlier. Thus, the derivation of a mean-field description from the spiking level, as well as the degree of synchronization at the spiking level is beginning to be well understood.

Several other papers use different models, or different connections to generalize one or a combination of the results above. In [12], the authors use the Kuramoto model, but extend the existing results to more realistic network topologies. The Ott-Antonsen ansatz is used to derive order parameters for an increasing family of models including the theta model in [16], the Winfree model in [73], and excitatory-inhibitory Alder units in [80]. Finally, the Ott-Antonsen ansatz is not the only method in use for this case. In [59], Laing considers all-to-all pulse-like coupling of theta neurons with and without synaptic delay and derives the order parameter using the Watanabe-Strogatz ansatz [94, 93]

In this dissertation, we are interested in deriving the mean field model and complementary spiking-level phase equations for general n- and m-dimensional slowly coupled oscillators. The connection between microscopic and macroscopic dynamics forms the motivating idea of chapter 4.

1.4 FREDHOLM ALTERNATIVE THEOREM

Consider the equation,

$$Lf = g,$$

where L is a compact linear operator defined on a Hilbert space H and g is a known T-periodic function in H. If the linear operator L has a nontrivial nullspace, we require additional assumptions to guarantee existence of the T-periodic solution f. According to the Fredholm alternative theorem, there exists a solution f if and only if $\langle g, v\rangle = 0$ for every function v in the nullspace of the adjoint operator L^* [47]. The inner product is defined as

$$\langle f, g\rangle = \int_0^T f(t) \cdot g(t) dt.$$

This theorem underlies the core mathematical techniques in chapters 2,3, and 4.

1.5 METHOD OF MULTIPLE TIMESCALES

The systems we consider have a sufficiently small parameter ε that introduces a natural separation of two timescales: a "fast" time $s = g(t, \varepsilon)$, which is on the timescale of a T-periodic solution, and a "slow" time, $\tau = \varepsilon t$, which is on the timescale of phenomena that occur in order $1/\varepsilon$ time. In particular, the order $1/\varepsilon$-time phenomena in our systems can be described in terms of scalar variables.

If we assume that s and τ are independent, we can use the method of timescales to make the scalar reduction rigorous. Recall the phase difference equation, (1.7), which is classically derived using the method of averaging. To demonstrate how we use the method of multiple

timescales in this dissertation, we re-derive Equation (1.7) by exploiting the difference in timescales.

Recall our starting assumption,

$$\begin{aligned}\dot{\mathbf{x}}_1 &= \mathbf{F}(\mathbf{x}_1) + \varepsilon \mathbf{G}(\mathbf{x}_1, \mathbf{x}_2),\\ \dot{\mathbf{x}}_2 &= \mathbf{F}(\mathbf{x}_2) + \varepsilon \mathbf{G}(\mathbf{x}_2, \mathbf{x}_1),\end{aligned} \tag{1.10}$$

where each vector field, when $\varepsilon = 0$, has a stable T-periodic limit cycle solution $\gamma(t)$. When $\varepsilon > 0$ and sufficiently small, each limit cycle influences the timing of the other in order $1/\varepsilon$ time. We take the coupling functions to be identical for simplicity, but the derivation is identical in the heterogeneous case.

To derive the phase difference dynamics, we make the following ansatz:

$$\begin{aligned}\mathbf{x}_1(t, \varepsilon) &= \gamma(s + \theta_1(\tau)) + \varepsilon \xi_1(s + \theta_1(\tau)) + O(\varepsilon^2),\\ \mathbf{x}_2(t, \varepsilon) &= \gamma(s + \theta_2(\tau)) + \varepsilon \xi_2(s + \theta_2(\tau)) + O(\varepsilon^2),\end{aligned}$$

where $s = t$, $\tau = \varepsilon t$, $\theta(\tau)$ is a slow timescale phase shift, γ is the T-periodic limit cycle representing the lowest-order solution, and ξ_i are first order terms to account for order ε changes in amplitude. Our goal is to derive dynamics for $\theta_i(\tau)$.

We substitute our ansatz into Equation (1.10), use the chain rule, and expand in order ε. The resulting equation is then

$$\begin{aligned}\gamma'(s + \theta_1(\tau)) \left[1 + \varepsilon \frac{d\theta_1}{d\tau}\right] + \varepsilon \xi_1'(s + \theta_1(\tau)) + O(\varepsilon^2)&\\ = \mathbf{F}(\gamma(s + \theta_1(\tau))) + \varepsilon D\mathbf{F}(\gamma(s + \theta_1(\tau)))\xi_1(s + \theta_1(\tau))&\\ + \varepsilon \mathbf{G}(\gamma(s + \theta_1(\tau)), \gamma(s + \theta_2(\tau))) + O(\varepsilon^2),&\end{aligned}$$

where $D\mathbf{F}$ is the Jacobian matrix of the vector F. Next, we group in terms of order ε, resulting in a hierarchy of equations,

$$\begin{aligned}\gamma'(s + \theta_1(\tau)) &= \mathbf{F}(\gamma(s + \theta_1(\tau)))\\ \gamma'(s + \theta_1(\tau)) \frac{d\theta_1}{d\tau} + \xi_1'(s + \theta_1(\tau)) &= D\mathbf{F}(\gamma(s + \theta_1(\tau)))\xi_1(s + \theta_1(\tau))\\ &\quad + \mathbf{G}(\gamma(s + \theta_1(\tau)), \gamma(s + \theta_2(\tau)))\\ &\vdots\end{aligned}$$

We rearrange the second line to yield:

$$L\xi_1 = -\gamma'(s+\theta_1(\tau))\frac{d\theta_1}{d\tau} + \mathbf{G}(\gamma(s+\theta_1(\tau)), \gamma(s+\theta_2(\tau))), \tag{1.11}$$

where

$$Lf = f' - D\mathbf{F}(\cdot)f.$$

The operator L is a linear compact operator acting on the space of T-periodic functions. Now the relevance of the Fredholm alternative theorem is clear: for there to exist a solution ξ_1 to Equation (1.11), we require the right hand side of Equation (1.11) to be orthogonal to all functions in the nullspace of the adjoint operator

$$L^*g = g' + D\mathbf{F}(\cdot)^T g.$$

In previous studies, the function in the nullspace of the adjoint operator for this system is the iPRC, $\mathbf{z}$, with the property that $\mathbf{z}(s)\cdot\gamma'(s) = 1$. Taking the inner product of $\mathbf{z}$ with the right hand side of Equation (1.11) yields by definition

$$\begin{aligned}\frac{d\theta_1}{d\tau}\int_0^T -\gamma'(s+\theta_1(\tau))\cdot\mathbf{z}(s+\theta_1(\tau))ds \\ + \int_0^T \mathbf{G}(\gamma(s+\theta_1(\tau)), \gamma(s+\theta_2(\tau)))\cdot\mathbf{z}(s+\theta_1(\tau))ds = 0,\end{aligned}$$

which simplifies to

$$\frac{d\theta_1}{d\tau} = \frac{1}{T}\int_0^T \mathbf{G}(\gamma(s+\theta_1(\tau)), \gamma(s+\theta_2(\tau)))\cdot\mathbf{z}(s+\theta_1(\tau))ds.$$

Because the terms $\theta_i(\tau)$ are effectively constant relative to s, we take the transformation $s' = s + \theta_1(\tau)$ to yield

$$\frac{d\theta_1}{d\tau} = \frac{1}{T}\int_0^T \mathbf{G}(\gamma(s'), \gamma(s'+\theta_2(\tau)-\theta_1(\tau)))\cdot\mathbf{z}(s')ds'.$$

The calculations are identical for $d\theta_2/d\tau$, which is straightforward to derive:

$$\frac{d\theta_2}{d\tau} = \frac{1}{T}\int_0^T \mathbf{G}(\gamma(s'), \gamma(s'+\theta_1(\tau)-\theta_2(\tau)))\cdot\mathbf{z}(s')ds'.$$

Finally, taking the phase difference $\phi = \theta_2 - \theta_1$ yields

$$\frac{d\phi}{d\tau} = [H(-\phi) - H(\phi)],$$

where

$$H(\phi) = \frac{1}{T}\int_0^T \mathbf{G}(\gamma(s), \gamma(s+\phi)) \cdot \mathbf{z}(s) ds.$$

This equation is identical to Equation (1.7), concluding our demonstration of the method of multiple timescales.

In each of the chapters to follow, we tailor the starting ansatz to fit the problem, but the concepts are invariant: we expand the general solution in powers of ε including a term for slow timescale phase shifts $\theta(\tau)$. We then list the equations in a hierarchy of linear maps ordered by powers of ε and use the Fredholm alternative to guarantee existence of each linear map. As a consequence of the Fredholm alternative theorm, we derive the dynamics of the unknown term $\theta(\tau)$.

1.6 OUTLINE

In chapter 2, we extend the theory of weakly coupled oscillators to the case where there is one slowly varying parameter. Once we derive the theory, we consider biological examples. In one example, we determine the synchronization of pairs of weakly coupled cortical oscillators modulated by the same slowly varying concentration of neurotransmitter. In the last example, we determine the degree of synchronization in a population of 51 all-to-all weakly coupled cortical oscillators.

In chapter 3, we analyze a neural field model by reducing the dynamics to scalar variables. On the ring (torus), the one (two) scalar variable(s) represent the position of the bump centroid. The analysis adds to existing studies by assuming a smooth firing rate function (without a necessarily high gain) and any even Mexican-hat shape kernel that produces a bump solution. Using our reduction we rigorously explore the existence and stability of solutions as well as their many bifurcations using classic dynamical systems theory.

In chapter 4, we derive a set of phase equations complementing the mean field description of neurons coupled by strong and slow synapses. By rephrasing the strong and slow coupling as weak and fast coupling, we make the system amenable to a classic phase reduction. We then derive a system of phase equations with the mean field synaptic values as an exogenous parameter. We then show that we can predict synchronization at the spiking level given the mean field description.

2.0 WEAKLY COUPLED OSCILLATORS IN A SLOWLY VARYING WORLD

This chapter is based on [68], with all figure-generation code available on GitHub:
https://github.com/youngmp/park_and_ermentrout_2016

2.1 INTRODUCTION

The theory of weakly coupled oscillators [53, 26, 27] has served very well as a predictor of the dynamics in networks of coupled neural oscillators (for a comprehensive review, see [83]). In the application of this theory, one generally assumes that, while the oscillators may have different intrinsic frequencies, these frequencies are fixed as are the vector fields of the uncoupled limit-cycle oscillators. However, more generally, local regions of the nervous system are constantly modulated by extrinsic inputs and by slow processes such as the accumulation of extracellular ions. Thus, synchronization and other properties are likely to change due to this modulation which can change the frequency, conductances, and even the synapses within an oscillatory network [74].

Neuronal modulators such as acetylcholine, norepinephrine [62], and dopamine [39] are known to alter the firing properties of neurons. These properties, in turn, could alter the synchronization behavior of neurons and more formally, the form that the weak coupling equations take. One of the key components to understanding synchronization of neuronal oscillators is the phase response curve (PRC) which describes how the phase of an oscillator is shifted by the timing of inputs. The PRC plays the key role in determining whether or not a pair of coupled neuronal oscillators will synchronize. In [86, 87], the authors directly

demonstrated that cholinergic modulation of a cortical pyramidal neuron had a profound effect on the shape of the PRC. Acetylcholine is known to directly act on the so-called M-type potassium current and in [20], they showed how changing the strength of this current made a huge difference on the shape of the PRC as well as in the ability of synaptically coupled neurons to synchronize. Neuronal properties are also affected by the extracellular milieu, notably, concentration of extracellular potassium which can profoundly alter excitability of neurons [17]. Rubin et al [81] showed that the synchronization between two coupled neurons was strongly dependent on the mean concentration of extracellular potassium. Jeong and Gutkin [45] showed the changes in the reversal potential of GABAergic conductances changed the ability of neurons to synchronize; the reversal potential is mainly driven by extracellular chloride. Thus, since many neuromodulators as well as the ionic concentrations are constantly changing, it is important to see how this time varying environment alters the ability of neurons to synchronize.

In two recent papers Kurebayashi et al [55, 56], extended the notion of phase reduction to oscillators that are subject to large slowly varying parameters. They demonstrated that the evolution of the phase depended, not just on the instantaneous frequency of the oscillator, but, also on the rate of change of the slowly varying parameter. in this chapter, we re-derive the phase equation in [55] by using the method of adiabatic invariance [47] (Chapter 12.1.2) and incorporate the slow variation of parameters into weak coupling of oscillators using the Fredholm alternative. Thus we have a theory to predict oscillator synchrony and whether or not synchrony is stable, in the presence of a slowly varying parameter. Moreover, because we only assume the parameter to be slowly varying, our theory is shown to accurately predict phase differences with periodic, quasi-periodic, and stochastic slowly varying parameters.

We first derive the equations for the phases and the phase-differences for a pair of coupled oscillators that are subject to slow changes in a parameter. Next, we apply the theory to the Hopf oscillator (so-called $\lambda - \omega$ system, [51]) where all of the required functions for our analysis can be exactly derived. We then consider a biophysical Hodgkin-Huxley model for pyramidal neurons (the simplified "Traub" model [20]). This model includes an M-type potassium current, so in our analysis and simulations, we allow the conductance to slowly change as a model for cholinergic modulation. We conclude with a discussion and contrast

the results with fast modulation.

2.2 METHODS

2.2.1 Weakly Coupled Oscillators With a Slowly Varying Parameter

We consider a pair of weakly coupled slowly-varying oscillators:

$$\begin{aligned} \frac{dX^a}{dt} &= F(X^a, q(\epsilon t)) + \epsilon G_a(X^b, X^a) \\ \frac{dX^b}{dt} &= F(X^b, q(\epsilon t)) + \epsilon G_b(X^a, X^b) \end{aligned} \tag{2.1}$$

where $0 < \epsilon \ll 1$ is a small parameter. We assume that the slowly varying parameter, q, lies in an interval $Q := [q^-, q^+]$ such that for each $q \in Q$, the system:

$$\frac{dX}{dt} = F(X, q)$$

has an asymptotically stable limit cycle with frequency $\omega(q)$. The period of the oscillators is just $T(q) = 2\pi/\omega(q)$. Thus, each of the two oscillators is modulated by a common slowly varying signal, $q(\epsilon t)$ that can alter the shape and frequency of the rhythm but does not destroy its existence. The functions $G_{a,b}$ represent the weak coupling between the two oscillators. If there is no modulation of the oscillations, then, we can regard equation (2.1) as a standard weakly coupled system. However, the slow modulation changes the dynamics and interactions in a way that we will now demonstrate. We point out that [55] derived the phase modulation for a single slowly varying oscillator using successive changes of variables and showed that the "naive" phase approximation was not valid. More precisely, the term $\beta(\tau)$ defined in equation (2.9) accounts for possibly large variations in the slowly varying parameter. Therefore, omitting this term (the "naive" approximation) from equations (2.7)–(2.8) results in a poor phase approximation in the case of a single forced oscillator. Here, we introduce a simpler way to derive the same equations using a standard adiabatic approximation [47], and extend the results to coupled oscillators. In the coupled oscillator case, the "naive" phase approximation is valid.

Clearly, there are two time scales in this problem, a slow time scale, $\tau = \epsilon t$ and a fast time scale, s that is related to t. To put everything on a similar fast time scale, we generally allow that

$$\frac{ds}{dt} = g(\tau, \epsilon)$$

and expand to get a relationship between s and t that is $\tau-$dependent. However, we need only terms in the lowest order in the fast time scale, so we will simply cut to the chase and write $s = \omega(q)t$, so that the oscillators are all $2\pi-$periodic in s. (For the time being, we have suppressed the implicit τ dependence of the fast time scale, by just putting the parameter q in the frequency, but, in fact, q is just shorthand notation for $q(\tau)$.)

Before continuing with the perturbation, we introduce some additional notation. Let $U_0(s, q)$ be the limit cycle solution to the uncoupled system

$$\omega(q)\partial U/\partial s = F(U, q), \tag{2.2}$$

and let $A(s, q) := D_U F(U_0, q)$ be the linearization of the uncoupled system evaluated at the limit cycle. By taking the derivative with respect to s on both sides of equation (2.2), we see that the linear equation

$$L(s, q)Y := \omega(q)\frac{\partial Y}{\partial s} - A(s, q)Y = 0 \tag{2.3}$$

has a periodic solution given by $\partial_s U_0(s, q)$ where the notation, ∂_s means differentiation with respect to the first component in U_0. Associated with the set of $2\pi-$periodic functions is an inner product defined as

$$\langle Y_1(s), Y_2(s)\rangle = \int_0^{2\pi} Y_1(s) \cdot Y_2(s)\ ds,$$

where $Y_1 \cdot Y_2$ is the standard Euclidean dot product. With this inner product, the linearized equation has a well-defined adjoint operator:

$$L^*(s, q)Y := \omega(q)\frac{\partial Y}{\partial s} + A^T(s, q)Y, \tag{2.4}$$

from which we attain the adjoint equation,

$$\omega(q)\frac{\partial Y^*}{\partial s} = -A^T(s, q)Y^*$$

where A^T is the transpose. There is a unique $2\pi-$periodic solution to the adjoint equation, which we call $Z(s,q)$ such that

$$Z(s,q) \cdot \frac{\partial U_0(s,q)}{\partial s} = 1.$$

Finally, the linearization has the Fredholm alternative property [47]. That is, there is a $2\pi-$periodic solution to:

$$L(s,q)Y = b(s) \tag{2.5}$$

where $b(s)$ is $2\pi-$periodic and L is defined in (2.3) if and only if

$$\int_0^{2\pi} Z(s,q) \cdot b(s)\ ds = 0.$$

With these preliminaries defined, we are now ready to analyze weak coupling of slowly varying oscillators.

We assume that the solutions to equation (2.1) can be expressed in a series in ϵ and have the form

$$\begin{aligned} X^a(t,\epsilon) &= X_0^a(s,\tau) + \epsilon X_1^a(s,\tau) + \dots \\ X^b(t,\epsilon) &= X_0^b(s,\tau) + \epsilon X_1^b(s,\tau) + \dots . \end{aligned}$$

To lowest order, we must have

$$\omega(q(\tau))\frac{\partial X_0^{a,b}(s,\tau)}{\partial s} = F(X_0^{a,b}(s,\tau), q(\tau)).$$

The $2\pi-$periodic limit cycle solution to this problem is

$$X_0^{a,b}(s,\tau) = U_0(s + \theta^{a,b}(\tau), q(\tau))$$

where $\theta^{a,b}(\tau)$ are slowly varying arbitrary phase shifts due to the time-translation invariance of the limit cycle. Our goal is to now derive equations for the slow evolution of the phase.

Using the chain rule, we see that $d/dt = \omega\partial/\partial s + \epsilon\partial/\partial\tau$. Thus, after a bit of rearranging, the next order equations are:

$$\begin{aligned} L(s,q(\tau))X_1^a(s,\tau) &= -\partial_s U_0(s+\theta^a(\tau),q(\tau))\frac{\partial\theta^a}{\partial\tau} \\ &\quad -\partial_q U_0(s+\theta^a(\tau),q(\tau))\frac{dq}{\partial\tau} \\ &\quad +G_a[U_0(s+\theta^b(\tau),q(\tau)),U_0(s+\theta^a(\tau),q(\tau))], \end{aligned} \tag{2.6}$$

where $L(s,q(\tau))$ is defined by (2.3). There is a similar equation for $X_1^b(s,\tau)$. Finally, we see that this equation has the form of (2.5), so that there is a $2\pi-$periodic solution if and only if the right-hand side is orthogonal to the adjoint. This leads to the following equations for the phases:

$$\frac{\partial\theta^a}{\partial\tau} = -\beta(\tau) + h_a(\theta^b-\theta^a,\tau) \tag{2.7}$$

$$\frac{\partial\theta^b}{\partial\tau} = -\beta(\tau) + h_b(\theta^a-\theta^b,\tau), \tag{2.8}$$

where,

$$\beta(\tau) = \int_0^{2\pi} Z(s,q(\tau))\cdot\partial_q U_0(s,q(\tau))\frac{\partial q}{\partial\tau}\,ds \tag{2.9}$$

$$h_{a,b}(\phi,\tau) = \int_0^{2\pi} Z(s,q(\tau))\cdot G_{a,b}[U_0(s+\phi,q(\tau)),U_0(s,q(\tau))]\,ds. \tag{2.10}$$

The extra $\beta(\tau)$ term arises due to the fact that the parameter q is slowly varying. Notice in its definition through equation (2.9), that it is proportional to the time derivative of $q(\tau)$. This is the term that [55] emphasized in their analysis. That is, we recover their results if we ignore coupling. We remark that the phase-interaction functions, $h_{a,b}(\cdot)$ are exactly those that would be obtained from standard weak-coupling theory with all parameters held fixed. In absence of coupling, the total phase evolves as

$$\theta(t) = \theta(0) + \omega(q(\tau))t - \epsilon\int_0^t \beta(\epsilon t')\,dt'.$$

If both oscillators are subject to the exact same slowly varying inputs, then the β term becomes irrelevant to their phase difference, $\phi := \theta^b - \theta^a$ which satisfies the simple scalar slowly varying equation [83]:

$$\frac{d\phi}{d\tau} = h_b(-\phi,\tau) - h_a(\phi,\tau) := G(\phi,\tau) \tag{2.11}$$

Equation (2.11) will be our main tool for comparing the phase reduced model to the full model. We remark that the interaction functions are $\tau-$dependent, so that the reduced system for the phase-difference is no longer autonomous and we will not be able to write exact solutions. However, if $h_a = h_b$, then the right-hand side of equation (2.11) is, for each τ, an odd periodic function of ϕ, so that $\phi = 0, \pi$ will always be equilibrium points. That is $G(0,\tau) = G(\pi,\tau) = 0$ for all τ. In this symmetric case, we define H_{odd} to be the odd part of the function h_a.

2.2.2 Mode Truncation

In order to study the phase-reduced equations, we need to get formulae for the $\tau-$dependent interaction functions, $h_{a,b}$. For our first application of the method, these functions are explicitly computable since the oscillation and the adjoint are simple sine and cosine functions. However, for the neural model that we also study (and which gives more interesting results), we need to somehow approximate the required slowly varying functions. To this end, we use `XPPAUTO` [19] to numerically compute the adjoint and interaction functions. For each interaction function we perform a mode truncation (that is, we keep just a few of the Fourier terms). We finish the approximation by deriving a q-dependent equation for the coefficients of the Fourier series expansion.

In general, we expect the q-dependent equation for the coefficients for the Fourier series expansion to be nonlinear, with a high number of terms to preserve any changes in stability. However, we found empirically that a linear relationship between the Fourier coefficients and the slow parameter q, as well as just two sine coefficients, were sufficient to preserve the change in synchrony and bistability between synchrony and antiphase ($\pi-$phase difference), and other interesting phenomena.

2.3 RESULTS

We apply our theory to the $\lambda - \omega$ system and a modified Traub model with adaptation. For each model, we consider three types of slowly varying parameters, which we briefly discuss before delving into the details of each model. We remark that all figure code and relevant data files are available on github at https://github.com/youngmp/park_and_ermentrout_2016

2.3.1 Slowly Varying Parameters

The slowly varying parameter, $q(\tau)$, is explicitly written as three types of slowly varying parameters: periodic (q_p), quasi-periodic (q_{qp}), and stochastic (q_s):

$$\begin{aligned} q_p(\tau) &:= q_0 + q_1 \cos(f\tau), \\ q_{qp}(\tau) &:= q_0 + (q_1/2)(\cos(f\tau) + \cos(f\tau\sqrt{2})), \\ q_s(\tau) &:= q_0 + q_1\zeta(\tau). \end{aligned} \tag{2.12}$$

The terms q_i, f, and ε depend on the system. For the $\lambda - \omega$ system, we choose $f = 1$ and various combinations of q_0 and q_1 because the choice of q_i affects the asymptotic dynamics. Surveying multiple values of q_i provides a more complete demonstration of the dynamics and the accuracy of our theory. For the Traub model, we chose by default $q_0 = 0.3$, $q_1 = 0.2$, and $f = 5$ unless otherwise stated (as in figure 13). The default choice of parameters represents a biophysically realistic parameter range, while the slightly different parameter choice in figure 13 demonstrates the accuracy of our theory when we avoid slow stability changes.

The noisy parameter, ζ, is an Ornstein-Uhlenbeck (OU) process satisfying the stochastic differential equation

$$\mu \mathrm{d}\zeta = -\zeta \mathrm{d}t + \sqrt{\mu}\mathrm{d}W,$$

where $\mu = 1000$. The raw random noise data is normalized so that

$$\zeta(\tau) \in [-1, 1], \quad \forall \tau,$$

and this data is used in all noisy simulations. The OU data may be reproduced by using XPP seeds 1–4.

2.3.2 Lambda-Omega System

We first apply our result to the $\lambda - \omega$ system [51] with weak diffusive coupling,

$$\begin{pmatrix} \dot{x}_j \\ \dot{y}_j \end{pmatrix} = \begin{pmatrix} \lambda(r_j) & -\omega(r_j, q(\tau)) \\ \omega(r_j, q(\tau)) & \lambda(r_j) \end{pmatrix} \begin{pmatrix} x_j \\ y_j \end{pmatrix} + \varepsilon \begin{pmatrix} 1 & -\kappa \\ \kappa & 1 \end{pmatrix} \begin{pmatrix} x_k - x_j \\ y_k - y_j \end{pmatrix} \tag{2.13}$$

where $j, k = 1, 2$ and $k \neq j$; $r_j := \sqrt{x_j^2 + y_j^2}$; and

$$\begin{aligned} \lambda(r) &= 1 - r^2 \\ \omega(r, q) &= 1 + q(r^2 - 1). \end{aligned}$$

When $\varepsilon = 0$, equation (2.13) is equivalent to the Hopf oscillator in polar coordinates,

$$\begin{aligned} \dot{r}_j &= r_j \lambda(r_j) \\ \dot{\theta}_j &= \omega(r_j, q(\tau)). \end{aligned}$$

One can verify the limit cycle for uncoupled system is

$$U_0(s, \tau) = [\cos(s), \sin(s)]^T,$$

and the solution to the adjoint equation (the iPRC) is

$$Z(t) = [q(\tau)\cos(t) - \sin(t), q(\tau)\sin(t) + \cos(t)]^T.$$

Finally, Equation (2.11) for the $\lambda - \omega$ system is

$$\frac{d\phi}{d\tau} = 2\left(\kappa q(\tau) - 1\right)\sin(\phi). \tag{2.14}$$

Note that synchrony ($\phi = 0$) is indeed a fixed point of Eq. 2.14. For a brief stability analysis, we note that equation (2.14) is a separable equation and solve for an implicit solution the differential equation:

$$\tan(\phi/2) = c \exp\left[\int_0^\tau (\kappa q(s) - 1) ds\right]. \tag{2.15}$$

We can write the inside of the exponential as $\tau Q(\tau)$ where $Q(\tau) = (1/\tau)\int_0^\tau [\kappa q(s) - 1]\, ds$. $Q(\tau)$ is the running average of the integrand. Since the integrand is bounded and continuous, the limit of $Q(\tau)$ exists as $\tau \to \infty$. If this limit is positive then the exponential diverges to $+\infty$ and the phase $\phi \to \pm\pi$. Similarly, if the limit is negative, then the exponential goes to zero and ϕ converges to 0.

Figure 6 shows the result of simulating equation (2.13) for different functions of $q(\tau)$. In the left column (labeled a,c,e) the mean value of $q(\tau)$ is less than 1, so that we expect that the phase differences will go to synchrony. In the right panels, the mean value of $q(\tau) > 1$ so that the theory predicts that phase-differences will go to π. This is clearly evident from the simulations of the full model. Furthermore, the approach to equilibrium predicted by the phase model is almost identical to that of the full simulations. There is very little error even in the stochastic cases (panels e,f). Even though this is a highly nonlinear system, the system goes to the stable state that is appropriate for the *average* of the slowly varying parameter. If we break the homogeneity, then the dynamics is more complex and interesting.

2.3.2.1 Heterogeneities So far, the model derivation assumes that both oscillators are identical. However, in general, this will not necessarily be the case. If the differences are $O(\epsilon)$ (that is, small) then we will get some additional terms in the phase equations. To account for this, in general, we add terms to equation (2.1) of the form:

$$\epsilon f_{a,b}(X^{a,b}, \tau) \tag{2.16}$$

where we could also include some τ-dependence in the heterogeneity. For example, in the $\lambda - \omega$ system, we could set

$$\omega_{a,b}(r, q) = 1 + q(\tau)(r^2 - 1) + \epsilon[d_{a,b} + c_{a,b}(\tau)(r^2 - 1)]$$

where the subscripts refer again to the two oscillators. Here, the parameters $d_{a,b}$ are just constants that affect the baseline frequency and $c_{a,b}(\tau)$ are modulatory. With the addition of

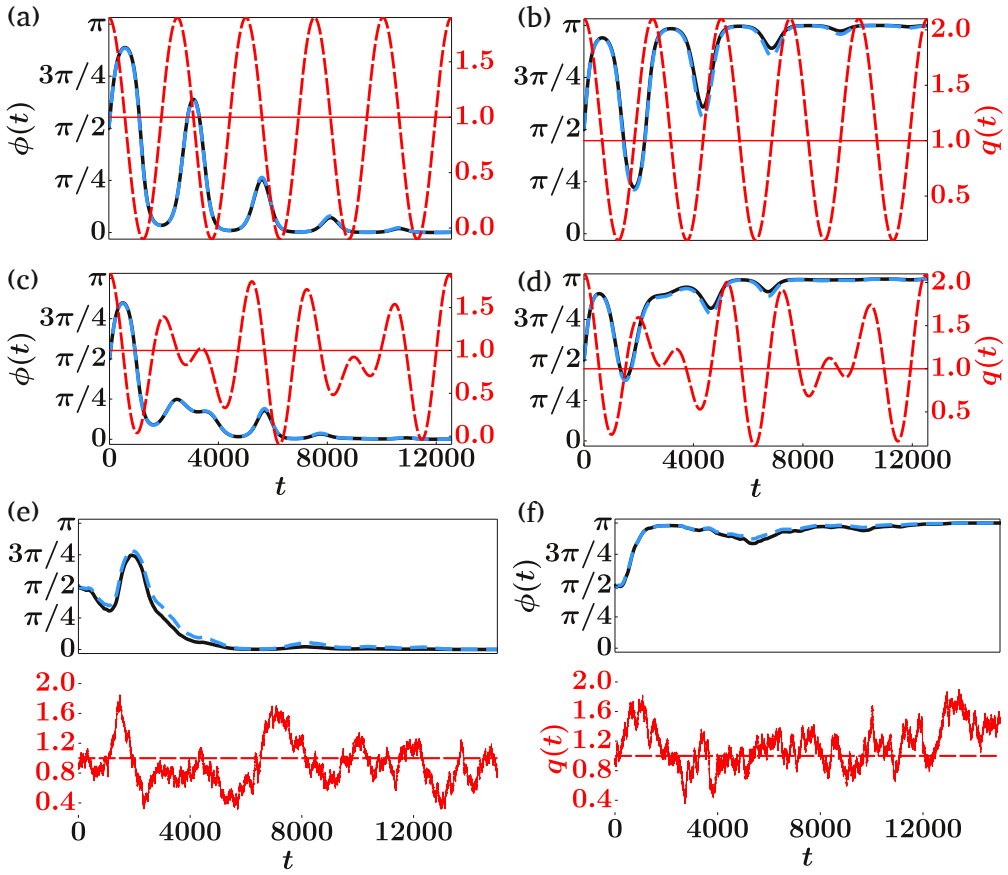

Figure 6: Periodic ((a),(b)), quasi-periodic ((c),(d)) and stochastic ((e),(f)) slowly varying parameters. The phase difference $\phi = \theta_2 - \theta_1$ theory (light blue dashed line) is plotted on top of numerics (black solid line). The slow periodic parameter is shown as a dashed red line. The horizontal line represents the parameter value q at which there is onset or offset of synchrony. For all subfigures, $\varepsilon = 0.0025$, $f = \kappa = q_1 = 1$. (a) Periodic, $q_0 = 0.9$, $\mathbb{E}[q] < 1$. (b) Periodic, $q_0 = 1.1$, $\mathbb{E}[q] > 1$. (c) Quasi-periodic, $q_0 = 0.9$, $\mathbb{E}[q] < 1$. (d) Quasi-periodic, $q_0 = 1.1$, $\mathbb{E}[q] > 1$. (e) Stochastic (OU), $q_0 = 0.85$, $\mathbb{E}[q] = 0.913$, XPP seed 2. (f) Stochastic (OU), $q_0 = 0.9$, $\mathbb{E}[q] = 1.145$, XPP seed 1.

the terms (2.16), the phase equations we get are like equations (2.7-2.8) but have additional

terms:

$$\begin{aligned}\frac{\partial\theta^a}{\partial\tau} &= -\beta(\tau)+\eta_a(\tau)+h_a(\theta^b-\theta^a,\tau)\\ \frac{\partial\theta^b}{\partial\tau} &= -\beta(\tau)+\eta_b(\tau)+h_b(\theta^a-\theta^b,\tau),\end{aligned}$$

where

$$\eta_{a,b}(\tau)=\int_0^{2\pi} Z(s,q(\tau))\cdot f_{a,b}(U_0(s,q(\tau)),\tau)\ ds.$$

Subtracting the two equations yields the more general phase equation with heterogeneities:

$$\frac{d\phi}{d\tau}=\eta_b(\tau)-\eta_a(\tau)+h_b(-\phi,\tau)-h_a(\phi,\tau):=G(\phi,\tau). \tag{2.17}$$

We have still eliminated the commmon $O(1)$ slow variation $\beta(\tau)$, but the explicit heterogeneities appear threough the differences $\eta_b(\tau)-\eta_a(\tau)$.

With this extension, we now alter the simple model by introducing a small frequency difference in the oscillators. For oscillator 2, we replace $\omega(r,q)=1+q(1-r^2)$ with $\omega(r,q)=1+\epsilon d+q(1-r^2)$, so that in absence of coupling, there is an order ϵ frequency difference, ϵd. In this case the equation for ϕ becomes

$$\frac{d\phi}{d\tau}=d+2\left(\kappa q(\tau)-1\right)\sin(\phi). \tag{2.18}$$

This means that $\phi(\tau)$ will no longer generally approach a steady state. In figure 7 we show two simulations with different values of ϵ when there is a slight difference in frequency. For $\epsilon=0.025$, the solutions match for most of the time, but there are places in each segment, where the solutions are about π out of phase. On the other hand, when we reduce ϵ by factor of 10, the solutions to the full model and the phase model are indistinguishable.

As the effects of heterogeneities are rather interesting, even in this simple case, we will now examine equation (2.18) in more detail in order to explain the behavior in figure 7. We can rewrite equation (2.18) as a system with the time rescaled:

$$\begin{aligned}\phi' &= (d+2(q(s)-1)\sin\phi)/f\\ s' &= 1.\end{aligned}$$

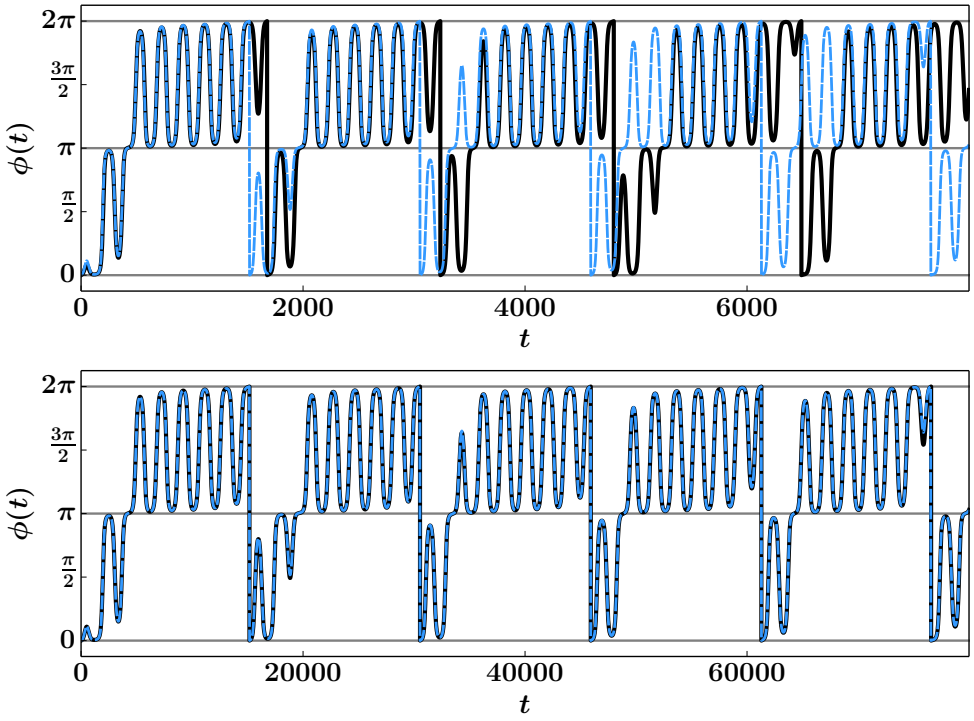

Figure 7: The effects of inhomogeneity on slowly modulated solutions. The slowly varying parameter is chosen to be periodic with $q_0 = 1.1, q_1 = 2, f = 1.3, d = 0.05$, $\kappa = 1$. (a) $\epsilon = 0.025$ (b) $\epsilon = 0.0025$. Black is the full model and blue dashed is the phase-reduced model. The solid gray lines at $\phi(t) = 0 \equiv 2\pi$ ($\phi(t) = \pi$) represent synchrony (anti-phase).

This is an equation on the torus and so the behavior is fairly restricted; in particular, the ratio $\rho = \lim_{\tau\to\infty} \phi/s$, called the rotation number is a continuous function of the parameters. We find three different behaviors as the inhomogeneity d and the frequency f vary. Figure 8 shows the behavior as these parameters are varied. In the upper left part of the diagram (high frequency), above the red curve, $\phi(\tau)$ has a winding number of 0. That is, $\phi(\tau+2\pi) = \phi(\tau)$. This means that the phase-difference, ϕ between the two oscillators is bounded between two values and one oscillator is consistently ahead of the other. In the lower right part of the diagram (low frequency), $\phi(\tau + 2\pi) = \phi(\tau) + 2\pi$, that is, ϕ has winding number 1. This means that the phase-difference between the two neurons stays close to 0 for about half a cycle and close to π for the other half and makes these switches rapidly and periodically; it does not get "stuck" at synchrony or anti-phase. Finally, the middle region (and also the choice used in figure 7) shows that the the phase makes rapid transition, first between π and 2π and then between π and 0. This explains the switching back and forth observed in figure 7. In sum, heterogeneity (even in the simplest form) can add good deal of complexity to the dynamics.

2.3.3 Traub Model with Adaptation

The membrane potential dynamics of the Traub model, V, satisfies

$$\begin{aligned} C\dot{V} &= -g_{Na}m^3h(V - E_{Na}) - (g_k n^4 + q(\tau)w)(V - E_k) - g_l(V - E_l) + I \\ &\equiv f(V, q(\tau)), \end{aligned} \tag{2.19}$$

where $q(\tau)$ is the slowly varying parameter with $q \in [0.1, 0.5]$, $q_0 = 0.3$, $q_1 = 0.2$, and gating variables n, m, h, w satisfying

$$\begin{aligned} \dot{n} &= a_n(V)(1 - n) - b_n(V)n, \\ \dot{m} &= a_m(V)(1 - m) - b_m(V)m, \\ \dot{h} &= a_h(V)(1 - h) - b_h(V)h, \\ \dot{w} &= (w_\infty(V) - w)/t_w(V). \end{aligned}$$

Adaptation in this model is controlled by the magnitude of the $M-$type potassium current (which appears in Equation (2.19) as $q(\tau)w$). This low-threshold, slow current can drastically

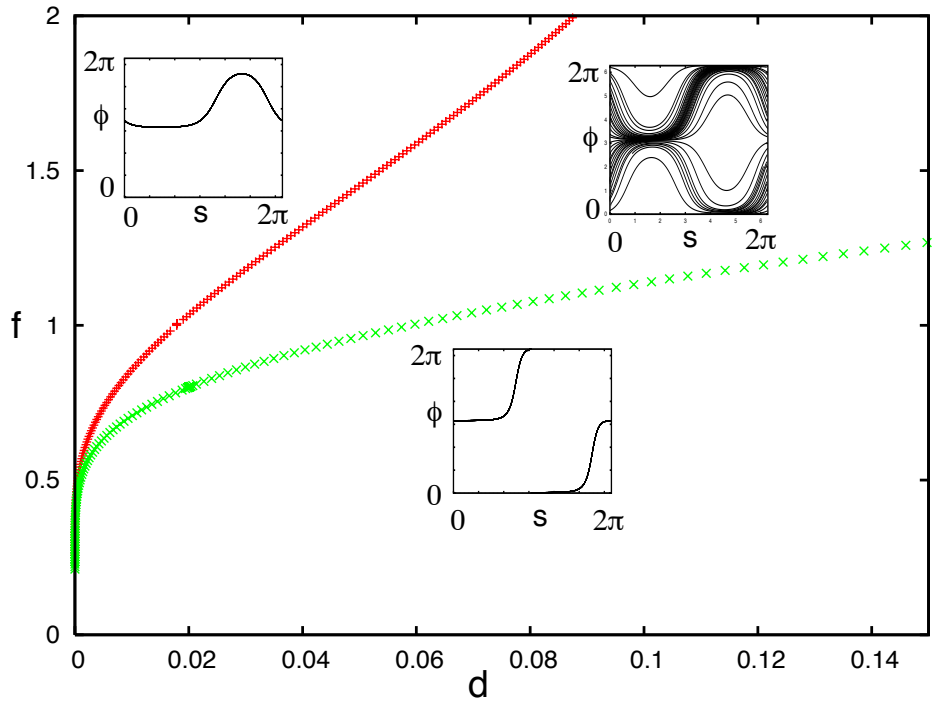

Figure 8: The behavior of equation (2.18) for periodic modulation as a function of the homogeneity, d and the modulation frequency, f. Green points show the border for $1:1$ locking; red points show the border for $0:1$ locking and between these are mixed solutions. Typical phase-planes are shown in each region.

affect the dynamics of the Traub model [20] changing it from Class I excitable (oscillation arises via a saddle-node infinite cycle or SNIC) to class II excitable (oscillation arises via a sub-critical Hopf bifurcation). Because of that change, the adjoint, $Z(t)$ can also drastically change [10, 21] and thus, the interaction function will also be strongly affected. Biologically, this current is quite important since it is altered by acetylcholine, a neuromodulator. Thus, since neuromodulators tend to operate at much slower time scales than the firing rates of neurons, the slow alteration of the $M-$type potassium current is an ideal example of the methods we have developed in this chapter.

We introduce weak coupling by adding a synaptic conductance

$$\frac{dV_1}{dt} = f(V_1, q(\tau)) + \varepsilon g s_2 (E_{syn} - V_1),$$
$$\frac{dV_2}{dt} = f(V_2, q(\tau)) + \varepsilon g s_1 (E_{syn} - V_2),$$

where s_i is the synaptic conductance of V_i and satisfies

$$\dot{s}_i = \alpha(V_i)(1 - s_i) - s_i/\tau_s,$$

where $\alpha(V) = 4/(1 + \exp(-v/5))$ [91].

Figure 9 shows the results of a numerical computation of the adjoint and the odd part of the interaction function. For small values of the M-current ($q = 0.1$) the adjoint (a) is almost strictly positive which is typical for so-called Class I excitable systems where the periodic orbit arises as a SNIC. On the lower panel (b) we see that the $H_{odd}(\phi)$ is small and that synchrony is unstable. (Recall that the phase model satisfies, $\phi' = -2H_{odd}(\phi)$, so that a negative (positive) slope at an equilibrium is unstable (stable).) Anti-phase ($\phi = \pi$) is also unstable, but there are two stable fixed points that are near anti-phase. When there is sufficient M-current ($q = 0.5$), the adjoint has a large negative lobe right after the spike. This qualitative change in the shape of the adjoint leads to the stabilization of the synchronous state (panel b). Thus, as q is varied from a low to high value, we expect that the phase-difference will move toward synchrony (at high values) and away from synchrony (at lower values). Panel b also shows that a two-term sine approximation is reasonable and captures the qualitative (and to some extent, quantitative) shape of the functions. In particular, the full $H_{odd}(\phi)$ and the two-term sine approximation have the same equilibrium point properties.

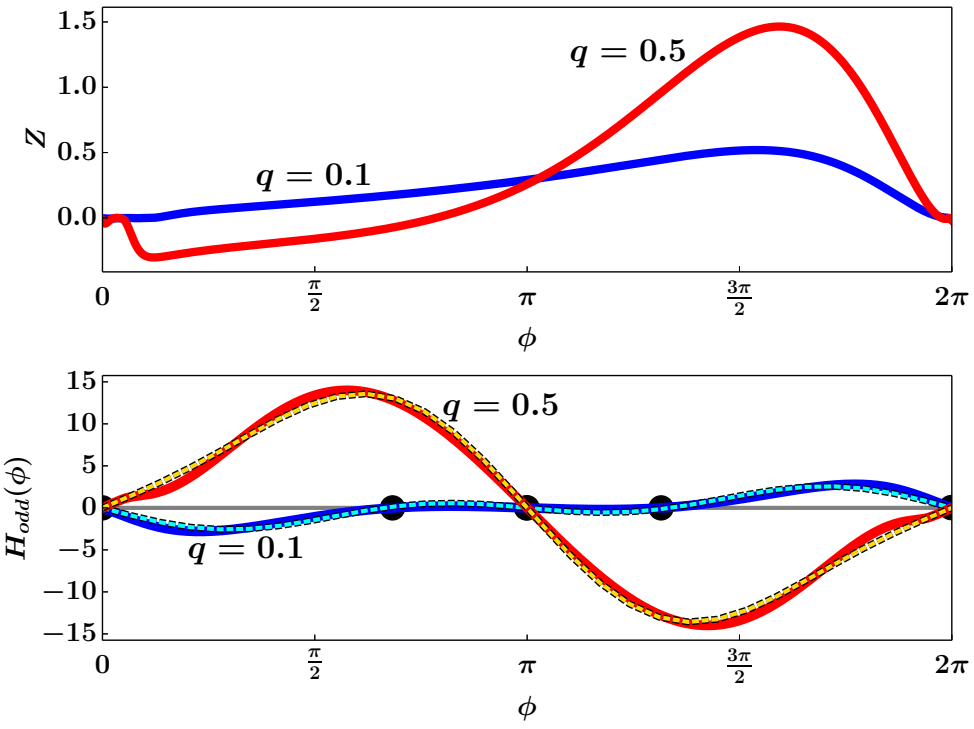

Figure 9: The Traub model (equation (2.19) for two fixed values of q, the M-type potassium current. (a) the adjoints for $q = 0.1$ and $q = 0.5$; (b) The odd part of the interaction functions for $q = 0.1, 0.5$ (thick lines) and two-term sine fit (thin dashed lines) of $H_{odd}(\phi)$. Zero crossings in (b) are denoted by black circles.

For this reason, we make a simple linear interpolation using a two term sine expansion of the interaction as q slowly varies. The approximation is thus:

$$-2H_{\text{odd}} \approx 2(b_1(q(\tau))\sin(\phi) + b_2(q(\tau))\sin(2\phi)),$$

where a linear approximation to $b_i(q)$ passing through the points $(0.1, b_i(0.1))$ and $(0.3, b_i(0.3))$ predicts onset and offset of synchrony sufficiently well:

$$b_i(q) = 5(\hat{b}_i(0.3) - \hat{b}_i(0.1))q + 1.5\hat{b}_i(0.1) - 0.5\hat{b}_i(0.3), \quad i = 1, 2.$$

The number represented by $\hat{b}_i(x)$ is the actual coefficient value at $q = x$ (see appendix A.1.1).

In order to compare the slowly varying phase model to the full model, we need a way to extract the phase from the full model. For the simple $\lambda - \omega$ model, we could get the exact phase since the limit cycle is a circle with a constant angular velocity. One method that is commonly used is to apply a Hilbert transform to the voltage and then extract the phase from this. However, for the Traub model (and, in fact, any model), we have more than just the voltage, so we can extract an approximate phase by picking a point on the unperturbed limit cycle that is closest to the point whose phase we wish to determine. (This is a fairly crude approximation; ideally, we would determine which isochron the point lies on by integrating the initial data forward for several periods and then matching the point. This method is very time consuming [18], so we have opted for the simpler approximation.) Figure 10 shows how this is done. We take the (V, n) coordinates of the simulation and find the value of (V, n) on the projected limit cycle that is closest in distance to the point on the actual trajectory. Since the voltage (V) spans a region of about 150mV and the recovery (n) spans values between 0 and 1, we scale the distance metric accordingly. We compute the variance of $V_0(t), n_0(t)$ over one cycle of the unperturbed limit cycle, call these (σ_V^2, σ_n^2). Thus the distance is:

$$\text{dist}(\Delta V, \Delta n) := \sqrt{(\Delta V)^2/\sigma_V^2 + (\Delta n)^2/\sigma_n^2}.$$

We define the phase of a point $(V(t), n(t))$ to be the value ϕ that minimizes:

$$\text{dist}(V(t) - V_0(\phi T/(2\pi)), n(t) - n_0(\phi T/(2\pi))),$$

where T is the natural period of the unperturbed limit cycle. We pick the comparison limit cycle (V_0, n_0) for a fixed value of the slowly varying parameter that is the mean value. However, as the figure shows, the phase portrait is very similar for two different values of q. As we will see later, this method produces a very reasonable approximation of the phase.

The next three figures compare the approximated phase model with the approximated phase extracted from the full model. That is, there are several levels of approximation to compare the theory to the full model. As described above, we approximate the function $G(\phi, \tau)$ in equation (2.11) by two sine terms whose coefficients are $\tau-$dependent (cf Figure 9b). We apply the same slowly varying function for the conductance of the adaptation current to get the $\tau-$dependence for the phase model. We extract the approximate phase-difference from the full model and compare the result with the phase-difference derived from equation (2.11). Figure 11 shows the result of letting q vary periodically in time; the period is 5 seconds. The dashed red curves show the modulation and the red line shows the mean value. The light blue curve is the phase-difference as predicted by equation (2.11) and the black dots are the instantaneous approximate phase-differences from the model equations. Each dot represnts the phase value at approximately 1/300 of one period. Because the period of the oscillation varies from 12.65s to 24.6s as a function of the slowly varying parameter, we can not give a precise total number of cycles. However, based on the total times one oscillator passes through zero phase, we estimate that there are 245 total cycles.

On the falling phase of the modulation (say, $t = 2.5 - 5$, $t = 8 - 10$, etc) the phase model and the full model agree very closely, On the rising phase, the reduced system lags the full system by quite a bit. Since both the rising and falling parts of the stimulus include all ranges of q, this difference cannot be due to a bad approximation of the interaction functions. As we noted above, the synchronous solution is a fixed point and for a range of q, it is attracting. Because synchrony is a fixed point and we are slowly changing from stable to unstable, there is great sensitivity at the transition. Small changes (such as ignoring small higher order terms in the perturbation) can have drastic effects on the "jump-up" time as synchrony loses stability. This is an example of a slow passage through a bifurcation [61]. To see what we mean here, we simulate the phase-model with the periodic stimulus and perturb the phase-difference, ϕ by slightly increasing it when it is close to 0. Figure 12 shows the

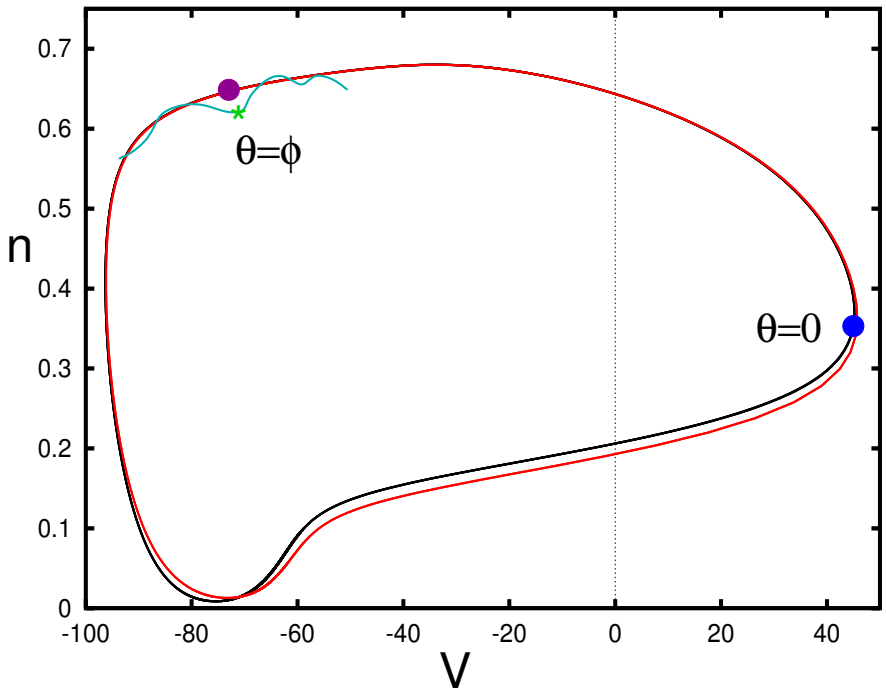

Figure 10: How the phase is extracted. A trajectory in green is shown near the limit cycle (red, for $q = 0.1$). The point (asterisk) on the trajectory is closest to the magenta point on the limit cycle which has phase ϕ, so we assign this phase. The black curve is the projection of the limit cycle for $q = 0.5$.

result of such a manipulation. By increasing $\phi(t = 164)$ from, say, 10^{-14} to 10^{-4} (this is still an order of magnitude smaller than the ϵ used in the simulations), we can advance the "jump-up" time by almost an eighth of the cycle. The inset of the figure shows that $d\phi/dt$ is very small at this point. For this reason, we can expect that the main error will be on the up-jump since ϕ has to escape from the equilibrium point at zero. We will see similar, although less drastic, effects in the subsequent comparisons. By reducing the range of the slow parameter so that it is never close to the value for which synchrony is an attractor, we can do a much better job of tracking the phase-difference through the reduced model. Figure 13 shows an example where the modulated adaptation never gets to a region where synchrony is stable. In this case, the phase-difference for the phase-reduced model never gets close to 0 and the modulation stays away from any bifurcation points.

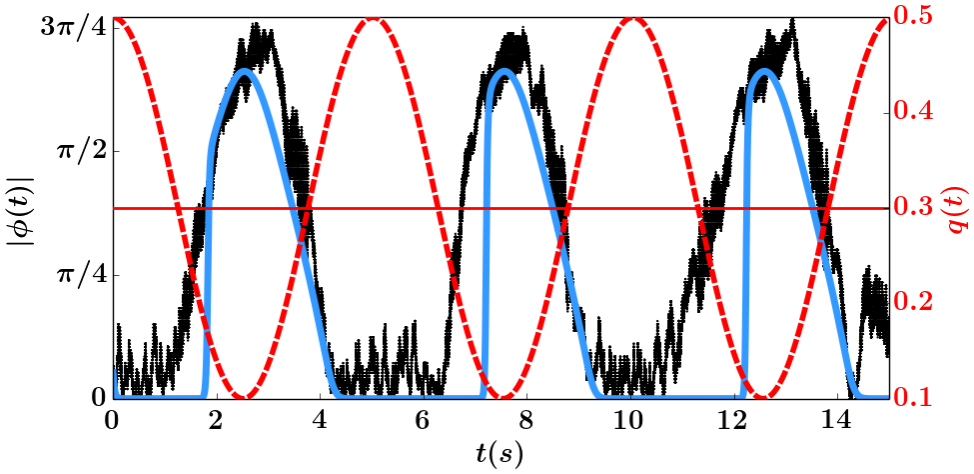

Figure 11: Periodic slowly varying parameter. Absolute value of phase difference $|\phi| = |\theta_2 - \theta_1| \in [0, 2\pi)$ theory (light blue) vs numerics (black dots). The slow periodic parameter is shown as a dashed red line. The horizontal line represents the parameter value q at which there is onset or offset of synchrony. $\varepsilon = 0.0025$, $f = 5$. 245 cycles.

Figure 14 is similar to figure 11, except that the modulation is quasi-periodic. As with the periodic modulation, the phase model follows the full model quite closely once the system jumps away from the synchronous equilibrium. However, like the periodic case, the phase model has a delayed jump-up from synchrony relative to the full model; this is especially

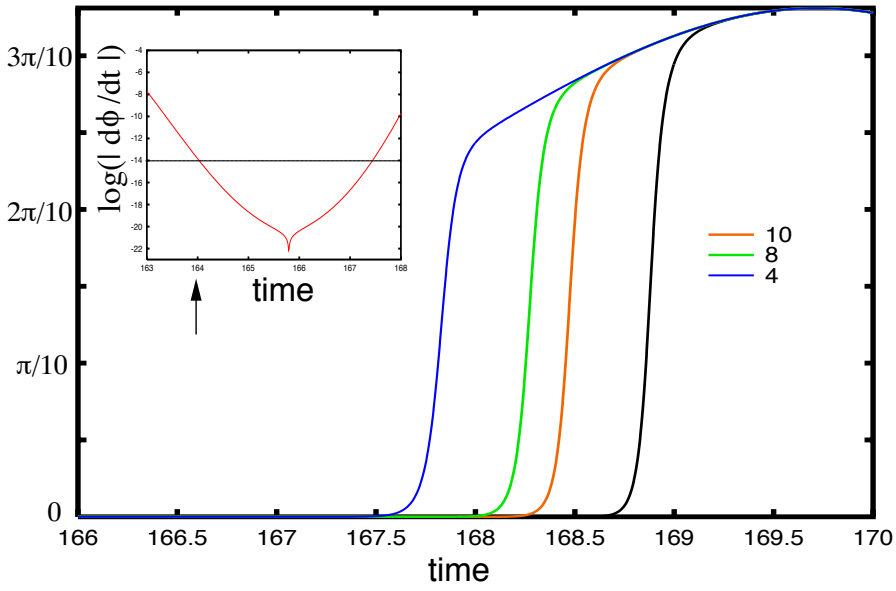

Figure 12: Small perturbations of the phase model near the transition. At $t = 164$, the value of ϕ is increased for 10^{-14} to $10^{-10}, 10^{-8}, 10^{-4}$ (red,green,blue), leading to an earlier jump-up time. Inset shows the log of $d\phi/dt$.

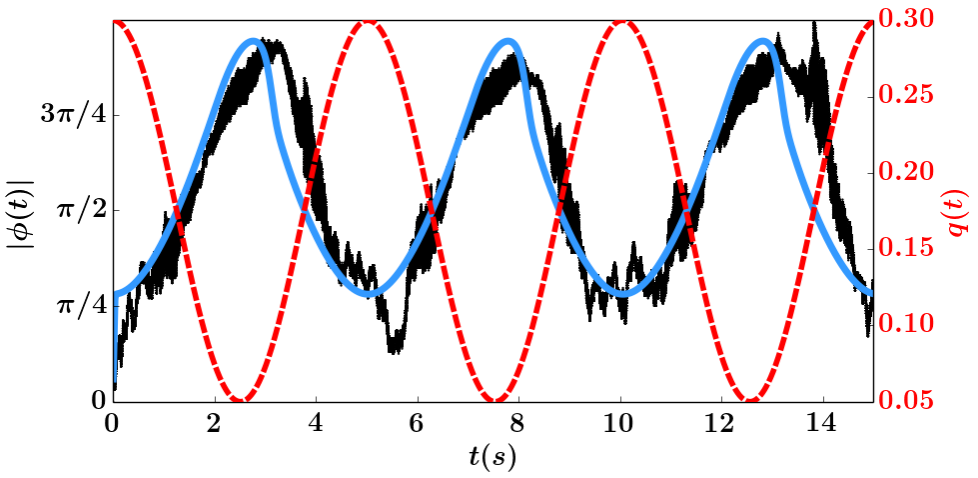

Figure 13: Periodic slowly varying parameter. Absolute value of phase difference $|\phi| = |\theta_2 - \theta_1| \in [0, 2\pi)$ theory (light blue) vs numerics (black dots). The slow periodic parameter is shown as a dashed red line. The slowly varying parameter constants are $q_0 = 0.175$, $q_1 = 0.125$. $\varepsilon = 0.0025$, $f = 5$. 219 cycles.

evident at $t \approx 25$.

Finally, in Figure 15, we use a slowly varying stochastic signal that is generated by an Ornstein-Uhlenbeck process and then rescaled so that the range is $[-1, 1]$. As in figures 11 and 14, the phase model does a fairly good job of tracking the full model. Similarly, the jump up from synchrony is often delayed (especially evident for $t \in [2.5, 4]$) as was the case in all the previous simulations.

The slowly modulated interaction function works well in spite of the many approximations that we have made in the biophysical model.

2.3.4 Networks and synchrony

The methods we have described have, so far, been applied only to two coupled oscillators. There is no reason why we cannot apply them to networks as well. In this case, it is interesting to consider the idea of global synchronization in the presence of modulation. Here we consider

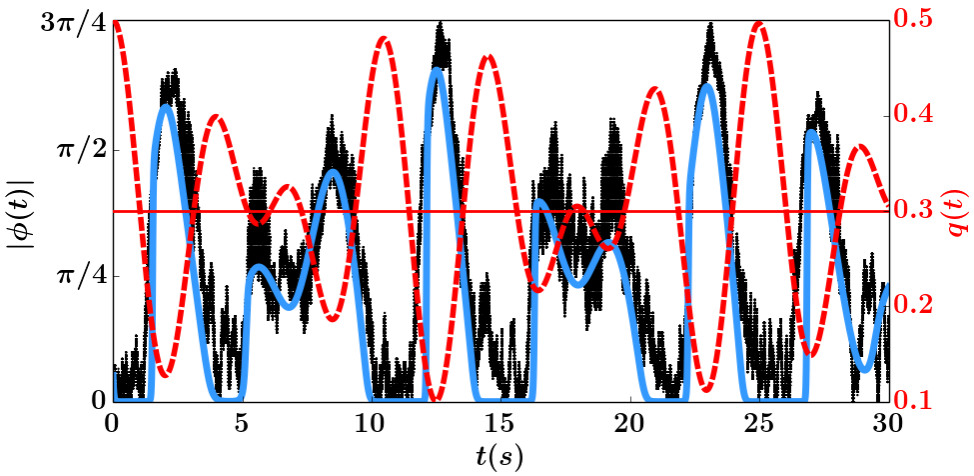

Figure 14: Quasi-periodic slowly varying parameter. The absolute value of phase difference $|\phi| = |\theta_2 - \theta_1| \in [0, 2\pi)$ in theory (light blue) vs numerics (black dots). The quasi-periodic parameter is shown as a dashed red line. $\varepsilon = 0.0025$, $f = 5$. 444 cycles.

(for simplicity) a population of N (we take $N = 51$, here) globally coupled neurons that are subject to slow modulation of the $M-$current as in the previous sections. We weakly couple the Traub model neurons with excitatory coupling and slow periodic modulation of the adaptation. Coupling is all-all and divided by the total number of neurons. Thus, each includes the synaptic current, $I_{syn} = g_{syn} s_{tot}(t)(V - E_{syn})$, where

$$s_{tot}(t) = \frac{1}{51} \sum_{j=0}^{50} s_j(t) \tag{2.20}$$

and $s_j(t)$ are the individual synaptic gating variables for each neuron. Figure 16 shows the result of the simulation. As a surrogate for, say, the local field potential, we look at the total voltage of all the oscillators, $V_{tot} = (1/N) \sum_j V_j(t)$. Panel A shows the full picture of $V_{tot}(t)$ over 12 seconds. It is difficult to see the synchronization, but can be roughly judged by looking at the variance of V_{tot}: larger variance means greater synchrony. (If the oscillators were completely asynchronous, their sum would be close to a constant and so the variance of the sum will be small. If they are completely synchronized, then the variance of the sum

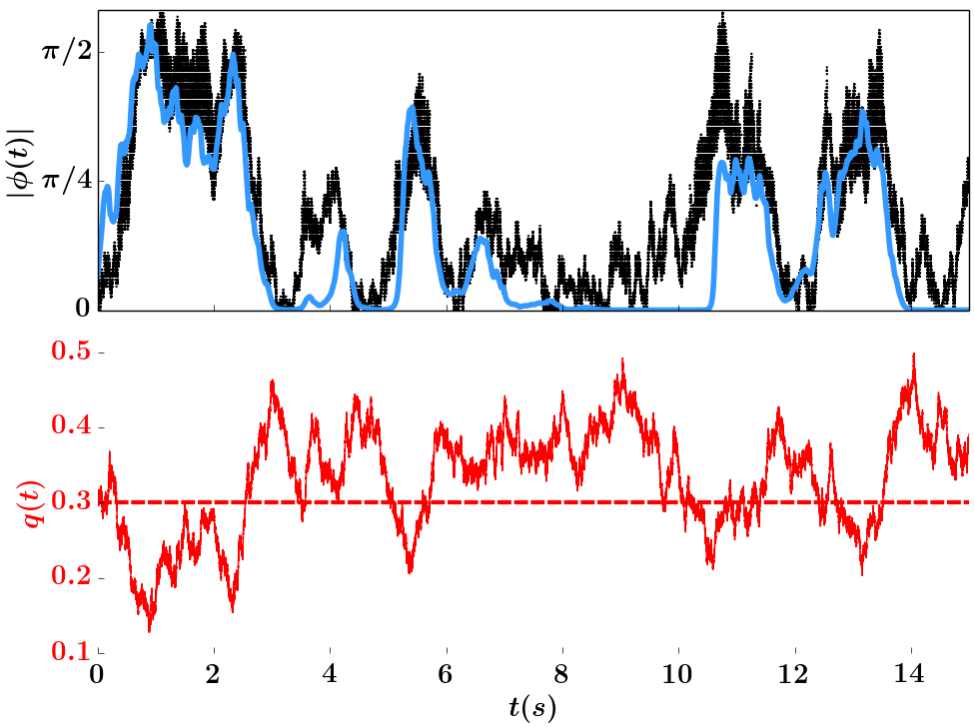

Figure 15: Noisy slowly varying parameter. Absolute value of phase difference $|\phi| = |\theta_2 - \theta_1| \in [0, 2\pi)$ theory (light blue) vs numerics (black dots). The noisy parameter is shown as a dashed red line. XPP seed 4. $\varepsilon = 0.0025$, $f = 5$. 404 cycles.

will be large as the voltage swings over a 150 mV range.) To better illustrate this point, we have also computed the spectrogram (panel B) over this period of time. Notice the large red band that starts at the peak of $q(t)$ and tails off as $q(t)$ tends to zero. Higher bands represent harmonics of the oscillations. This panel also illustrates the dramatic effect that adaptation has on the frequency of the rhythm which ranges between 40 and 100 Hz. Higher frequencies correspond to lower adaptation and weaker synchrony. We can apply the same phase reduction methods to this model to get a system of phase equations:

$$\theta_i' = \frac{1}{N+1} \sum_{j=0}^{N} H(\theta_j - \theta_i, \tau) + \sigma \xi_j$$

where we have added some weak noise, σ to push off the invariant synchrony manifold. To quantify the synchronization, we look at the order parameter:

$$\text{OP} = \frac{1}{N+1}\left|\sum_{j=0}^{N} e^{i\theta_j}\right|.$$

Figure 16c shows the clear periodic waxing and waning of OP as the slowly varying potassium conductance goes from large to small. When $q(t)$ is close to zero (no adaptation), the OP is also near zero and as $q(t)$ tends to its maximum value of 0.5, OP gets very close to 1. Thus, we see that slow modulation of this type of network shows transitions in and out of synchrony. We expect similar effects for non-periodic modulation as long as it is sufficiently slow.

2.4 DISCUSSION

We have shown that it is possible to accurately apply weak coupling theory and phase reduction to oscillators even in a changing environment when the changes are occurring at a sufficiently slow time scale. In a previous paper [81], the authors showed that slow *coupling* between oscillators was equivalent to weak coupling and that when the slow parameters were frozen, then the spike-to-spike synchrony in some moderate interval of time could be predicted by the corresponding interaction function. Here, we formalize this notion and demonstrate that the interaction functions are time-dependent (with respect to the slowly varying parameter) and thus, we do not need to freeze any parameters. In the present theory, the slow forcing was exogenous and imposed on the system. In contrast, in bursting systems, the slow modulation is internally generated as the slow variable goes through various bifurcations between quiescence and oscillations. In [84], Sherman studied two weakly coupled bursters and observed that during the spiking phase (when the fast system is periodic), spikes did not synchronize but were driven to asymmetric and out-of-phase oscillations. The methods we have developed here require the existence of a limit cycle, so they cannot be applied globally to the spike synchronization during autonomous bursting. However, if we make the reasonable assumption that during the quiescent stage of the burst, the two cells

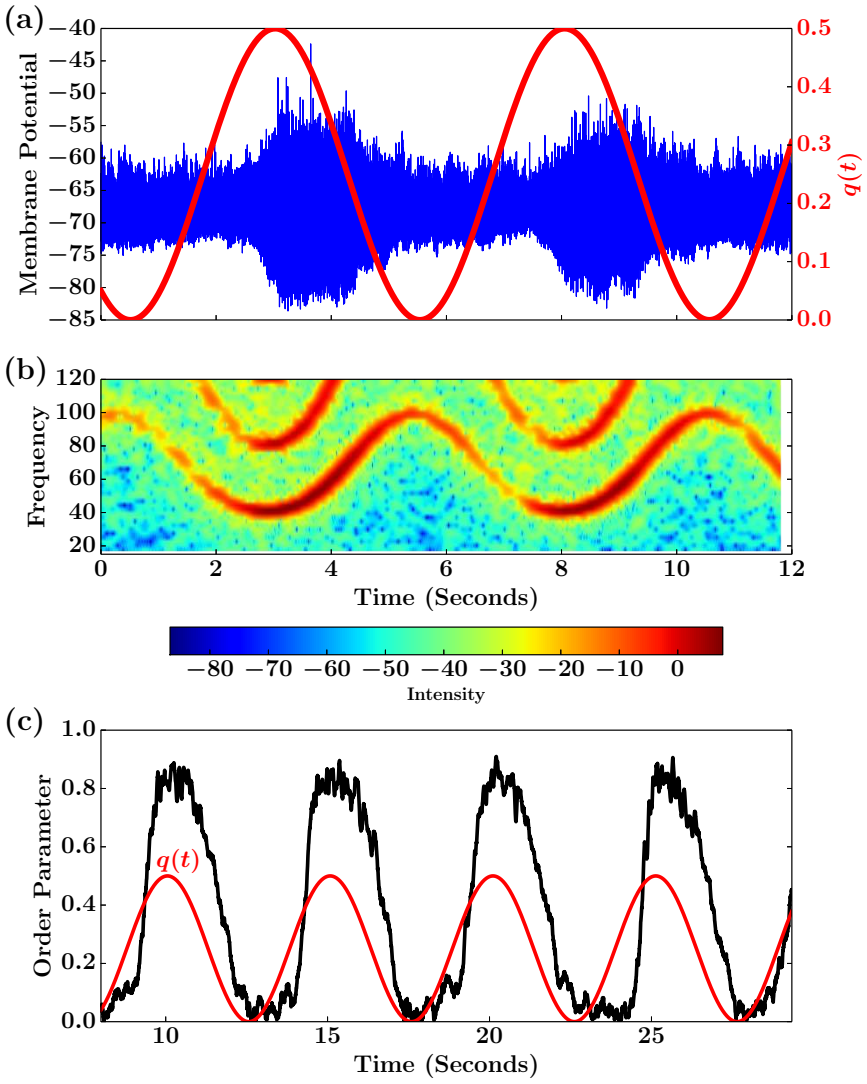

Figure 16: Network of 51 Traub oscillators all-all coupled as in previous figures. (a) Summed voltage $V_{tot} = \sum_j V_j(t)$ along with the modulation of the potassium conductance; (b) Spectrogram showing greatly increased power when the conductance is high; (c) Order parameter from the phase reduction showing a similar increase

are drawn to the slowly changing equilibrium, then, when they jump up, they will be nearly synchronous (but, not quite; if they were precisely synchronous, then they would stay that way for all time). We can then use the theory developed here to study the dynamics of the

spike-to-spike synchrony during the active period of the burst and thus explain in a more formal matter Sherman's results.

Gutkin et al [40] looked at how spiking neural oscillators subjected to a slowly varying input responded to brief perturbations given between spikes. They measured the inter-spike interval (ISI) without the perturbation and then fixed the input so the oscillator had the same period as the ISI. With this fixed oscillator, they computed the phase response curve (the function $Z(t)$ solving the adjoint problem) and used this to predict how the perturbation would affect the spike time in the slowly varying system. The method developed here, could be used to improve this estimate since we know both the slowly varying frequency and the slowly varying function $Z(t;\tau)$. This type of correction was, in fact, the goal of [55].

Slowly varying inputs differ in ways both quantitative and, more importantly, qualitative from faster inputs. For example, suppose that two oscillators receive identical periodic inputs that have a frequency close to the unforced frequency of the oscillators. Then for some range of input amplitudes, we can expect the oscillators to lock in a 1:1 manner with each other and thus be completely synchronized even in absence of coupling. Similarly, weak identical noise applied to two uncoupled oscillators will also synchronize them [75, 88, 23], but the noise has to be sufficiently fast; synchrony falls off rapidly as the time constant of the noise slows down [38]. Thus, fast common rapidly changing inputs will tend to synchronize uncoupled oscillators. But the slow modulations we study here have no such properties. Indeed, looking at equations (2.7-2.8), the common *slow* input cannot move the phase-difference without direct coupling. It would be interesting to look at the synchronization between two slowly varying oscillators that are subjected to fast correlated noise and derive some equations for the expected phase-difference.

2.5 CONCLUSION

The Fredholm alternative provides a useful proof method to re-derive the phase equation in Kurebayashi et al. After obtaining the phase equation, we use the theory of weakly coupled oscillators to derive the interaction function, from which we can study the stability

of synchrony and anti-synchrony.

Despite the phase estimation and the mode truncation, our theory accurately predicts the phase of the Traub model with periodic, quasi-periodic, and stochastic slowly varying parameters (we have similar positive results for the $\lambda - \omega$ system). Because the mode truncation depends on the accuracy of the numerically derived interaction functions, and because the interaction functions in turn depend only on the coupling terms and the iPRC, we can apply the mode truncation method (and subsequently our result) to any autonomous system for which the iPRC and coupling terms are known. The methods here show that we can extend the notion of weak coupling and synchronization of nonlinear neural oscillators to the more realistic scenario in which the environment is changing.

3.0 SCALAR REDUCTION OF A NEURAL FIELD MODEL WITH SPIKE FREQUENCY ADAPTATION

This chapter is based on [70], with all figure-generation code available on GitHub:
https://github.com/youngmp/park_and_ermentrout_2017

3.1 INTRODUCTION

Spatially coherent activity states exist during normal brain function including mammalian path integration, head direction tracking, visual hallucination, working memory, spatial object location, and object orientation [15, 14, 32]. Neural field models (also called continuous attractor neural networks) are one way to understand the mechanism underlying such spatially coherent phenomena [36, 34, 35]. In neural recordings and field models, these spatio-temporal dynamics manifest as traveling waves, spirals, or single or multiple localized "bumps" or "pulses" of activity [15].

Extensive literature exists on the analysis of these behaviors. In particular, [98] show the existence and stability of traveling bumps using multiple-layer neural fields. Several other studies use one of or a combination of short term depression and spike frequency adaptation. In [50], the authors show that traveling pulses exist in a model with synaptic depression and adaptation when synaptic depression is sufficiently weak. For stronger synaptic depression, the traveling pulse ceases to exist via a saddle-node bifurcation. In [34] the authors show that spontaneous motion of a bump solution exists for a neural field with only spike frequency adaptation, and in a similar neural field model with only short term synaptic depression. The authors in [76] show the existence of a traveling pulse solution in a neural field model with

spike frequency adaptation. The previous two studies also show the existence of traveling wavefronts in their respective neural field models.

In addition to the analysis of traveling bumps or wavefronts, rich oscillatory solutions of neural fields are also possible. For example, with spatially localized input current and spike frequency adaptation, a bump solution may oscillate in diameter (breathers)[9, 31, 32, 33], which may play a role in generating epileptiform activity [33] and the processing of sensory stimuli [32]. There also exist studies of a combination of traveling and breathing pulses in an inhibitory-excitatory neural field [30]. In addition to breathers, there exist pulse-emitting neural fields [50, 49], oscillatory wavefronts [8, 9], and spiral waves [49].

Despite this large body of literature, the analyses often require particular assumptions. For example, the existence of "sloshing" solutions – bump solutions that oscillate periodically in the centroid – that arise through a Hopf bifurcation is known under certain assumptions. In early work, sloshers are shown to exist numerically using a rate model with a threshold nonlinearity [41]. In recent work, the authors of [22] show the existence of a Hopf bifurcation with a cosine kernel and a particular choice of smooth firing rate function. In [29], Folias computes a normal form for the Hopf bifurcation using a general kernel, but for a Heaviside firing rate function.

Proving existence of other phenomena also require special assumptions. In [28], the authors consider a neural field model on the real line with synaptic depression and prove the existence of a traveling pulse without a Heaviside assumption, but use the particular choice of a normalized exponential kernel. In [48], the authors use a center manifold reduction to analyze the existence of moving bump solutions. They allow the firing rate to be sigmoidal or a Heaviside, but require a cosine kernel. Similar assumptions are made in [60], where they assume a hyperbolic tangent firing rate function and a cosine kernel.

The most general of such studies, [76], considers a neural field model on the real line with spike frequency adaptation and a singular perturbation approach to construct a constant velocity traveling pulse on the real line with a general firing rate function and a general kernel. However, the existence of other phenomena are not shown.

In this chapter, we introduce a method to analyze the dynamics of a neural field model on a one- and two-dimensional domain with periodic boundary conditions and assume a

smooth firing rate and an even, periodic kernel. Using our method, with standard numerical and analytical dynamical systems tools, we show existence and stability of traveling pulse solutions and oscillatory dynamics. In particular, we analyze sloshing solutions on the ring and torus.

The neural field we consider in this chapter is defined as

$$\begin{aligned} \frac{\partial u(\mathbf{x},t)}{\partial t} &= -u(\mathbf{x},t) + \int_\Omega K(\mathbf{x}-\mathbf{y}) f(u(\mathbf{y},t))\, d\mathbf{y} \\ &+ \varepsilon \left[qI(\mathbf{x}) - gz(\mathbf{x},t) \right], \end{aligned} \tag{3.1}$$

$$\frac{\partial z(\mathbf{x},t)}{\partial t} = \varepsilon\beta[-z(\mathbf{x},t) + u(\mathbf{x},t)], \tag{3.2}$$

where the parameter ε is small, $0 < \varepsilon \ll 1$, and $\mathbf{x}, \mathbf{y} \in \mathbb{R}^n$. For $n = 2$, the kernel function K is an even function in the sense that, $K(-x, y) = K(x, -y) = K(x, y)$, and doubly periodic in the sense that $K(x+2n\pi, y+2m\pi) = K(x, y)$, for any integers n, m. The terms q, g, β are constants. For convenience, we will denote the domain $\Omega = [-\pi, \pi)^m$, with $m = 1, 2$. Thus in one-dimension the domain is a ring and in two-dimensions a torus. The variable $z(\mathbf{x}, t)$ represents linear adaptation [76] and $I(\mathbf{x})$ an external input to the network. External inputs represent persistent stimuli that can be used to entrain the bump and move it to a specific location [6]. We have chosen to make both the timescale of adaptation and *its magnitude* to be small. While there is good biological justification for the former assumption as there are many forms of slow adaptation ([46] section 7.4), the assumption that the adaptation is small is less biological. For the existence of traveling waves, adaptation need not be small [76], but in order to study how the adaptation interacts with stimuli, we need both the adaptation and the stimuli to be the same order of magnitude. The effects of large stimuli to general neural field models are not easy to analyze, so that by treating them as perturbations, we are able to consider the effects in a great deal of detail. Thus, one can regard this assumption as a starting point for the continuation of these phenomena to large amplitude stimuli and adaptation.

Our goal in this chapter is to analyze Equations (3.1),(3.2) when ε is small. When $\varepsilon = 0$, there is a stable "bump" attractor, $u_0(\mathbf{x})$, in the scalar neural field (3.1), i.e., a local stationary peak of $u(\mathbf{x}, t)$ centered at $\mathbf{x} = 0$. The bump attractor satisfies

$$u_0(\mathbf{x}) = \int_\Omega K(\mathbf{x}-\mathbf{y}) f(u_0(\mathbf{y})) d\mathbf{y},$$

where u_0 is nonconstant and even.

Although we allow for a general even, doubly periodic kernel in one- and two-dimensions and a general smooth threshold nonlinearity f, we make particular choices for numerical simulations. We choose f as

$$f(x) = \frac{1}{\exp(-r(x-u_{th}))},$$

where $r = 15, u_{th} = 0.25$. In the one-dimensional case, we choose the kernel to be $K(x) = A + B\cos(x)$ with $A = -0.5, B = 3$ unless stated otherwise. In the two-dimensional case, we form the Mexican-hat function,

$$\hat{K}(r) = Ae^{-(r/\sigma_e)^2} - Be^{-(r/\sigma_i)^2},$$

where $r \equiv r(x, y, n, m) = \sqrt{(x + 2\pi n)^2 + (y + 2\pi m)^2}$. We make the the function $\hat{K}$ periodic in two dimensions using the definition

$$K(x, y) = \sum_{m=-\infty}^{\infty} \sum_{n=-\infty}^{\infty} \hat{K}(r(x, y, n, m)).$$

The parameters here are

$$A = \frac{1}{\sqrt{\pi}\sigma_e}, \quad B = \frac{1}{\sqrt{\pi}\sigma_i},$$

where $\sigma_e = 2$, and $\sigma_i = 3$. For numerical simulations, we find it sufficient to replace the infinite sum with a finite sum from $n, m = -5$ to $n, m = 5$. This is because the function $\hat{K}(r)$ is a decaying exponential and therefore negligible for large r. For example, if a bump solution remains close to the origin, contributions from terms a distance of 10π (i.e., n or m=5) are negligible because $\exp(-(10\pi)^2) \approx 2 \times 10^{-429}$.

To analyze particular dynamics in more detail, we numerically compute the periodic kernel above, then take the Fourier truncation of this doubly periodic kernel,

$$K(x, y) = k_0 + k_1(\cos x + \cos y) + k_2 \cos x \cos y.$$

We now outline the organization of the chapter, as follows: We reduce Equations (3.1),(3.2) to a set of integro-differential equations for the centroid of the bump solution on the ring and torus. We study bifurcations of these equations using numerical and analytical techniques

to show existence and stability of constant velocity traveling bumps and sloshing bumps. Depending on the parameter values g, q, these traveling bumps may traverse the domain periodically or exhibit chaos. Next we turn to the torus domain and perform similar analyses: we study bifurcations of these equations using numerical and analytical techniques to show existence and stability of constant velocity traveling bumps. In addition to the sloshing solutions found in the one-dimensional model, we also find several types of traveling bumps and modulated traveling bumps that densely fill the torus. We also find chaotic motion in some cases. We conclude with a discussion and some contrasts to previous analyses. We remark that all figure generation code and relevant data files with documentation is available on GitHub at https://github.com/youngmp/park_and_ermentrout_2017

3.2 DERIVATION OF THE PHASE EQUATION

We start with Equations (3.1),(3.2). Let $\tau = \varepsilon t$ be a slow timescale and assume that both z and u depend only on $(\mathbf{x}, \tau)$. In this case, we can integrate equation (3.2) to obtain:

$$z(\mathbf{x}, \tau) = z(\mathbf{x}, 0)e^{-\beta\tau} + \beta \int_0^\tau e^{-\beta(\tau - s)} u(\mathbf{x}, s)\ ds.$$

Since we are mainly interested in long term behavior, we can ignore the first exponentially decaying term. With these assumptions, we obtain the following scalar integro-differential equation:

$$\begin{aligned} \varepsilon \frac{\partial u(\mathbf{x}, \tau)}{\partial \tau} &= -u(\mathbf{x}, \tau) + \int_\Omega K(\mathbf{x} - \mathbf{y}) f(u(\mathbf{y}, \tau))\ d\mathbf{y} \\ &+ \varepsilon \left[qI(\mathbf{x}) - g\beta \int_0^\tau e^{-\beta(\tau - s)} u(\mathbf{x}, s)\ ds \right]. \end{aligned} \tag{3.3}$$

We will assume $u(\mathbf{x}, \tau) = U(\mathbf{x}, \tau, \varepsilon)$ and expand U as a power series in ε to get an approximate solution. Thus,

$$U(x, \tau, \varepsilon) = U_0(\mathbf{x}, \tau) + \varepsilon U_1(\mathbf{x}, \tau) + O(\varepsilon^2).$$

Here, we are saying that the lowest order term in the expansion, U_0 is generally some time-dependent function, but we have not yet asserted exactly what form it takes. Substituting this power series into (3.3), we get (with a bit of re-arrangement):

$$0 = -U_0(\mathbf{x},\tau) + \int_\Omega K(\mathbf{x}-\mathbf{y}) f(U_0(\mathbf{y},\tau)) d\mathbf{y} \tag{3.4}$$

$$(LU_1)(\mathbf{x},\tau) = \frac{\partial U_0(\mathbf{x},\tau)}{\partial \tau} - R_1(\mathbf{x},\tau), \tag{3.5}$$

where

$$(Lv)(\mathbf{x},\tau) = -v(\mathbf{x},\tau) + \int_\Omega K(\mathbf{x}-\mathbf{y}) f'(U_0(\mathbf{y},\tau)) v(\mathbf{y},\tau)\ d\mathbf{y},$$

and

$$R_1(\mathbf{x},\tau) = qI(\mathbf{x}) - g\beta \int_0^\tau e^{-\beta(\tau-s)} U_0(\mathbf{x},s)\ ds.$$

The equation for $U_0(\mathbf{x},\tau)$ is the general function for the lowest term in the expansion. However, this lowest order term is not only the steady-state bump solution, but the steady-state bump solution is translation invariant. Thus,

$$U_0(\mathbf{x},\tau) = u_0(\mathbf{x} + \boldsymbol{\theta}(\tau))$$

where $\boldsymbol{\theta}(\tau)$ is a $\tau-$dependent phase shift of the bump, and u_0 is the stationary bump solution. Our goal, then is to determine the dynamics of $\boldsymbol{\theta}(\tau)$. Figure 17 shows typical examples of the stationary bump $u_0(x)$ for one- and two-dimensions.

Before continuing with the perturbation calculation, we establish a few preliminaries. We define the compact linear operator

$$(L_0 v)(\mathbf{x}) = -v(\mathbf{x}) + \int_\Omega K(\mathbf{x}-\mathbf{y}) f'(u_0(\mathbf{y})) v(\mathbf{y})\ d\mathbf{y}$$

and establish several properties of it. Recall that the bump, $u_0(\mathbf{x})$ satisfies

$$-u_0(\mathbf{x}) + \int_\Omega K(\mathbf{x}-\mathbf{y}) f(u_0(\mathbf{y}))\ d\mathbf{y} = 0.$$

By making a change of variables and noting that all functions are periodic in $\mathbf{x}$ (that is, periodic in each of the components of $\mathbf{x}$), then $u_0(\mathbf{x})$ satisfies

$$-u_0(\mathbf{x}) + \int_\Omega K(\mathbf{y}) f(u_0(\mathbf{x}-\mathbf{y}))\ d\mathbf{y} = 0. \tag{3.6}$$

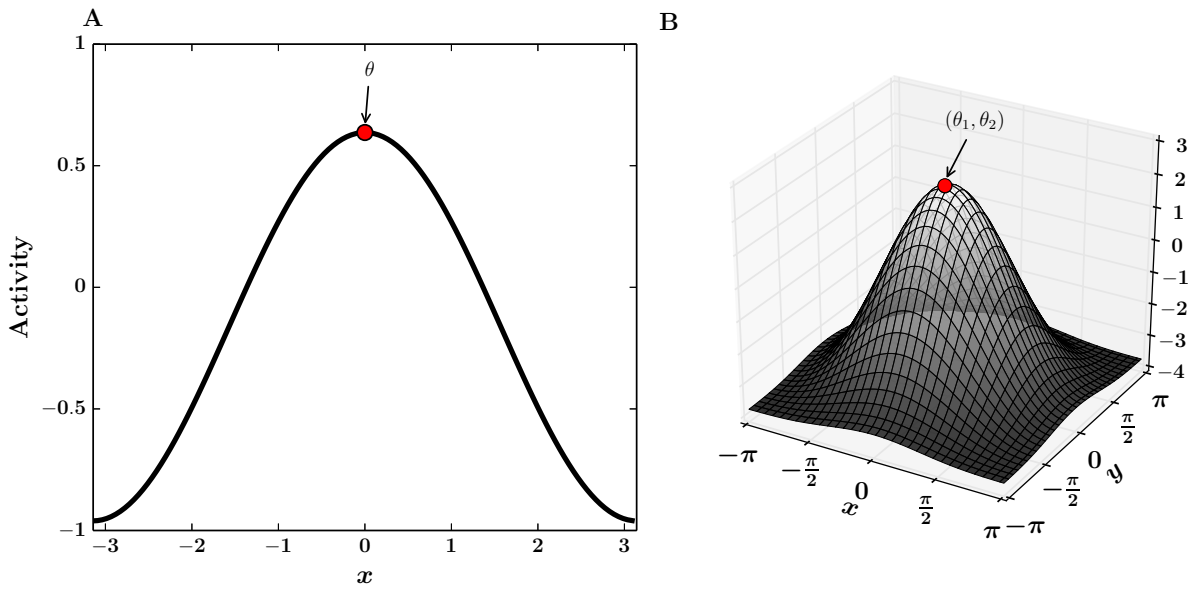

Figure 17: Numerically computed stationary bump solutions on the ring A:, and torus B:. The red circle denotes the centroid of each bump solution. On the ring, we denote the centroid by θ, while we denote the centroid of the bump on the torus by (θ_1, θ_2). Our phase model (Equation (3.9)) describes shifts in the centroid.

Recalling that the domain is $\Omega = [-\pi, \pi)^m$, with $m = 1, 2$, we center u_0 at the origin. Thus, $u_0(\mathbf{x})$ is an even periodic function of $\mathbf{x}$, component-wise. Let $\partial_i u(\mathbf{x})$ denote the partial derivative of $u(\mathbf{x})$ along the x_i direction where $\mathbf{x} = (x_1, x_2)$. If we differentiate (3.6) along one of the axes, we see that

$$-\partial_i u_0(\mathbf{x}) + \int_\Omega K(\mathbf{y}) f'(u_0(\mathbf{x} - \mathbf{y})) \partial_i u_0(\mathbf{x} - \mathbf{y}) \, d\mathbf{y} = 0.$$

and changing variables again, we rewrite this as

$$-\partial_i u_0(\mathbf{x}) + \int_\Omega K(\mathbf{x} - \mathbf{y}) f'(u_0(\mathbf{y})) \partial_i u_0(\mathbf{y}) \, d\mathbf{y} = 0, \tag{3.7}$$

so we see that $L_0 \partial_i u_0(\mathbf{x}) = 0$. In other words, the linear operator, L_0 has an $m-$dimensional nullspace spanned by the principle directional derivatives of $u_0(\mathbf{x})$. With the natural inner product

$$\langle u(\mathbf{x}), v(\mathbf{x}) \rangle = \int_\Omega u(\mathbf{x}) v(\mathbf{x}) \, d\mathbf{x}$$

the operator L_0 has an adjoint

$$(L^* v)(\mathbf{x}) = -v(\mathbf{x}) + f'(u_0(\mathbf{x})) \int_\Omega K(\mathbf{x} - \mathbf{y}) v(\mathbf{y}) \, d\mathbf{y}.$$

By multiplying equation (3.7) by $f'(u_0(\mathbf{x}))$, we see that the nullspace of L^* is spanned by $v_i^*(\mathbf{x}) = f'(u_0(\mathbf{x})) \partial_i u_0(\mathbf{x})$. Since $u_0(\mathbf{x})$ is an even periodic function, componentwise, we note that $\partial_1 u_0(\mathbf{x})$ is even in x_2 and odd in x_1 where $\mathbf{x} = (x_1, x_2)$; $v_1^*(\mathbf{x})$ has the same property, while $\partial_2 u_0(\mathbf{x}), v_2^*(\mathbf{x})$ are even in x_1 and odd in x_2. These properties imply the $\langle \partial_i u_0(\mathbf{x}), v_k^*(\mathbf{x}) \rangle = 0$ when $i \neq k$. We also have

$$\langle \partial_i u_0(\mathbf{x}), v_i^*(\mathbf{x}) \rangle = \int_\Omega f'(u_0(\mathbf{x})) [\partial_i u_0(\mathbf{x})]^2 \, d\mathbf{x} = \mu > 0.$$

Finally, the Fredholm alternative holds for L_0. That is, for any continuous periodic function $b(\mathbf{x})$,

$$(L_0 v)(\mathbf{x}) = b(\mathbf{x})$$

has a bounded solution if and only if

$$\langle v_i^*(\mathbf{x}), b(\mathbf{x}) \rangle = 0$$

for $i = 1, \ldots, m$ [47].

With these technical issues aside, we turn to equation (3.5), which we can rewrite as

$$(L_0 U_1)(\mathbf{x}, \tau) = (\partial_1 u_0(\mathbf{x} + \boldsymbol{\theta}(\tau)), \partial_2 u_0(\mathbf{x} + \boldsymbol{\theta}(\tau))) \cdot \frac{d\boldsymbol{\theta}(\tau)}{d\tau} - R_1(\mathbf{x}, \tau)$$

Writing $\boldsymbol{\theta}(\tau) = (\theta_1(\tau), \theta_2(\tau))$ and applying the m conditions for the Fredholm alternative, we arrive at

$$\mu \frac{d\theta_i}{d\tau} = q J_i(\boldsymbol{\theta}) + W_i(\boldsymbol{\theta}) - g\beta \int_0^\tau e^{-\beta(\tau - s)} H_i(\boldsymbol{\theta}(s) - \boldsymbol{\theta}(\tau)) ds \tag{3.8}$$

where

$$\begin{aligned}
\mu &= \int_\Omega f'(u_0(\mathbf{x}))[\partial_i u_0(\mathbf{x})]^2 \, d\mathbf{x}, \\
J_i(\boldsymbol{\theta}) &= \int_\Omega f'(u_0(\mathbf{x}+\boldsymbol{\theta}))\partial_i u_0(\mathbf{x}+\boldsymbol{\theta}) I(\mathbf{x}) \, d\mathbf{x}, \\
H_i(\boldsymbol{\theta}) &= \int_\Omega f'(u_0(\mathbf{x}))\partial_i u_0(\mathbf{x}) u_0(\mathbf{x}+\boldsymbol{\theta}) \, d\mathbf{x}.
\end{aligned}$$

We note that because of the symmetry of $u_0(\mathbf{x})$, the functions, $H_i(\boldsymbol{\theta})$ have a similar symmetry which we will exploit in the analysis of Equation (3.8). The derivation here has been fairly general and holds in any dimension although we will focus only on one- and two-dimensional bumps in this model. Figure 18 shows the functions $H(\theta)$, $J(\theta)$ in the one-dimensional case, while Figure 19 shows the functions $H_i(\theta)$, $J_i(\theta)$ in the two-dimensional case.

Remark We have assumed *linear* adaptation in our derivation of the reduced model, but, this is not necessary. We could replace Equation (3.2) by

$$\frac{\partial z(\mathbf{x},t)}{\partial t} = \varepsilon\beta[-z(\mathbf{x},t) + M(u(\mathbf{x},t))]$$

where $M(u)$ is an arbitrary monotonically increasing continuously differentiable function. In this case, we find

$$H_i(\boldsymbol{\theta}) = \int_\Omega f'(u_0(\mathbf{x}))\partial_i u_0(\mathbf{x}) M(u_0(\mathbf{x}+\boldsymbol{\theta})) \, d\mathbf{x}.$$

The new version of H_i has exactly the same properties as the linear case since $M(u_0(x))$ is an even function and its derivative with respect to x is an odd function.

We have reduced the problem of the bump dynamics to slow timescale phase shifts of the bump solution, represented as an integro-differential equation. For simplicity and convenience, we ignore transients by changing the limits of integration in Equation (3.8) from $[0,\tau]$ to $(-\infty,\tau]$. Without this domain change, we would be forced to keep track of transient terms that decay for large τ. We are only concerned with large τ, thus we choose to ignore these transient terms by changing the domain. By applying the change of variables $\xi = \tau - s$, we rewrite the system as

$$\mu\frac{d\theta_i}{d\tau} = qJ_i(\boldsymbol{\theta}) - g\beta\int_0^\infty e^{-\beta\xi} H_i(\boldsymbol{\theta}(\tau-\xi) - \boldsymbol{\theta}(\tau))d\xi.$$

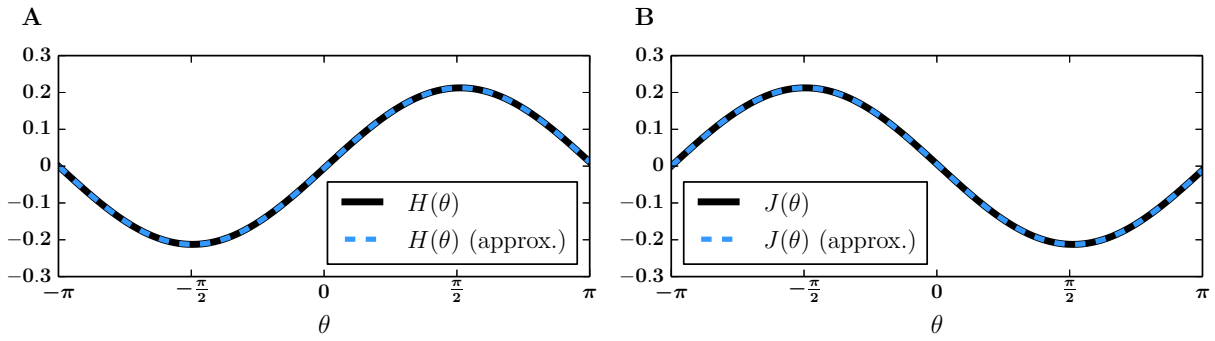

Figure 18: Numerically computed functions for the one-dimensional phase model. A: H (black solid), plotted against sine-function approximation (light blue, dashed). B: J (black solid), plotted against its sine-function approximation (light blue, dashed). Parameters: $I(x) = u_0(x)$ and $K(x) = A + B\cos(x)$, $A = -0.5, B = 3$.

With a trivial change of notation, we arrive at the equations

$$\mu \frac{d\theta_i}{d\tau} = qJ_i(\boldsymbol{\theta}) - g\beta \int_0^\infty e^{-\beta s} H_i(\boldsymbol{\theta}(\tau - s) - \boldsymbol{\theta}(\tau))ds, \quad i = 1, \ldots, m. \tag{3.9}$$

We study stability properties and bifurcations in this form. Note that H_i is implicitly a function of the kernel K.

To facilitate calculations, we first prove the following statements:

1. Each function H_i is odd, i.e., $H_i(-\theta_1, -\theta_2) = -H_i(\theta_1, \theta_2)$. In particular, H_1 is odd in the first coordinate and even in the second coordinate.
2. $H_1(\theta_1, \theta_2) = H_2(\theta_2, \theta_1)$.
3. If the input current $I(\mathbf{x})$ is defined as the steady-state bump solution, then $H_i(\boldsymbol{\theta}) = -J_i(\boldsymbol{\theta})$.

For the first statement, fix θ_1, θ_2 and consider the sum $H_1(-\theta_1, \theta_2) + H(\theta_1, \theta_2)$. By definition this sum is the sum of integrals

$$\int_\Omega f'(u_0(\mathbf{x}))\partial_1 u_0(\mathbf{x})[u_0(x_1 + \theta_1, x_2 + \theta_2) + u_0(x_1 - \theta_1, x_2 + \theta_2)]d\mathbf{x}.$$

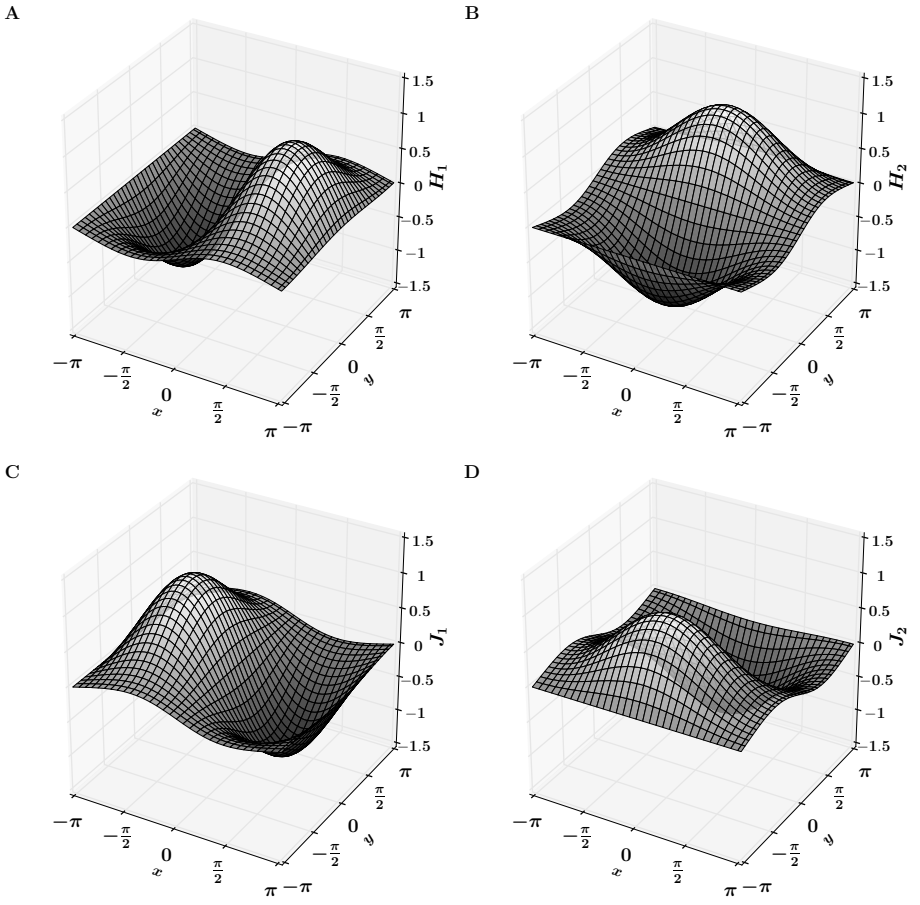

Figure 19: Numerically computed functions for the two-dimensional phase model A: H_1, B: H_2, C: J_1, D: J_2. Note that $H_2(x, y) = H_1(y, x)$. We always choose $I(x) = u_0(x)$. That is, we always use the steady-state bump as the pinning function. With this choice, $J_i = -H_i$ in 1- and 2-dimensions.

Given x_2, and for the sake of clarity, consider the temporary function $\Phi(x_1) := [u_0(x_1 + \theta_1, x_2 + \theta_2) + u_0(x_1 - \theta_1, x_2 + \theta_2)]$. $\Phi(x_1)$ is an even function in x_1 because

$$\begin{aligned}\Phi(-x_1) &\equiv u_0(-x_1 + \theta_1, x_2 + \theta_2) + u_0(-x_1 - \theta_1, x_2 + \theta_2) \\ &= u_0(x_1 - \theta_1, x_2 + \theta_2) + u_0(x_1 + \theta_1, x_2 + \theta_2) \\ &\equiv \Phi(x_1).\end{aligned}$$

These lines follow by the even assumption on each coordinate of the bump solution u_0. The remaining terms in the integrand, $\partial_1 u_0(\mathbf{x})$, and $f'(u_0(\mathbf{x}))$, are odd and even in x_1, respectively. Thus, the integrand is odd in x_1 and the integral evaluates to zero for each x_2 (and indeed, for each θ_1, θ_2). It follows that $H_1(-\theta_1, \theta_2) + H(\theta_1, \theta_2) = 0$, i.e., that the first coordinate is odd.

To show that the second coordinate is even, we use a similar argument. Again, fix θ_1, θ_2 and consider the sum $H_1(\theta_1, -\theta_2) - H(\theta_1, \theta_2)$. By definition, this sum is the sum of integrals

$$\int_\Omega f'(u_0(\mathbf{x}))\partial_1 u_0(\mathbf{x})[u_0(x_1 + \theta_1, x_2 - \theta_2) - u_0(x_1 + \theta_1, x_2 + \theta_2)]d\mathbf{x}.$$

Given x_1, we redefine our temporary function Φ as $\Phi(x_2) := [u_0(x_1 + \theta_1, x_2 - \theta_2) - u_0(x_1 + \theta_1, x_2 + \theta_2)]$ and show that it is an odd function in x_2.

$$\begin{aligned}
\Phi(-x_2) &\equiv u_0(x_1 + \theta_1, -x_2 - \theta_2) - u_0(x_1 + \theta_1, -x_2 + \theta_2) \\
&= u_0(x_1 + \theta_1, x_2 + \theta_2) - u_0(x_1 + \theta_1, x_2 - \theta_2) \\
&= -[u_0(x_1 + \theta_1, x_2 - \theta_2) - u_0(x_1 + \theta_1, x_2 + \theta_2)] \\
&\equiv -\Phi(x_2).
\end{aligned}$$

Again, these lines follow by the even assmption on each coordinate of the bump solution u_0. The integrand term $\partial_1 u_0(\mathbf{x})$ is even in the second coordinate as is the term $f'(u_0(\mathbf{x}))$. Thus, the integrand is odd in x_2 and the integral evaluates to zero for each x_1 (and indeed, for each θ_1, θ_2). It follows that $H_1(\theta_1, -\theta_2) - H(\theta_1, \theta_2) = 0$, i.e., that the second coordinate is even.

We have shown that H_1 is an odd function that is odd in the first coordinate and even in the second coordinate. The proof of H_2 being an odd function that is even in the first coordinate and odd in the second follows using the same arguments, or by using the second statement, which we prove next.

To prove the second statement, we proceed by definition.

$$H_1(\theta_1, \theta_2) = \int_\Omega f'(u_0(x_1, x_2))\partial_1 u_0(x_1, x_2) u_0(x_1 + \theta_1, x_2 + \theta_2) dx_1 dx_2.$$

The steady-state bump solution is invariant under reflections about the unit line, and due to the radial symmetry of the bump solution, its partial derivatives are related by $\partial_1 u_0(x_1, x_2) = \partial_2 u_0(x_2, x_1)$. Thus,

$$H_1(\theta_1, \theta_2) = \int_\Omega f'(u_0(x_2, x_1))\partial_2 u_0(x_2, x_1) u_0(x_1 + \theta_1, x_2 + \theta_2) dx_1 dx_2.$$

Next we relabel the coordinates and flip the order of integration

$$H_1(\theta_1, \theta_2) = \int_\Omega f'(u_0(x_1, x_2))\partial_2 u_0(x_1, x_2) u_0(x_2 + \theta_1, x_1 + \theta_2) dx_1 dx_2.$$

Then we flip the coordinates of u_0, and the resulting integral is by definition $H_2(\theta_2, \theta_1)$:

$$\begin{aligned} &= \int_\Omega f'(u_0(x_1, x_2))\partial_2 u_0(x_1, x_2) u_0(x_1 + \theta_2, x_2 + \theta_1) dx_1 dx_2 \\ &= H_2(\theta_2, \theta_1). \end{aligned}$$

To prove the third statement, suppose that a function $\hat{h}$ on a periodic two-dimensional domain $[0, 2\pi] \times [0, 2\pi]$ is odd in the first coordinate and even in the second so that $\hat{h}(x_1, x_2) = \hat{h}(x_1, -x_2) = -\hat{h}(-x_1, -x_2)$. In particular, it follows that for a given value x_2,

$$\int_0^{2\pi} \hat{h}(x_1, x_2) dx_1 = 0,$$

and therefore

$$\int_\Omega \hat{h}(\mathbf{x}) d\mathbf{x} = 0.$$

This integral property holds when $\hat{h}$ is even in the first coordinate and odd in the second with a similar argument.

If we choose $I(\mathbf{x})$ to be the steady-state bump, then

$$\begin{aligned} J_i(\boldsymbol{\theta}) &= \int_\Omega f'(u_0(\mathbf{x} + \boldsymbol{\theta}))\partial_i u_0(\mathbf{x} + \boldsymbol{\theta}) u_0(\mathbf{x}) \, d\mathbf{x} \\ &= \int_\Omega f'(u_0(\mathbf{x}))\partial_i u_0(\mathbf{x}) u_0(\mathbf{x} - \boldsymbol{\theta}) \, d\mathbf{x}. \end{aligned}$$

Then taking the sum $H_i(\boldsymbol{\theta}) + J_i(\boldsymbol{\theta})$ yields

$$H_i(\boldsymbol{\theta}) + J_i(\boldsymbol{\theta}) = \int_\Omega f'(u_0(\mathbf{x}))\partial_i u_0(\mathbf{x}) [u_0(\mathbf{x} + \boldsymbol{\theta}) + u_0(\mathbf{x} - \boldsymbol{\theta})] \, d\mathbf{x}.$$

For a given $\boldsymbol{\theta}$, the term $[u_0(\mathbf{x}+\boldsymbol{\theta})+u_0(\mathbf{x}-\boldsymbol{\theta})]$ in the integrand is even in both coordinates. The remaining term, $f'(u_0(\mathbf{x}))\partial_i u_0(\mathbf{x})$, when $i=1$ ($i=2$), is odd (even) in the first coordinate and even (odd) in the second. Therefore, when $i=1$ ($i=2$), the integrand is an odd function in the first (second) coordinate and the integral evaluates to zero. It follows trivially that

$$H_i(\boldsymbol{\theta}) = -J_i(\boldsymbol{\theta}). \tag{3.10}$$

This property remains true on the ring using the same argument.

These statements will come in useful in the sections to follow. We now proceed with an analysis of the reduced equations on the ring domain.

3.3 THE RING DOMAIN

In this section, we choose the domain Ω to be the ring. First, we thoroughly analyze the full neural field model through a bifurcation analysis. We then turn to Equation (3.9) on the ring and perform the same bifurcation analysis and through analytical study.

3.3.1 Equivalent Neural Field Model on the Ring

To classify the bifurcations of the full neural field model on the ring, we transform the equations to an equivalent 6-dimensional system of ODEs, allowing us to use dynamical systems software and techniques to analyze the model. Recall that for numerical simulations on the ring, we choose a cosine kernel $K(x) = A + B\cos(x)$. This technique and choice of kernel is the same as that used in [60], where as part of the study they analyze a rate model similar to the model in the current study, but in contrast, the adaptation and input current terms are input directly to the firing rate function. They provide sufficient detail with regards to transforming their rate model to a system of ODEs, but as the details differ from our model, we include the derivation of our model here (in particular they include a phase lag between the peak of the bump activity u and the peak of the adaptation activity z which results in slightly different equations).

Note that with this choice of kernel, the bump solution is also sinusoidal and without loss of generality takes the form $u_0(x) = C + D\cos(x)$. For simplicity we choose $J(x) = u_0(x)$. We are now ready to transform the equations.

Since the functions $u(x,t), z(x,t)$ are periodic in x, we expand them in a Fourier series,

$$u(x,t) = \hat{a}_0(t) + \sum_{n=1}^{\infty} \hat{a}_n(t)\cos nx + \hat{b}_n(t)\sin nx,$$
$$z(x,t) = \hat{c}_0(t) + \sum_{n=1}^{\infty} \hat{c}_n(t)\cos nx + \hat{d}_n(t)\sin nx.$$

and plug into equations (3.1),(3.2). First, a direct substitution into the dynamics of u yields

$$\begin{aligned}
&\hat{a}_0' + \sum_{n=1}^{\infty} \hat{a}_n'\cos(nx) + \hat{b}_n\sin(nx) \\
&= -\hat{a}_0 - \left[\sum_{n=1}^{\infty} \hat{a}_n\cos nx + \hat{b}_n\sin nx\right] \\
&\quad + A\int_\Omega f(u(y,t))dy \\
&\quad + B\cos(x)\int_\Omega \cos(y)f(u(y,t))dy \\
&\quad + B\sin(x)\int_\Omega \sin(y)f(u(y,t))dy \\
&\quad + \varepsilon\left[q(C + D\cos(x)) - g\left(\hat{c}_0(t) + \sum_{n=1}^{\infty} \hat{c}_n(t)\cos nx + \hat{d}_n(t)\sin nx\right)\right].
\end{aligned}$$

We have used the elementary trigonometric identity $\cos(x-y) = \cos(x)\cos(y) + \sin(x)\sin(y)$ to separate the kernel and distribute the integrals. A direct substitution into the dynamics of z yields

$$\begin{aligned}
&\hat{c}_0' + \sum_{n=1}^{\infty} \hat{c}_n'\cos(nx) + \hat{d}_n\sin(nx) \\
&= \varepsilon\beta\left[-\hat{c}_0(t) - \sum_{n=1}^{\infty} \hat{c}_n(t)\cos nx + \hat{d}_n(t)\sin nx\right. \\
&\qquad \left. + \hat{a}_0(t) + \sum_{n=1}^{\infty} \hat{a}_n(t)\cos nx + \hat{b}_n(t)\sin nx\right]
\end{aligned}$$

Next, we group like terms in the Fourier basis, starting with the Fourier coefficients of u:

$$\begin{aligned}
\hat{a}_0' &= -\hat{a}_0 + A\int_\Omega f(u(y,t))dy + \varepsilon[qC - g\hat{c}_0] \\
\hat{a}_1' &= -\hat{a}_1 + B\cos(x)\int_\Omega \cos(y)f(u(y,t))dy + \varepsilon[qD - g\hat{c}_1] \\
\hat{a}_2' &= -\hat{a}_2 + \varepsilon[-g\hat{c}_2] \\
\hat{a}_3' &= -\hat{a}_3 + \varepsilon[-g\hat{c}_3] \\
&\vdots
\end{aligned}$$

and

$$\begin{aligned}
\hat{b}_1' &= -\hat{b}_1 + B\sin(x)\int_\Omega \sin(y)f(u(y,t))dy + \varepsilon[-g\hat{d}_1] \\
\hat{b}_2' &= -\hat{b}_2 + \varepsilon[-g\hat{d}_2] \\
\hat{b}_3' &= -\hat{b}_3 + \varepsilon[-g\hat{d}_3] \\
&\vdots
\end{aligned}$$

We repeat this grouping for the Fourier coefficients of z:

$$\begin{aligned}
\hat{c}_0 &= \varepsilon\beta(-\hat{c}_0 + \hat{a}_0) \\
\hat{c}_1 &= \varepsilon\beta(-\hat{c}_1 + \hat{a}_1) \\
&\vdots
\end{aligned}$$

and

$$\begin{aligned}
\hat{d}_0 &= \varepsilon\beta(-\hat{d}_0 + \hat{b}_0) \\
\hat{d}_1 &= \varepsilon\beta(-\hat{d}_1 + \hat{b}_1) \\
&\vdots
\end{aligned}$$

The pattern is clear at this point: The coefficients of all Fourier modes, where $i > 1$, satisfy

$$\begin{aligned}
\hat{a}_i' &= -\hat{a}_i - \varepsilon g \hat{c}_i, \\
\hat{b}_i' &= -\hat{b}_i - \varepsilon g \hat{d}_i, \\
\hat{c}_i' &= \varepsilon\beta(-\hat{c}_i + \hat{a}_i), \\
\hat{d}_i' &= \varepsilon\beta(-\hat{d}_i + \hat{b}_i).
\end{aligned}$$

Through an elementary stability analysis, all solutions to these equations decay to zero so they are unnecessary to consider. We proceed with the remaining nontrivial terms,

$$\begin{aligned}
u(x,t) &= \hat{a}_0(t) + \hat{a}_1(t)\cos x + \hat{b}_1(t)\sin x, \\
z(x,t) &= \hat{c}_0(t) + \hat{c}_1(t)\cos x + \hat{d}_1(t)\sin x.
\end{aligned}$$

Using this notation, we have the system

$$\begin{aligned}
\hat{a}_0' &= -\hat{a}_0 + A\int_\Omega f(u(y,t))dy + \varepsilon(qC - g\hat{c}_0), \\
\hat{a}_1' &= -\hat{a}_1 + B\int_\Omega \cos(y) f(u(y,t))dy + \varepsilon(qD - g\hat{c}_1), \\
\hat{b}_1' &= -\hat{b}_1 + B\int_\Omega \sin(y) f(u(y,t))dy - \varepsilon g\hat{d}_1, \\
\hat{d}_1' &= \varepsilon\beta(-\hat{d}_1 + \hat{b}_1), \\
\hat{c}_i' &= \varepsilon\beta(-\hat{c}_1 + \hat{a}_1), \quad i = 0, 1.
\end{aligned}$$

Note that we do not need to explicitly write the full Fourier series of f or extract any of its coefficients. In fact, only the lowest two Fourier modes of each integral containing $f(u)$ are relevant as we will now show.

Consider the Fourier series of $f(u(x,t))$:

$$f(u(x,t)) = \hat{\alpha}_0(t) + \sum_{n=1}^{\infty} \hat{\alpha}_n(t)\cos(nx) + \hat{\beta}_n(t)\sin(nx)$$

This expansion exists because f is bounded and integrable on $[0, 2\pi]$. We now evaluate each integral, $\int_\Omega f(u(y,t))dy$, $\int_\Omega \cos(y) f(u(y,t))dy$, and $\int_\Omega \sin(y) f(u(y,t))dy$ in turn. First,

$$\begin{aligned}\int_\Omega f(u(y,t))dy &= \int_\Omega \alpha_0 + \sum_{n=1}^{\infty} \alpha_n \cos(ny) + \beta_n \sin(ny) dy \\ &= \alpha_0 \int_\Omega dy + \sum_{n=1}^{\infty} \alpha_n \int_\Omega \cos(ny)dy + \beta_n \int_\Omega \sin(ny)dy \\ &= 2\pi\alpha_0.\end{aligned}$$

Next,

$$\begin{aligned}&\int_\Omega \cos(y) f(u(y,t))dy = \cos x \int_\Omega \cos(y) \left[\alpha_0 + \sum_{n=1}^{\infty} \alpha_n \cos(ny) + \beta_n \sin(ny)\right] dy \\ &= \alpha_0 \cos x \int_\Omega \cos(y)dy + \sum_{n=1}^{\infty} \alpha_n \int_\Omega \cos(y)\cos(ny)dy + \beta_n \int_\Omega \cos(y)\sin(ny)dy \\ &= \pi\alpha_1\end{aligned}$$

and finally,

$$\begin{aligned}&\int_\Omega \sin(y) f(u(y,t))dy = \sin x \int_\Omega \sin(y) \left[\alpha_0 + \sum_{n=1}^{\infty} \alpha_n \cos(ny) + \beta_n \sin(ny)\right] dy \\ &= \alpha_0 \sin x \int_\Omega \sin(y)dy + \sum_{n=1}^{\infty} \alpha_n \int_\Omega \sin(y)\cos(ny)dy + \beta_n \int_\Omega \sin(y)\sin(ny)dy \\ &= \pi\beta_1.\end{aligned}$$

Thus, the nonlinearity f in the integrand only appears in the dynamics of the first few Fourier coefficients. At each time step in the numerics, we compute the integrals $\int_\Omega f(u(y,t))dy$, $\int_\Omega \cos(y) f(u(y,t))dy$, and $\int_\Omega \sin(y) f(u(y,t))dy$ using Riemann integration at each time step as it is more straightforward than extracting the necessary Fourier coefficients.

We focus our numerical studies on the coefficients $\hat{a}_1$ and $\hat{b}_1$ because they produce the most salient features of the bump solution (the $\hat{a}_0$ coefficient changes as a function of time, but only up to order $O(\varepsilon)$, while the terms $\hat{c}_i$ and $\hat{d}_i$ represent aggregate behavior of the adaptation variable z). By following the fixed points and oscillatory behavior in $\hat{a}_1$ and $\hat{b}_1$, we produce a bifurcation diagram of this system in Figure 20.

Figure 20 shows that there are three main solution types: the pinned or stationary bump, the sloshing bump, and the traveling bump, which traverses the ring at some finite speed. In addition there are small regions of bistability between the sloshing bump and the traveling bump.

3.3.2 Phase Model on the Ring

We now turn to the analysis of the phase dynamics on the ring. The analysis to follow depends on proving the following statements:

1. $H(0) = 0$,
2. $H'(0) > 0$,
3. If $K(x) = A + B\cos(x)$, then $H(\theta) = A'\sin(\theta)$, $A' > 0$, where A' depends on the parameters A, B.

Recall the scalar version of the functions $H_i(\boldsymbol{\theta})$ and $v_i^*(\mathbf{x})$:

$$H(\theta) = \int_\Omega u^*(y)u_0(y+\theta)dy$$
$$u^*(x) = f'(u_0(x))u_0'(x),$$

Because u_0 is even, it follows that $f'(u_0)$ is even, u_0' is odd, and therefore u^* is odd. Noting that

$$H(0) = \int_\Omega u^*(y)u_0(y)dy,$$

where the function $u^*(y)u_0(y)$ is odd, the first statement follows.

For the second statement, we follow the definitions to arrive at

$$H'(0) = \int_\Omega f'(u_0(y))u_0'(y)u_0'(y)dy.$$

The function f is an increasing sigmoidal, thus $f' > 0$. In addition, $u_0'^2 > 0$. Thus, $H'(0) > 0$.

Next, we prove the third statement. With the kernel choice $K(x) = A + B\cos(x)$, the steady-state bump solution is some shifted multiple of cosine, $u_0(x) = C + D\cos(x)$, where C, D implicitly depend on the kernel parameters A, B. Plugging this u_0 into $H(\theta)$ yields

$$H(\theta) = \int_{-\pi}^{\pi} f'(C + D\cos(y))[-D\sin(y)][C + D\cos(y+\theta)]dy.$$

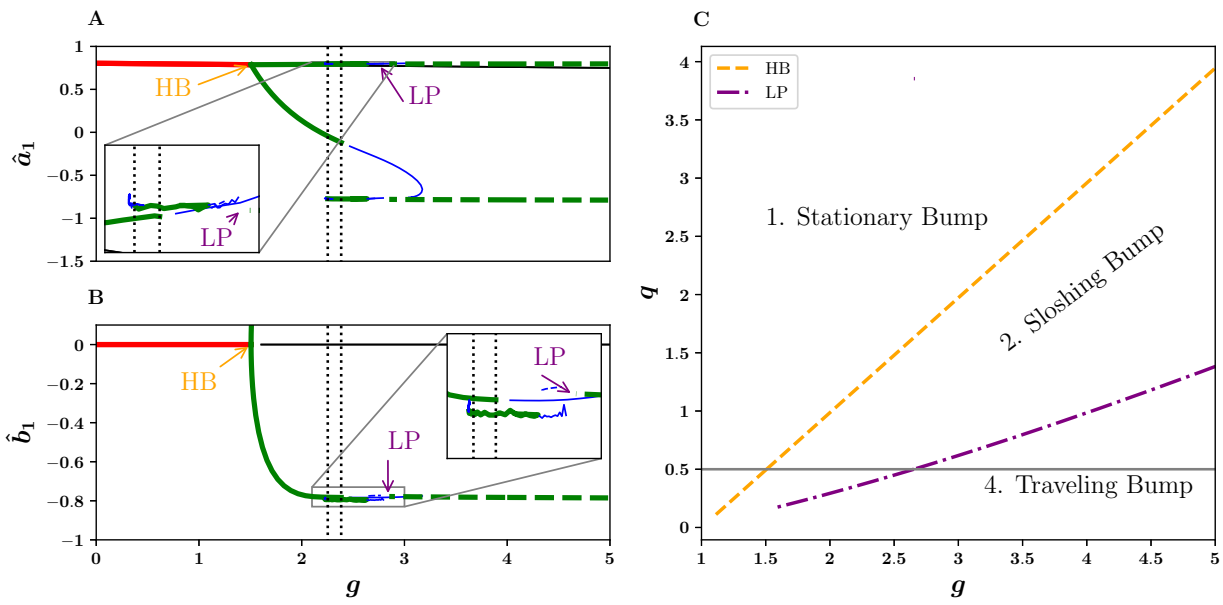

Figure 20: 1- and 2-parameter bifurcation diagrams of the neural field model on the ring. Solid red lines: Stable equilibrium. Solid Green: Stable periodic solutions. Solid blue: Unstable periodic solutions. Solid black: unstable equilibrium. (A,B) Bifurcation diagram in $\hat{a}_1$ and $\hat{b}_1$ for fixed $q = 0.5$. As g increases from 0 to 5, the system undergoes a Hopf bifurcation (HB, orange). Solutions here slosh with a small deviation from the origin. By increasing g, we see a region of bistability (shown in the insets with the interval of bistability marked by vertical dotted black lines), marking the emergence of large-sloshing solutions alongside sloshing solutions. Next, the system reaches a limit point (LP, purple) beyond which there exists a traveling bump solution. For panel B:, the branches of the Hopf bifurcation are symmetric over the x-axis, thus we only show one branch. C: Two parameter bifurcation diagram in g and q. To the left of the Hopf bifurcation (HB, dashed orange line), there is only a stationary bump solution (1.). Motion exists to the right of this dividing line in the form of sloshes (2.) and a traveling bump solution (4.).

Let $h(y) = f'(C + D\cos(y))[D\sin(y)]$, which is an odd function. Recalling that $\cos(y+x) = \cos(y)\cos(x) - \sin(y)\sin(x)$, H simplifies to

$$H(\theta) = -C\int_{-\pi}^{\pi} h(y)dy - \int_{-\pi}^{\pi} h(y)D[\cos(y)\cos(\theta) - \sin(y)\sin(\theta)]dy.$$

Because $h(y)$ is odd, some integrals cancel, and we are left with

$$H(\theta) = A'\sin(\theta),$$

where $A' = D\int_{-\pi}^{\pi} h(y)\sin(y)dy$.

From these statements, it follows that $\frac{dJ}{d\theta}\big|_{\theta=\overline{\theta}} < 0$ and $J(\overline{\theta}) = 0$ where $\overline{\theta}$ represents a steady-state bump peak. WLOG, we let $\overline{\theta} = 0$ because we generally choose the center of the steady-state bump to be the origin.

Remark: For the more general adaptation (c.f. above), as long as $M(u)$ is differentiable and monotonically increasing, we still have that $H'(0) > 0$..

3.3.2.1 Equivalent Phase Model on the Ring We next show that there are really only two relevant parameters. We can rescale time to obtain

$$\mu\beta\frac{d\theta}{d\tau} = qJ(\theta) - g\int_0^{\infty} e^{-s}H(\theta(\tau - s) - \theta(\tau))ds,$$

where we have re-used τ as the now scaled time $\beta\tau$. Next, divide by $\mu\beta$ to obtain

$$\frac{d\theta}{d\tau} = \hat{q}J(\theta) - \hat{g}\int_0^{\infty} e^{-s}H(\theta(\tau - s) - \theta(\tau))ds, \tag{3.11}$$

with $\hat{q} = \frac{q}{\mu\beta}$ and $\hat{g} = \frac{g}{\mu\beta}$. This rearrangement shows that making adaptation slower by decreasing β is equivalent to increasing the rescaled parameters $\hat{g}$ and $\hat{q}$. For analytic calculations, we will often reference this equation without the hats on the parameters.

For numerical studies of bifurcations in this system, we let $H(\theta) = A'\sin\theta$, from which J follows immediately (see Equation (3.10) and statement 2 above). We once more abuse notation and absorb A' into $\hat{g}$ and into $\hat{q}$, then drop the hats. So we will now study

$$\frac{d\theta}{d\tau} = -q\sin(\theta) - g\int_0^{\infty} e^{-s}\sin(\theta(\tau - s) - \theta(\tau))ds,$$

To numerically integrate this phase equation, we rewrite this differential equation as a system of three equations by exploiting basic differentiation properties of integrals. To begin, we use a trigonometric identity to rewrite the integral in the right-hand side

$$\begin{aligned}\frac{d\theta}{d\tau} &= -q\sin(\theta) - g\int_0^\infty e^{-s}\sin(\theta(\tau-s)-\theta(\tau))ds \\ &= -q\sin(\theta) - g[\cos(\theta)S(\tau) - \sin(\theta)C(\tau)],\end{aligned}$$

where

$$\begin{aligned}S(\tau) &= \int_0^\infty e^{-s}\sin(\theta(\tau-s))ds, \\ C(\tau) &= \int_0^\infty e^{-s}\cos(\theta(\tau-s))ds.\end{aligned}$$

With the change of variables $s' = \tau - s$, S, C become

$$\begin{aligned}S(\tau) &= \int_{-\infty}^\tau e^{-(\tau-s')}\sin(\theta(s'))ds', \\ C(\tau) &= \int_{-\infty}^\tau e^{-(\tau-s')}\cos(\theta(s'))ds'.\end{aligned}$$

By differentiating, we rewrite S and C as ODEs:

$$\begin{aligned}\frac{dS}{d\tau} &= -S(\tau) + \sin\theta, \\ \frac{dC}{d\tau} &= -C(\tau) + \cos\theta.\end{aligned}$$

We have transformed a single integro-differential equation into a system of three ODEs, simplifying the numerics considerably:

$$\begin{aligned}\frac{d\theta}{d\tau} &= -q\sin(\theta) - g[\cos(\theta)S(\tau) - \sin(\theta)C(\tau)] \\ \frac{dS}{d\tau} &= -S(\tau) + \sin\theta, \\ \frac{dC}{d\tau} &= -C(\tau) + \cos\theta.\end{aligned}$$

The bifurcation diagram in Figure 21 summarizes the dynamics of the phase model on the ring. On the left panel, we fix a parameter value $q = 0.5$ and as we vary the parameter g, the system transitions from steady-state to sloshing solutions, then to a co-existence of large-amplitude and relatively small amplitude sloshing solutions, and eventually to a steady traveling pulse. On the right panel, we find that the parameter space is separated into several

regions. In particular, for $q \geq 0$ arbitrarily small, there exists a traveling bump for some nonzero g.

In the following sections, we analyze the existence of these bifurcations including the Hopf bifurcation leading to sloshing solutions, and the saddle-node bifurcation leads to the constant-velocity traveling bump.

3.3.3 Constant Velocity Bump Solution on the Ring

To show the existence of a constant velocity traveling bump solution, we require that $q = 0$ and $g > 0$. For the first part of this analysis, we do not require the kernel to take a particular form. We only require the kernel to be even and admit a steady-state bump solution to Equation (3.1). We make a traveling bump ansatz, $\theta(\tau) = \nu\tau$, where ν corresponds to the traveling bump velocity. We first determine the existence and stability of the zero velocity bump solution. Plugging the ansatz into Equation (3.11) yields

$$\begin{aligned} \nu &= -g \int_0^\infty e^{-s} H(-\nu s) ds \\ &= g \int_0^\infty e^{-s} H(\nu s) ds, \end{aligned} \tag{3.12}$$

where the last line follows by the oddness of H. Because $H(0) = 0$, $\nu = 0$ is a solution. To determine the stability of the zero velocity solution, we consider a small perturbation, $\theta(\tau) = \nu\tau + \varepsilon\psi$. By plugging this perturbation into Equation (3.11), we extract the dynamics of the perturbed variable ψ,

$$\frac{d\psi}{d\tau} = -g \int_0^\infty e^{-s} H'(\nu s)[\psi(\tau - s) - \psi(\tau)] ds. \tag{3.13}$$

Assuming $\psi(\tau) = e^{\lambda\tau}$ and $\nu = 0$, we obtain the stability equation,

$$\lambda = -g \int_0^\infty e^{-s} H'(0) \left[e^{-\lambda s} - 1\right] ds.$$

We integrate the right-hand side and rearrange to yield

$$\lambda = gH'(0) \frac{\lambda}{1 + \lambda}.$$

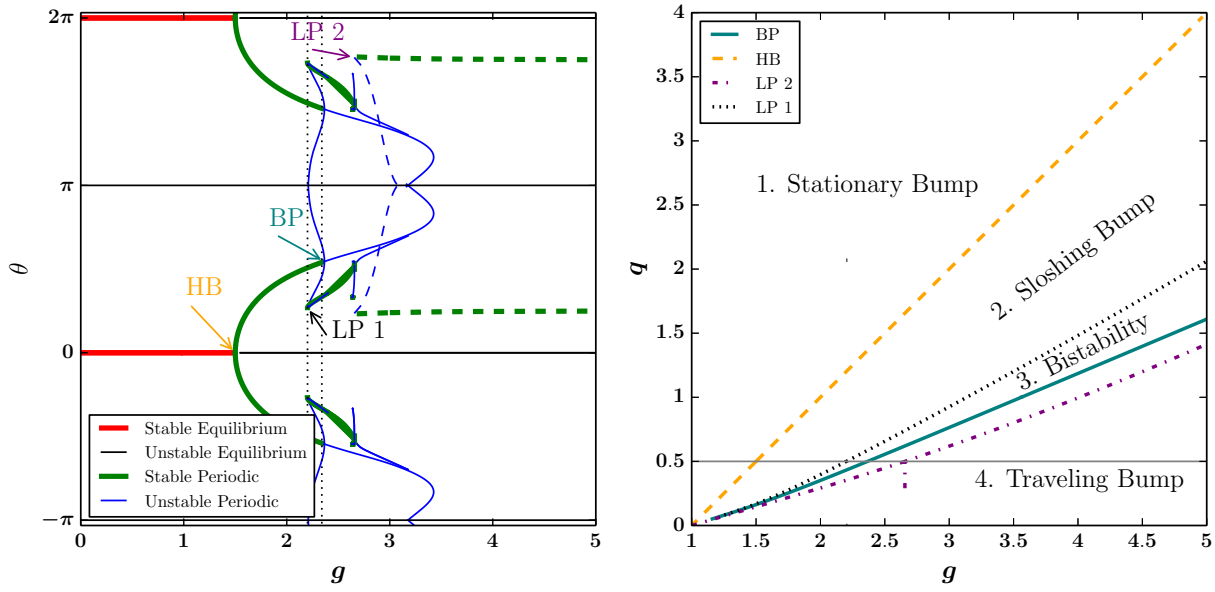

Figure 21: 1- and 2-parameter bifurcation diagrams of the phase equation on the ring. (A,B) Bifurcation diagram in for fixed $q = 0.5$. As g increases from 0 to 5, the system undergoes a Hopf bifurcation (HB, orange) then produces a limit point (LP 1, black), a branch point (BP, teal), and another limit point (LP 2, purple), respectively. Between the limit point LP1 and branch point BP, there is bistability, the interval of which is denoted by vertical dotted black lines. Beyond the second limit point LP2, there exists a traveling bump solution. This traveling bump solution is distinct from the equilibria and periodic solutions denoted by solid lines, thus we label it with a dashed green line. B: Two parameter bifurcation diagram in g and q. To the left of the Hopf bifurcation (HB, dashed orange line), there is only a stationary bump solution (1.). Motion exists to the right of this dividing line in the form of sloshes (2., 3.) and a traveling bump solution (4.).

Thus, either $\lambda = 0$, or $\lambda = -1 + gH'(0)$. Moreover, the zero velocity solution becomes unstable when $g > 1/H'(0)$.

In general, we may view the relationship between g and ν by rearranging Equation (3.12)

into the function

$$g = \Gamma(\nu) := \frac{\nu}{\int_0^\infty e^{-s} H(\nu s) ds}. \tag{3.14}$$

We show examples of Γ in Figure 22. In the left panel, the relationship between the adaptation strength g and bump velocity ν is straightforward: as g increases, there is some critical value ν where a nonzero velocity traveling bump exists. However, the choice of kernel may change the shape of Γ, and therefore change the relationship between g and ν, as well as the stability of traveling bump solutions. For example, a kernel of the form $K(x) = a + b\cos(x) + c\cos(2x)$ results in an H function of the form

$$H(\theta) = a' \sin(\theta) + b' \sin(2\theta).$$

Using this H function to plot Γ results in the right panel of Figure 22. The branch with negative slope represents another traveling bump solution. We now show that if $\Gamma'(\nu) < 0$, then the traveling bump with velocity ν is unstable.

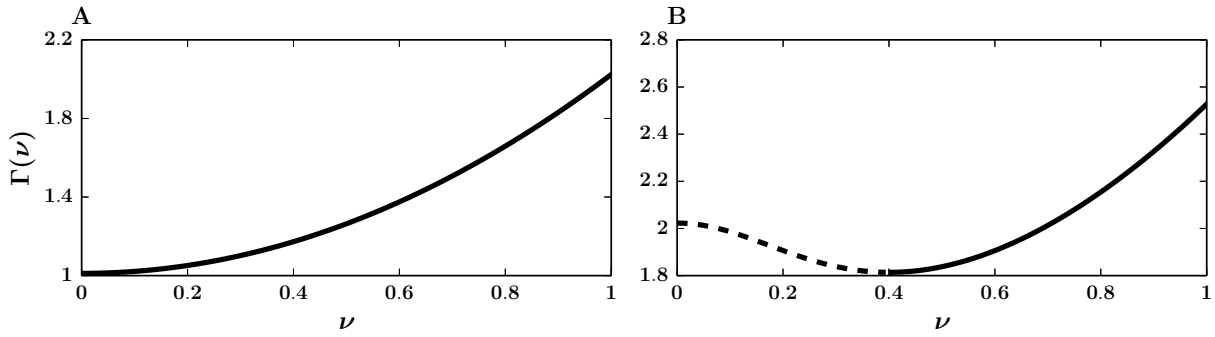

Figure 22: Examples of the function $\Gamma(\nu)$. A: Γ constructed using our usual H function, $H(x) = \sin(x)$. B: Γ constructed using a different H function, $H(x) = \sin(x) - 0.25\sin(2x)$, resulting from a different choice of kernel. The dashed black line represents an unstable traveling bump velocity.

Recall again Equation (3.13). Assuming $\psi(\tau) = e^{\lambda\tau}$ and $\nu \neq 0$, we obtain the stability equation,

$$f(\lambda) \equiv 1 + g \int_0^\infty e^{-s} H'(\nu s) \left[\frac{e^{-\lambda s} - 1}{\lambda} \right] ds. \tag{3.15}$$

To prove the statement, we seek to show that $\lim_{\lambda\to\infty} f(\lambda) > 0$ and $\lim_{\lambda\to 0} f(\lambda) < 0$. Then by continuity of f, there exists a positive root to Equation (3.15). We take each limit in turn, starting with the limit as $\lambda \to \infty$.

$$\begin{aligned}\lim_{\lambda\to\infty} f(\lambda) &= 1 + g\int_0^\infty e^{-s}H'(\nu s)\lim_{\lambda\to\infty}\left[\frac{e^{-\lambda s}-1}{\lambda}\right]ds \\ &= 1 > 0.\end{aligned}$$

Thus, the positive λ limit is positive. For the other limit, we rearrange Equation (3.14) into

$$\Gamma(\nu)D(\nu) = \nu,$$

where $D(\nu) = \int_0^\infty e^{-\beta s}H(\nu s)ds$, and differentiate with respect to ν to obtain

$$\Gamma(\nu)D'(\nu) + \Gamma'(\nu)D(\nu) = 1.$$

Solving for $\Gamma'(\nu)$ yields

$$\Gamma'(\nu) = \frac{1-\Gamma(\nu)D'(\nu)}{D(\nu)}.$$

Note that $D(\nu) > 0$ at least within a neighborhood of $\nu = 0$ since $H(0) = 0$ and $H'(0) > 0$. In addition, $D'(\nu) = \int_0^\infty e^{-s}H'(\nu s)sds$. Using the hypothesis that $\Gamma'(\nu) < 0$, we have the inequality

$$1 < \Gamma(\nu)D'(\nu).$$

We use this fact in the next limit

$$\begin{aligned}\lim_{\lambda\to 0} f(\lambda) &= 1 + g\int_0^\infty e^{-s}H'(\nu s)\lim_{\lambda\to 0}\left[\frac{e^{-\lambda s}-1}{\lambda}\right]ds \\ &= 1 - g\int_0^\infty e^{-s}H'(\nu s)sds \\ &= 1 - gD'(\nu) \\ &= 1 - \Gamma(\nu)D'(\nu) < 0.\end{aligned}$$

Thus, the zero λ limit is negative. Because $f(0)$ is negative, and $f(\lambda)$ is positive for asymptotically large values of λ, there exists a positive root λ of $f(\lambda)$ by continuity. It follows that

branches of $\Gamma(\nu)$ with negative slope indicate an unstable traveling bump at least within a neighborhood of $\nu = 0$.

For the next part of this analysis, we show how to compute a formula for the velocity of the traveling bump when the kernel is $K(x) = A + B\cos(x)$. With this kernel, the H function is proportional to $\sin(x)$, and Equation (3.12) becomes explicitly computable. Computing the integral results in a formula for the nontrivial bump velocity ν,

$$\nu = \pm\sqrt{g-1}. \tag{3.16}$$

Equation (3.16) corresponds to the branches of a pitchfork bifurcation in the velocity of the traveling bump. We show a particular example of a constant-velocity traveling bump in Figure 23A. We note that any odd H will lead to a pitchfork bifurcation to a traveling bump. In particular, it is trivial to derive the following bifurcation equation:

$$\nu^2 = (1 - gH'(0))/gH'''(0).$$

This equation tells us that the pitchfork bifurcation is super-critical if $H'''(0) < 0$ and sub-critical otherwise.

3.3.4 Andronov-Hopf Bifurcation on the Ring

We now prove the existence of a Hopf bifurcation. For this analysis, we do not require H or J to take a particular form. However, we do require that H and J be sufficiently differentiable, along with the properties $H(0) = J(0) = 0$, $H'(0) > 0$,$J'(0) < 0$, H odd, and $g, q > 0$.

Consider again the simplified phase model, Equation (3.11). Let us fix q and absorb the parameter into J. We write J and H as Taylor expansions,

$$J(\theta) = j_1\theta + j_2\theta^2 + j_3\theta^3,$$
$$H(\theta) = h_1\theta + h_3\theta^3.$$

Then to first order,

$$\frac{d\theta}{d\tau} = j_1\theta - gh_1\int_0^\infty e^{-s}[\theta(\tau - s) - \theta(\tau)]ds.$$

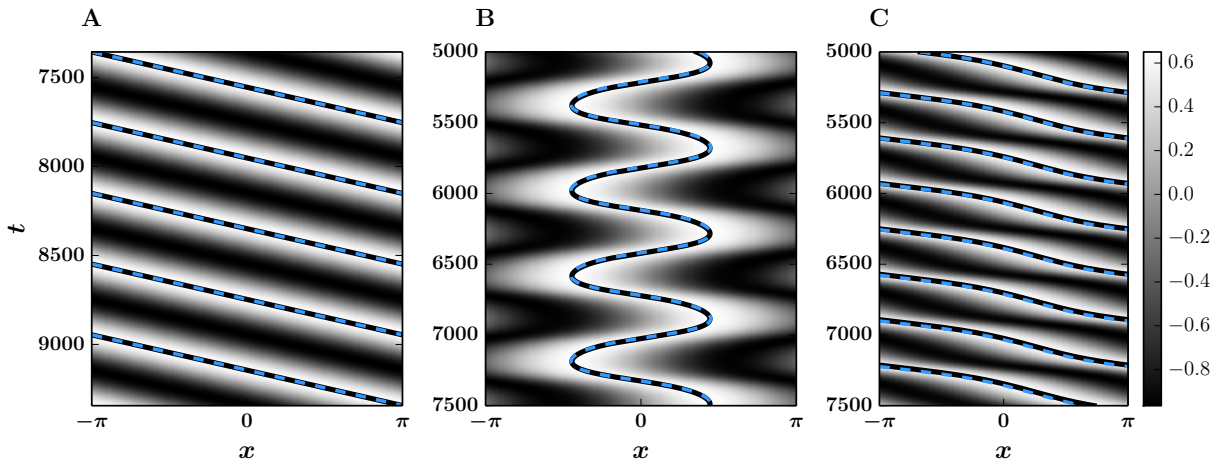

Figure 23: Dynamics of the traveling bump on the ring. Each row represents the bump solution at a particular time. White represents high activity, while black represents low or inhibited activity. The numerical centroid (black solid) is plotted against the analytic prediction (dashed blue). A: A constant-velocity bump, $g = 3.5$,$q = 0$. B: A sloshing bump, $g = 3$, $q = 1$. C: A non-constant velocity bump, $g = 5.5$, $q = 1$. For each panel, we shift the theory along the time axis to show qualitative agreement with the numerics. Parameter $\varepsilon = 0.01$.

Letting $\theta = e^{\lambda t}$ and rearranging the resulting equation yields

$$\lambda = j_1 + gh_1 - \frac{gh_1}{\lambda + 1},$$

or equivalently,

$$\lambda^2 + \lambda(1 - j_1 - gh_1) - j_1 = 0.$$

Since $j_1 < 0$ and $h_1 > 0$, there exists a Hopf bifurcation when

$$g^* = \frac{1 - j_1}{h_1}.$$

This bifurcation leads to oscillations in the peak of the bump solution. We show a particular example of this oscillatory behavior in Figure 23B.

3.3.4.1 Normal Form for the Hopf Bifurcation on the Ring We wish to analyze the bifurcation to a sloshing pulse for the general integral equation:

$$\frac{d\theta}{d\tau} = -qJ(\theta) - g\int_0^\infty e^{-s}H(\theta(\tau - s) - \theta(\tau))\, ds \tag{3.17}$$

as g increases. For simplicity, we will assume $J(\theta)$ is an odd periodic function (as is the case for $H(\theta)$ and through suitable rescaling of g, q, we will assume:

$$\begin{aligned} J(\theta) &= \theta + j_3\theta^3 + \dots \\ H(\theta) &= \theta + h_3\theta^3 + \dots . \end{aligned}$$

We also assume $q > 0$ so that $\theta = 0$ is stable without adaptation. If, we use $H(\theta) = J(\theta) = \sin(\theta)$, then $j_3 = h_3 = -(1/6)$. The linearization about $\theta = 0$ has the form:

$$\theta_\tau = -q\theta - g\int_0^\infty e^{-s}(\theta(\tau - s) - \theta(\tau))\, ds$$

which has the general solution, $e^{\lambda\tau}$. After some simplification, we find that

$$\lambda^2 + (1 + q - g)\lambda + q = 0$$

so there is an imaginary eigenvalue, $i\sqrt{q} := i\omega$ when $g = 1 + q \equiv g_0$, so we expect a Hopf bifurcation will occur.

All nonlinearities are odd, so we can assume the multiple timescale expansion

$$g = g_0 + \delta^2 g_2, \qquad \theta = \delta\theta_1(\zeta, \xi) + \delta^3\theta_3(\zeta, \xi),$$

where δ is the amplitude of the bifurcating solution, $\zeta = \tau$ is a "fast" time, and $\xi = \delta^2\tau$ is a "slow" time. We detail the remaining steps of the normal form analysis in Appendix B.1 and jump to the conclusion,

$$\alpha\frac{dz}{d\xi} = z[\hat{\gamma}_0 + \hat{\gamma}_3|z|^2] \tag{3.18}$$

where

$$\alpha = 1 - \frac{g_0}{1 + 2i\omega - \omega^2} = \frac{2}{1+q}(q + \sqrt{q}i)$$
$$\hat{\gamma}_0 = g_2 \frac{i\omega}{1 + i\omega} = \frac{g_2}{1+q}(q + \sqrt{q}i)$$
$$\hat{\gamma}_3 = \frac{3q}{4q+1}\left[[q(12h_3 - 4j_3) - j_3] + i18h_3\sqrt{q}\right].$$

To get the actual normal form, we divide (3.18) by α, to obtain:

$$\frac{dz}{d\xi} = z(g_2/2 + \gamma_3|z|^2)$$

where

$$\gamma_3 = \frac{3}{8q+2}\left[q(12qh_3 - 4qj_3 - j_3 + 6h_3) + i\sqrt{q}(6qh_3 - 4qj_3 - j_3)\right].$$

If we assume that $j_3 = h_3$ as would be the case if the input was the bump, itself, then

$$\gamma_3 = h_3 \frac{3q(8q+5)}{8q+2} - ih_3 \frac{3\sqrt{q}(2q-1)}{8q+2}.$$

We compare the normal form calculation to the numerics in Figure 24. We use `XPPAUTO` [19] to compute the numerical bifurcation diagram. As expected, the normal form approximation is quite accurate near the bifurcation.

3.3.5 Non-Constant Velocity Bump Solution on the Ring

When adaptation is made even stronger, the solution breaks free from the oscillating state and travels across the periodic domain (Figure 23C. The onset is shown numerically in the bifurcation diagrams of Figures 20 and 21, purple LP2). Due to the pinning term, the velocity of the bump is nonconstant.

Remark. As $q \to 0$, we see in figure 21B that all the two-parameter curves converge to the point g^* which is the point of onset of the traveling bumps with no input stimulus.

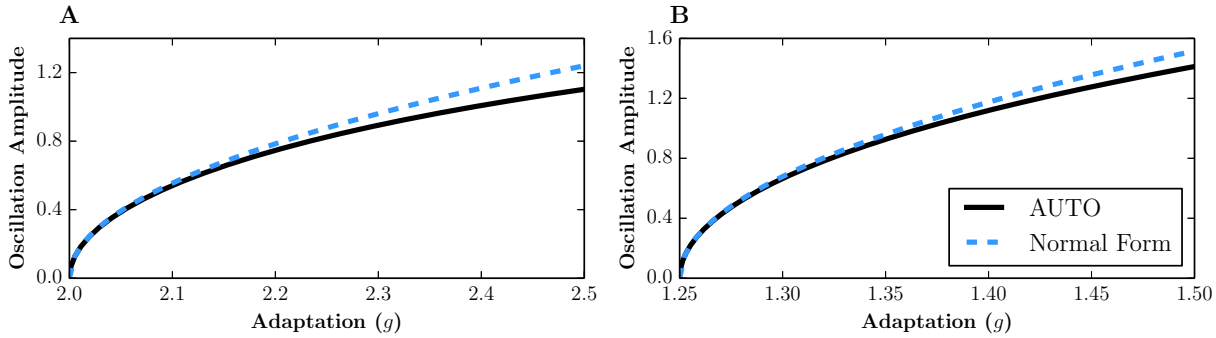

Figure 24: Normal form calculation for the neural field model on the ring. A: Amplitude of oscillations predicted by the normal form calculation (dashed blue) compared to the actual amplitude (solid black). $q = 1$. B: Amplitude of oscillations predicted by the normal form calculation (dashed blue) compared to the actual amplitude (solid black). $q = 0.25$.

3.3.6 Chaos on the Ring

With $g, q > 0$, there exists a small parameter range in which the neural field exhibits chaotic movement about the ring. Examples of this behavior are shown in Figure 25. In both panels, the initial conditions differ by 1e-7. The solutions in each panel remain nearly identical for a long time (we have truncated a significant portion of the simulation).

This section completes our analysis of the one-dimensional case. We have found a good match between the phase-reduced equations and the full neural model. For a fixed amplitude of the external input, we find a transition from a stationary bump to "sloshers", and, finally to bumps that move completely around the ring, modulated traveling bumps. In the sections to follow, we repeat the analytical and numerical analysis for the two-dimensional domain.

3.3.7 Lurching Bump

In this section, we explore the effects of allowing the input current to vary slowly in time. In particular, we take $I(x, \tau)$ to have a constant velocity, $I(x, \tau) = I(x + \Omega\tau)$, and assume

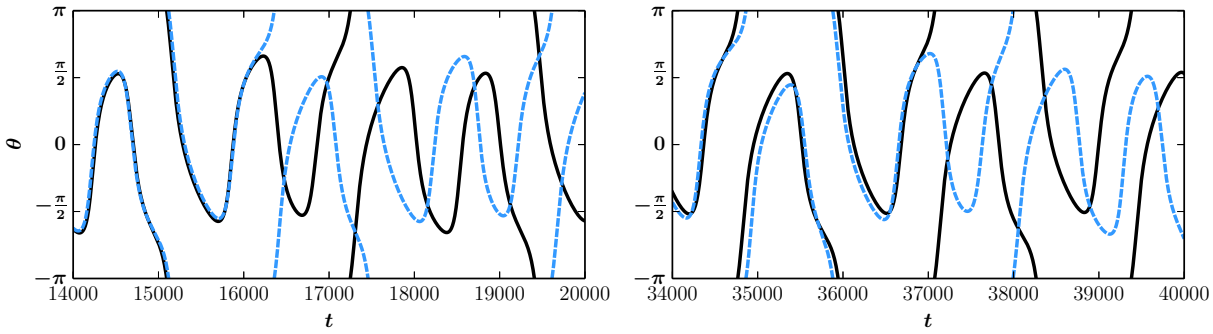

Figure 25: Chaotic dynamics of the traveling bump in the full neural field model (left) and the reduced phase model (right) on the ring. Original solutions are shown in black. Solutions with a different initial condition is shown in dashed blue. For each panel, initial conditions differ by 1e-7. A: $g = 2.65, q = 0.5$. B: $g = 2.661, q = 0.5$. For all simulations in this figure, $\varepsilon = 0.01$.

that we have a cosine kernel $K(x) = A + B\cos(x)$, which allows us to assume , without loss of generality, that $H(x) = \sin(x)$. We seek to find solutions of the form $\theta(\tau) = \nu\tau + \psi$ and determine the stability, where ϕ represents a possible lag between the bump position θ and the traveling input current. Plugging into the phase equation (3.8) and integrating yields

$$\Omega = -q\sin(\psi) + g\frac{\Omega}{1+\Omega^2}.$$

Because ψ is the only unknown, we use a symbolic solver to solve for ψ:

$$\psi(\Omega) = \arcsin\left(\frac{-\Omega + g\Omega - \Omega^3}{q(1+\Omega^2)}\right) + 2\pi n,$$

where $n \in \mathbb{N}$. We show typical examples of ψ in Figure 26

To determine the stability of a stimulus-locked solution ($\nu = \Omega$), we use the ansatz $\theta(\tau) = \nu\tau + \psi + \varepsilon e^{\lambda\tau}$. Plugging into Equation (3.9) and integrating yields the equation

$$\lambda = -q\cos(-\psi(\Omega)) - g\left[-\frac{1}{1+\Omega^2} + \frac{1+\lambda}{(1+\lambda)^2+\Omega^2}\right]. \tag{3.19}$$

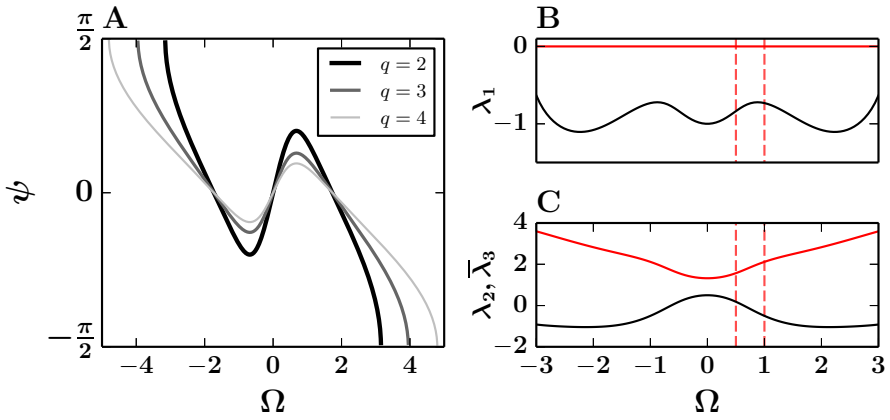

Figure 26: Phase lag ψ and stability eigenvalues λ_i as a function of input velocity Ω. A: Phase lag ϕ between the peak of the bump solution and the peak of the input current as a function of input velocity Ω. Examples of ψ are shown for $q = 2, 3, 4$. For a given input strength q, slow velocities Ω result in small phase lags. Larger velocities can result in greater phase lags. If Ω is chosen to be outside of the domain of ψ, the solution is a non-constant velocity traveling bump. B: The first root of Equation (3.19) when $q = 2$. Its real part (black) is negative for the given range of velocities Ω. The vertical dashed red lines (one at $\Omega = 0.5$ and the other at $\Omega = 1$) indicate the velocity values used in Figure 27. C: The two other eigenvalues are complex conjugates. For $\Omega = 0.5$, the real parts are positive, while for $\Omega = 1$ the real parts are negative. Parameter $g = 4$.

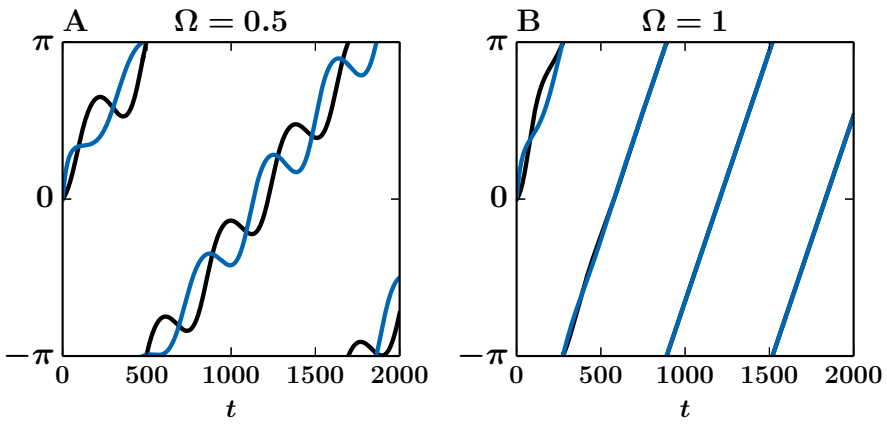

Figure 27: Two examples of solutions with the same parameter values as in Figure 26B,C. Black: numerical simulation of the original neural field model. Blue: phase reduced model. In panel A, as predicted above, for the velocity $\Omega = 0.5$, the constant velocity solution is unstable, leading to lurching waves. Panel B confirms our prediction above where for $\Omega = 1$, the constant velocity solution is stable.

3.4 TORUS DOMAIN

In this section, we define the domain Ω as the torus, or the square $[-\pi, \pi] \times [-\pi, \pi]$ with periodic boundary conditions. We seek to analyze the full neural field model on this domain using the same bifurcation analysis performed in the one-dimensional case. We begin by considering simplifications that allow us to use standard bifurcation analysis tools like `XPPAUTO`.

3.4.1 Approximation of the Neural Field Model on the Torus

In order to numerically investigate the full neural field equation (3.1-3.2), we need to either discretize space in two-dimensions or use an approximation of the kernel that is degenerate. (Since the integral operator is compact, it can be approximated to arbitrary precision by a degenerate integral operator ;see section 2.8 [77]). Thus to study the dynamics of the full neural field model on a two-dimensional domain, we take a Fourier truncation of the kernel to make the integral in Equation (3.3) separable. This truncation allows us to rewrite the infinite dimensional system as a finite system of ODEs and use traditional dynamical systems tools like `XPPAUTO` to analyze the system. To begin, take the truncated Fourier approximation to the kernel,

$$K(x, y) = k_{00} + k_{10}\cos(x) + k_{01}\cos(y) + k_{11}\cos(x)\cos(y), \tag{3.20}$$

and plug it into Equation (3.3):

$$u(\mathbf{x}) = \int_{\Omega} K(x_1 - y_1, x_2 - y_2) f(u(\mathbf{y}))d\mathbf{y}.$$

After expanding the kernel using standard trigonometric identities, we derive the time-varying solutions

$$\begin{aligned}
u(\mathbf{x},t) &= a_{00}(t) + a_{10}(t)\cos(x_1) + a_{01}(t)\cos(x_2) \\
&\quad + b_{10}(t)\sin(x_1) + b_{01}(t)\sin(x_2) \\
&\quad + a_{11}(t)\cos(x_1)\cos(x_2) + b_{11}(t)\sin(x_1)\sin(x_2) \\
&\quad + c_1(t)\sin(x_1)\cos(x_2) + c_2(t)\cos(x_1)\sin(x_2). \\
z(\mathbf{x},t) &= E_{00}(t) + E_{10}(t)\cos(x_1) + E_{01}(t)\cos(x_2) \\
&\quad + F_{10}(t)\sin(x_1) + F_{01}(t)\sin(x_2) \\
&\quad + E_{11}(t)\cos(x_1)\cos(x_2) + F_{11}(t)\sin(x_1)\sin(x_2) \\
&\quad + G_1(t)\sin(x_1)\cos(x_2) + G_2(t)\cos(x_1)\sin(x_2).
\end{aligned} \tag{3.21}$$

where the coefficients satisfy

$$\begin{aligned}
a'_{ij} &= -a_{ij} + k_{ij}p_{ij}(t) + \varepsilon(qu_{ij} - gE_{ij}), \\
b'_{ij} &= -b_{ij} + k_{ij}r_{ij}(t) - \varepsilon gF_{ij}, \\
c'_i &= -c_i + k_{11}s_i(t) - \varepsilon gG_i, \\
\xi' &= \varepsilon\beta(-\xi + \zeta),
\end{aligned} \tag{3.22}$$

where $i = 0, 1$ and $j = 0, 1$. The dummy variables ξ, ζ represent each of the pairs (a_{ij}, E_{ij}), (b_{ij}, F_{ij}), and (c_i, G_i). The time-varying functions p_{ij}, r_{ij}, s_i are defined as

$$\begin{aligned}
p_{00}(t) &= \textstyle\int_\Omega f(u(\mathbf{y},t))d\mathbf{y} & p_{01} &= \textstyle\int_\Omega \cos(y_2)f(u(\mathbf{y},t))d\mathbf{y} \\
p_{10}(t) &= \textstyle\int_\Omega \cos(y_1)f(u(\mathbf{y},t))d\mathbf{y} & p_{11} &= \textstyle\int_\Omega \cos(y_1)\cos(y_2)f(u(\mathbf{y},t))d\mathbf{y}
\end{aligned}$$

$$\begin{aligned}
r_{01}(t) &= \textstyle\int_\Omega \sin(y_2)f(u(\mathbf{y},t))d\mathbf{y} & r_{10} &= \textstyle\int_\Omega \sin(y_1)f(u(\mathbf{y},t))d\mathbf{y} \\
r_{11}(t) &= \textstyle\int_\Omega \sin(y_1)\sin(y_2)f(u(\mathbf{y},t))d\mathbf{y}
\end{aligned}$$

$$s_1(t) = \textstyle\int_\Omega \cos(y_1)\sin(y_2)f(u(\mathbf{y},t))d\mathbf{y} \quad s_2 = \textstyle\int_\Omega \sin(y_1)\cos(y_2)f(u(\mathbf{y},t))d\mathbf{y},$$

and the coefficients u_{ij} are taken from the truncated Fourier series of the steady-state solution,

$$u_0(x,y) = u_{00} + u_{10}\cos(x) + u_{01}\cos(y) + u_{11}\cos(x)\cos(y).$$

The coefficient values of the kernel and steady-state bump solutions are shown in Tables 4 and 5, respectively. Details on how we approximate the spatial integrals of p_{ij}, r_{ij}, s_i are in Appendix B.3.

We show the bifurcation diagram and salient solutions of this system in Figure 28. The only bifurcations classified by `XPPAUTO` are a subcritical Hopf bifurcation (HB, orange) and limit points (limit points occur at each change in stability of periodic solutions). The Hopf bifurcation leads to small amplitude unstable solutions. We attribute the existence of a subcritical Hopf bifurcation to the coarse discretization of the spatial domain in the parameters of Equation (3.22). Although not shown here, a finer discretization of the spatial domain using 200 intervals results in a qualitatively supercritical Hopf bifurcation.

To summarize, we find the usual types of oscillatory solutions in this truncated neural field model as we found in the neural field model. A stable limit cycle of this system is shown in the first bottom left panel (A, which corresponds to the initial conditions taken from the point A in the bifurcation diagram). A large-sloshing solution exists for slightly larger g (B,C), and eventually, for sufficiently large g, there exist only traveling bump solutions D. Additional non-periodic attractors are shown in panels E–G. The attractors shown in this figure are simply those with the largest basins of attraction. Generally, starting random initial conditions with g anywhere in the range $1.55 < g < 1.95$ (the gray shaded area labeled F in the main plot) results in solutions that qualitatively match panel F. The same holds for the shaded areas E and F, with their corresponding panels. Indeed, there exist several attractors not shown in this figure that are more difficult to find numerically. However, the focus of this study is not the thorough classification of attractors in the truncated neural field model, so we move on to the analysis of the phase model on the torus.

3.4.2 Approximations of the Phase Model on the Torus

We now turn to the analysis of the phase dynamics in two-dimensions and begin by reducing the number of parameters with the same rescaling used to obtain Equation (3.11) in the one dimensional case,

$$\frac{d\theta_i}{d\tau} = qJ_i(\boldsymbol{\theta}) - g\int_0^\infty e^{-s}H_i(\boldsymbol{\theta}(\tau - s) - \boldsymbol{\theta}(\tau))ds, \quad i = 1, 2, \tag{3.23}$$

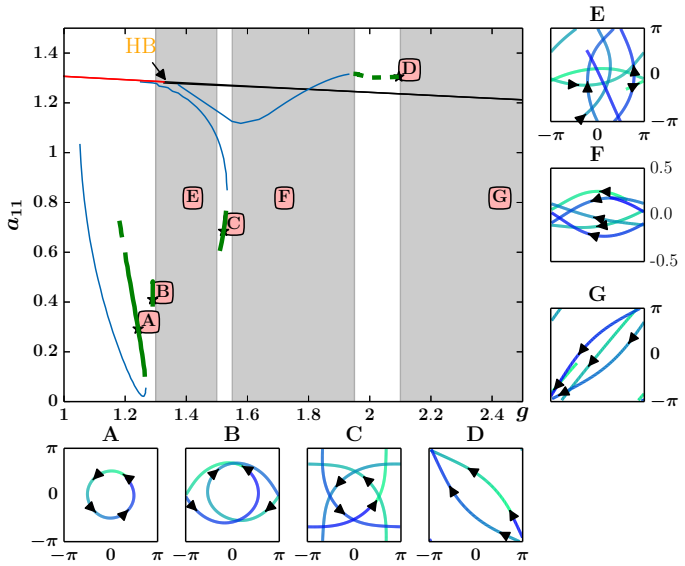

Figure 28: Bifurcation diagram of the truncated neural field model on the torus with g as a bifurcation parameter and $q = 0.1$. The stable fixed point (red line) undergoes a subcritical Hopf bifurcation (HB, orange) and becomes an unstable fixed point (black line). The green and blue lines represent stable and unstable oscillations, respectively. Thick, solid green lines represent stable oscillations. Thick, dashed green lines represent stable oscillations that wrap around the torus. Thin solid blue lines represent unstable periodic solutions. Stable attractors are shown in panels A–D. In panels E–G, we show solutions in parameter regimes without stable periodic attractors. These solutions are displayed in a relatively short time window after integrating for long times and travel from light to dark. In panel E ($g = 1.4$), we integrate for $t = 5000$ time units and show the last 30% of the data. In panel F ($g = 1.7$), we integrate for $t = 8000$ time units and show the last 10% of the data. In panel G ($g = 2.4$), we integrate for $t = 8000$ time units and show the last 6% of the data. We initialize the solutions of panels E–F using standard normally distributed random variables. Parameter $\varepsilon = 0.01$.

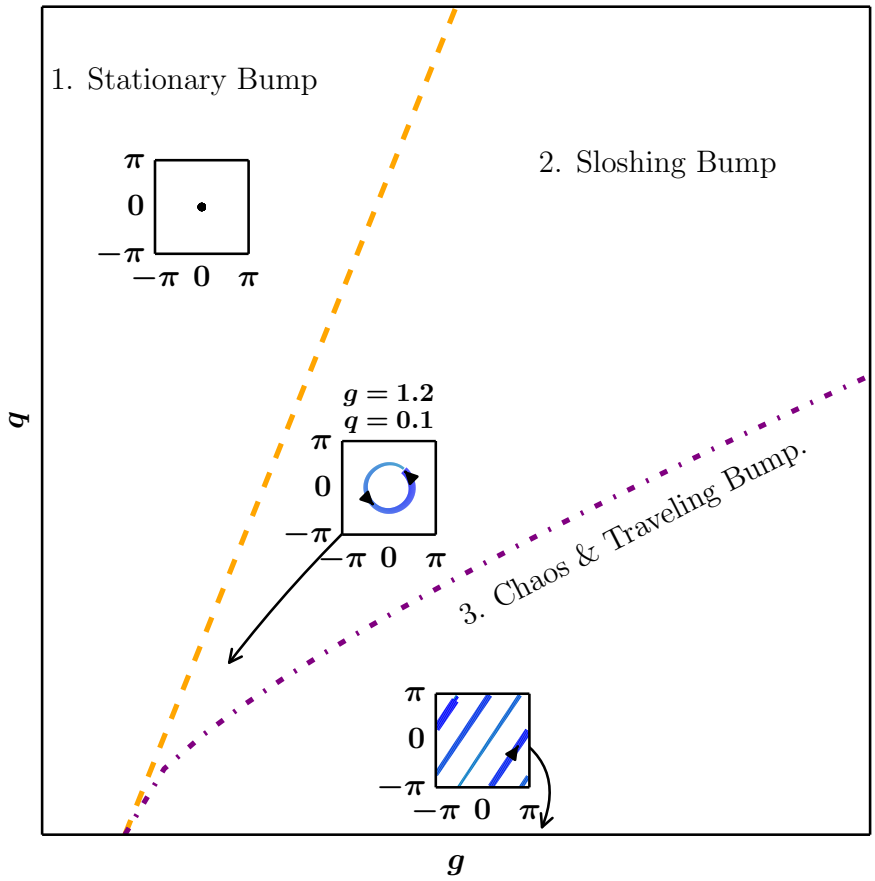

Figure 29: Cartoon of the parameter space of the approximate neural field model on the torus (Equation (3.22)). The most salient solutions are shown. Solutions advance in time from light to dark, thin to thin. For sufficiently small g or sufficiently large q, the bump solution tends to a stationary solution. By increasing g or decreasing q to $g = 1.2, q = 0.1$, the centroid of the bump solution oscillates about the origin. For larger g, say $g = 4, q = 0.5$, the solution begins to traverse chaotically about the domain. When $q = 0$, there exists a constant velocity traveling bump solution for g sufficiently large, e.g., $g = 3$. Parameter $\varepsilon = 0.01$.

and recall that

$$H_i(\boldsymbol{\theta}) = \int_\Omega f'(u_0(\mathbf{x}))\partial_i u_0(\mathbf{x}) u_0(\mathbf{x}+\boldsymbol{\theta})\, d\mathbf{x}.$$

Details on the numerical integration of the integro-differential equation, Equation (3.23), are shown in Appendix B.3.

To facilitate the study of existence and stability of solutions, we consider two approximations to H_i to be used in Equation (3.23): the first is a high-accuracy Fourier series of H_i, and the second is a low-accuracy Fourier series of H_i. We detail these approximations in turn.

For the accurate Fourier series approximation of H_i, we use one of two equivalent forms

$$H_1(\boldsymbol{\theta}) = \sum_{n,m\in\mathbb{Z}} a_{nm} \sin(n\theta_1)\cos(m\theta_2), \tag{3.24}$$

where, due to the odd (even) property of the first (second) coordinate, the coefficients have the property that $a_{n,\pm m} = -a_{-n,\pm m}$. We can then rewrite this Fourier series into the equivalent form,

$$H_1(\boldsymbol{\theta}) = \sum_{n,m\in\mathbb{Z}} \hat{a}_{nm} \sin(n\theta_1 + m\theta_2), \tag{3.25}$$

where $\hat{a}_{nm} = 4a_{nm}$. This equivalent form makes integrals much easier to compute. We use both forms interchangeably as we see fit, and abuse notation in Equation (3.25) by removing the hats from the coefficients. We find that 30 Fourier coefficients provides a sufficiently good approximation for simulations on a 64×64 domain (the error is on the order of 1e-7).

For the low-accuracy Fourier series, we consider a more substantial truncation of the interaction function using only 3 Fourier coefficients. While this truncation is drastic, it allows us to analyze Equation (3.23) more rigorously. We derive the 3 term H_i-function starting with the same Fourier truncation of the kernel as above, which leads to the same steady-state bump solution,

$$u_0(x,y) = u_{00} + u_{10}\cos(x) + u_{01}\cos(y) + u_{11}\cos(x)\cos(y),$$

which in turn leads to a truncated H_i function,

$$H_1^F(\theta_1,\theta_2) = \sin(\theta_1)(h_{10} + h_{11}\cos(\theta_2)),$$

where

$$h_{10} = 4u_{10} \int_{\Omega} \sin^2(x)(u_{10} + 2\cos(y)u_{11})dxdy,$$
$$h_{11} = 8u_{11} \int_{\Omega} \cos(y)\sin^2(x)(u_{10} + 2\cos(y)u_{11})dxdy.$$

For simplicity, analysis of this H_i function uses the simpler form

$$H_1^F(\theta_1, \theta_2) = \sin(\theta_1)(1 + b\cos(\theta_2)), \tag{3.26}$$

where we have absorbed h_{10} into the parameter g of Equation (3.23), and relabeled h_{11}/h_{10} as b. Naturally, it follows that $H_2^F(x, y) = H_1^F(y, x)$ and $H_i^F = -J_i^F$.

Using the truncated interaction function H_1^F enables us to use traditional dynamical systems tools and techniques to identify qualitative dynamics of Equation (3.23) through a bifurcation analysis.

Finally, for H_i and all of its approximations, we require the following properties to hold:

1. $\partial H_1(0,0)/\partial y = \partial H_2(0,0)/\partial x = 0$,
2. $\partial H_1(0,0)/\partial x, \partial H_2(0,0)/\partial y > 0$,
3. $\partial J_1(0,0)/\partial x, \partial J_2(0,0)/\partial y < 0$.

Properties 1 and 2 follow from the evenness of the $\varepsilon = 0$ bump solution and 3 is made WLOG since we could just change the sign of q otherwise.

To summarize, we consider two approximations to H_i:

$$H_1(\boldsymbol{\theta}) = \sum_{n,m=1}^{30} a_{nm}\sin(n\theta_1)\cos(m\theta_2) \propto \sum_{n,m=1}^{30} a_{nm}\sin(n\theta_1 + m\theta_2),$$
$$H_1^F(\boldsymbol{\theta}) = \sin(\theta_1)(1 + b\cos(\theta_2)).$$

We note that the second approximation, H_1^F, is a result of using the truncated kernel in Equation (3.20).

3.4.2.1 Equivalent Truncated Phase Model on the Torus For the truncated function H_i^F, we transform the delay integro-differential equations into a system of ordinary differential equations using identical arguments used to transform the phase equation on the ring from a delay integro-differential equation into a system of ODEs. The new system is

$$\begin{aligned} \theta_i' &= qJ_i^F(\boldsymbol{\theta}) - g(\eta_{i1} + \eta_{i2}), \quad i = 1, 2 \\ N' &= -N + P \\ M' &= -M + Q \end{aligned} \tag{3.27}$$

where

$$\begin{aligned} (N, P) &\in \{(cx, \cos\theta_1), (cy, \cos\theta_2), (sx, \sin\theta_1), (sy, \sin\theta_2)\} \\ (M, Q) &\in \{(sxsy, \sin(\theta_1)\sin(\theta_2)), (sxcy, \sin(\theta_1)\cos(\theta_2)), \\ &\qquad (cxsy, \cos(\theta_1)\sin(\theta_2)), (cxcy, \cos(\theta_1)\cos(\theta_2))\} \\ \eta_{11} &= sx\cos(\theta_1) - cx\sin(\theta_1) \\ \eta_{12} &= b[\cos(\theta_1)\cos(\theta_2)sxcy - \sin(\theta_1)\cos(\theta_2)cxcy \\ &\qquad + \cos(\theta_1)\sin(\theta_2)sxsy - \sin(\theta_1)\sin(\theta_2)cxsy]. \end{aligned}$$

The function η_{21} (η_{22}) is the same as η_{12} (η_{11}) with θ_1 and θ_2 flipped and each x and y flipped in the notation (for example, $sxcy$ and $\cos(\theta_2)$ in η_{12} become $sycx$ and $\cos(\theta_1)$ in η_{21}, respectively).

We show the many bifurcations and salient solutions of this system in Figure 30. We find that there exists a stable sloshing bump solution that arises from a Hopf bifurcation (solution A, bifurcation HB). Due to the symmetry of the system, there is also an unstable sloshing solution in an axial direction (G) that arises from the same Hopf bifurcation. For slightly larger parameter values, there is bistability of large-sloshing solutions (H and B), and an even larger-sloshing solution (F) that loses stability through a torus bifurcation (TR). For this choice of $q = 0.1$, the solutions are chaotic for parameter values between the first torus bifurcation (TR1) and the first period doubling bifurcation (PD1). The multitude of period doubling bifurcations beyond this point represents the onset of chaotic behavior of the system due to the Fourier truncation, the error of which is proportional to g. This error

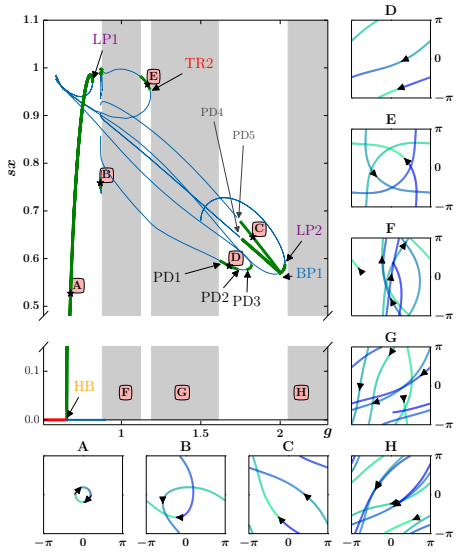

Figure 30: Bifurcation diagram of the equivalent truncated phase model on the torus over varying values of g with $q = 0.1$. Some branches refined using `XPPY` [65]. Sample solutions (labeled A–H in the bifurcation diagram) are shown in the subplots to the bottom and right of the diagram. Bifurcations are labeled according to the type: Hopf (HB), limit point (LP), torus (TR), period-doubling (PD), and branch point (BP). The number following each bifurcation type correspond to the same bifurcation type and number in the two parameter bifurcation in Figure 31. Panels A–E show stable attractors. In panels F–H, we show solutions in parameter regimes without stable periodic attractors. These solutions are displayed in a relatively short time window after integrating for long times and travel from light to dark. In panel F ($g = 1.05$), we integrate for $t = 500$ time units and show the last 9% of the data. In panel F ($g = 1.5$), we integrate for $t = 500$ time units and show the last 7% of the data. In panel G ($g = 2.15$), we integrate for $t = 500$ time units and show the last 5% of the data. We initialize the solutions of panels F–H using standard normally distributed random variables. Parameter $\varepsilon = 0.01$.

is more apparent beyond limit point LP2 where there are no more traveling bump solutions, which qualitatively disagrees with the original system where traveling bump solutions exist for even relatively large g.

The most salient bifurcations are captured in the two-parameter bifurcation in Figure 31. There are several qualitative similarities to the two parameter bifurcation diagram of the phase model on the ring. In particular the transition from the stationary bump to the sloshing bump, and from sloshing to large-sloshing. However, for the two-dimensional domain, there are much larger regions of chaotic solutions.

In the following sections, we study the dynamics of the original phase model and the truncated phase model and repeat most of the analysis as completed in the ring domain. In particular, using a combination of numerical and analytical methods, we analyze the existence and stability of traveling bump solutions, and the existence of a Hopf bifurcation.

3.4.3 Constant Velocity Bump Solution on the Torus

In this section, we analyze the existence and stability of constant velocity bump solutions on the torus for $q = 0$, the only case in which there can be constant velocity traveling bumps. Figure 32 shows the type of solutions we analyze in this section: constant velocity traveling bump solutions in the full neural field model (panel A), the reduced model with the accurate Fourier approximation (panel B), and the truncated reduced model (panel C).

3.4.3.1 Existence To show existence of solutions in the axial directions, we only need to show existence of the solution $\theta_1(\tau) = \nu\tau$ and $\theta_2(\tau) = 0$. We plug this ansatz into (3.23) and rearrange to yield

$$g = \Gamma(\nu) \equiv \frac{\nu}{\int_0^\infty e^{-s} H_1(\nu s, 0) ds}. \tag{3.28}$$

The analysis of this equation is identical to the one-dimensional case, Equation (3.14). By varying ν from zero, we can find the values of g where there are solutions. Values of g for which ν is nonzero imply there exists a traveling bump solution. In the case of the truncated H function, we compute this integral explicitly to derive the velocity ν as a function of

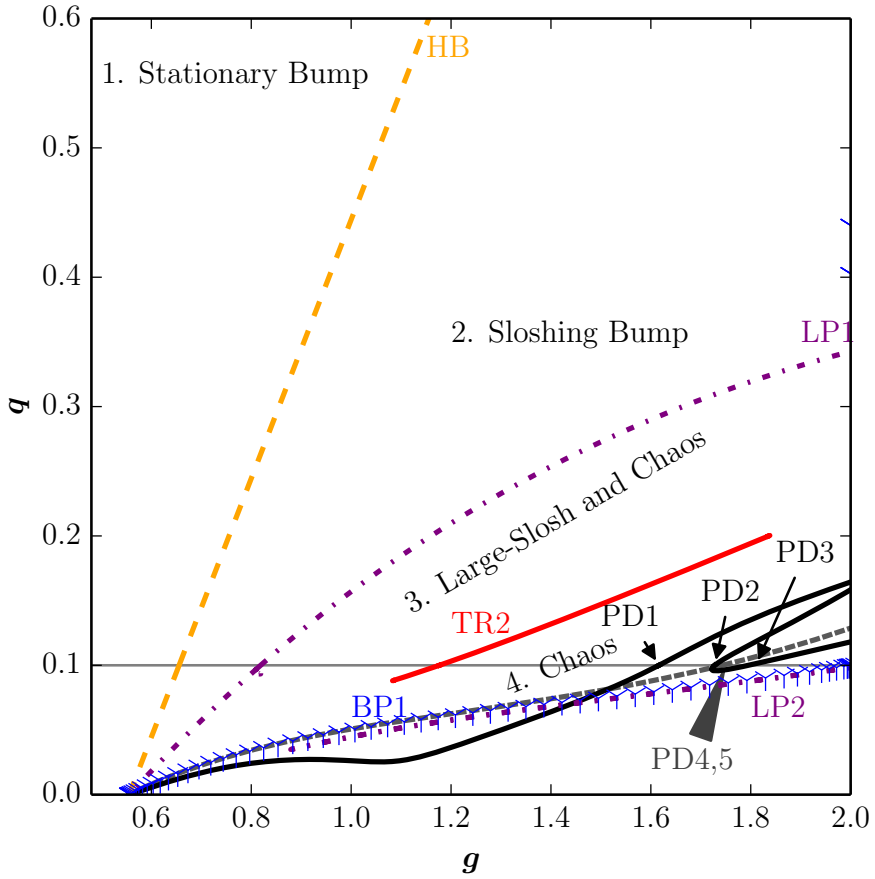

Figure 31: Two parameter bifurcation diagram of the equivalent truncated phase model on the torus. The parameter regions are separated into stationary solutions (1.), sloshing solutions (2.), large-sloshing solutions (3.), and generally chaotic solutions (4.). To the right of the curve LP2 (purple dashed) for $g \geq 1.5$, the qualitative behavior breaks down as this bifurcation point marks the end of traveling bump solutions. Parameter $b = 0.8$.

adaptation strength g:

$$\Gamma(\nu) = \frac{1+\nu^2}{1+b}.$$

To determine the critical value for the existence of axial constant velocity bump solutions, we take the limit $\lim_{\nu\to 0}\Gamma(\nu)$:

$$g^* = \lim_{\nu\to 0}\Gamma(\nu) = \frac{1}{1+b}.$$

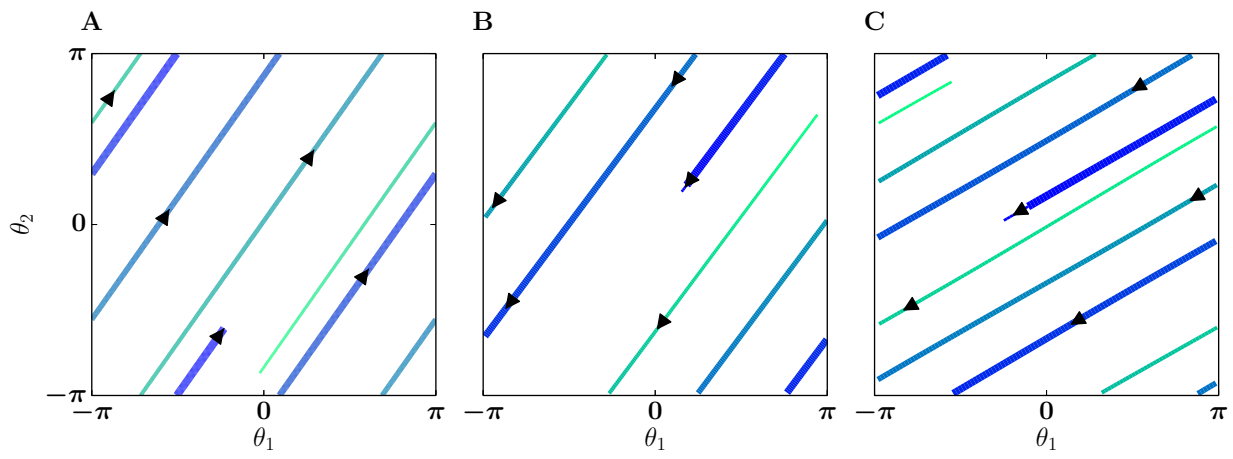

Figure 32: Constant velocity dynamics of the traveling bump on the torus. The curve that goes from light to dark and thin to thick represents the movement of the centroid over time. A: Full neural field model on the torus, $q = 0, g = 3$, simulated for $t = 7000$ time units with the last 60% of the data shown. B: Phase model on the torus with the accurate Fourier series of H_i, $q = 0, g = 2.2$, simulated for $t = 6,700$ time units with the last 10% of the data shown. C: Phase model on the torus with the truncated Fourier series H_i^F, $q = 0, g = 2.5$, simulated for $t = 3,500$ time units with the last 20% of the data shown. For these parameter choices, the axial directions are unstable and over long times converge to non-axial directions. Parameter $\varepsilon = 0.01$.

To show existence of non-axial solutions, we use the ansatz $\theta_1(\tau) = \nu_1\tau$ and $\theta_2(\tau) = \nu_2\tau$ where $\nu_1, \nu_2 \neq 0$. There exist non-axial traveling bump solutions if ν_1, ν_2 simultaneously satisfy

$$\begin{aligned} 0 &= -\nu_1 + gG(\nu_1, \nu_2), \\ 0 &= -\nu_2 + gG(\nu_2, \nu_1), \end{aligned} \tag{3.29}$$

where

$$G(\nu_1, \nu_2) = \int_0^\infty e^{-s} H_1(\nu_1 s, \nu_2 s) ds.$$

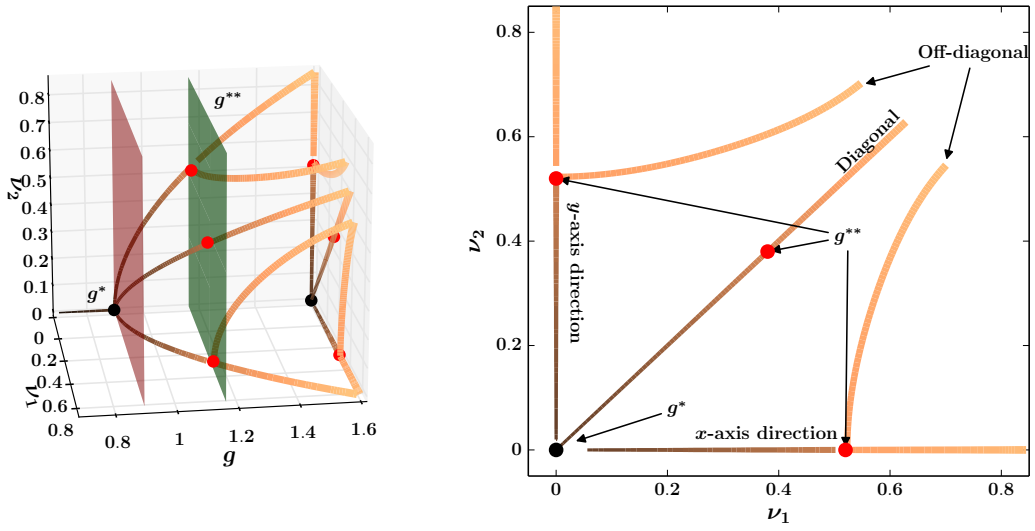

Figure 33: Existence of traveling bump solutions using the accurate approximation to the interaction function H_i. Left: After a first critical value (g^*) of the bifurcation parameter g (red plane), there exist traveling bumps in the axial directions. After a second critical value (g^{**}) (marked by a green plane), off-diagonal solutions form and continue to persist for large g. The dark to light color gradient and thin to thick thickness gradient corresponds to increasing values of g. Right: The projection of the branches on the left onto the $g = 1.6$ plane. A given point on one of these branches marks the magnitude and direction of a traveling bump. If necessary, one can approximate the parameter value g of this traveling bump by looking at the thickness and color of the chosen point and looking back at the branches in the left panel.

We can not compute the velocities ν_1, ν_2 explicitly as a function of g, but we can exploit the Fourier series of H_i to compute G explicitly, allowing us to use `XPPAUTO` to follow the velocities as a function of the adaptation parameter g. The existence of traveling solutions using the accurate Fourier series is shown in Figure 33, and the existence of traveling solutions using the truncated Fourier series is shown in Figure 34.

In these figures, we find that the truncated model (Figure 34) exhibits a similar set of traveling bump solutions as the full phase model (Figure 33). In particular, each system at

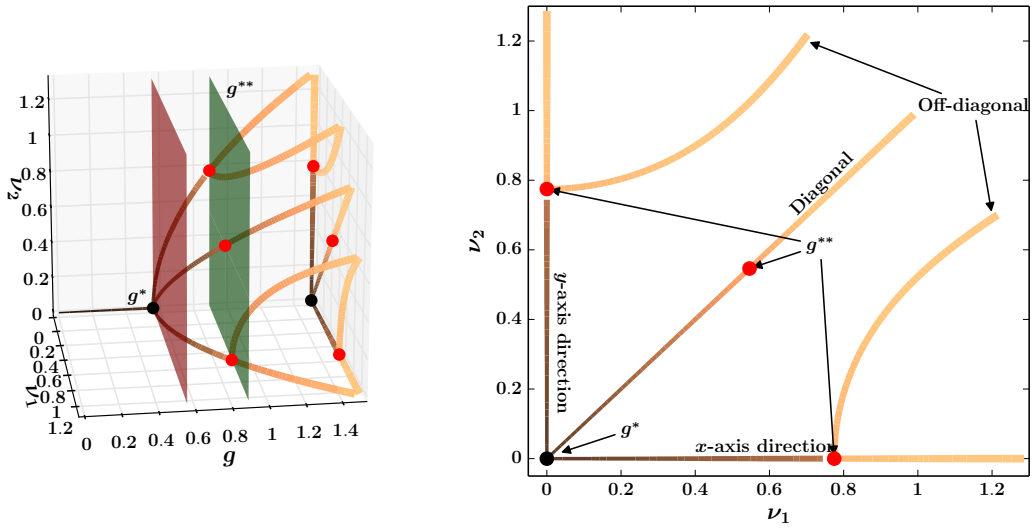

Figure 34: Existence of traveling bump solutions using the truncated interaction function H_i^F $(q = 0, b = 0.8)$. Left: After a first critical value (g^*) of the bifurcation parameter g (red plane), there exist traveling bumps in the axial directions. After a second critical value (g^{**}) (marked by a green plane), off-diagonal solutions form and continue to persist for large g. The dark to light color gradient and thin to thick thickness gradient corresponds to increasing values of g. Right: The projection of the branches on the left onto the $g = 4$ plane. A given point on one of these branches marks the magnitude and direction of a traveling bump. If necessary, one can approximate the parameter value g of this traveling bump by looking at the thickness and color of the chosen point and looking back at the branches in the left panel.

a critical value g^*, bifurcates into two axial solutions and one diagonal solution. For larger g, the system bifurcates again at another critical value g^{**}, giving rise to two non-axial, non-diagonal constant velocity directions. Indeed, negative velocity solutions exist, but as these solutions are symmetric up to multiples of a 90-degree rotation about the g-axis, we only show the positive directions. The "mixed" solutions that branch off for $g > g^{**}$ are, in general, not rationally related so that the resulting traveling bumps will densely cover the torus. As such quasi-periodic solutions are often not structurally stable, we expect to see

complex and possibly chaotic behavior when $q > 0$. Indeed, looking at Figure 31, we see that most of the complex behavior occurs for a small value of q and g sufficiently large.

Now that we have shown existence of traveling bump solutions, we proceed with a stability analysis.

3.4.3.2 Stability We begin this section with stability of traveling bump solutions in the axial directions. We perturb off the axial solution, $\theta_1(\tau) = \nu\tau + \varepsilon e^{\lambda_1 \tau}$ and $\theta_2(\tau) = 0 + \varepsilon e^{\lambda_2 \tau}$, with $\mathrm{Re}(\lambda_i) > -1$. The first order terms yield two independent eigenvalue problems

$$\lambda_1 = -g \int_0^\infty e^{-s} \frac{\partial H_1}{\partial x}(\nu s, 0)[e^{-\lambda_1 s} - 1]ds,$$
$$\lambda_2 = -g \int_0^\infty e^{-s} \frac{\partial H_1}{\partial x}(0, \nu s)[e^{-\lambda_2 s} - 1]ds,$$

which we combine with Equation (3.28) to yield two independent eigenvalue equations,

$$\lambda_1 = -\frac{\nu}{\int_0^\infty e^{-s} H_1(\nu s, 0)ds} \int_0^\infty e^{-s} \frac{\partial H_1}{\partial x}(\nu s, 0)[e^{-\lambda_1 s} - 1]ds,$$
$$\lambda_2 = -\frac{\nu}{\int_0^\infty e^{-s} H_1(\nu s, 0)ds} \int_0^\infty e^{-s} \frac{\partial H_1}{\partial x}(0, \nu s)[e^{-\lambda_2 s} - 1]ds.$$

Using these equations, we may determine stability of a traveling bump solution as a function of its velocity. We rephrase this problem and consider the independent scalar valued functions

$$\Lambda_1(\nu, \lambda) = \lambda + \frac{\nu}{\int_0^\infty e^{-s} H_1(\nu s, 0)ds} \int_0^\infty e^{-s} \frac{\partial H_1}{\partial x}(\nu s, 0) \left(e^{-\lambda s} - 1\right) ds, \tag{3.30}$$
$$\Lambda_2(\nu, \lambda) = \lambda + \frac{\nu}{\int_0^\infty e^{-s} H_1(\nu s, 0)ds} \int_0^\infty e^{-s} \frac{\partial H_1}{\partial x}(0, \nu s) \left(e^{-\lambda s} - 1\right) ds. \tag{3.31}$$

For a given Λ_i, the zero level curves in (ν, λ) space determine stability properties of traveling bump solutions.

We begin the analysis of these equations using the accurate Fourier series of H_i and compute the integrals explicitly. The zero level set of the resulting function is shown in Figure 35. On the left panel, find that for any velocity, the x-direction is always stable. On the right, we find that for sufficiently small velocities, $\theta_2(\tau) = 0$ is a stable solution. Thus, constant velocity traveling solutions in this parameter regime will converge to the x-axis.

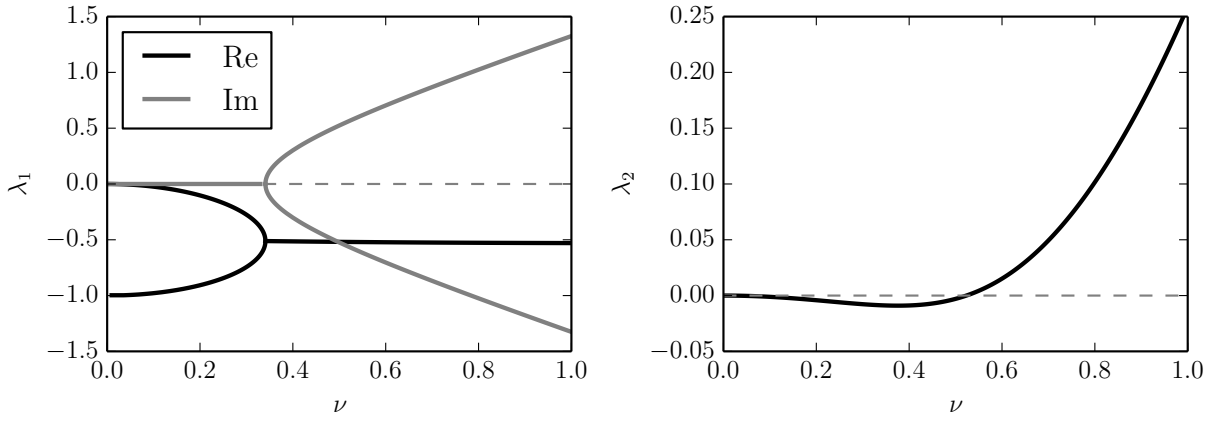

Figure 35: Stability of solutions in the horizontal axial direction (calculated using the phase model with the accurate Fourier series). Both plots show the level curves where $\mathrm{Re}(\Lambda_i) = 0$ (black) and $\mathrm{Im}(\Lambda_i) = 0$ (gray). For small velocities ν, both components are stable. For larger velocities, the horizontal velocity remains stable, but the vertical velocity loses stability. The dashed gray line shows where $\lambda_i = 0$.

Finally, for greater traveling bump velocities, the vertical direction loses stability, giving rise to non-axial solutions.

With the truncated H_i, which we recall to be $H_i^F(\theta_1, \theta_2) = \sin(\theta_1)(1 + b\cos(\theta_2))$, we may compute the equations $\Lambda_i = 0$ explicitly as polynomials,

$$\begin{aligned} 0 &= \lambda_1^2 + \lambda_1 + 2\nu^2 \\ 0 &= \lambda_2^3 + c_2\lambda_2^2 + c_1\lambda_2 + c_0, \end{aligned}$$

where

$$\begin{aligned} c_0 &= \frac{(2b-1)\nu^2 - \nu^4}{b+1}, \\ c_1 &= \frac{(1+b+(2b-1)\nu^2)}{b+1}, \\ c_2 &= \frac{(2(b+1)-\nu^2)}{b+1}. \end{aligned} \tag{3.32}$$

The coefficients of Equation (3.32) determine the stability of the horizontal traveling solution. Note that for ν sufficiently small, all coefficients are positive and the product c_1c_2 dominates the coefficient c_0. Thus, for small velocities, the coefficients have the properties $c_1c_2 > c_0$ and $c_2, c_0 > 0$, which implies stability by the Routh Hurwitz criterion. When $\nu^* = \pm\sqrt{2b-1}$, the coefficient c_0 is no longer positive and the stability condition fails.

We have found that horizontal traveling bump solutions lose stability at some critical velocity ν^*, giving rise to non-axial traveling bump solutions. By symmetry, this argument holds for vertical traveling bump solutions: after the same critical ν^*, constant velocity traveling bumps in the vertical direction lose stability and become non-axial solutions.

Now that we understand the existence of and stability of axial constant velocity traveling solutions, we turn our attention to the stability of non-axial traveling bump solutions.

To determine the stability of non-axial directions, we consider the solution, $\theta_1(\tau) = \nu\tau + \phi_1 e^{\lambda\tau}$ and $\theta_2(\tau) = \nu\tau + \phi_2 e^{\lambda\tau}$. This ansatz results in the equations,

$$\begin{aligned}
\lambda\phi_1 &= -g\phi_1 \int_0^\infty Q_1(s)\left(e^{-\lambda s} - 1\right) ds - g\phi_2 \int_0^\infty Q_2(s)\left(e^{-\lambda s} - 1\right) ds, \\
\lambda\phi_2 &= -g\phi_1 \int_0^\infty Q_3(s)\left(e^{-\lambda s} - 1\right) ds - g\phi_2 \int_0^\infty Q_4(s)\left(e^{-\lambda s} - 1\right) ds,
\end{aligned}$$

where

$$\begin{aligned}
Q_1(s) &= \int_0^\infty e^{-s} \frac{\partial H_1}{\partial x}(-\nu_1 s, -\nu_2 s), \quad Q_2(s) = \int_0^\infty e^{-s} \frac{\partial H_1}{\partial y}(-\nu_1 s, -\nu_2 s), \\
Q_3(s) &= \int_0^\infty e^{-s} \frac{\partial H_1}{\partial y}(-\nu_2 s, -\nu_1 s), \quad Q_2(s) = \int_0^\infty e^{-s} \frac{\partial H_1}{\partial x}(-\nu_2 s, -\nu_1 s).
\end{aligned}$$

By rewriting the integrals in the more compact form,

$$\begin{aligned}
\lambda\phi_1 &= -g\phi_1 \hat{Q}_1(\lambda) - g\phi_2 \hat{Q}_2(\lambda), \\
\lambda\phi_2 &= -g\phi_1 \hat{Q}_3(\lambda) - g\phi_2 \hat{Q}_4(\lambda),
\end{aligned}$$

where $\hat{Q}_i = \int_0^\infty Q_i(s)(e^{-\lambda s} - 1)ds$, the problem reduces to finding an eigenvector $(\phi_1, \phi_2)^T$ with corresponding eigenvalue $-\lambda$:

$$g \begin{pmatrix} \hat{Q}_1(\lambda) & \hat{Q}_2(\lambda) \\ \hat{Q}_3(\lambda) & \hat{Q}_4(\lambda) \end{pmatrix} \begin{pmatrix} \phi_1 \\ \phi_2 \end{pmatrix} = -\lambda \begin{pmatrix} \phi_1 \\ \phi_2 \end{pmatrix}. \tag{3.33}$$

This condition holds if and only if the determinant

$$\mathcal{E}(\lambda) = \left| g \begin{pmatrix} \hat{Q}_1(\lambda) & \hat{Q}_2(\lambda) \\ \hat{Q}_3(\lambda) & \hat{Q}_4(\lambda) \end{pmatrix} + \lambda I_2 \right| \tag{3.34}$$

is zero. This determinant is the Evans function, and we use its roots to determine stability properties of the constant velocity solutions.

Using the accurate Fourier series of H_i, the integrals of the eigenvalue problem (3.33) are explicitly computable. Given a value g, it is straightforward to compute the contours of $\mathcal{E} = 0$ using a standard contour plot routine. In panels A and B of Figure 36, we show the Evans function when $g = 1.5$, and $g = 3$, respectively.

The domain values where the real part of the Evans function is zero is shown as a black contour, while the domain values where the imaginary part is zero is shown in gray. Intersections of these contours show roots of the Evans function. Generally, there exists a root of the Evans function at the origin due to translation invariance of the underlying bump solution. Thus we ignore this root and consider only those nontrivial roots with real part sufficiently greater than -1. These nontrivial roots are marked with red dots.

We follow these roots using `XPPAUTO` and generate the bifurcation diagram shown in the right panel of Figure 36. The real part of the root remains negative for the range of g that we consider, thus the constant traveling bump solution remains stable for a large range of adaptation strengths.

We repeat the analysis of the Evans function using the truncated Fourier interaction function, H^F. Once again, the integrals of the eigenvalue problem (3.33) are explicitly computable and we follow the roots of the Evans function using `XPPAUTO` in two parameters, b and g, the Fourier coefficient, and adaptation strength, respectively. The right panel of Figure 37 shows the result of this continuation: within the unstable region (marked in light blue), constant velocity solutions are unstable, as demonstrated by the lower inset showing θ_1 as a function of time. Because the instability arises through a Hopf bifurcation, the traveling bumps begin to "wobble". In the stable region, bump solutions travel with constant velocity, as demonstrated by the upper inset showing θ_1 as a function of time.

The left panels (A and B) of Figure 37 demonstrates the existence of a Hopf bifurcation on the boundary between stable and unstable regions. These panels correspond to points

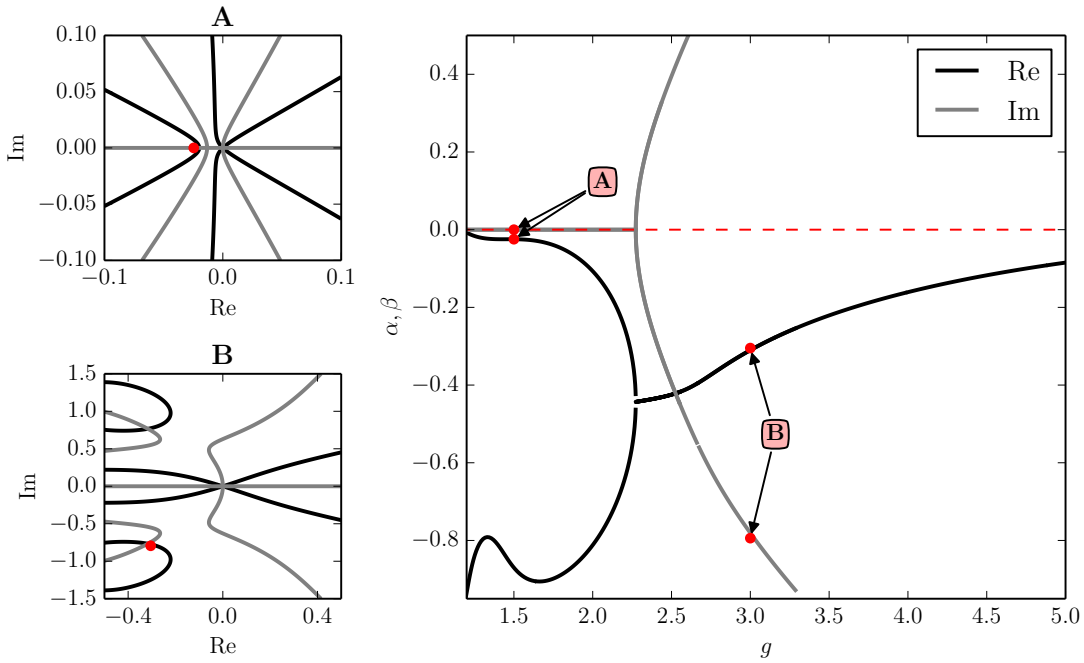

Figure 36: Evans function for the accurate Fourier series H. Left panels A and B: roots of the real (black) and imaginary (gray) parts of the evans function for $g = 1.5$ and $g = 3$, respectively. Intersections of the gray and black lines denote zeros of the Evans function. We use α and β to denote the real and imaginary part of the Evans function, respectively. Right panel: The real and imaginary parts of the nontrivial root(s) of the Evans function for various choice of g. The horizontal red dashed line denotes the real axis.

labeled A and B on the right panel. In each case, we find a complex conjugate pair of eigenvalues that cross the imaginary axis.

In this section, we analyzed the reduced neural field model with nonzero adaptation strength ($g > 0$) and no input current ($q = 0$). We now explore the dynamics arising from activating the time-invariant input current.

3.4.4 Hopf Bifurcation on the Torus

We have seen in Figures 31, 28 that for nonzero g and q, the system may produce a traveling

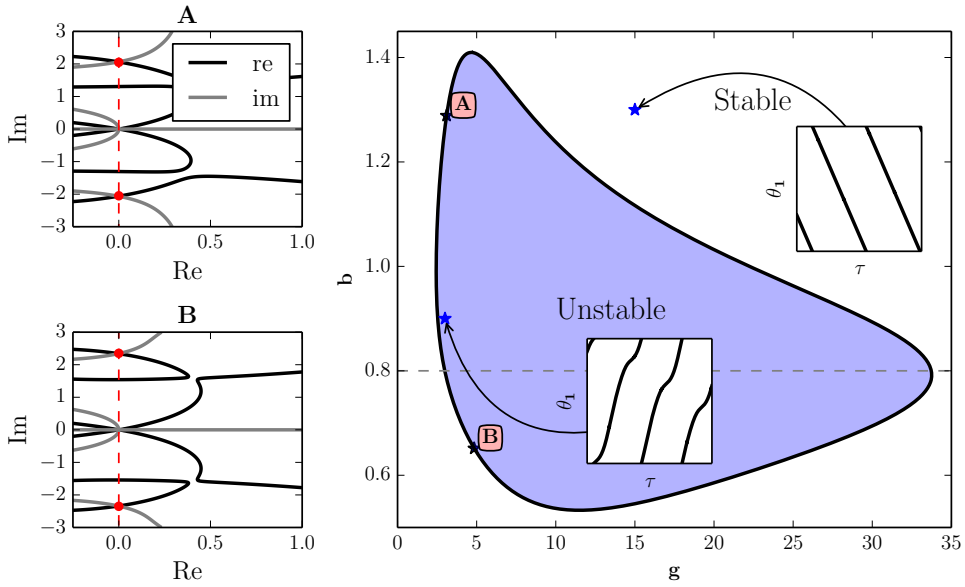

Figure 37: Evans function for the truncated interaction function H^F. Left panels A and B: roots of the real (black, $g = 3.1$, $b = 2.28$) and imaginary (gray, $g = 4.84$, $b = 0.65$) parts of the evans function demonstrating a loss of stability through a Hopf bifurcation. Intersections of the gray and black lines denote zeros of the Evans function. Right panel: the black line denotes where the real part of the Evans function is zero in b and g parameter space (i.e., where the bump solution loses stability). The points labeled A and B correspond to panels A and B, respectively. The horizontal dashed gray line shows our usual choice of the parameter value $b = 0.8$.Two insets with example solutions of $\theta_1(\tau)$ over slow time τ are shown, corresponding to the blue star in parameter space. In the stable region, the traveling bump solution moves with constant velocity (inset parameter values $g = 15$,$b = 1.3$ integrated over $t = 20000$ time units with the last 7.5% of the data shown). In the unstable region, the traveling bump solution loses stability through a Hopf bifurcation and begins to travel with nonconstant velocity (inset parameter values $g = 3$,$b = 0.9$ integrated over $t = 20000$ time units with the last 2.5% of the data shown). Parameter: $\varepsilon = 0.01$.

bump solution that oscillates about the origin-centered input. For a fixed parameter value q, the origin is stable for $g = 0$, and with increasing g eventually becomes unstable through a Hopf bifurcation. We study this phenomenon with Equation (3.23), using the same technique as used on the ring: linearization about the origin.

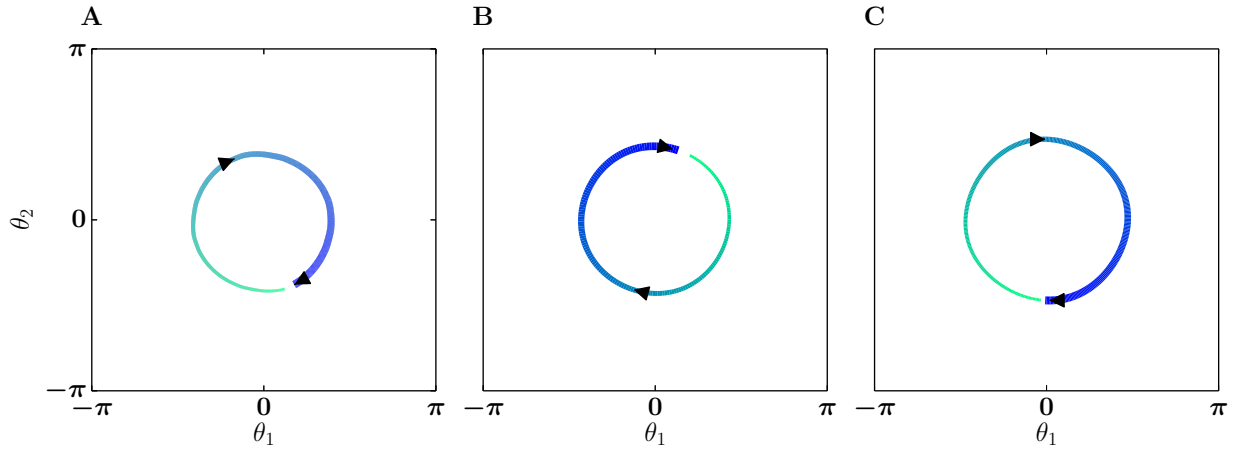

Figure 38: Limit cycle dynamics of the traveling bump on the torus. The curve that goes from light to dark and thin to thick represents the movement of the centroid over time. A: Full neural field model on the torus, $q = 2$, $g = 5$, period of $t = 805$ time units. B: Phase model on the torus with the accurate Fourier series approximation of H_i, $q = 1$, $g = 3$, period of $t = 187$ time units. C: Phase model on the torus with the truncated Fourier series H_i^F, $q = 0.2$, $g = 1$, period of $t = 370$ time units. Parameter $\varepsilon = 0.01$.

Let $(\theta_1(\tau), \theta_2(\tau)) = (e^{\lambda\tau}, e^{\lambda\tau})$. Plugging into Equation (3.23) results in a system of two decoupled equations,

$$\lambda = q\hat{J}_i^0 - g\hat{H}_i^0 \int_0^\infty e^{-s}(e^{-\lambda s} - 1)ds,$$

where

$$\hat{J}_i^0 = \frac{\partial J_i}{\partial x}(0,0) + \frac{\partial J_i}{\partial y}(0,0),$$
$$\hat{H}_i^0 = \frac{\partial H_i}{\partial x}(0,0) + \frac{\partial H_i}{\partial y}(0,0).$$

Evaluating the integral and solving for λ yields

$$2\lambda = -(1 - q\hat{J}_i^0 - g\hat{H}_i^0) \pm \sqrt{(1 - q\hat{J}_i^0 - g\hat{H}_i^0)^2 + 4q\hat{J}_i^0}.$$

Thus, as in the case of the ring, for a fixed q and given g sufficiently large, there exists a Hopf bifurcation at the critical value

$$g = \frac{1 - q\hat{J}_i^0}{\hat{H}_i^0}.$$

For the truncated interaction function H_i^F, the critical value is

$$g = \frac{1 + q(1 + b)}{1 + b}.$$

3.4.5 Non-Constant Velocity Bump Solution on the Torus

As we have seen in earlier sections, stable oscillating solutions exist for particular choices of input current strength and adaptation on both the ring and torus. The similarities of solutions on the ring and torus continue as adaptation strength increases. On the ring, the oscillating solution gives way to a bump solution that travels around the ring with non-constant velocity. Similarly, with sufficiently large adaptation g, the bump solution on the torus also breaks free from the oscillating solution and traverses the domain with non-constant velocity. Figure 39 shows examples of these solutions in the full model (panel A), the phase model with the accurate Fourier series (panel B), and the phase model with the truncated Fourier series (panel C).

There are plenty of other examples of these types of solutions (Figures 30,29,28) that are in fact chaotic. To demonstrate the existence of chaos numerically, we use the truncated phase model and a Poincaré section through $cy = 0$, as we find that generically the variable cy consistently crosses zero throughout simulations.

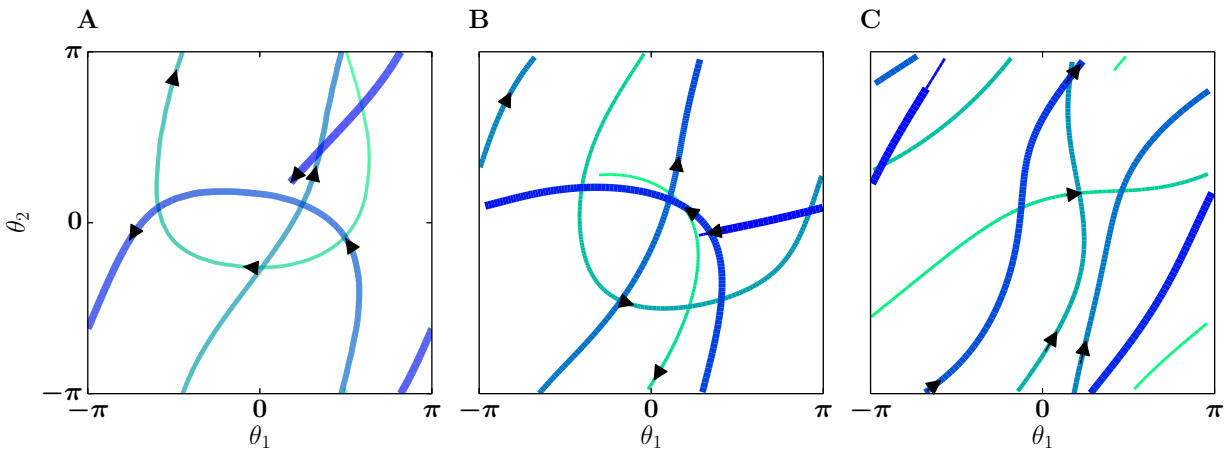

Figure 39: Non-constant velocity dynamics of the traveling bump on the torus. The curve that goes from light to dark and thin to thick represents the movement of the centroid over time. A: Full neural field model on the torus, $q = 1$, $g = 5$, simulated for $t = 5,000$ time units with the last 60% of the data shown. B: Phase model on the torus with the accurate Fourier series of H_i, $q = 1$, $g = 5$, simulated for $t = 6,700$ time units with the last 8% of the data shown. C: Phase model on the torus with the truncated Fourier series H_i^F, $q = .5$, $g = 4.5$, simulated for $t = 6,700$ time units with the last 7% of the data shown. Parameter: $\varepsilon = 0.01$.

3.4.5.1 Chaos on the Torus For a given g, we simulate the truncated phase model (Equation (3.27)) for $t = 150000$ time units and ignore the first 7000 time units to remove transients. By plotting the appropriate state variables, we are able to determine whether a system is aperiodic (and possibly chaotic) or periodic. The top panel of Figure 40 shows one example of one such plot, where for each g value we plot all cy values for the duration of the simulation. The black regions of Figure 40 correspond to the gray regions of Figure 30: the approximate range $0.85 < g < 1.1$ corresponds to region **F**, the approximate range $1.18 < g < 1.61$ corresponds to region **G**, and the approximate range $g > 2.05$ corresponds to region **H**, respectively.

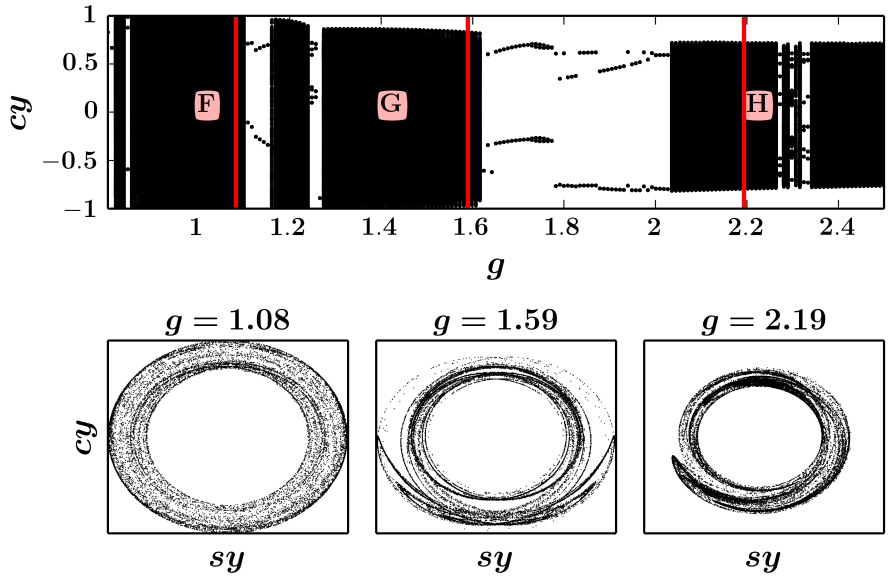

Figure 40: Chaotic attractors. Top panel: crude bifurcation diagram of cy as a function of parameter g. Black regions correspond to aperiodic and possibly chaotic behavior, while regions with dots correspond to periodic solutions. Parameter: $q = 0.1$.

We show sample solutions of the chaotic attractors in regions **F**,**G**,**H** in the bottom three panels of Figure 40. The vertical red line in the top panel denotes the parameter value corresponding to each attractor.

3.5 DISCUSSION

Our motivation for this work was to understand the behavior of the model presented in [43] where the authors showed that heterogeneities in a recurrent network with adaptation produced a seemingly randomly moving bump of activity. Similar moving bump dynamics was also found in a homogeneous bump model with adaptation in [37]; here the authors report only axially moving bumps with no external inputs. The neural field model considered in this chapter (Equations (3.1),(3.2)) is also capable of producing a rich variety of solutions on the ring and torus. On the ring, the centroid of the bump solution exhibits sloshing and large-sloshing behaviors (for moderate strengths of input current and adaptation) that, for stronger adaptation, lead to non-constant velocity traveling bump solutions. With no input current and sufficient adaptation, the system generates a constant velocity traveling bump solution. We also observe chaotic solutions for a narrow range of adaptation strengths.

On the torus, the qualitative solutions are similar to those on the ring: Stationary bump solutions give rise to sloshing solutions (for moderate strengths of input current and adaptation), as well as non-constant velocity traveling bump solutions (with sufficient adaptation) and constant velocity traveling solutions (with no input current and sufficient adaptation). In this system, we do not see pulses that change in diameter with a fixed centroid (breathers) on the ring or torus.

Neural fields with nonsmooth firing rate functions (i.e., the Heaviside or rectifying nonlinearity) reproduce many of these qualitative behaviors. The existence and bifurcation of sloshing solutions on the ring are analyzed in [29, 22], and constant velocity solutions are shown to exist on the ring ([97, 22]), the real line ([50]), and the plane ([34]). Nonconstant velocity bump solutions are shown to exist in [22]. However, there are no studies showing the existence of aperiodic attractors on the torus (assuming a deterministic system with an even kernel), or the existence of chaos on the ring.

In this study, we contributed to the analysis of the known behaviors by using a smooth firing rate function and a caveat of weak and slow adaptation. This assumption on the adaptation variable allowed us to reduce the neural field model, which is a distributed partial integro-differential equation, to a system of scalar delay integro-differential equations

describing the centroid of the bump solution. Moreover, our only restriction on the kernel is of Mexican-hat type. Put together, these assumptions and our results are more general than what currently exists in literature.

In one spatial dimension, for example, we derived the normal form for the Hopf bifurcation in the one-dimensional neural field model and determined the conditions for super- and sub-criticality. Although normal form calculations exist for neural field models on the ring or the real line, our calculation allows for a general choice of kernel and a smooth firing rate function (as opposed to a particular choice of kernel or a non-smooth Heaviside firing rate function [22, 29]).

As mentioned previously, existing studies require particular choices of kernels or Heaviside firing rate functions where a smooth firing rate function would be desirable ([8] note that a smooth firing rate function allows for a straightforward normal form analysis). Although these assumptions are restrictive, these studies have advantages that the current study does not address. In particular, our analysis requires that adaptation is weak and slow and that the input current is weak. As a result, we can only study phenomena that evolve on a slow timescale. These weak and slow assumptions are well-suited for studying long-lasting sequences of spatially coherent activity in the absence of changing external stimuli [72, 43], but may not be as well suited to study phenomena on a faster timescale, like the effects of weak modulatory interactions mediated by the reciprocal, long-range *patchy connections* in primary visual cortex [29].

Generally speaking, one might ask why we need the adaptation to be both slow and weak. For example, in [76], the adaptation was slow but not weak. One could imagine doing a perturbation analysis for a weak stimulus such as in [24] where a weak slowly moving stimulus is applied to a system that has a stable traveling bump. However, strong adaptation, will alway induce movement in a bump so that we can never pin the bump with *weak* inputs. Furthermore, by keeping the adaptation $O(1)$, one needs to compute the adjoint solution to a two-variable traveling bump, a difficult task in one spatial dimension, and impossible (as far as we can tell) in two spatial dimensions. Thus, by working with weak inputs and weak/slow adaptation, we have hit a sweet spot from which many of the interesting dynamics emerges.

One type of behavior that has been observed in this class of models that does not occur

in our analysis is the so-called breathing solutions [31]. Breathers are periodic solutions to the neural field equations that occur when the bump solution loses stability via a *symmetric* mode. In contrast, sloshers appear when there is a Hopf bifurcation to an *anti-symmetric* mode. In the breather case, the centroid of the bump does not change, so our reduced equations cannot detect such a bifurcation. In contrast, sloshers lead to modulation of the centroid and thus our analysis can capture that. To further explore this, we were able to induce bifurcation to a breathing solution in equations (3.1,3.2) but only when ε is sufficiently large. We find that it is possible to continue this bifurcation in ε and make ε quite small, but only if we increase both the strength of adaptation g and the heterogeneity, q such that $\varepsilon q, \varepsilon g$ remain $O(1)$. That is, breathers can only occur when the adaptation and input magnitudes are large compared to the rate of adaptation. Our analysis, therefore, cannot include the appearance of breathers.

The effects of noise on the phase equations is one possible direction for future study. Several cited papers analyze the movement of bump solutions in the presence of noise. Near the drift bifurcation for traveling bump solutions with sufficiently strong linear adaptation, it is possible to derive a stochastic amplitude equation when the adaptation strength and stochastic forcing are similar in magnitude [48]. Sufficiently far from the bifurcation, the stochastic forcing leads to diffusive wandering of the bump solution. Other studies analyze the diffusive behavior of solutions to neural field models and how pinning eliminates diffusive behavior [78]. In [60], the authors add Gaussian noise to the adaptation term of a neural field model similar to the model in this chapter, but with strong input and adaptation, which is not necessarily slow. In this case, the bump solution velocity decreases as a function of noise level. Laing and Longtin then consider colored noise (noise with temporal correlations) to adaptation, and show that the bump velocity decreases as a function of noise correlation time. The authors compute the effects of adding noise to the normal form of the pitchfork bifurcation, and show that greater noise levels delay the onset of moving bumps. As mentioned previously, these studies assume either a particular firing rate function or kernel. The general case remains unexplored.

4.0 A MULTIPLE TIMESCALES APPROACH TO BRIDGING SPIKING- AND POPULATION-LEVEL DYNAMICS

This chapter is based on [69], with all figure-generation code available on GitHub:
https://github.com/youngmp/park_and_ermentrout_2018

4.1 INTRODUCTION

Neural mean field models are a useful framework for studying mesoscopic and macroscopic spatio-temporal activity in the cortex. Examples include mammalian path integration, head direction tracking, visual hallucination, working memory, spatial object location, and object orientation [15, 14, 32, 7].

Existing studies derive macroscopic quantities starting at the spiking level, but require particular assumptions including asynchronous firing [58, 57, 79] and Poisson statistics [4, 3]. These studies contain no information about synchronization at the spiking level, which could underpin the loss or gain of power in electroencephalogram (EEG) frequency bands [16].

Recent studies relax the asynchronous firing assumption with the goal of predicting population synchrony, and have successfully used low-dimensional spiking models like the Kuramoto model [85], theta model [27, 16], Alder units [80], and quadratic integrate-and-fire models [63] to this end. These models are amenable to the Ott-Antonsen ansatz [67], which results in a complementary order parameter in addition to the mean field variables, e.g., firing rate.

In contrast to these studies, the goal of the present study is to derive a metric of synchrony at the spiking level for general oscillators. In particular, we derive a set of phase equations for

each oscillator as a function of the mean field. Moreover, the existence of multiple timescales allows us to derive the phase equations as a function of the mean field dynamics.

We begin with a finite network of N, n-dimensional excitatory spiking neurons and N, m-dimensional inhibitory spiking neurons connected by slow synapses:

$$\frac{d\mathbf{x}_i}{dt} = \mathbf{F}^x(\mathbf{x}_i, s^x, s^y) + \varepsilon \mathbf{G}_i^x(\mathbf{x}_i), \tag{4.1}$$

$$\frac{d\mathbf{y}_i}{dt} = \mathbf{F}^y(\mathbf{y}_i, s^x, s^y) + \varepsilon \mathbf{G}_i^y(\mathbf{y}_i), \tag{4.2}$$

$$\mu^x \frac{ds^x}{dt} = \varepsilon \left[-s^x + \frac{1}{N} \sum_{j=1}^{N} \delta(t - t_{j,\mathbf{x}}) \right], \tag{4.3}$$

$$\mu^y \frac{ds^y}{dt} = \varepsilon \left[-s^y + \frac{1}{N} \sum_{j=1}^{N} \delta(t - t_{j,\mathbf{y}}) \right], \tag{4.4}$$

where $i = 1 \ldots, N$, the term $t_{j,\mathbf{x}}$ represents the spike times of each neuron $i = 1, \ldots, N$, $\mathbf{F}^k$ is the vector field for neuron type $k = x, y$, and $\mathbf{G}_i^k$ represents heterogeneity in oscillator i of vector field k. For conductance-based models, we take the spike time be the upwards zero-crossing of the membrane potential. The same notation holds for the inhibitory population $\mathbf{y}$.

Equations (4.3) and (4.4) exhibit fast and slow changes: s^x (s^y) resets instantaneously as $s^x \mapsto \bar{s}^x + \varepsilon/(N\mu^x)$ ($s^y \mapsto \bar{s}^y + \varepsilon/(N\mu^y)$) whenever neuron i spikes in either population. With these notations defined, we turn to the assumptions.

- The term ε is small, $0 < \varepsilon \ll 1$. Thus the synapses increment instantaneously with order ε, but decay slowly between spikes.
- There is a separation of timescales into a "fast" time t and a "slow" time $\tau = \varepsilon t$.
- The mean synaptic values, $\bar{s}^x$ and $\bar{s}^y$, are constant and differ at most by a small amount $O(\varepsilon)$. If the mean values are the same, we denote the mean synaptic values by $\bar{s}$, where $\bar{s} = \bar{s}^x = \bar{s}^y$.
- In the decoupled case without heterogeneity ($\varepsilon = 0$), we assume that there exists a T-periodic limit cycle $\Phi^k(t, \tau)$ satisfying Equations (4.1),(4.2) for a range of values $\bar{s}^k \in [s^-, s^+]$ where $k = x, y$.
- Generally, $\bar{s}^k > 0$, and there may exist no limit cycle when $\bar{s}^k = 0$.

- The vector field dimensions are arbitrary: $\mathbf{F}^x, \mathbf{G}_i^x : \mathbb{R}^n \times \mathbb{R} \times \mathbb{R} \to \mathbb{R}^n$ and $\mathbf{F}^y, \mathbf{G}_i^y : \mathbb{R}^m \times \mathbb{R} \times \mathbb{R} \to \mathbb{R}^m$, where $n, m \geq 1$.

These assumptions appear in a similar form in [81]. The authors show that when the mean synaptic values are constant with slow synaptic decay, the slow and strong coupling problem becomes a fast and weak coupling problem, and thus amenable to the classic phase reduction. However, we are also interested in the case where the synaptic variables s^x, s^y are slowly varying. Thus, we allow that

- There can exist small amplitude (order ε) oscillations in the mean slow variables $\bar{s}^x, \bar{s}^y$ for some parameter values μ^x, μ^y satisfying the mean field description of Equations (4.1)–(4.4)

$$\begin{aligned} \mu^x \frac{d\bar{s}^x}{dt} &= \varepsilon[-\bar{s}^x + \omega^x(I^x(\bar{s}^x, \bar{s}^y))], \\ \mu^y \frac{d\bar{s}^y}{dt} &= \varepsilon[-\bar{s}^y + \omega^y(I^y(\bar{s}^x, \bar{s}^y))], \end{aligned} \tag{4.5}$$

  where ω^k is the frequency of population $k = x, y$ as a function of an input current I^k that depends on the mean synaptic variables $\bar{s}^x$ and $\bar{s}^y$. The input current is the total current applied to the neural membrane as a result of the synaptic activity. The small oscillation amplitude is independent of ε, and generally may be orders of magnitude greater than ε. However, if the mean field description can produce oscillations, we are only interested in small, order ε oscillations, so for simplicity we say that the oscillations, if they exist, are order ε.

Thus the mean-field dynamics are determined entirely by the frequency-current (FI) curves of the neural models we consider in this chapter (Section 4.3.6). We show examples of FI curves for the models we consider in Figure 41. In panel A we show the FI curve for the Traub model with calcium, and in panel B we show the FI curve for the Wang-Buzsáki model. In general, these FI curves are computed numerically using `XPPAUTO` [19]. In some cases they can be computed explicitly as in the theta model, which is another model we consider in this chapter (Section 4.3.1).

The goal of this chapter is to derive a system of equations describing the phase locking properties of the network (Equations (4.1)–(4.4)) that complement the mean field description

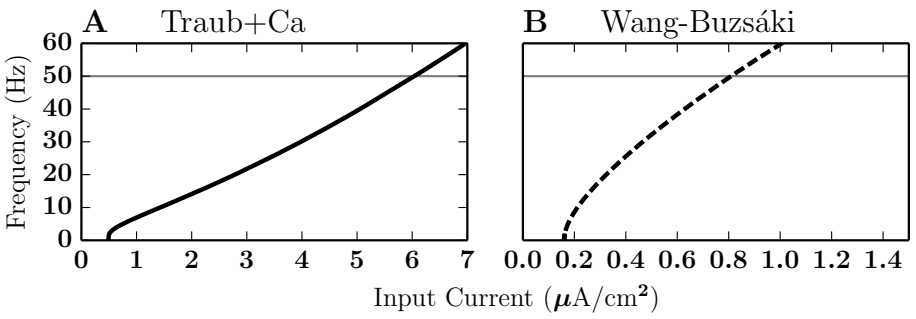

Figure 41: The frequency-current (FI) curves of the Traub with calcium model (solid black) and Wang-Buzsáki model (dashed black). Frequency is in units of cycles per millisecond. The horizontal gray line through the frequency value 0.05Hz denotes our choice of fixed mean synaptic current. Small and slow oscillations of the synaptic variables in this network are about this mean value and are fully determined by the values of these FI curves.

of the network (Equation (4.5)). The primary contribution of the chapter is to show that the phase reduction is valid when the synapses are slowly varying with small amplitude.

4.2 DERIVATION OF THE PHASE MODEL

We begin the reduction to phase oscillators with the ansatz

$$\begin{aligned}
\mathbf{x}_i(t,\tau) &= \mathbf{x}_i(t+\theta_i(\tau),\bar{s}) = \Phi^x(t+\theta_i^x(\tau),\bar{s}) + \varepsilon\xi_i^x(t+\theta_i^x(\tau),\bar{s}) + O(\varepsilon^2),\\
\mathbf{y}_i(t,\tau) &= \mathbf{y}_i(t+\theta_i(\tau),\bar{s}) = \Phi^y(t+\theta_i^y(\tau),\bar{s}) + \varepsilon\xi_i^y(t+\theta_i^y(\tau),\bar{s}) + O(\varepsilon^2),\\
s^x(t,\tau) &= \bar{s}^x(\tau) + \frac{\varepsilon}{N\mu^x}\sum_j f\left(t+\theta_j^x(\tau)\right) + O(\varepsilon^2),\\
s^y(t,\tau) &= \bar{s}^y(\tau) + \frac{\varepsilon}{N\mu^y}\sum_j f\left(t+\theta_j^y(\tau)\right) + O(\varepsilon^2),
\end{aligned} \tag{4.6}$$

where $\bar{s}^k(\tau)$ is the slowly varying mean synaptic value for $k = x, y$, and f represents the effects of fast timescale, small-magnitude spikes on the synaptic variable. Technically, $\mathbf{x}_i$, $\mathbf{y}_i$, ϕ^k, and ξ_i^x have arguments of the form $(t+\theta_i(\tau), \bar{s}^x(\tau), \bar{s}^y(\tau))$, but because we evaluate these

functions at the fixed mean value $\bar{s} = \bar{s}^x = \bar{s}^y$, we abbreviate the notation of the redundant inputs by writing $(t + \theta_i(\tau), \bar{s})$.

Using the periodicity of $s^k(\tau)$ on the fast timescale and small delta function impulses of order ε, one can derive f explicitly as

$$f(t + \theta^k(\tau)) = \left[\left(1 - (t + \theta^k(\tau))/T \mod 1\right) - 1/2\right].$$

We detail the calculations in appendix C.2. For notational convenience, we do not write f explicitly for the remainder of the derivation.

Next, because the slow oscillations are small amplitude (order ε), we include an additional term in the expansion:

$$\begin{aligned} s^k(t,\tau) &= \bar{s}^k(\tau) + \bar{s} - \bar{s} + \frac{\varepsilon}{N\mu^x}\sum_j f\left(t + \theta_j^k(\tau)\right) \\ &= \bar{s} + \varepsilon\left(\frac{\bar{s}^k(\tau) - \bar{s}}{\varepsilon}\right) + \frac{\varepsilon}{N\mu^x}\sum_j f\left(t + \theta_j^k(\tau)\right), \end{aligned}$$

where $\bar{s}$ stands for the constant fixed mean values $\bar{s}^x = \bar{s}^y$.

Plugging in Equation (4.6) into Equation (4.1) and grouping in terms of small order ε results in the system of equations,

$$\begin{aligned} &\frac{\partial \Phi^x}{\partial t} = \mathbf{F}^x[\Phi^x(t + \theta_i^x(\tau)), \bar{s}], \\ &\frac{d\theta_i^x}{d\tau}\frac{\partial \Phi^x}{\partial t}(t + \theta_i^x(\tau), \bar{s}) + \frac{d}{dt}\xi_i^x(t + \theta_i^x(\tau), \bar{s}) \\ &\quad = \mathbf{F}^x_{\Phi^x}(\Phi^x(t + \theta_i^x(\tau)), \bar{s})\xi_i^x(t + \theta_i^x(\tau), \bar{s}) \\ &\qquad + \mathbf{F}^x_{s^x}(\Phi^x(t + \theta_i^x(\tau)), \bar{s})\left([\bar{s}^x(\tau) - \bar{s}]/\varepsilon + \frac{1}{N\mu^x}\sum_j f\left(t + \theta_j^x(\tau)\right)\right) \\ &\qquad + \mathbf{F}^x_{s^y}(\Phi^x(t + \theta_i^x(\tau)), \bar{s})\left([\bar{s}^y(\tau) - \bar{s}]/\varepsilon + \frac{1}{N\mu^y}\sum_j f\left(t + \theta_j^y(\tau)\right)\right) \\ &\qquad + \mathbf{G}_i^x(\Phi^x(t + \theta_i^x(\tau))) \end{aligned}$$

For an n-dimensional (m-dimensional) vector field $\mathbf{F}^x$ ($\mathbf{F}^y$), the derivative $\mathbf{F}^x_{\Phi^x}$ ($\mathbf{F}^y_{\Phi^y}$) represents the Jacobian matrix. Rewriting yields,

$$\begin{aligned}
&L\xi_i^x(t+\theta_i^x(\tau)) \\
&= \frac{d\theta_i^x}{d\tau}\frac{d\Phi^x}{dt}(t+\theta_i^x(\tau),\bar{s}) \\
&\quad - \mathbf{F}^x_{s^x}(\Phi^x(t+\theta_i^x(\tau)),\bar{s})\left([\bar{s}^x(\tau)-\bar{s}]/\varepsilon + \frac{1}{N\mu^x}\sum_j f\left(t+\theta_j^x(\tau)\right)\right) \\
&\quad - \mathbf{F}^x_{s^y}(\Phi^x(t+\theta_i^x(\tau)),\bar{s})\left([\bar{s}^y(\tau)-\bar{s}]/\varepsilon + \frac{1}{N\mu^x}\sum_j f\left(t+\theta_j^y(\tau)\right)\right) \\
&\quad - \mathbf{G}_i^x(\Phi^x(t+\theta_i^x(\tau)))
\end{aligned} \tag{4.7}$$

where

$$Lu \equiv -\frac{du}{dt} + \mathbf{F}^x_{\Phi^x}(\Phi^x(t+\theta_i^x(\tau)),\bar{s})u.$$

Note that we have already collected terms in order ε, so we have no need to keep the ε/ε term and neglect it from now on. It is straightforward to show that the adjoint of L is

$$L^*v = v' + \left[\mathbf{F}^x_{\Phi^x}(\Phi^x(t+\theta_i^x(\tau)),\bar{s})\right]^T v.$$

We find that a function $\mathbf{z}^x$ in the nullspace of this adjoint operator satisfies

$$\frac{d\mathbf{z}^x}{dt}(t+\theta_i^x(\tau)) = -\left[\mathbf{F}^x_{\Phi^x}(\Phi^x(t+\theta_i^x(\tau)),\bar{s})\right]^T \mathbf{z}^x(t+\theta_i^x(\tau)),$$

and

$$\mathbf{z}^x \cdot \frac{d\Phi^x}{dt} = 1.$$

The function $\mathbf{z}^x$ is the same as the infinitesimal phase response curve of the oscillator Φ^x [25].

Next, we require the existence of a bounded periodic function ξ_i^x satisfying Equation (4.7). Because the operator L has a closed range defined on the space of real-valued T-periodic functions, it follows that there exists a function u satisfying $Lu = b$ if and only if $\langle u, v\rangle = 0$ for all v in the nullspace of L^* [47], where

$$\langle u, v\rangle = \int_0^T u \cdot v \; dt.$$

Applying the existence condition directly to the right hand side of Equation (4.7) yields (with a bit of rearrangement)

$$\begin{aligned}
&\int_0^T \frac{d\theta_i^x}{d\tau}\frac{d\Phi^x}{dt}(t,\bar{s})\cdot\mathbf{z}^x(t,\bar{s})\ dt \\
&= \int_0^T \mathbf{F}^x_{s^x}(\Phi^x(t),\bar{s})\cdot\mathbf{z}^x(t,\bar{s})\left(\frac{\bar{s}^x(\tau)-\bar{s}}{\varepsilon}+\frac{1}{N\mu^x}\sum_j f\left(t+\theta_j^x-\theta_i^x\right)\right)\ dt \\
&\quad+\int_0^T \mathbf{F}^x_{s^y}(\Phi^x(t),\bar{s})\cdot\mathbf{z}^x(t,\bar{s})\left(\frac{\bar{s}^y(\tau)-\bar{s}}{\varepsilon}+\frac{1}{N\mu^x}\sum_j f\left(t+\theta_j^y-\theta_i^x\right)\right)\ dt \\
&\quad+\int_0^T \mathbf{G}_i^x(\Phi^x(t),\bar{s})\cdot\mathbf{z}^x(t,\bar{s})\ dt.
\end{aligned}$$

Simplifying and rewriting, we arrive at the phase equations:

$$\begin{aligned}
\frac{d\theta_i^x}{d\tau} &= [\bar{s}^x(\tau)-\bar{s}]\beta^{xx}/\varepsilon+[\bar{s}^y(\tau)-\bar{s}]\beta^{xy}/\varepsilon+B_i^x \\
&\quad+\frac{1}{N\mu^x}\sum_{j=1}^N H^{xx}(\theta_j^x(\tau)-\theta_i^x(\tau))+\frac{1}{N\mu^x}\sum_{j=1}^N H^{xy}(\theta_j^y(\tau)-\theta_i^x(\tau))
\end{aligned} \tag{4.8}$$

where

$$\begin{aligned}
\beta^{xy} &= \frac{1}{T}\int_0^T \mathbf{F}^x_{s^y}(\Phi^x(t),\bar{s})\cdot\mathbf{z}^x(t,\bar{s})dt \\
\beta^{xx} &= \frac{1}{T}\int_0^T \mathbf{F}^x_{s^x}(\Phi^x(t),\bar{s})\cdot\mathbf{z}^x(t,\bar{s})dt, \\
H^{xx}(\phi) &= \frac{1}{T}\int_0^T \mathbf{F}^x_{s^x}(\Phi^x(t),\bar{s})\cdot\mathbf{z}^x(t,\bar{s})f(t+\phi)dt, \\
H^{xy}(\phi) &= \frac{1}{T}\int_0^T \mathbf{F}^x_{s^y}(\Phi^x(t),\bar{s})\cdot\mathbf{z}^x(t,\bar{s})f(t+\phi)dt, \\
B_i^x &= \frac{1}{T}\int_0^T \mathbf{G}_i^x(\Phi^x(t),\bar{s})\cdot\mathbf{z}^x(t,\bar{s})\ dt.
\end{aligned}$$

The vigilant reader may notice a possible issue with the term $(\bar{s}^x(\tau)-\bar{s})/\varepsilon$, where ε is small. We require that the deviations of $\bar{s}^x(\tau)$ from $\bar{s}$ to be small, in particular to be of order ε. In our derivation, the order ε term cancels so that we can treat the difference $(\bar{s}^x(\tau)-\bar{s})$ as order ε. Thus, the term $(\bar{s}^x(\tau)-\bar{s})/\varepsilon$ is order $O(1)$.

Using the same arguments, we arrive at the phase equations for the y population,

$$\begin{aligned}\frac{d\theta_i^y}{d\tau} &= [\bar{s}^x(\tau)-\bar{s}]\beta^{yx}/\varepsilon + [\bar{s}^y(\tau)-\bar{s}]\beta^{yy}/\varepsilon + B_i^y \\ &\quad + \frac{1}{N\mu^y}\sum_{j=1}^{N} H^{yx}(\theta_j^x(\tau)-\theta_i^y(\tau)) + \frac{1}{N\mu^y}\sum_{j=1}^{N} H^{yy}(\theta_j^y(\tau)-\theta_i^y(\tau)),\end{aligned} \tag{4.9}$$

where

$$\begin{aligned}\beta^{yx} &= \frac{1}{T}\int_0^T \mathbf{F}^y_{s^x}(\Phi^y(t),\bar{s})\cdot\mathbf{z}^y(t,\bar{s})dt,\\ \beta^{yy} &= \frac{1}{T}\int_0^T \mathbf{F}^y_{s^y}(\Phi^y(t),\bar{s})\cdot\mathbf{z}^y(t,\bar{s})dt,\\ H^{yx}(\phi) &= \frac{1}{T}\int_0^T \mathbf{F}^y_{s^x}(\Phi^y(t),\bar{s})\cdot\mathbf{z}^y(t,\bar{s})f(t+\phi)dt,\\ H^{yy}(\phi) &= \frac{1}{T}\int_0^T \mathbf{F}^y_{s^y}(\Phi^y(t),\bar{s})\cdot\mathbf{z}^y(t,\bar{s})f(t+\phi)dt,\\ B_i^y &= \frac{1}{T}\int_0^T \mathbf{G}^y_i(\Phi^y(t),\bar{s})\cdot\mathbf{z}^y(t,\bar{s})\ dt.\end{aligned}$$

Note that in the phase equations (4.8) and (4.9), the synaptic variables are exogenous and do not depend on the microscopic solutions – only the microscopic solutions depend on the mean field. Thus, the microscopic dynamics are fully described by properties of the individual oscillators (the iPRC $\mathbf{z}^k$, the vector field $\mathbf{F}^k$), and the mean synaptic variables $\bar{s}^k$.

When analyzing solutions, we use the phase differences $\phi_i^x = \theta_i^x - \theta_1^x$, $\phi_i^y = \theta_i^y - \theta_1^y$, where $i = 1,\ldots,N$, and $\phi^z = \theta_1^y - \theta_1^x$. By definition, $\phi_1^x = \phi_1^y = 0$ and $d\phi_1^x/d\tau = d\phi_1^y/d\tau = 0$, so we only plot phase differences for $i > 1$. As we have shown in our derivation, our theory tolerates order ε heterogeneities in the vector fields. The phase difference dynamics are then

$$\begin{aligned}N\mu^x\frac{d\phi_i^x}{d\tau} &= \sum_{j=1}^{N}\left[H^{xx}\left(\phi_j^x-\phi_i^x\right)-H^{xx}\left(\phi_j^x\right)\right] + B_i^x - B_1^x \\ &\quad + \sum_{j=1}^{N}\left[H^{xy}\left(\phi_j^y-\phi_i^x+\phi^z\right)-H^{xy}\left(\phi_j^y+\phi^z\right)\right],\end{aligned} \tag{4.10}$$

$$
\begin{aligned}
N\mu^y \frac{d\phi_i^y}{d\tau} &= \sum_{j=1}^{N} \left[H^{yy}\left(\phi_j^y - \phi_i^y\right) - H^{yy}\left(\phi_j^y\right) \right] + B_i^y - B_1^y \\
&\quad + \sum_{j=1}^{N} \left[H^{yx}\left(\phi_j^x - \phi_i^y - \phi^z\right) - H^{yx}\left(\phi_j^x - \phi^z\right) \right],
\end{aligned} \tag{4.11}
$$

$$
\begin{aligned}
\frac{d\phi^z}{d\tau} &= [\bar{s}^x(\tau) - \bar{s}](\beta^{yx} - \beta^{xx})/\varepsilon + [\bar{s}^y(\tau) - \bar{s}](\beta^{yy} - \beta^{xy})/\varepsilon \\
&\quad + \frac{1}{N\mu^y} \sum_{j=1}^{N} \left[H^{yx}\left(\phi_j^x - \phi^z\right) + H^{yy}\left(\phi_j^y\right) \right] \\
&\quad - \frac{1}{N\mu^x} \sum_{j=1}^{N} \left[H^{xx}\left(\phi_j^x\right) + H^{xy}\left(\phi_j^y + \phi^z\right) \right] \\
&\quad + B_1^y - B_1^x
\end{aligned} \tag{4.12}
$$

where $i = 1, \ldots, N$. When the mean synaptic variables, $\bar{s}^k(\tau)$, which satisfy Equation (4.5), are slowly varying, the terms $\bar{s}^k(\tau) - \bar{s}$ in the right hand side of $d\phi^z/d\tau$ are what contribute to large phase drifts between the populations.

To aid in the numerics and analysis, we make note of some facts, starting with the relationship between constant mean synapses and frequency.

4.2.1 Relationship Between Constant Mean Synapses and Frequency

Suppose that the mean $\bar{s}^k$ is constant. Recall that following a spike,

$$
s^k(t) = s^k(0)e^{-\varepsilon t/\mu^k}, t < T^-,
$$

where T^- is the period of the fast oscillator up to and not including the spike. We may determine the initial condition by solving

$$
s^k(T^+) = s^k(0)e^{-\varepsilon T/\mu^k} + \varepsilon/\mu^k = s^k(0),
$$

which yields

$$
s^k(0) = \frac{\varepsilon}{\mu^k} \frac{1}{1 - e^{-\varepsilon T/\mu^k}}.
$$

Taking the mean value of $s^k(t)$ over one period,

$$\bar{s}^k = \frac{1}{T}\int_0^T s^k(t)dt,$$

we find that

$$\bar{s}^k = \frac{1}{T}. \tag{4.13}$$

That is, $\bar{s}$ is the same as the fast frequency.

4.2.2 Fourier Approximation

Because the domain of each function H^{jk} is periodic, we can use a Fourier series approximation to make the numerics tractable. We extract the Fourier coefficients using the fast Fourier transform (FFT) and construct an approximation by writing

$$H^{jk}(x) = \sum_{n=0}^{M}(a_n \cos(nx/T) + b_n \sin(nx/T)).$$

All right hand sides can be written as a sum of sines and cosines, thus amenable to a bifurcation analysis using `XPPAUTO`. Constructing the Jacobian matrix using derivatives of H^{jk} is also straightforward, since we only need to take the derivative of sines and cosines:

$$\frac{dH^{jk}}{dx}(x) = \sum_{n=0}^{M}\left[-na_n \cos(nx/T)/T + nb_n \sin(nx/T)/T\right].$$

See Tables 9, 10 for the values of the Fourier coefficients.

4.3 RESULTS

We now turn to the simulation of neural models to test our theory. We begin by considering a population of excitatory and inhibitory theta neurons [27] and look at two cases: first when the mean synaptic values are fixed, and second when the mean synaptic values are slowly varying with small amplitude about a fixed point. In the first case we show the existence and stability of various phase locked solutions. In the second case we use numerics to demonstrate the accuracy of our phase model.

We conclude by repeating the same comparison using biophysically realistic models. The models we consider are excitatory Traub models with calcium [89], and inhibitory Wang-Buzsáki models [92].

4.3.1 Theta Neurons

Consider a network of excitatory and inhibitory theta neurons with all-to-all coupling,

$$\begin{aligned}
\frac{dx_j}{dt} &= \pi(1-\cos(x_j)+(1+\cos(x_j))[a^x+b^x s^x - c^x s^y]),\\
\frac{dy_j}{dt} &= \pi(1-\cos(y_j)+(1+\cos(y_j))[a^y+b^y s^x - c^y s^y]),\\
\mu^x \frac{ds^x}{dt} &= \varepsilon\left[-s^x + \frac{1}{N}\sum_j \delta(x_j-\pi)\right],\\
\mu^y \frac{ds^y}{dt} &= \varepsilon\left[-s^y + \frac{1}{N}\sum_j \delta(y_j-\pi)\right].
\end{aligned} \tag{4.14}$$

Given values $\bar{s}^x$ and $\bar{s}^y$, the period T^k of oscillators in population k is given by the integral

$$T^k = \frac{1}{\pi}\int_{-\pi}^{\pi} \frac{dx}{1-\cos(x)+(1+\cos(x))I^k}, \quad k=x,y,$$

where $I^k = a^k + b^k\bar{s}^x - c^k\bar{s}^y$. We skip the details, but this integral is explicitly computable [25], allowing us to express the period T^k as a function of the input I^k:

$$T^k(I^k) = 1/\sqrt{[I^k]_+},$$

where $[x]_+ = \max\{0, x\}$. The reciprocal of the period T^k is the frequency,

$$\omega^k(I^k) = \sqrt{[I^k]_+}.$$

Thus, the averaged dynamics are

$$\mu^x \frac{ds^x}{dt} = \varepsilon \left(-s^x + \sqrt{[I^x]_+} \right), \tag{4.15}$$

$$\mu^y \frac{ds^y}{dt} = \varepsilon \left(-s^y + \sqrt{[I^y]_+} \right). \tag{4.16}$$

For this system, the limit cycle and iPRC are, respectively [25],

$$\Phi^i(t, \bar{s}) \equiv \Phi(t, \bar{s}) = 2 \arctan(\bar{s} \tan(\bar{s}\pi(t + T/2)),$$
$$Z^i(t, \bar{s}) \equiv Z(t, \bar{s}) = [\cos^2(\bar{s}\pi(t + T/2)) + \bar{s}^2 \sin^2(\bar{s}\pi(t + T/2))]/(2\bar{s}^2\pi),$$

where $\bar{s}$ is the fixed point $\bar{s}^x = \bar{s}^y$. To compute the H functions, we note that the partial derivatives of the right-hand side of Equation (4.14) evaluated on the limit cycle $\Phi(t, \bar{s}$ and mean synaptic value $\bar{s}$ are:

$$\begin{aligned}
\pi \frac{\partial}{\partial s^x} (1 - \cos(x_j) + (1 + \cos(x_j))[a^x + b^x s^x - c^x s^y])|_{x_j = \Phi(t,\bar{s}), s^x = s^y = \bar{s}} \\
= b^x \pi [1 + \cos(\Phi(t, \bar{s}))], \\
\pi \frac{\partial}{\partial s^y} (1 - \cos(x_j) + (1 + \cos(x_j))[a^x + b^x s^x - c^x s^y])|_{x_j = \Phi(t,\bar{s}), s^x = s^y = \bar{s}} \\
= -c^x \pi [1 + \cos(\Phi(t, \bar{s}))], \\
\pi \frac{\partial}{\partial s^x} (1 - \cos(y_j) + (1 + \cos(y_j))[a^y + b^y s^x - c^y s^y])|_{y_j = \Phi(t,\bar{s}), s^x = s^y = \bar{s}} \\
= b^y \pi [1 + \cos(\Phi(t, \bar{s}))], \\
\pi \frac{\partial}{\partial s^y} (1 - \cos(y_j) + (1 + \cos(y_j))[a^y + b^y s^x - c^y s^y])|_{y_j = \Phi(t,\bar{s}), s^x = s^y = \bar{s}} \\
= -c^y \pi [1 + \cos(\Phi(t, \bar{s}))],
\end{aligned}$$

Thus the H functions of Equations (4.8) and (4.9) for this system are given by

$$\begin{aligned}
H^{xx}(\phi) &= \frac{b^x \pi}{T\mu^x} \int_0^T Z(t,\bar{s})[1+\cos(\Phi(t,\bar{s}))] f(t+\phi)dt, \\
H^{xy}(\phi) &= -\frac{c^x \pi}{T\mu^y} \int_0^T Z(t,\bar{s})[1+\cos(\Phi(t,\bar{s}))] f(t+\phi)dt, \\
H^{yx}(\phi) &= \frac{b^y \pi}{T\mu^x} \int_0^T Z(t,\bar{s})[1+\cos(\Phi(t,\bar{s}))] f(t+\phi)dt, \\
H^{yy}(\phi) &= -\frac{c^y \pi}{T\mu^y} \int_0^T Z(t,\bar{s})[1+\cos(\Phi(t,\bar{s}))] f(t+\phi)dt.
\end{aligned} \tag{4.17}$$

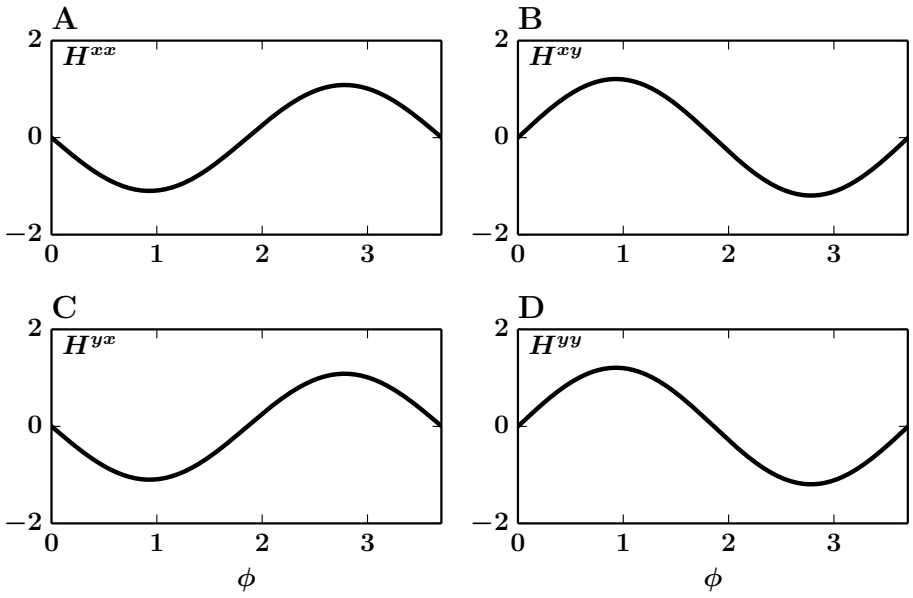

Figure 42: Example H-functions of the theta model. Panel A: H^{xx}. Panel B: H^{xy}. Panel C: H^{yx}. Panel D: H^{yy}. In all panels, parameter values are $a^x = a^y = 0.1$, $b^x = b^y = 1$, $c^x = c^y = 1.1$, and $\mu^x = \mu^y = 1$.

We show examples of the H-functions in Figure 42. For clarity in the calculations to follow, we define a new function $\hat{H}^{jk}$ in order to write the parameters explicitly.

$$\begin{aligned}
b^x \hat{H}^{xx}(\phi)/\mu^x &= H^{xx}(\phi) \\
-c^x \hat{H}^{xy}(\phi)/\mu^y &= H^{xy}(\phi) \\
b^y \hat{H}^{yx}(\phi)/\mu^x &= H^{yx}(\phi) \\
-c^y \hat{H}^{yy}(\phi)/\mu^y &= H^{yy}(\phi).
\end{aligned}$$

Note that the slope of $\hat{H}^{ky}$ is the opposite of the slope of H^{ky} for $k = x, y$.

Using the tools developed up to this point, we can begin to explore the limitations of the mean field description and test if our phase reduction successfully captures the spiking-level synchronization. For a rudimentary demonstration of a mean field description that carries no information about microscopic dynamics, we direct our attention to Figure 43.

In this figure, we simulate a small network of $N = 2$ excitatory and $N = 2$ inhibitory theta neurons (for simplicity we define $\phi^x = \theta_2^x - \theta_1^x$, $\phi^y = \theta_2^y - \theta_1^y$, and $\phi^z = \theta_1^y - \theta_1^x$). In the left column, panel A represents the dynamics of the mean field description overlaid on the simulated synaptic variables plotted in gray. Panel C shows the synchronization properties of the spiking model, and and panel E shows our proposed theory. The theory correctly predicts synchronization of all oscillators. In the right column, panels B, D, and F show the mean field model, spiking model, and proposed theory, respectively. All panels A–F use the same parameters as in Figure 42, except for the right column (panels B, D, and F) where we take $\mu^y = 1.4$. The antiphase lines representing $T^x/2$ (gray solid) and $T^y/2$ (gray dashed) are hard to distinguish because they happen to nearly coincide.

Strikingly, we observe changes in the microscopic synchronization despite virtually no change in the mean field description. There is a slight quantitative change in the mean field descriptions when μ^y changes from $\mu^y = 1$ to $\mu^y = 1.4$. In particular, when $\mu^y = 1$, the fixed point is an asymptotically stable node with real negative eigenvalues. When we increase μ^y to $\mu^y = 1.4$, the fixed point remains stable but becomes a spiral node with small imaginary eigenvalues. Thus, the fixed point remains asymptotically stable and a numerical analysis of the mean field does not reveal any bifurcation points. Moreover, prior knowledge of this quantitative difference gives no indication with regards to the change in synchronization properties.

4.3.2 Existence of Synchronous Solutions

The existence of synchronous solutions is straightforward to show. Generically, the synchronous solution $\phi_i^x = \phi_i^y = 0$ for $i = 2, \ldots, N$ exists independent of ϕ^z (all right-hand-side terms cancel with these values), even when the mean synaptic variables are slowly varying.

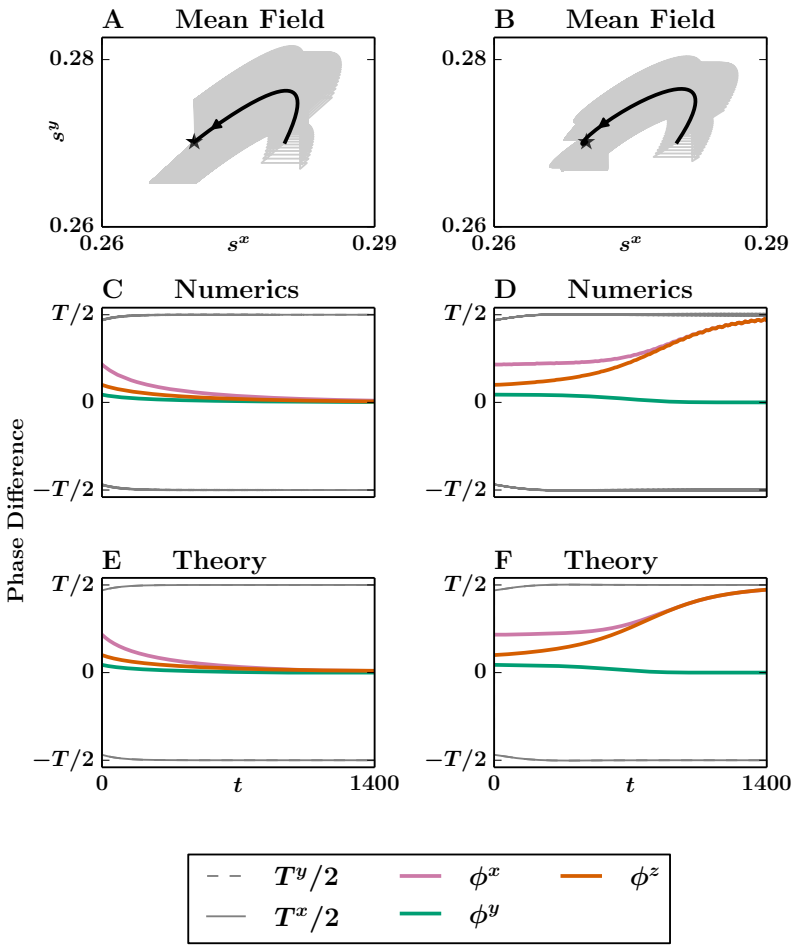

Figure 43: Mean field and microscopic behavior with constant mean synapses. Panel A: mean field synaptic variables (black) plotted on top of the simulated synaptic variables (gray). The black star denotes a stable fixed point. Panel C: phase difference at the spiking level in the full simulation. The estimated anti-phase value is shown in gray solid ($T^x/2$) and gray dashed ($T^y/2$) (they happen to overlap substantially and are almost impossible to distinguish). Panel E: phase difference using our proposed phase reduction. Parameters are the same as in Figure 42 with $\mu^x = \mu^y = 1$ and $\varepsilon = 0.01$. In the right column (panels B, D, and F), we increase $\mu^y = 1$ to $\mu^y = 1.4$ and plot data in the same order as panels A, C, and E, respectively, .

However, in this slowly varying case, there is synchrony within each excitatory or inhibitory population, but not between populations – the variable ϕ^z undergoes a large phase drift.

Similar solutions are just as straightforward to show. For example, $\phi_i^x = 0$ ($\phi_i^y = 0$) for $i = 1, \ldots, N$ gives us $d\phi_i^x/d\tau = 0$ ($d\phi_i^y/d\tau = 0$) independent of the dynamics of ϕ_i^y (ϕ_i^x) and ϕ^z. Thus, it is possible for the excitatory (inhibitory) population to remain synchronous despite a phase drift between populations and possibly asynchronous behavior in the inhibitory (excitatory) population. By inspection, using Equations (4.10), (4.11), and (4.12), we see that the same terms cancel. Thus, this behavior is not restricted to the theta model and exist generically..

4.3.3 Existence and Stability of Phase-Locked Solutions (Fixed Mean)

We now determine the stability of a given phase-locked solution to Equations (4.10),(4.11), and (4.12) in the case of a fixed mean. To this end, we begin with the most general case of a generic phase-locked solution and construct the Jacobian matrix using the following derivatives:

$$\left[\frac{\partial}{\partial\phi_2^x}\cdots\frac{\partial}{\partial\phi_N^x},\ \frac{\partial}{\partial\phi_2^y}\cdots\frac{\partial}{\partial\phi_N^y},\ \frac{\partial}{\partial\phi^z}\right].$$

First, consider the partial derivatives with respect to ϕ_k^x, ϕ_k^y, and ϕ^z of the right hand side of $d\phi_i^x/d\tau$:

$$\begin{aligned}
N\frac{\partial}{\partial\phi_k^x}\frac{d\phi_i^x}{d\tau} &= \sum_{j=1}^{N}\left[H_\phi^{xx}(\phi_j^x-\phi_i^x)(\delta_{jk}-\delta_{ik}) - H_\phi^{xx}(\phi_j^x)\delta_{jk}\right] \\
&\quad + \sum_{j=1}^{N} H_\phi^{xy}(\phi_j^y-\phi_i^x+\phi^z)(-\delta_{ik}) \\
N\frac{\partial}{\partial\phi_k^y}\frac{d\phi_i^x}{d\tau} &= \sum_{j=1}^{N}\left[H_\phi^{xy}(\phi_j^y-\phi_i^x+\phi^z)\delta_{jk} - H_\phi^{xy}(\phi_j^y+\phi^z)\delta_{jk}\right] \\
N\frac{\partial}{\partial\phi^z}\frac{d\phi_i^x}{d\tau} &= \sum_{j=1}^{N}\left[H_\phi^{xy}(\phi_j^y-\phi_i^x+\phi^z) - H_\phi^{xy}(\phi_j^y+\phi^z)\right]
\end{aligned} \tag{4.18}$$

The Kronecker delta functions are defined as

$$\delta_{ij} = \begin{cases} 1, & \text{if } i = j, \\ 0, & \text{else,} \end{cases}$$

and H_ϕ denotes the derivative of H with respect to its independent variable. Next, the partials with respect to ϕ_k^x, ϕ_k^y, ϕ^z of the right hand side of $d\phi_i^y/d\tau$:

$$\begin{aligned}
N\frac{\partial}{\partial\phi_k^x}\frac{d\phi_i^y}{d\tau} &= \sum_{j=1}^{N}\left[H_\phi^{yx}(\phi_j^x-\phi_i^y-\phi^z)\delta_{jk}-H_\phi^{yx}(\phi_j^x-\phi^z)\delta_{jk}\right]\\
N\frac{\partial}{\partial\phi_k^y}\frac{d\phi_i^y}{d\tau} &= \sum_{j=1}^{N}H_\phi^{yx}(\phi_j^x-\phi_i^y-\phi^z)(-\delta_{ik})\\
&\quad+\sum_{j=1}^{N}\left[H_\phi^{yy}(\phi_j^y-\phi_i^y)(\delta_{jk}-\delta_{ik})-H_\phi^{yy}(\phi_j^y)\delta_{jk}\right]\\
N\frac{\partial}{\partial\phi_k^z}\frac{d\phi^y}{d\tau} &= \sum_{j=1}^{N}\left[H_\phi^{yx}(\phi_j^x-\phi_i^y-\phi^z)(-1)-H_\phi^{yx}(\phi_j^x-\phi^z)(-1)\right]
\end{aligned}\tag{4.19}$$

Finally, the partials with respect to ϕ_k^x, ϕ_k^y, ϕ^z of the right hand side of $d\phi^z/d\tau$

$$\begin{aligned}
N\frac{\partial}{\partial\phi_k^x}\frac{d\phi^z}{d\tau} &= \sum_{j=1}^{N}\left[H_\phi^{yx}(\phi_j^x-\phi^z)\delta_{jk}-H_\phi^{xx}(\phi_j^x)\delta_{jk}\right]\\
N\frac{\partial}{\partial\phi_k^y}\frac{d\phi^z}{d\tau} &= \sum_{j=1}^{N}\left[H_\phi^{yy}(\phi_j^y)\delta_{jk}-H_\phi^{xy}(\phi_j^y+\phi^z)\delta_{jk}\right]\\
N\frac{\partial}{\partial\phi_k^z}\frac{d\phi^z}{d\tau} &= \sum_{j=1}^{N}\left[H_\phi^{yx}(\phi_j^x-\phi^z)(-1)-H_\phi^{xy}(\phi_j^x+\phi^z)\right].
\end{aligned}\tag{4.20}$$

The synchronous solution, $\phi_i^y=\phi_i^x=0$ is most straightforward to analyze. In this case, all off-diagonal terms cancel except the last row, so the Jacobian matrix is lower-triangular with diagonal entries

$$\begin{aligned}
NJ_{ii} &= -b^x\hat{H}_\phi^{xx}(0)/\mu^x+c^x\hat{H}_\phi^{xy}(0)/\mu^y, \quad i=1,\dots,N-1\\
NJ_{ii} &= -b^y\hat{H}_\phi^{yx}(0)/\mu^x+c^y\hat{H}_\phi^{yy}(0)/\mu^y, \quad i=N,\dots,2N-2\\
NJ_{2N-1,2N-1} &= -b^y\hat{H}_\phi^{yx}(0)/\mu^x+c^x\hat{H}_\phi^{xy}(0)/\mu^y.
\end{aligned}\tag{4.21}$$

These entries form the eigenvalues of the Jacobian matrix. We have seen in Figure 42 that $H^{kx}(0)$ has negative slope for $k=x,y$ (panels A,C) and $H^{ky}(0)$ has positive slope (and hence negative slope for $\hat{H}^{ky}(0)$) for $k=x,y$ (panels B,D). Then, for μ^y sufficiently large, the negative contributions from functions H^{ky} are small and the eigenvalues may become positive, indicating a loss of stability to the synchronous solution. This loss of stability confirms our observation in Figure 43.

We found that non-synchronous fixed point attractors of this network take the form $(\phi^x, 0, 0)$, or $(\phi^x, 0, \phi^z)$. For the remainder of this subsection, we analyze the existence and stability of fixed points starting with the synchronous solution $\phi^x = \phi^y = \phi^z = 0$.

We can show that the bifurcation point occurs at $\mu^y = 1.1$ by writing down the eigenvalues of this system (Equation (4.21) with $N = 2$):

$$\lambda_1 = \left[-H_\phi^{xx}(0) - H_\phi^{xy}(0)\right],$$
$$\lambda_2 = \left[-H_\phi^{yx}(0) - H_\phi^{yy}(0)\right],$$
$$\lambda_3 = \left[-H_\phi^{yx}(0) - H_\phi^{xy}(0)\right].$$

These H functions are identical except for the choice of parameters $b^x = b^y = 1$, and $c^x = c^y = 1.1$ (Equation (4.17)). By inspection, the eigenvalues are zero when when $\mu^x = 1$ and $\mu^y = 1.1$ indicating a change of stability at $\mu^y = 1.1$. This change in stability is shown in Figure 44. When the fixed point loses stability through a transcritical bifurcation, the stable attractor becomes a fixed point of the form $(\phi^x, 0, 0)$, where $\phi^x \neq 0$. For $\mu^y \approx 1.4$, the stable solution approximately takes the form $(-T/2, 0, 0)$, indicating that the excitatory population is stable near anti-phase.

We now turn to the final stable branch, which takes the form $(\phi^x, 0, \phi^z)$ (Figure 45). In panel A, we show the ϕ^x coordinate value as a function of μ^y and panel B shows the ϕ^z coordinate value as a function of μ^y. Initially, synchrony is stable, until the bifurcation at $\mu^y = 1.1$, which leads to a stable branch that asymptotically approaches anti-phase as a function of μ^y, and an unstable branch at the origin. We used `XPPAUTO` to follow the equilibria as a function of μ^y. There exist no other stable fixed points, concluding our analysis of existence and stability in the case of the fixed mean.

4.3.4 Existence and Stability of Phase-Locked Solutions (Slowly Varying Mean)

With particular coupling parameter choices, the mean field undergoes a supercritical Hopf bifurcation and gives rise to slow, stable oscillations (Figure 46A). This slowly varying mean has the effect of forcing the excitatory population to spike at a different frequency from the inhibitory population. The goal of this section is to analyze the existence and stability of fixed points of the phase model in this case.

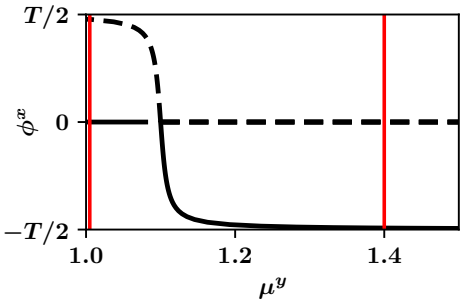

Figure 44: Stability of the fixed point taking the form $(\phi^x, 0, 0)$. The solution $\phi^x = 0$ is stable when $\mu^y = 1$, and becomes unstable as μ^y increases through $\mu^y = 1.1$. When $\mu^y = 1.4$, the stable solution is of the form $(-T/2, 0, 0)$ indicating anti-phase solutions are stable in the excitatory population. The vertical red lines correspond to the two values of parameter μ^y in Figure 43. The left line corresponds to $\mu^y = 1$ and the left column (panels A,C,E) of Figure 43. The right line corresponds to $\mu^y = 1.4$ and the right column (panels B,D,F) of Figure 43.

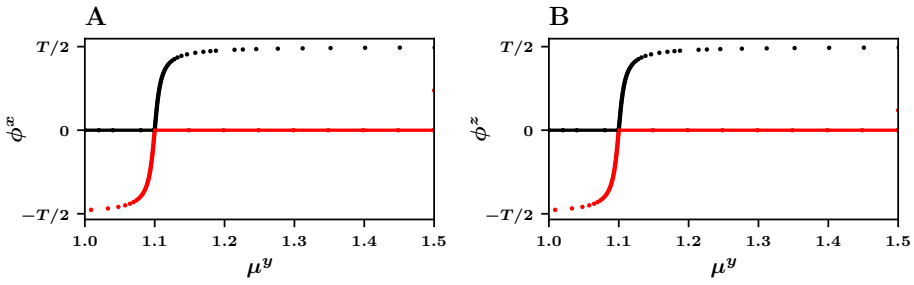

Figure 45: Stability analysis of phase-locked solutions of the form $(\phi^x, 0, \phi^z)$ using parameters from Figures 43 and 42. Black dots and lines: stable fixed points. Red dots and lines: unstable fixed points. A: x-coordinate values of fixed points. B: z-coordinate values of fixed points.

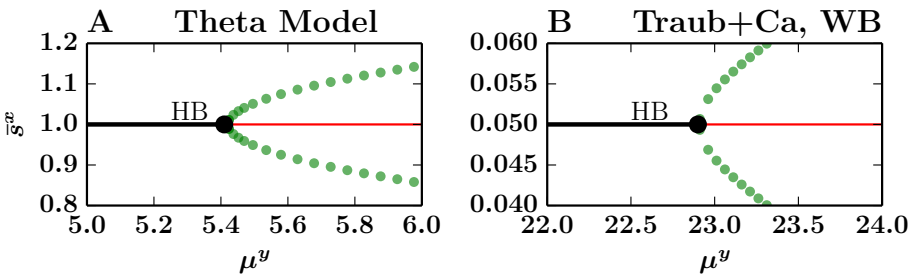

Figure 46: Hopf bifurcations in the mean field. A: Supercritical Hopf bifurcation in the mean field of the theta network Equations (4.15) and (4.16). Parameters $a^x = 0.5, b^x = 7, c^x = 6.5, a^y = 1.1, b^y = 25, c^y = 25.1, \mu^x = 1$. Black: stable fixed point. red solid: unstable fixed point. Green: stable periodic solution. B: Supercritical Hopf bifurcation in the mean field of the Traub+Ca and Wang-Buzsáki network. Parameters $I^{xx} = 101.5\mu\text{A/cm}^2, I^{xy} = 104\mu\text{A/cm}^2, I^{yx} = 13\mu\text{A/cm}^2, I^{yy} = 10.5\mu\text{A/cm}^2, \mu^x = 1\text{ms}$

4.3.4.1 Hopf Bifurcation in the Slowly Varying Case

Figure 47A shows slow, periodic behavior in the mean synaptic values. This periodic solution is a stable limit cycle solution arising from a supercritical Hopf bifurcation. By using the mean field in Equations (4.15) and (4.16), we show existence of of a Hopf bifurcation and its criticality numerically.

4.3.4.2 Phase Models Modulated by Slowly Varying Synapses

Figure 47B shows the results of the numerical simulation in terms of phase differences. Due to the slowly varying synaptic variables, the period of the oscillators change (as shown by the dashed gray and solid gray anti-phase lines). The excitatory population (pink) tends towards antiphase and the inhibitory population (green) tends towards synchrony. The difference in periods of the oscillators contributes to the phase drift (orange).

Figure 47C shows the results of the phase model simulation in terms of phase differences. We see the same general trends: excitatory population to anti-phase (pink), inhibitory population to synchrony (green), and a phase drift between populations (orange).

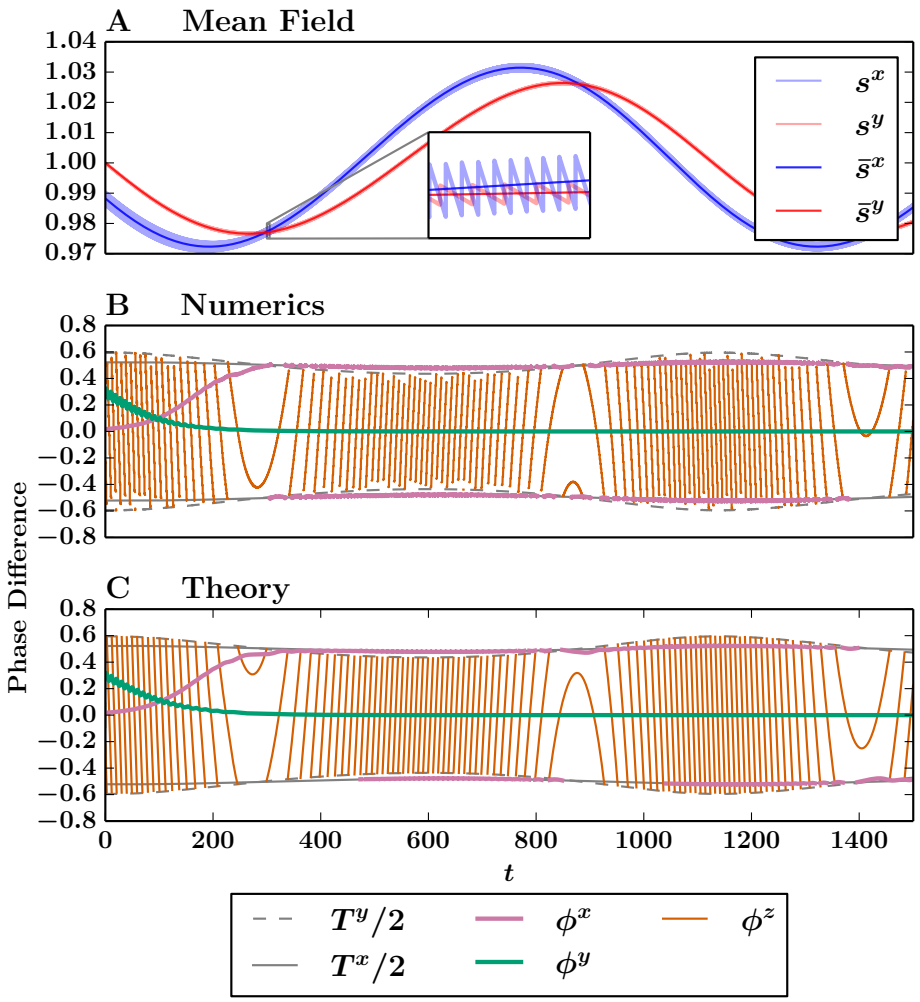

Figure 47: Numerics and theory for the theta model with slowly varying synapses. A: Mean field solutions (solid lines) vs numerical synaptic variables (opaque lines). Inset: Example of mean field solution plotted over the numerically simulated synaptic solutions. B: Theta model simulation. C: Phase model simulation. Purple: $\phi^x = \theta_2^x - \theta_1^x$. Green: $\phi^y = \theta_2^y - \theta_1^y$. Orange: $\phi^z = \theta_1^y - \theta_1^x$. Gray solid and gray dashed lines denote antiphase values $T^x/2$ and $T^y/2$ over time, respectively. Parameters as in Figure 46 and $\varepsilon = 0.005$.

4.3.5 Theta Models with Input Heterogeneities

In this section, we consider the same theta neurons as above with $N = 2$ with an additional input heterogeneity:

$$\begin{aligned}
\frac{dx_j}{dt} &= \pi(1-\cos(x_j)+(1+\cos(x_j))[(a^x+\varepsilon\eta_j^x)+b^x s^x - c^x s^y]),\\
\frac{dy_j}{dt} &= \pi(1-\cos(y_j)+(1+\cos(y_j))[(a^y+\varepsilon\eta_j^y)+b^y s^x - c^y s^y]),\\
\mu^x\frac{ds^x}{dt} &= \varepsilon\left[-s^x+\frac{1}{N}\sum_j \delta(x_j-\pi)\right],\\
\mu^y\frac{ds^y}{dt} &= \varepsilon\left[-s^y+\frac{1}{N}\sum_j \delta(y_j-\pi)\right].
\end{aligned} \tag{4.22}$$

We place no restriction on the heterogeneities η_j^k, so long as they are chosen such that $\varepsilon\eta_j^k$ remains order ε. In this example, we choose four numbers `[0.097, 0.43, 0.21, 0.089]`. We show an example of a simulation in Figure 48.

In Figure 48A, the full network simulation of the mean field (transparent blue, red labeled s^x, s^y) differs slightly in mean from the mean field approximation without input heterogeneities (solid blue, red labeled $\bar{s}^x, \bar{s}^y$). In Figure 48B, the input heterogeneity results in a phase drift in the excitatory population (pink). Figure 48C shows our proposed theory, which accurately captures the transient dynamics as well as the phase drift in the excitatory population.

4.3.6 Wang-Buzsáki and Traub with Calcium

We now repeat the analysis above using biophysically realistic models. In this section, we consider the synchronization properties in two populations of excitatory and inhibitory conductance-based models. The Excitatory population consists of the Traub model [89] with calcium current, while the inhibitory population consists of the Wang Buzsáki model [92]. As in the previous section, we consider two cases. In the first case, the synaptic mean values are fixed, and in the second case, the synaptic mean values are slowly varying.

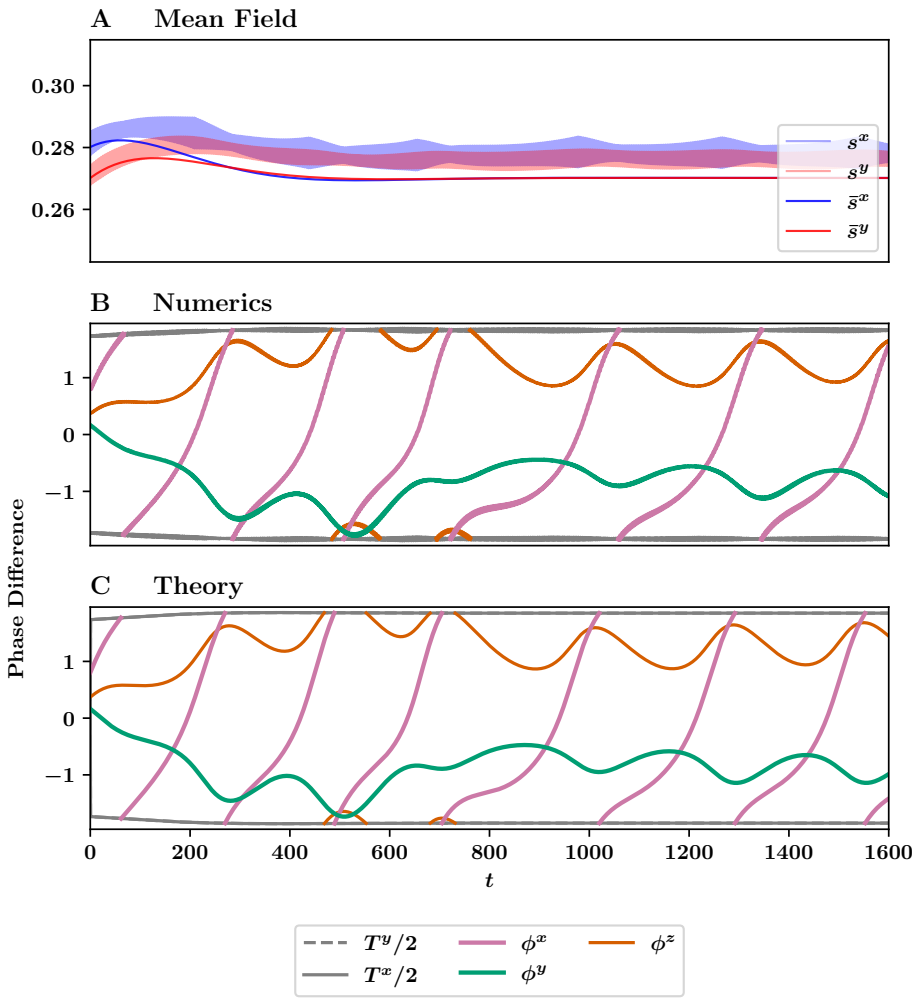

Figure 48: Effects of input heterogeneity. A: The full network simulation of the mean field (transparent blue, red labeled s^x, s^y) and the mean field approximation without input heterogeneities (solid blue, red labeled $\bar{s}^x, \bar{s}^y$). B: Oscillator phase differences in the full network simulation. C: Predicted oscillator phase differences in the reduced model. Parameter values are the same as in Figure 42 and Figure 43, with $\mu^y = 1.5$, $\varepsilon = 0.01$.

The Traub model with calcium is defined by the system

$$\dot{\mathbf{x}} = \frac{d}{dt}\begin{pmatrix} V \\ x \\ w \\ [\text{Ca}] \end{pmatrix} = \begin{pmatrix} (-I_{\text{ionic}} + I_{\text{ext}})/C \\ a_x(V)(1-x) - b_x(V)x \\ (w_\infty(V) - w)/\tau_w(V) \\ (-\alpha I_{\text{Ca}} - [\text{Ca}]/\tau_{\text{Ca}}) \end{pmatrix} = \mathbf{F}^x(\mathbf{x}, I_{\text{ext}}) \tag{4.23}$$

where x represents the dynamics of gating variables h, m, and n. The ionic currents are listed in Equation (C.1) of Appendix C.1.1.

The Wang-Buzsáki system is given by

$$\dot{\mathbf{y}} = \frac{d}{dt}\begin{pmatrix} V \\ x \end{pmatrix} = \begin{pmatrix} -I_{\text{ionic}} + I_{\text{ext}} \\ \phi(x_\infty - x)/\tau_x \end{pmatrix} = \mathbf{F}^y(\mathbf{y}, I_{\text{ext}}), \tag{4.24}$$

where x represents the dynamics of gating variables h and n. The ionic currents are listed in Equation (C.2) of Appendix C.1.1.

We introduce coupling through currents:

$$\begin{aligned} \frac{d\mathbf{x}_i}{dt} &= \mathbf{F}^x(\mathbf{x}_i, I^x + I^{xx}s^x - I^{xy}s^y), \\ \frac{d\mathbf{y}_i}{dt} &= \mathbf{F}^y(\mathbf{y}_i, I^y + I^{yx}s^x - I^{yy}s^y), \\ \mu^x \frac{ds^x}{dt} &= \varepsilon\left[-s^x + \frac{1}{N}\sum_{j=1}^{N}\delta(t - t_{j,\mathbf{x}})\right], \\ \mu^y \frac{ds^y}{dt} &= \varepsilon\left[-s^y + \frac{1}{N}\sum_{j=1}^{N}\delta(t - t_{j,\mathbf{y}})\right]. \end{aligned} \tag{4.25}$$

The terms $I^{xx}, I^{xy}, I^{yx}, and I^{yy}$ are constants with units of $\mu\text{A/cm}^2$ that we modify throughout this section.

Aside: While we also could include synaptic coupling using conductance-based synapses, the mean field equations are more complex as they are not just functions of sums of excitatory and inhibitory currents. Thus, we will use the simpler type of coupling shown in Equation (4.25).

The synapses s^x, s^y (dimensionless) increment each time the voltage variable of the neural models cross $V = 0$ from negative to positive. Unless otherwise stated, we choose $\bar{s} = 0.05$.

The mean field dynamics obey Equation (4.5), where ω^x is given by the frequency-input current (FI) function shown by the black curve in Figure 41 and ω^y is shown by the FI curve given by the dashed curve in the same figure. We compute both curves numerically using `XPPAUTO`.

This choice of coupling in Equation (4.25) results in scalar derivatives:

$$\begin{aligned}
\mathbf{F}^x_{s^x}(\Phi^x(t), \bar{s}, \bar{s}) &= (I^{xx}, 0, 0, 0, 0, 0, 0)^T \\
\mathbf{F}^x_{s^y}(\Phi^x(t), \bar{s}, \bar{s}) &= (-I^{xy}, 0, 0, 0, 0, 0, 0)^T \\
\mathbf{F}^y_{s^x}(\Phi^y(t), \bar{s}, \bar{s}) &= (I^{yx}, 0, 0)^T \\
\mathbf{F}^y_{s^y}(\Phi^y(t), \bar{s}, \bar{s}) &= (-I^{yy}, 0, 0)^T
\end{aligned}$$

Thus the H functions of Equations (4.8) and (4.9) for this system are given by

$$\begin{aligned}
H^{xx}(\phi) &= \frac{I^{xx}}{T\mu^x} \int_0^T Z^x(t, \bar{s}) f(t + \phi) dt, \\
H^{xy}(\phi) &= -\frac{I^{xy}}{T\mu^y} \int_0^T Z^x(t, \bar{s}) f(t + \phi) dt, \\
H^{yx}(\phi) &= \frac{I^{yx}}{T\mu^x} \int_0^T Z^y(t, \bar{s}) f(t + \phi) dt, \\
H^{yy}(\phi) &= -\frac{I^{yy}}{T\mu^y} \int_0^T Z^y(t, \bar{s}) f(t + \phi) dt.
\end{aligned} \tag{4.26}$$

We show plots of these H functions in Figure 49.

In Figure 50, we simulate 2 excitatory Traub with calcium conductance-based models (Traub with calcium, Equation (4.23)), and 2 inhibitory conductance-based models (Wang-Buzsáki, Equation (4.24)) with constant mean-field dynamics. All parameter values are the same except the parameter $\mu^y = 1$ (left column) and $\mu^y = 2.5$ (right column).

We plot the mean field in panels A and B using the same scale to emphasize the qualitative difference in the mean field description. The stability remains the same between the left and right columns (negative real eigenvalues in both cases). The double-headed red arrow indicates the magnitude of the perturbation off the fixed point. In both columns we choose to perturb the s^x variable by magnitude $\varepsilon/4$, where $\varepsilon = 0.0025$. Interestingly, this system

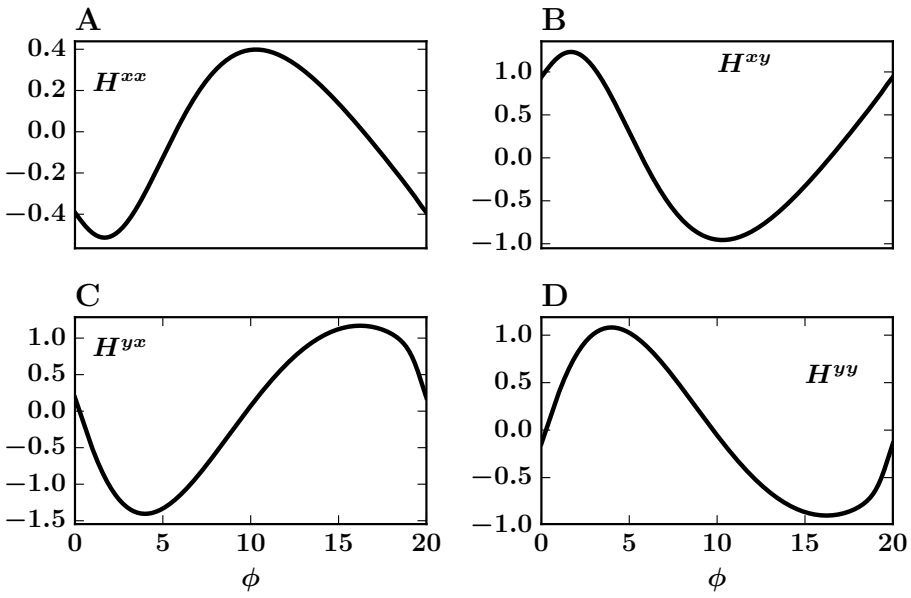

Figure 49: The H functions of the Traub with calcium and Wang-Buzsáki network. A: H^{xx}. B: H^{xy}. C: H^{yx}. D: H^{yy}. Parameter values $I^{xx} = 10\mu\text{A/cm}^2, I^{xy} = 14\mu\text{A/cm}^2, I^{yx} = 13\mu\text{A/cm}^2, I^{yy} = 10\mu\text{A/cm}^2, \mu^x = \mu^y = 1\text{ms}$.

exhibits similar features in the mean field description shown in Figure 43, and the microscopic dynamics reach different steady-states despite no detectable changes to the stability of the mean field model.

Panel C shows that the excitatory (ϕ^x, purple) and inhibitory populations (ϕ^y, green) approach synchrony. In panel D, we re-initialize the simulation with the same initial conditions for all variables with only one change in the synaptic time constant from $\mu^y = 1$ to $\mu^y = 2.4$. The excitatory population reaches a non-synchronous steady-state phase locked value, indicating nearly a quarter-period difference in spike times. Panels E and F show that our theory correctly predicts the differing steady state dynamics in panels C and D, respectively.

4.3.6.1 Existence and Stability of Phase-Locked Solutions (Fixed Mean) We now analyze the phase locked solutions of this system in the case of constant-mean synapses.

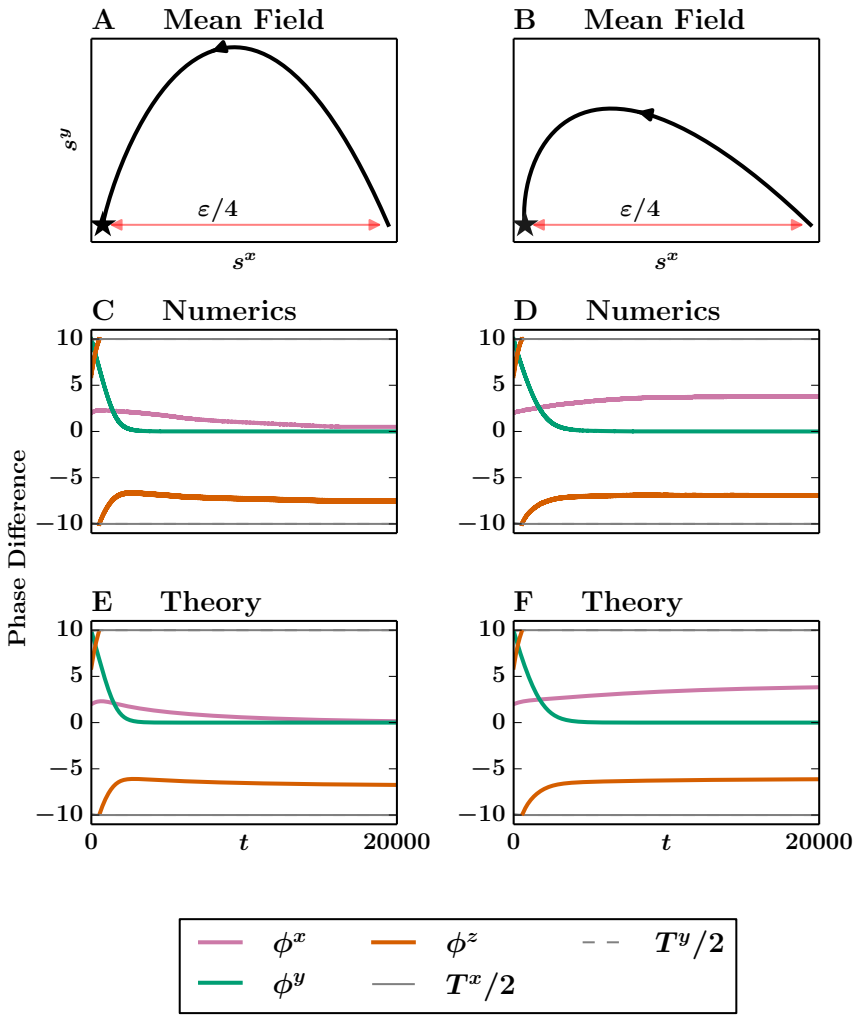

Figure 50: Mean field description and microscopic behavior with constant mean synapses. A: mean synaptic variables (black). The star denotes a stable fixed point. C: phase difference at the spiking level in the full conductance-based model simulation. The estimated half-period is shown in gray solid ($T^x/2$) and gray dashed ($T^y/2$) (they happen to overlap substantially and are almost impossible to distinguish). E: phase difference using our proposed phase reduction. Parameters are the same as in Figure 49, and $\mu^x = \mu^y = 1$. In the right column, we increase $\mu^y = 1$ to $\mu^y = 2.5$ and plot the same data in the same order with the same initial conditions. Other parameters: $\varepsilon = 0.0025$, $I^x = 6.74\mu\text{A/cm}^2$, $I^y = 0.66\mu\text{A/cm}^2$.

As in the network of theta neurons, we use coupling parameters that lead to changes in the synchronization properties of the oscillators as a function of μ^y, while the mean field remains invariant. We show the existence and stability of phase locked solutions of Figure 50 in Figure 51.

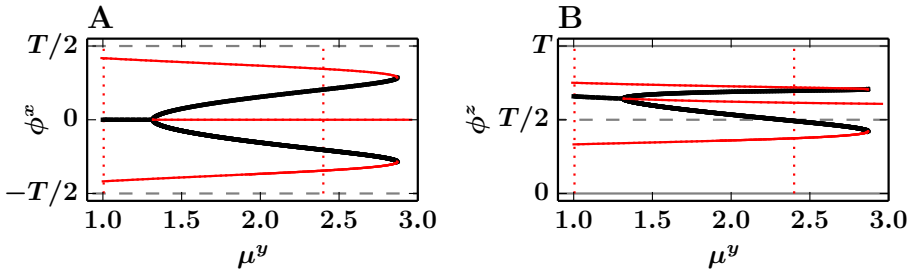

Figure 51: Existence and stability of phase locked solutions in the Traub Wang-Buzsáki network. Vertical red dotted lines denote the two parameter values corresponding to the left and right columns of Figure 50. Black curves denote stable values and solid red curves denote unstable values. A: Branches of ϕ^x fixed point values. B: Branches of ϕ^z fixed point values. Generally, $\phi^y = 0$ (data not shown). Note that for $\mu^y = 1$, the only fixed point that exists agrees with the steady-state in Figure 50. For $\mu^y = 2.4$, the fixed point corresponding to the upper stable branch of panel A and the upper stable branch of panel B coincides with the right column of Figure 50. Parameter values are identical to Figure 50.

In Figure 51 we plot the value of each coordinate as a function of μ^y (ϕ^x in panel A and ϕ^z in panel B). We do not show ϕ^y because $\phi^y = 0$ for this parameter range. As expected, the point $(\phi^x, \phi^y, \phi^z) \approx (0, 0, 3T/4)$ is stable for $\mu^y = 1$. As we increase μ^y, the system undergoes a pitchfork bifurcation, resulting in two stable fixed points. The fixed point we see in Figure 50 corresponds to the upper branch of both panels, where $(\phi^x, \phi^y, \phi^z) \approx (T/4, 0, 3T/4)$.

4.3.6.2 Phase Locked Solutions (Slowly Varying Mean) Finally, as in the theta network, the mean field of the Traub+Ca and Wang-Buzsáki network may undergo a supercritical Hopf bifurcation (Figure 46B). In this section, we demonstrate that our theory accurately predicts the phase locking properties in this case of a slowly varying mean (Figure

52). We show the synaptic variables and mean field approximations in the top panel, the full numerical simulation in the middle panel, and our proposed theory in the bottom panel. We find that our theory correctly predicts the general trend of ϕ^x (pink) which tends towards antiphase, and of ϕ^y (green) which remains close to its initial condition.

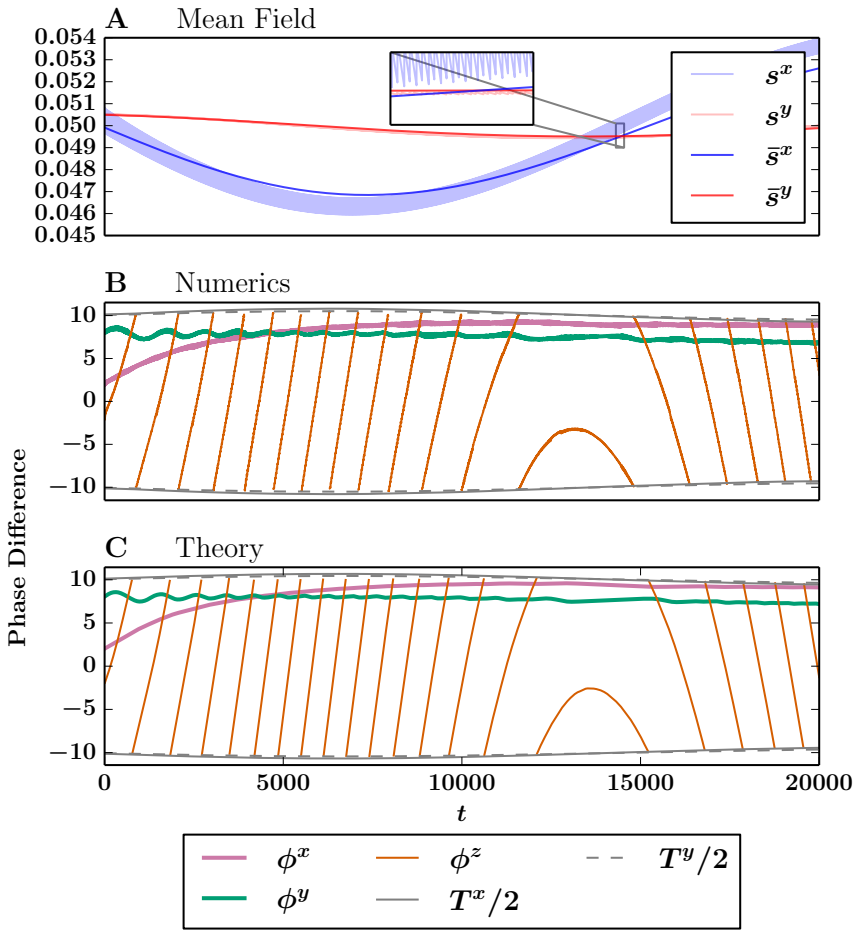

Figure 52: Numerics and theory for the Wang-Buzsáki and Traub with calcium models with nonconstant mean synapses. A: Mean field solutions (solid lines) vs numerical synaptic variables (opaque lines). Inset: Example of mean field solution plotted over the numerically simulated synaptic solutions. B: Theta model simulation. C: Phase model simulation. Parameters $I^{xx} = 101.5\mu\text{A/cm}^2, I^{xy} = 104\mu\text{A/cm}^2, I^{yx} = 13\mu\text{A/cm}^2, I^{yy} = 10.5\mu\text{A/cm}^2, \mu^x = 1\text{ms}, \mu^y = 24.79\text{ms}, \varepsilon = 0.00125$.

4.4 DISCUSSION

In the current study, we have shown that in an all-to-all, homogeneously coupled network of heterogeneous oscillators, there are two cases of the mean synaptic values that make the oscillators amenable to a phase reduction. In the first case, the mean synaptic values are fixed and equal, or fixed and different up to a small difference of order ε. In the second case, the mean synaptic values are slowly varying with small amplitude up to order ε. Using neurophysiologically motivated models, we demonstrate that the phase reduction is accurate for at least order $1/\varepsilon$ time and explore the existence and stability of phase locked solutions in both cases.

The first case of fixed mean synapses follows the classic stability analysis of phase locked states. However, our contribution is that with changes to the timescale of the inhibitory synapse of the mean field description, we are able to predict different phase locked states despite very little qualitative changes to the mean field. In the second case of variable mean synapses, we are able to predict the long timescale synchronization properties of the networks despite large phase drift between the oscillator populations. Moreover, our model reduction shows explicitly that the large phase drift is due to the deviations of the mean synaptic values from the fixed point in the mean field.

Our choice of coupling in the Traub, Wang-Buzsáki network also simplifies the analysis, but we need not restrict the form of the input current. In fact, a biophysically realistic synaptic input current of the form $s^k g(V - V^k)$, where g represents a conductance, V^k the reversal potential, and s^k the synaptic variable, is well within the scope of this study. In this case, we would add more complexity to the H functions in Equation (4.26) and in the mean field equations, but the analysis remains otherwise unchanged.

The title of this dissertation involves the dimension reduction of neural models, thus a few words on how this chapter fits in with the idea of dimension reductions are appropriate. In this chapter, the dimension reduction is restricted entirely to the change of high-dimensional conductance-based models to a single phase variable for each model. Thus, for large population sizes, say $N = 100$, the phase Equations (4.8) and (4.9) become substantially more complicated. So in contrast to Chapter 3, the dimension reduction here does not allow for an

easier analysis of large populations, but only enables a rigorous study of small populations.

Particular elements and motives of the current study are similar to existing works. Early studies in bridging spiking models to the mean field description use leaky integrate-and-fire (LIF) models with Poisson statistics [4, 3]. Later studies derive additional statistics like the coefficient of variation in the interspike interval [79]. However, deriving equations measuring the degree of synchrony in a population of neurons (the order parameter [54]) is more recent. This reduction was first shown in [66], where the authors use what is now called the Ott-Antonsen ansatz to reduce an infinite number of Kuramoto oscillators into a simple pair of differential equations for the order parameter.

In [63], the authors derive a pair of ordinary differential equations for other macroscopic observables like the mean membrane potential and the firing rate by starting at the spiking level. They then show that the network is also amenable to the order parameter reduction using the Ott-Antonsen ansatz. Thus, it is possible to derive a complementary set of equations describing the mean field activity and the associated degree of synchronization. This derivation has also been applied to theta neurons in [16], where the authors derive a complementary set of ordinary differential equations describing the population firing rate and the degree of synchrony.

The excitatory-inhibitory network structure has also been studied previously. In [80], Roulet and Mindlin use the Ott-Antonsen ansatz to derive low dimensional differential equations for the order parameters of networks of excitatory and inhibitory Alder units:

$$\begin{aligned}\dot{\theta}_i &= \omega_i - \cos\theta_i + I(\theta_j, \tilde{\theta}_j),\\ \dot{\tilde{\theta}}_i &= \tilde{\omega}_i - \cos\tilde{\theta}_i + \tilde{I}(\theta_j, \tilde{\theta}_j),\end{aligned}$$

where the untilded variables refer to units in the excitatory population and the tilded variables refer to units in the inhibitory population. The coupling functions are defined as

$$I(\theta_j, \tilde{\theta}_j) = \frac{k_E}{N}\sum_{j=1}^{N}(1-\cos\theta_j) - \frac{k_I}{\tilde{N}}\sum_{j=1}^{\tilde{N}}(1-\cos\tilde{\theta}_j),$$

where $k, \tilde{k} > 0$ denote the coupling strengths, N and $\tilde{N}$ denote the number of neurons in each of the two populations.

Roulet and Mindlin then derive low dimensional differential equations for the order parameters of excitatory and inhibitory theta models:

$$\dot{\theta}_i = 1 - \cos\theta_i + (1 + \cos(\theta_i))[\eta_i + I(\theta_j, \tilde{\theta}_j)],$$
$$\dot{\tilde{\theta}}_i = 1 - \cos\tilde{\theta}_i + (1 + \cos\tilde{\theta}_i))[\tilde{\eta}_i + \tilde{I}(\theta_j, \tilde{\theta}_j)],$$

with the same coupling functions as above. The equations are similar to the theta model we consider in this chapter, except that the mean of the input current is slaved to the fixed parameters η_i and thus the mean can not drift over time.

In [85], the authors consider the effects of time-varying coupling on the synchronization properties of a network of Kuramoto oscillators. In particular, they show that with sufficiently fast binary switching of coupling strengths, the network exhibits behavior characteristic of a static network. In contrast, our results apply only to slow, continuous changes in input current.

Another aspect of the our results that have been studied in the past includes pulse coupled oscillators. Pazó and Montbrió, in [73], use the Winfree model with a smooth pulse-like coupling of the form $P(x) = a_n(1 + \cos(x))^n$. Combined with the Ott-Antonsen ansatz, they derive a pair of differential equations for the order parameter. In [13], the authors consider a network of theta models with similar pulse-like coupling and derive the order parameter using the Ott-Antonsen ansatz. In addition, they relax the all-to-all coupling hypothesis and apply the Ott-Antonsen ansatz to a randomly generated network given an arbitrary degree distribution. General network structure satisfying classic weak coupling assumptions are studied in [52]. In [59], the author considers all-to-all pulse-like coupling of theta neurons with and without synaptic delay and derives the order parameter using the Watanabe-Strogatz ansatz [94, 93].

Generalizing the synaptic weights is also a natural next step of the current study. In

this case, the system becomes

$$\begin{aligned}
\frac{d\mathbf{x}_i}{dt} &= \mathbf{F}^x\left(\mathbf{x}_i, \sum_{j=1}^{N} w_{ij}^{xx} s_j^x, \sum_{j=1}^{N} w_{ij}^{xy} s_j^y\right), \\
\frac{d\mathbf{y}_i}{dt} &= \mathbf{F}^y\left(\mathbf{y}_i, \sum_{j=1}^{N} w_{ij}^{yx} s_j^x, \sum_{j=1}^{N} w_{ij}^{yy} s_j^y\right), \\
\mu_i^x \frac{ds_i^x}{dt} &= \varepsilon\left[-s_i^x + \delta(t - t_{j,\mathbf{x}})\right], \\
\mu_i^y \frac{ds_i^y}{dt} &= \varepsilon\left[-s_i^y + \delta(t - t_{j,\mathbf{y}})\right], \quad i = 1\ldots, N.
\end{aligned}$$

To ensure that all neurons have the same firing rate when the synaptic variables are constant and identical, we require that

$$\sum_j w_{ij}^{jk} = \bar{w}^{jk}, \quad i = 1, \ldots, N, \text{ for } j, k = x, y,$$

where $\bar{w}^{jk}$ is a constant for each $j, k = x, y$. We are then free to choose coupling types of the form $W_{ij} = K(|i - j|\Delta x)$, where K is a typical even kernel, like a Gaussian or difference of Gaussians, and $\Delta x = 1/N$. This type of modification brings us closer to classic spatially distributed neural field models and the resulting system remains amenable to the methods of the current study. This direction also ties in with [58, 57], where bump-type solutions are shown to exist *a priori* in large networks of theta models. Our method could show the same results with more general models.

The Ott-Antonsen ansatz is an undoubtedly powerful tool for understanding oscillator models. However, it has some limitations which the current chapter addresses directly. Our proposed theory offers a general dimension reduction of a finite number of N- and M-dimensional coupled oscillators. While our theory tolerates only small heterogeneities, we place no restrictions on how the heterogeneities are distributed. However, our theory is restrictive in that the interactions must be on a slow timescale.

Another natural next step to consider involves the effects of noise on synchronization. In [64], where a network of these oscillators are driven by a common Gaussian noise signal, the authors analytically show noise-induced synchronization, and suggest that weak common noise generally promotes synchronization of weakly coupled oscillators. We have shown to a

limited extent the effects of noise by introducing input heterogeneities drawn from a uniform distribution. However, analyzing the effects of a single time-dependent noisy input signal in our framework requires different techniques beyond the scope of this chapter, and warrants close study in its own right.

5.0 CONCLUSION

In this dissertation, we applied the method of multiple timescales to three spatial scales: microscopic single-neuron, macroscopic infinite-neuron continuum limit, and an in-between scale of a finite neuron population. In each problem we introduced slow phase shifts $\theta(\tau)$ representing the slow timescale dynamics, and used the Fredholm alternative to derive dynamics for $\theta(\tau)$, effectively reducing the dynamics of each system of scalar variables. Remarkably, we found that the phase variables reproduce the dynamics of the original system for at least order $O(1/\varepsilon)$ time, and found the phase dynamics much more amenable to standard analytical and numerical dynamical systems tools. Thus, we gained much more insight into the dynamics of the original system by rigorously and comprehensively analyzing the dynamics of the phase dynamics.

In Chapter 2, we not only recapitulated the results in [55, 56], where the phase response properties are shown to depend on both the instantaneous frequency of the oscillator and the rate of change of the slowly varying parameter, but extended their results to weakly coupled oscillators with a slowly varying parameter. Such a case is plausible in the cortex when a slowly varying concentration of acetylcholine substantially modulates the synchronization properties of cortical oscillators [86, 87]. Our result applies to a general set of models, and we step through several examples starting with the analytically tractable Lambda-Omega system [51], to the neurophysiologically motivated Traub model with adaptation [91]. In each example we showed that our theory accurately predicts oscillator phase differences over long times when the slowly varying parameter is periodic, quasi-periodic, and stochastic (in the stochastic case, the parameter is taken to be an Ornstein-Uhlenbeck process where the drift is slow, thus the stochastic process is effectively slow). In our final example, we demonstrated an accurate characterization of synchrony in a population of 51 neurons with

adaptation.

In Chapter 3, we reduced the dynamics of a neural field model to two scalar delay differential equations given that the input and adaptation are weak, and that adaptation is slow. The reduction allowed an exact analysis of a neural field model with a general even kernel and general smooth firing rate function, generalizing existing results that either fix a particular kernel or take the high-gain limit of the firing rate function. Using our scalar reduction, we demonstrated its ability to accurately reproduce the many spatio-temporal dynamics of the original system (standing, constant-velocity, sloshing, and chaotic bumps) on the ring and torus, then analytically determined the existence and stability of many of the spatio-temporal dynamics. The weak input and weak adaptation are restrictive because many cortical dynamics are influenced by strong input and adaptation. However, our analysis serves as a strong starting point for future studies with greater parameter values.

In Chapter, 4, we derived a set of phase equations for finite populations of inhibitory and excitatory oscillators given that the global synaptic variables are slowly varying. As in [81], we showed that strong slow synapses can be rewritten as weak and fast coupling, making the original system amenable to classic phase reduction methods. We derived phase equations with the mean synaptic variables as exogenous parameters, which allowed us to determine spiking-level synchrony given the mean field synaptic dynamics. We demonstrated through two examples: a network of two inhibitory and two excitatory theta neurons, and a network of two inhibitory Wang-Buzsáki and two excitatory Traub with calcium models. In each example, we found that it is possible for the synaptic dynamics to change very little, but for the spiking dynamics to change nontrivially. We were also able to accurately predict phase differences with slowly varying oscillating mean synapses. In this case, the difference in the mean synaptic values resulted in large frequency differences of the populations. In the phase reduction, the exogenous mean synaptic term faithfully captured and reproduced the phase drift.

APPENDIX A

WEAKLY COUPLED OSCILLATORS IN A SLOWLY VARYING WORLD

A.1 TRAUB MODEL WITH ADAPTATION

All other equations for the Traub model are defined as follows

$$
\begin{aligned}
t_w(V) &= \tau_w/(3.3\exp((V - V_{wt})/20) + \exp(-(V - V_{wt})/20)) \\
w_\infty(V) &= 1/(1 + \exp(-(V - V_{wt})/10)) \\
a_m(V) &= 0.32(54 + V)/(1 - \exp(-(V + 54)/4)) \\
b_m(V) &= 0.28(V + 27)/(\exp((V + 27)/5) - 1) \\
a_h(V) &= 0.128\exp(-(V - V_{hn})/18) \\
b_h(V) &= 4/(1 + \exp(-(V + 27)/5)) \\
a_n(V) &= 0.032(V + 52)/(1 - \exp(-(V + 52)/5)) \\
b_n(V) &= 0.5\exp(-(57 + V)/40) \\
\alpha(V) &= a_0/(1 + \exp(-(V - V_t)/V_s))
\end{aligned}
$$

A.1.1 Fourier Coefficients

The Fourier coefficients used in the approximation are shown in Table 2

Table 1: Traub parameter values

Parameter	Value
C	$1\mu\text{F/cm}^2$
g	5mS/cm^2
ε	0.0025
f	$0.5(\frac{1000\varepsilon}{2\pi}\text{Hz})$
I	$3\mu\text{A/cm}^2$
V_{wt}	-35mV
τ_w	100ms
E_k	-100mV
E_{Na}	50mV
E_l	-67mV
g_l	0.2mS/cm^2
g_k	80mS/cm^2
g_{Na}	100mS/cm^2
V_{hn}	-50mV
a_0	4
τ	4ms
V_t	0mV
V_s	5mV
E_{syn}	0mV
q_0	0.3mS/cm^2
q_1	0.2mS/cm^2

Table 2: Traub Fourier Coefficients

Cosine	Sine
$a_0(0.1) = 19.6011939665$	-
$a_0(0.3) = 17.4255017198$	-
$a_1(0.1) = -3.32476526025$	$b_1(0.1) = 0.721387113706$
$a_1(0.3) = -6.97305767558$	$b_1(0.3) = -1.5028098729$
$a_2(0.1) = -0.255371105623$	$b_2(0.1) = 0.738312597998$
$a_2(0.3) - 0.83690237427$	$b_2(0.3) = 1.03494013487$

APPENDIX B

SCALAR REDUCTION OF A NEURAL FIELD WITH SPIKE FREQUENCY ADAPTATION

B.1 NORMAL FORM FOR THE HOPF BIFURCATION ON THE RING

Recall that we analyze the bifurcation to sloshing pulses for the general integral equation,

$$\frac{d\theta}{d\tau} = -qJ(\theta) - g\int_0^\infty e^{-s}H(\theta(\tau - s) - \theta(\tau))\, ds \tag{B.1}$$

as g increases. For simplicity, we assume the expansions

$$\begin{aligned} J(\theta) &= \theta + j_3\theta^3 + \dots \\ H(\theta) &= \theta + h_3\theta^3 + \dots, \end{aligned}$$

and $q > 0$. Based on the eigenvalue equation,

$$\lambda^2 + (1 + q - g)\lambda + q = 0$$

we expect a Hopf bifurcation to occur.

To analyze the Hopf bifurcation, we use a multiple time scale expansion. We assume that $\theta(\tau)$ is a function of a "fast" time $\zeta = \tau$ and a "slow" time $\xi = \delta^2\tau$ where δ measures the amplitude of the bifurcating solution. As the nonlinearities are all odd, we can assume that

$$g = g_0 + \delta^2 g_2, \qquad \theta = \delta\theta_1(\zeta, \xi) + \delta^3\theta_3(\zeta, \xi)$$

to order δ^3. We develop a perturbation expansion to obtain the normal form. Before continuing, we need to briefly describe how the integral equation gets expanded in multiple scales. If $f(\zeta, \xi)$ is a function of the fast and slow time-like variable, then, clearly

$$\frac{df}{d\tau} = \frac{\partial f}{\partial \zeta} + \delta^2 \frac{\partial f}{\partial \xi}$$

and

$$\int_0^\infty e^{-s} f(\tau - s)\ ds = \int_0^\infty e^{-s} f(\zeta - s, \xi - \delta^2 s)\ ds.$$

We expand this expression to order δ^2 to get:

$$\int_0^\infty e^{-s} f(\tau - s)\ ds \approx \int_0^\infty e^{-s} f(\zeta - s, \xi)\ ds - \delta^2 \int_0^\infty s e^{-s} \frac{\partial f(\zeta - s, \xi)}{\partial \xi}\ ds. \tag{B.2}$$

Let

$$(Lu)(\zeta) := \frac{\partial u}{\partial \zeta} + qu + g_0 \int_0^\infty e^{-s} [u(\zeta - s) - u(\zeta)]\ ds.$$

By our choice of g_0, L has a nullspace $e^{\pm i\omega\zeta}$ and since it is a scalar, so does the adjoint operator under the usual inner product

$$\langle u, v \rangle := \int_0^{2\pi/\omega} \bar{u}(s) v(s)\ ds.$$

We plug in all the expansions and find to first order that

$$\theta_1 = z(\xi) e^{i\omega\zeta} + c.c$$

where $z(\xi)$ is a complex function of ξ and c.c means complex conjugates. Our goal is to derive equations for z. To cubic order, we obtain:

$$\begin{aligned}
(L\theta_3)(\zeta) = {} & z_\xi e^{i\omega\zeta} \left(-1 + \frac{g_0}{1 + 2i\omega - \omega^2} \right) + c.c \\
& + g_2 z e^{i\omega\zeta} \frac{i\omega}{1 + i\omega} + c.c \\
& + -q j_3 \left[z e^{i\omega\zeta} + \bar{z} e^{-i\omega\zeta} \right]^3 \\
& + -g h_3 \int_0^\infty \left[z(\xi) e^{i\omega\zeta} (e^{-i\omega s} - 1) + \bar{z}(\xi) e^{-i\omega\zeta} (e^{i\omega s} - 1) \right]^3\ ds.
\end{aligned}$$

The first line comes from applying equation (B.2). Taking the inner product of this equation with $\exp(i\omega\zeta)$ (essentially, the Fredholm alternative), yields the equation for $z(\xi)$:

$$\alpha\frac{dz}{d\xi} = z[\hat{\gamma}_0 + \hat{\gamma}_3|z|^2] \tag{B.3}$$

where

$$\begin{aligned}
\alpha &= 1 - \frac{g_0}{1+2i\omega-\omega^2} = \frac{2}{1+q}(q+\sqrt{q}i) \\
\hat{\gamma}_0 &= g_2\frac{i\omega}{1+i\omega} = \frac{g_2}{1+q}(q+\sqrt{q}i) \\
\hat{\gamma}_3 &= \frac{3q}{4q+1}\left[[q(12h_3-4j_3)-j_3] + i18h_3\sqrt{q}\right].
\end{aligned}$$

B.2 COMPUTATION OF FUNCTIONS H_I AND J_I

To numerically integrate the phase models on the ring or torus, we require an approximation to the functions H_i, and J_i. These functions depend on and use lookup tables for the steady state bump u_0 (`u0ss`), the derivative of the firing rate evaluated at the steady state bump $f'(u_0)$ (`df_u0b`), and the partial derivatives of the steady state bump, $\partial u_0/\partial x$, $\partial u_0/\partial y$ (`ux`,`uy`). On the toroidal domain, each lookup table has $N \times N$ entries, where for the coefficients below, we choose $N = 64$.

To compute H_i in Equation (3.9),we use the following procedure

```
H1 = zeros(N,N)
H2 = zeros(N,N)
for i=1:N
  for j=1:N
    temp1 = 0
    temp2 = 0
    for n=1:N
      for m=1:N
        xn = mod(n+i+N/2,N)
```

```
        xm = mod(m+j+N/2,N)
        temp1+=ux[n,m]*df_u0b[n,m]*u0ss[xn,xm]
        temp2+=uy[n,m]*df_u0b[n,m]*u0ss[xn,xm]
      end
    end
    H1[i,j] = temp1
    H2[i,j] = temp2
  end
end
H1 *= (2*pi)^2/N^2
H2 *= (2*pi)^2/N^2
```

To compute J_i in Equation (3.9), we use the following procedure

```
J1 = zeros(N,N)
J2 = zeros(N,N)
for i=1:N
  for j=1:N
    temp1 = 0
    temp2 = 0
    for n=1:N
      for m=1:N
        xn = mod(n+i+N/2,N)
        xm = mod(m+j+N/2,N)
        temp1+=ux[xi,xj]*df_u0b[xn,xm]*I[n,m]
        temp2+=uy[xi,xj]*df_u0b[xn,xm]*I[n,m]
      end
    end
    J1[i,j] = temp1
    J2[i,j] = temp2
  end
```

```
end
J1 *= (2*pi)^2/N^2
J2 *= (2*pi)^2/N^2
```

On the torus, taking the difference $J_i - (-H_i)$ results in a negligible error, revealing that $J_i = -H_i$. Thus, for all phase computations involving J_i, we use the same Fourier approximations for H_i and J_i.

On the ring, the computations are virtually identical with the obvious exception of array shapes.

B.2.1 Fourier Approximations

After creating the lookup tables `H1,H2`, we perform a Fourier approximation to make numerical integration easier. The following function and corresponding coefficients and frequencies (Table 3) provide an excellent approximation to the lookup tables `H1,H2`. A basic error analysis shows that the supremum norm difference between the lookup tables `H1,H2` and their Fourier approximations,$\overline{H}_1, \overline{H}_2$, is $\|\texttt{H1} - \overline{H}_1\|_\infty \approx 3.354\text{e}{-7}$.

$$\overline{H}_1(x,y) = -\sum_{k=1}^{26} \frac{a_k}{N^2} \sin(xn_k + ym_k). \tag{B.4}$$

The coefficients in Table 3 are computed using Python with the numerics package Numpy by taking the Fourier transform of the lookup tables `H1,H2`.

B.3 NUMERICAL INTEGRATION

In this section, we detail the various numerical methods used to evaluate the many integro-delay-differential equations of this chapter.

Table 3: Fourier Coefficients of `H1` for $N = 64$. The maximum pointwise difference between this approximation of H_1 and the original H_1 is `3.53733478176e-07`

k	a_k	(n_k, m_k)	k	a_k	(n_k, m_k)
0	-0.299041640592	(1,0)	16	8.78193375764e-06	(-2,2)
1	-0.0123427222227	(2,0)	17	0.00134078962566	(-1,2)
2	-2.92404662557e-07	(3,0)	18	-0.00134078962566	(1,-2)
3	2.92404662711e-07	(-3,0)	19	-8.78193375764e-06	(2,-2)
4	0.0123427222227	(-2,0)	20	-1.40550932907e-07	(3,-2)
5	0.299041640592	(-1,0)	21	1.4055093291e-07	(-3,-2)
6	-0.110662059947	(1,1)	22	8.78193375763e-06	(-2,-2)
7	-0.00255677958311	(2,1)	23	0.00134078962566	(-1,-2)
8	-1.30119169782e-07	(3,1)	24	-0.110662059947	(1,-1)
9	1.30119169839e-07	(-3,1)	25	-0.00255677958311	(2,-1)
10	0.00255677958311	(-2,1)	26	-1.30119169783e-07	(3,-1)
11	0.110662059947	(-1,1)	27	1.30119169839e-07	(-3,-1)
12	-0.00134078962566	(1,2)	28	0.00255677958311	(-2,-1)
13	-8.78193375763e-06	(2,2)	29	0.110662059947	(-1,-1)
14	-1.40550932909e-07	(3,2)			
15	1.40550932908e-07	(-3,2)			

Table 4: Fourier Coefficients of the steady-state coefficients. Plotting $u_{00} + 2u_{10}\cos(x) + 2u_{01}\cos(y) + 4u_{11}\cos(x)\cos(y)$ gives a reasonable approximation to the numerically computed steady-state bump solution.

k	u_k	(n_k, m_k)
0	-2.17382490474	(0, 0)
1	-0.74563470929	(0, 1)
5	-0.74563470929	(1, 0)
6	0.338867473649	(1, 1)
7	0.340507108446	(1, -1)
10	-0.74563470929	(-1, 0)
11	0.340507108446	(-1, 1)
12	0.338867473649	(-1, -1)

Table 5: Fourier Coefficients of the kernel. Plotting $k_{00} + 2k_{10}\cos(x) + 2k_{01}\cos(y) + 4k_{11}\cos(x)\cos(y)$ gives a reasonable approximation to the original periodix kernel.

k	k_k	(n_k, m_k)
0	-0.473945684407	(0, 0)
1	0.19095061386	(0, 1)
4	0.19095061386	(0, -1)
5	0.19095061386	(1, 0)
6	0.108965377668	(1, 1)
7	0.111033925698	(1, -1)
10	0.19095061386	(-1, 0)
11	0.111033925698	(-1, 1)
12	0.108965377668	(-1, -1)

B.3.1 Truncated Neural Field Model on the Torus

The integration of Equation (3.22) requires the approximation of several double integrals. In the interest of reducing computation time, we use Riemann integrals and a relatively coarse discretization of the spatial domain. For example, for a given time t, the coefficient $p_{10}(t)$ is approximated as

$$p_{10}(t) \approx \sum_{n=1}^{N}\sum_{m=1}^{N} \cos(y_m) f(u(x_n, y_m, t)) \frac{(2\pi)^2}{N^2}.$$

Because a linear increase in N leads to a quadratic increase in the total number of operations, we keep $N = 100$, which is an acceptable compromise between speed and accuracy for this problem. All other double sums that appear in p_{ij}, r_{ij}, and s_i are computed this way.

When computing the bifurcation diagram using this system, we use `XPPAUTO` and the numerical options shown in Table 6. The most important options are Ntst and Dsmin. If Ntst is less than 1000, `XPPAUTO` is unreliable in determining the stability of periodic solutions. If Dsmin is too large, `XPPAUTO` will skip bifurcation points.

B.3.2 Delay Integro-Differential Equations

We implement the right hand side of the integro-differential in Equation (3.23) as

$$f\begin{pmatrix} t_k \\ \vec{x}_M \\ \vec{y}_M \end{pmatrix} = \left(-g\left(\sum_{n=0}^{M-1} e^{-ndt} H_1[x_{k-n} - x_k, y_{k-n} - y_k] \right) dt + qJ_1(x_k, y_k) \right)$$

$$h\begin{pmatrix} t_k \\ \vec{x}_M \\ \vec{y}_M \end{pmatrix} = \left(-g\left(\sum_{n=0}^{M-1} e^{-ndt} H_2[x_{k-n} - x_k, y_{k-n} - y_k] \right) dt + qJ_2(x_k, y_k) \right),$$

where dt is the time step and

$$\vec{x}_M = \begin{pmatrix} x_k \\ \vdots \\ x_{k-(M-1)} \end{pmatrix}, \quad \vec{y}_M = \begin{pmatrix} y_k \\ \vdots \\ y_{k-(M-1)} \end{pmatrix}$$

Table 6: `XPPAUTO` parameters for the bifurcation diagram Figure 28. `XPPAUTO` version 8 has a third column of numerics options, which we left at default values.

AUTO Option	Value
Ntst	1000
Nmax	200
NPr	2
Ds	0.01
Dsmin	0.0001
Ncol	4
EPSL	0.0001
Dsmax	0.1
Par Min	0
Par Max	5
Norm Min	0
Norm Max	1000
EPSU	0.0001
EPSS	0.0001

are the arrays containing solution values for M previous time steps. The functions H_i and J_i are either the accurate Fourier approximation (Equations (3.24),(3.25)), or the truncated Fourier series (Equation (3.26)). The time step dt is the same as the discretization of the integral.

The algorithm is a straightforward Euler method. For a given time step `i`,

```
th1[i+1] = th1[i] + dt*f(t[i],th1[i],..,th1[i-(M-1)],
                                th2[i],..,th2[i-(M-1)])
th2[i+1] = th2[i] + dt*h(t[i],th1[i],..,th1[i-(M-1)],
                                th2[i],..,th2[i-(M-1)])
```

The initial condition for this algorithm requires an array of M time steps. If the parameters are chosen such that a limit cycle exists, then we initialize in an arc:

```
r0 = 1
n0 = linspace(0,-.01,M)
for k = 0:M-1
  th1[k] = r0*cos(n0[k])
  th2[k] = r0*sin(n0[k]).
```

If the parameters are chosen such that a constant-velocity bump exists, then we initialize in a line:

```
x_line = linspace(0,1,M)
y_line = linspace(2,3,M)
for k = 0:M-1
  th1[k] = x[k]
  th2[k] = y[k].
```

When plotting solutions, we disregard at least the first M entries of the solution vector.

B.4 SCALAR REDUCTION OF NEURAL FIELDS WITH OTHER SPATIO-TEMPORAL DYNAMICS

The method of multiple timescales does not depend on the spato-temporal dynamics of just bump solutions. In this section, we detail an extension of the existing theory in Chapter 3 to the case of slowly traveling waves.

The neural field we consider in this appendix is defined as

$$\begin{aligned} \frac{\partial u(\mathbf{x},t)}{\partial t} &= -u(\mathbf{x},t) + \int_\Omega K(\mathbf{x}-\mathbf{y}) f(u(\mathbf{y},t)-\alpha)\, d\mathbf{y} \qquad \text{(B.5)} \\ &+ \varepsilon\left[qI(\mathbf{x}+\Omega\varepsilon t) - gz(\mathbf{x},t)\right], \\ \frac{\partial z(\mathbf{x},t)}{\partial t} &= \varepsilon\beta[-z(\mathbf{x},t)+u(\mathbf{x},t)], \qquad \text{(B.6)} \end{aligned}$$

where the parameter ε is small, $0 < \varepsilon \ll 1$, and $\mathbf{x}, \mathbf{y} \in \mathbb{R}^n$. For $n = 2$, the kernel function K is an even function in the sense that, $K(-x, y) = K(x, -y) = K(x, y)$ and normalized such that

$$\int_\Omega K(x)dx = 1.$$

The parameters q, g, α, β are constants. For convenience, we will denote the domain $\Omega = \mathbb{R}^m$, with $m = 1, 2$. Thus in one-dimension the domain is the real line, and in two-dimensions the real plane. The variable $z(\mathbf{x}, t)$ represents linear adaptation [76] and $I(\mathbf{x}, t)$ an possibly time-varying external input to the network.

In the simplest case, we define $I(x, t)$ it to be strictly monotonic, $I(-\infty) = 0$, $I(\infty) = 1$, and $0 \leq I(\mathbf{x}, t) \leq 1$ for all $\mathbf{x} \in \mathbb{R}^n$ and all $t \in \mathbb{R}$. However, the input current does not have to take this form, so long as its values are order 1. Generally, we assume the function f is sigmoidal and smooth.

Our goal in this appendix is to analyze Equations (B.5),(B.6) when ε is small. When $\varepsilon = 0$, there is a stable attracting "wave", $u_0(\mathbf{x}, t)$, in the scalar neural field (B.5). If we carefully choose the threshold value α, the wave has zero velocity, which we denote without the time dependence, $u_0(\mathbf{x})$. The wave solution satisfies

$$u_0(\mathbf{x}) = \int_\Omega K(\mathbf{x}-\mathbf{y}) f(u_0(\mathbf{y})-\alpha_0) d\mathbf{y},$$

where u_0 is nonconstant and monotonic. The standing and traveling wave solutions we consider are monotonic such that for some vector $\mathbf{y}$ on a line L in the plane, $u(\mathbf{x}) \to 0$ for all large $\mathbf{x}, \mathbf{y}$ s.t. $\langle \mathbf{x}, \mathbf{y} \rangle > 0$ and $u(\mathbf{x}) \to 1$ for all large $\mathbf{x}, \mathbf{y}$ s.t. $\langle \mathbf{x}, \mathbf{y} \rangle < 0$ that is positioned such that its threshold crossing is at $\mathbf{x} = 0$.

For ε nonzero, we write the threshold α as $\alpha = \alpha_0 + \varepsilon\alpha_1$, where α_0 is the standing wave value, and α_1 is the perturbation away from this balanced state. Remarkably, the scalar reduction in this case is nearly identical to [70].

B.4.1 Derivation of the Phase Equation for Slowly Traveling Waves

We start with Equations (B.5),(B.6). Let $\tau = \varepsilon t$ be a slow timescale and assume that both z and u depend only on $(\mathbf{x}, \tau)$. In this case, we can integrate equation (B.6) to obtain:

$$z(\mathbf{x}, \tau) = z(\mathbf{x}, 0)e^{-\beta\tau} + \beta \int_0^\tau e^{-\beta(\tau - s)} u(\mathbf{x}, s)\ ds.$$

Since we are mainly interested in long term behavior, we can ignore the first exponentially decaying term. With these assumptions, we obtain the following scalar integro-differential equation:

$$\begin{aligned} \varepsilon \frac{\partial u(\mathbf{x}, \tau)}{\partial \tau} = -u(\mathbf{x}, \tau) &+ \int_\Omega K(\mathbf{x} - \mathbf{y}) f(u(\mathbf{y}, \tau) - \alpha_0)\ d\mathbf{y} \\ &+ \varepsilon \Big[qI(\mathbf{x} + \Omega\varepsilon t) \\ &- \alpha_1 \int_\Omega K(\mathbf{x} - \mathbf{y}) f'(u(\mathbf{y}, \tau) - \alpha_0)\ d\mathbf{y} \\ &- g\beta \int_0^\tau e^{-\beta(\tau - s)} u(\mathbf{x}, s)\ ds \Big]. \end{aligned} \tag{B.7}$$

We will assume $u(\mathbf{x}, \tau) = U(\mathbf{x}, \tau, \varepsilon)$ and expand U as a power series in ε to get an approximate solution. Thus,

$$U(x, \tau, \varepsilon) = U_0(\mathbf{x}, \tau) + \varepsilon U_1(\mathbf{x}, \tau) + O(\varepsilon^2).$$

Substituting this power series into (B.7), we get (with a bit of re-arrangement):

$$0 = -U_0(\mathbf{x}, \tau) + \int_\Omega K(\mathbf{x} - \mathbf{y}) f(U_0(\mathbf{y}, \tau) - \alpha_0) d\mathbf{y} \tag{B.8}$$

$$(LU_1)(\mathbf{x}, \tau) = \frac{\partial U_0(\mathbf{x}, \tau)}{\partial \tau} - R_1(\mathbf{x}, \tau), \tag{B.9}$$

where

$$(Lv)(\mathbf{x},\tau) := -v(\mathbf{x},\tau) + \int_\Omega K(\mathbf{x}-\mathbf{y}) f'(U_0(\mathbf{y},\tau)-\alpha_0) v(\mathbf{y},\tau)\ d\mathbf{y},$$

and

$$\begin{aligned} R_1(\mathbf{x},\tau) = qI(\mathbf{x}) - \alpha_1 \int_\Omega K(\mathbf{x}-\mathbf{y}) f'(U_0(\mathbf{y},\tau)-\alpha_0)\ d\mathbf{y} \\ - g\beta \int_0^\tau e^{-\beta(\tau-s)} U_0(\mathbf{x},s)\ ds \end{aligned}$$

The equation for $U_0(\mathbf{x},\tau)$ is the equation for the standing wave solution and since it is translation invariant, we see that

$$U_0(\mathbf{x},\tau) = u_0(\mathbf{x}+\boldsymbol{\theta}(\tau))$$

where $\boldsymbol{\theta}(\tau)$ is a $\tau-$dependent phase shift of the wavefront. Our goal, then is to determine the dynamics of $\boldsymbol{\theta}(\tau)$.

Before continuing with the perturbation calculation, we establish a few preliminaries. We define the compact linear operator

$$(L_0 v)(\mathbf{x}) := -v(\mathbf{x}) + \int_\Omega K(\mathbf{x}-\mathbf{y}) f'(u_0(\mathbf{y})-\alpha_0) v(\mathbf{y})\ d\mathbf{y}$$

and establish several properties of it. Recall that the bump, $u_0(\mathbf{x})$ satisfies

$$-u_0(\mathbf{x}) + \int_\Omega K(\mathbf{x}-\mathbf{y}) f(u_0(\mathbf{y})-\alpha_0)\ d\mathbf{y} = 0.$$

By making a change of variables and noting that all functions are periodic in $\mathbf{x}$ (that is, periodic in each of the components of $\mathbf{x}$), then $u_0(\mathbf{x})$ satisfies

$$-u_0(\mathbf{x}) + \int_\Omega K(\mathbf{y}) f(u_0(\mathbf{x}-\mathbf{y})-\alpha_0)\ d\mathbf{y} = 0. \tag{B.10}$$

Recalling that the domain is $\Omega = \mathbb{R}^m$, with $m = 1, 2$, we center u_0 at the origin. Thus, $u_0(\mathbf{x})$ is an even periodic function of $\mathbf{x}$, component-wise. Let $\partial_i u(\mathbf{x})$ denote the partial derivative of $u(\mathbf{x})$ along the x_i direction where $\mathbf{x} = (x_1, x_2)$. If we differentiate (B.10) along one of the axes, we see that

$$-\partial_i u_0(\mathbf{x}) + \int_\Omega K(\mathbf{y}) f'(u_0(\mathbf{x}-\mathbf{y})-\alpha_0) \partial_i u_0(\mathbf{x}-\mathbf{y})\ d\mathbf{y} = 0.$$

and changing variables again, we rewrite this as

$$-\partial_i u_0(\mathbf{x}) + \int_\Omega K(\mathbf{x}-\mathbf{y}) f'(u_0(\mathbf{y}) - \alpha_0)\partial_i u_0(\mathbf{y})\ d\mathbf{y} = 0, \tag{B.11}$$

so we see that $L_0 \partial_i u_0(\mathbf{x}) = 0$. In other words, the linear operator, L_0 has an $m-$dimensional nullspace spanned by the principle directional derivatives of $u_0(\mathbf{x})$. With the natural inner product

$$\langle u(\mathbf{x}), v(\mathbf{x})\rangle = \int_\Omega u(\mathbf{x})v(\mathbf{x})\ d\mathbf{x}$$

the operator L_0 has an adjoint

$$(L^* v)(\mathbf{x}) = -v(\mathbf{x}) + f'(u_0(\mathbf{x}) - \alpha_0)\int_\Omega K(\mathbf{x}-\mathbf{y})v(\mathbf{y})\ d\mathbf{y}.$$

By multiplying equation (B.11) by $f'(u_0(\mathbf{x}) - \alpha_0)$, we see that the nullspace of L^* is spanned by $v_i^*(\mathbf{x}) = f'(u_0(\mathbf{x}) - \alpha_0)\partial_i u_0(\mathbf{x})$. Finally, the Fredholm alternative holds for L_0. That is, for any continuous bounded function $b(\mathbf{x})$,

$$(L_0 v)(\mathbf{x}) = b(\mathbf{x})$$

has a bounded solution if and only if

$$\langle v_i^*(\mathbf{x}), b(\mathbf{x})\rangle = 0$$

for $i = 1, \ldots, m$ [47].

With these technical issues aside, we turn to equation (3.5), which we can rewrite as

$$(LU_1)(\mathbf{x}, \tau) = (\partial_1 u_0(\mathbf{x} + \boldsymbol{\theta}(\tau)), \partial_2 u_0(\mathbf{x} + \boldsymbol{\theta}(\tau))) \cdot \frac{d\boldsymbol{\theta}(\tau)}{d\tau} - R_1(\mathbf{x}, \tau)$$

Writing $\boldsymbol{\theta}(\tau) = (\theta_1(\tau), \theta_2(\tau))$ and applying the m conditions for the Fredholm alternative, we arrive at

$$\frac{d\boldsymbol{\theta}}{d\tau} = \mathbf{M}^{-1}\mathbf{R} \tag{B.12}$$

where $d\boldsymbol{\theta}/d\tau = \left(\frac{d\theta_1}{d\tau}, \frac{d\theta_2}{d\tau}, \ldots, \frac{d\theta_n}{d\tau}\right)^T$, the i^{th} coordinate of $\mathbf{R} = (R_1, R_2, \ldots, R_n)^T$ is

$$R_i = qJ_i(\boldsymbol{\theta}, \tau) - \alpha_1 D_i + W_i - g\beta \int_0^\tau e^{-\beta(\tau - s)} H_i(\boldsymbol{\theta}(s) - \boldsymbol{\theta}(\tau))ds,$$

the $(i,j)^{\text{th}}$ coordinate of $\mathbf{M}$ is

$$\mathbf{M}_{ij} = \langle v_i^*(\mathbf{x}), \partial_j u_0(\mathbf{x}) \rangle,$$

and

$$\begin{aligned} J_i(\boldsymbol{\theta}, \tau) &= \int_\Omega f'(u_0(\mathbf{x}+\boldsymbol{\theta}) - \alpha_0) \partial_i u_0(\mathbf{x}+\boldsymbol{\theta}) I(\mathbf{x}+\Omega\tau)\ d\mathbf{x}, \\ D_i &= \int_\Omega f'(u_0(\mathbf{x}) - \alpha_0) \partial_i u_0(\mathbf{x}) \int_\Omega K(\mathbf{x}-\mathbf{y}) f'(u_0(\mathbf{y}) - \alpha_0)\ d\mathbf{y}\ d\mathbf{x}, \\ H_i(\boldsymbol{\theta}) &= \int_\Omega f'(u_0(\mathbf{x}) - \alpha_0) \partial_i u_0(\mathbf{x}) u_0(\mathbf{x}+\boldsymbol{\theta})\ d\mathbf{x}. \end{aligned}$$

Because the standing wave solution u_0 is not even, we are unable to directly simplify the matrix M to a diagonal matrix as in ympgbe2.

B.4.2 One-Dimensional Domain

In this section, we restrict our attention to the one-dimensional domain. Here, the phase equation is one scalar differential equation,

$$\frac{d\theta}{d\tau} = qJ(\theta) - \alpha_1 D - g\beta \int_0^\tau e^{-\beta(\tau-s)} H(\theta(s) - \theta(\tau)) ds,$$

where J, D, and H are as in the n-dimensional case above, but the partial derivatives are now regular derivatives.

B.4.2.1 Classic Traveling Wave Consider the phase equation (B.12), with no heterogeneities, and $g = \alpha_0 = 0$. Then we are left with

$$\frac{d\theta}{d\tau} = \alpha_1 D. \tag{B.13}$$

Note that if the input current is uniform, the input current appears as a constant term on the right hand side of the phase equation. The result is the same.

B.4.2.2 Sloshing Solutions Suppose that a fixed point exists at $\theta = \theta^*$ for $g, q, \alpha_1 > 0$ and let $\theta(\tau) = \theta^* + \delta\psi(\tau)$. To lowest order, the fixed point θ^* satisfies

$$0 = qJ(\theta^*) - \alpha_1 D - gH(\theta^*).$$

The order δ terms determine stability:

$$\lambda = qJ'(\theta^*) + gH'(\theta^*)\left[\frac{\lambda}{1+\lambda}\right].$$

Solving for λ yields

$$2\lambda = -(1 - qJ'(\theta^*)) \pm \sqrt{(1 - qJ'(\theta^*))^2 - 4(-qJ'(\theta^*) - gH'(\theta^*))}.$$

For a Hopf bifurcation to occur, we require that $1 - qJ'(\theta^*) = 0$ and

$$0 < 4(-qJ'(\theta^*) - gH'(\theta^*)).$$

Generally, $H'(\theta), D'(\theta) > 0$ and $J'(\theta) < 0$, thus for appropriate choices of q, α_1, and g, a Hopf bifurcation is possible.

APPENDIX C

A MULTIPLE TIMESCALES APPROACH TO BRIDGING SPIKING- AND POPULATION-LEVEL DYNAMICS

C.1 MODEL EQUATIONS AND PARAMETERS

C.1.1 Traub With Calcium

$$\dot{\mathbf{x}} = \frac{d}{dt}\begin{pmatrix} V \\ x \\ w \\ [\mathrm{Ca}] \end{pmatrix} = \begin{pmatrix} (-I_{\mathrm{ionic}} + I_{\mathrm{ext}})/C \\ a_x(V)(1-x) - b_x(V)x \\ (w_\infty(V) - w)/\tau_w(V) \\ (-\alpha I_{\mathrm{Ca}} - [\mathrm{Ca}]/\tau_{\mathrm{Ca}}) \end{pmatrix} = \mathbf{F}^x(\mathbf{x}, I_{\mathrm{ext}})$$

where x represents the dynamics of gating variables h, m, and n, and

$$\begin{aligned} I_{\mathrm{ionic}} &= I_{\mathrm{Na}} + I_{\mathrm{K}} + I_{\mathrm{Ca}} + I_{\mathrm{ahp}} + I_{\mathrm{M}} + g_{\mathrm{L}}(V - E_{\mathrm{L}}) \\ I_{\mathrm{Na}} &= g_{\mathrm{Na}} m^3 h (V - E_{\mathrm{Na}}) \\ I_{\mathrm{K}} &= g_{\mathrm{K}} n^4 (V - E_{\mathrm{K}}) \\ I_{\mathrm{Ca}} &= g_{\mathrm{Ca}} M_{L\infty}(V)(V - E_{\mathrm{Ca}}) \\ I_{\mathrm{ahp}} &= \frac{g_{\mathrm{ahp}}[\mathrm{Ca}](V - E_{\mathrm{K}})}{[\mathrm{Ca}] + K_{\mathrm{d}}} \\ I_{\mathrm{M}} &= g_{\mathrm{M}} w (V - E_{\mathrm{K}}) \end{aligned} \tag{C.1}$$

The voltage variable V has dimensions of mV, all currents are in dimensions of $\mu\mathrm{A/cm}^2$, time is in units of milliseconds, the variables n, m, h, and w are dimensionless, and the

variable [Ca] represents the intracellular calcium concentration in millimolar units. We show dimensions of all model parameters in Table 7.

$$
\begin{aligned}
a_m(V) &= \frac{0.32(V+54)}{1-\exp(-(V+54)/4)} \\
b_m(V) &= \frac{0.28(V+27)}{\exp((V+27)/5)-1} \\
a_h(V) &= 0.128\exp(-(V+50)/18) \\
b_h(V) &= \frac{4}{1+\exp(-(V+27)/5)} \\
a_n(V) &= \frac{0.032(V+52)}{1-\exp(-(V+52)/5)} \\
b_n(V) &= 0.5\exp(-(V+50)/40) \\
\tau_w(V) &= \frac{\tau_w}{3.3\exp((V-V_{wt})/20)+\exp(-(V-V_{wt})/20)} \\
w_\infty(V) &= \frac{1}{1+\exp(-(V-V_{wt})/10)} \\
M_{L\infty}(V) &= 1/(1+\exp(-(V-V_{\mathrm{Lth}})/V_{\mathrm{shp}}))
\end{aligned}
$$

C.1.2 Wang-Buzsáki

$$
\dot{\mathbf{y}} = \frac{d}{dt}\begin{pmatrix} V \\ x \end{pmatrix} = \begin{pmatrix} -I_{ionic} + I_{\mathrm{ext}} \\ \phi(x_\infty - x)/\tau_x \end{pmatrix} = \mathbf{F}^y(\mathbf{y}, I_{\mathrm{ext}}),
$$

where x represents the dynamics of gating variables h and n, and

$$
\begin{aligned}
I_{\mathrm{ionic}} &= g_{\mathrm{L}}(V-E_{\mathrm{L}}) + I_{\mathrm{Na}} + I_{\mathrm{K}} \\
I_{\mathrm{Na}} &= g_{\mathrm{Na}} m_\infty^3 h(V-E_{\mathrm{Na}}) \\
I_{\mathrm{K}} &= g_{\mathrm{K}} n^4 (V-E_{\mathrm{K}})
\end{aligned}
\tag{C.2}
$$

As in the Traub model above, the variable V has dimensions of mV, time units of milliseconds, the variables h and n are dimensionless, and currents are in units of $\mu\mathrm{A/cm}^2$. We show dimensions of all model parameters in Table 8.

Table 7: Traub with calcium parameter values

Parameter	Value
C	1 μF/cm^2
E_K	-100mV
E_{Na}	50mV
E_L	-67mV
E_{Ca}	120mV
g_L	0.2mS/cm^2
g_K	80mS/cm^2
g_{Na}	100mS/cm^2
g_m	0mS/cm^2
g_{Ca}	1mS/cm^2
g_{ahp}	0.5mS/cm^2
K_d	1mM
α	0.002mmol/(cm $\times$ nC)
τ_{Ca}	80ms
V_{shp}	2.5mV
V_{Lth}	-25mV
V_{sshp}	2mV
V_{th}	-10mV
V_{wt}	-35mV
τ_w	100ms

Table 8: Wang-Buzsáki parameter values

Parameter	Value
E_K	-90mV
E_{Na}	55mV
E_L	-65mV
g_L	0.1mS/cm^2
g_{Na}	35mS/cm^2
g_K	9mS/cm^2
ϕ	5

$$
\begin{aligned}
\alpha_m(V) &= \frac{0.1(V+35)}{1-\exp(-(V+35)/10} \\
\beta_m(V) &= 4\exp(-(V+60)/18) \\
\alpha_h(V) &= 0.07\exp(-(V+58)/20) \\
\beta_h(V) &= \frac{1}{1+\exp(-(V+28)/10)} \\
\alpha_n(V) &= \frac{0.01(V+34)}{1-\exp(-(V+34)/10)} \\
\beta_n(V) &= 0.125\exp(-(V+44)/80) \\
x_\infty &= x_1/(x_1+x_2) \\
\tau_x &= 1/(x_1+x_2)
\end{aligned}
$$

where x in the last two lines represents m, h, or n and x_1, x_2 may be α_x and β_x, respectively.

C.2 DERIVATION OF SPIKING TERM

Recall our starting ansatz for the phase equation,

$$\begin{aligned}
\mathbf{x}_i(t,\tau) &= \mathbf{x}_i(t+\theta_i(\tau),\bar{s}) = \Phi^x(t+\theta_i^x(\tau),\bar{s}) + \varepsilon\xi_i^x(t+\theta_i^x(\tau),\bar{s}) + O(\varepsilon^2),\\
\mathbf{y}_i(t,\tau) &= \mathbf{y}_i(t+\theta_i(\tau),\bar{s}) = \Phi^y(t+\theta_i^y(\tau),\bar{s}) + \varepsilon\xi_i^y(t+\theta_i^y(\tau),\bar{s}) + O(\varepsilon^2),\\
s^x(t,\tau) &= \bar{s}(\tau) + \frac{\varepsilon}{N\mu^x}\sum_j f\left(t+\theta_j^x(\tau)\right) + O(\varepsilon^2),\\
s^y(t,\tau) &= \bar{s}(\tau) + \frac{\varepsilon}{N\mu^y}\sum_j f\left(t+\theta_j^y(\tau)\right) + O(\varepsilon^2),
\end{aligned}$$

where

$$f(t+\theta) = \left[(1-(t+\theta)/T \mod 1) - 1/2\right].$$

In this section, we derive the order ε term f.

For simplicity, consider a network consisting of one excitatory neuron $\mathbf{x}_1$ with one synaptic variable $s^x(t,\tau)$. Note that following a spike, the solution $\mathbf{x}_1$ increments by $\varepsilon_k \equiv \varepsilon/\mu^k$ and decays exponentially. Moreover, each s^k is periodic with $s^k(T^+) = s^k(0)$, where $k = x, y$. Putting these facts together, we have that

$$s^k(T^+) = s^k(0)e^{-\varepsilon_k T} + \varepsilon_k = s^k(0).$$

Solving for $s^k(0)$ reveals

$$s^k(0) = \frac{\varepsilon_k}{1-e^{-\varepsilon_k T}}.$$

Therefore, $s^k(t)$ after a spike is

$$s^k(t) = \frac{\varepsilon_k}{1-e^{\varepsilon_k T}}e^{-\varepsilon_k t}.$$

Notice that

$$s^k(t) = \frac{\varepsilon_k}{1-e^{-\varepsilon_k T}}e^{-\varepsilon_k t} = \frac{1}{T} + \varepsilon_k f(t),$$

which after a trivial rearrangement yields

$$\varepsilon_k f(t) = \frac{\varepsilon_k}{1-e^{-\varepsilon_k T}}e^{-\varepsilon_k t} - \frac{1}{T}.$$

Since ε_k is small, we take a Taylor expansion of the exponential and simplify in a series of algebraic steps:

$$\begin{aligned}
\varepsilon_k f(t) &= \frac{\varepsilon_k(1-\varepsilon_k t + O(\varepsilon_k^2))}{1-(1-\varepsilon_k T + (\varepsilon_k T)^2/2 + O(\varepsilon_k^3))} - \frac{1}{T} \\
&= \frac{1-\varepsilon_k t + O(\varepsilon_k^2)}{T - \varepsilon_k T^2/2 + O(\varepsilon_k^2)} - \frac{1}{T} \\
&= \frac{1}{T}\frac{1-\varepsilon_k t + O(\varepsilon_k^2)}{1-\varepsilon_k T/2 + O(\varepsilon_k^2)} - \frac{1}{T} \\
&= \frac{1}{T}\left(\frac{1-\varepsilon_k t + O(\varepsilon_k^2)}{1-\varepsilon_k T/2 + O(\varepsilon_k^2)} - \frac{1-\varepsilon_k T/2 + O(\varepsilon_k^2)}{1-\varepsilon_k T/2 + O(\varepsilon_k^2)}\right) \\
&= \frac{1}{T}\frac{\varepsilon_k T/2 - \varepsilon_k t + O(\varepsilon_k^2)}{1-\varepsilon_k T/2 + O(\varepsilon_k^2)}\frac{1+\varepsilon_k T/2 + O(\varepsilon_k^2)}{1+\varepsilon_k T/2 + O(\varepsilon_k^2)} \\
&= \frac{1}{T}\frac{\varepsilon_k T/2 - \varepsilon_k t + O(\varepsilon_k^2)}{1 + O(\varepsilon_k^2)} \\
&\approx \frac{1}{T}\varepsilon_k(T/2 - t).
\end{aligned}$$

Thus,

$$f(t) = \left(\frac{1}{2} - \frac{t}{T}\right),$$

over one period. For multiple periods, the resulting function is a sawtooth. In our implementations we write

$$f(t) = ((1 - t/T) \mod 1) - 1/2.$$

In general, we need to account for possible slow timescale phase shifts $\theta_j^k(\tau)$ and the contributions from multiple spikes. We simply sum these contributions to arrive at the desired form:

$$\frac{\varepsilon}{N\mu^x}\sum_j f\left(t + \theta_j^x(\tau)\right).$$

C.3 FOURIER COEFFICIENTS

We use many Fourier truncations in the chapters above. For convenience to the reader, and to aid in helping keep the dissertation style consistent, we list only an abridged list of the tables and refer the reader to the paper that contains the full list of coefficients [70].

Table 9: H-function coefficients of the theta model. The series takes the form $\sum_{i=1}^{n} a_i \cos(ix) + b_i \sin(ix)$. Error = 7e-3.

Coefficient	H^{xx}	H^{xy}	H^{yx}	H^{yy}
a_1	0.006693442	-0.00736278	0.006693442	-0.00736278
b_1	-1.09191412	1.201105540	-1.09191412	1.201105540

Table 10: Abridged H-function cosine coefficients of the Traub with calcium (H^{xx}, H^{xy}) and Wang-Buzsáki (H^{yx}, H^{yy}). $a_0 + \sum_{i=1}^{n} a_i \cos(ix) + b_i \sin(ix)$. Maximum pointwise error = 1e-2.

Coefficient	H^{xx}	H^{xy}	H^{yx}	H^{yy}
a_0	-0.00014179	0.000340298		
a_1	-0.40559133	0.973419204	0.014799680	-0.01138436
a_2	-0.00296584	0.007118019	0.120314654	-0.09254973
a_3	0.008194908	-0.01966778	0.045877649	-0.03529049
b_1	-0.14512093	0.348290252	-1.29140450	0.993388080
b_2	-0.07327966	0.175871190	-0.22112111	0.170093167
b_3	-0.01561869	0.037484866	-0.07939645	0.061074193
b_4	-0.00449755	0.010794122	-0.03842115	0.029554737

BIBLIOGRAPHY

[1] Larry F Abbott. Lapicque's introduction of the integrate-and-fire model neuron (1907). *Brain research bulletin*, 50(5-6):303–304, 1999.

[2] Shun-ichi Amari. Dynamics of pattern formation in lateral-inhibition type neural fields. *Biological cybernetics*, 27(2):77–87, 1977.

[3] Daniel J Amit and Nicolas Brunel. Dynamics of a recurrent network of spiking neurons before and following learning. *Network: Computation in Neural Systems*, 8(4):373–404, 1997.

[4] Daniel J Amit and Nicolas Brunel. Model of global spontaneous activity and local structured activity during delay periods in the cerebral cortex. *Cerebral cortex (New York, NY: 1991)*, 7(3):237–252, 1997.

[5] R Ben-Yishai, R Lev Bar-Or, and H Sompolinsky. Theory of orientation tuning in visual cortex. *Proceedings of the National Academy of Sciences*, 92(9):3844–3848, 1995.

[6] Rani Ben-Yishai, David Hansel, and Haim Sompolinsky. Traveling waves and the processing of weakly tuned inputs in a cortical network module. *Journal of computational neuroscience*, 4(1):57–77, 1997.

[7] Michael Breakspear. Dynamic models of large-scale brain activity. *Nature neuroscience*, 20(3):340–352, 2017.

[8] Paul C. Bressloff and Stefanos E Folias. Front bifurcations in an excitatory neural network. *SIAM Journal on Applied Mathematics*, 65(1):131–151, January 2004.

[9] Paul C. Bressloff, Stefanos E Folias, A. Prat, and Y.-X. Li. Oscillatory waves in inhomogeneous neural media. *Physical Review Letters*, 91(17):178101, October 2003.

[10] Eric Brown, Jeff Moehlis, and Philip Holmes. On the phase reduction and response dynamics of neural oscillator populations. *Neural computation*, 16(4):673–715, 2004.

[11] Nicolas Brunel and Mark CW Van Rossum. Lapicque's 1907 paper: from frogs to integrate-and-fire. *Biological cybernetics*, 97(5-6):337–339, 2007.

[12] Sarthak Chandra, David Hathcock, Kimberly Crain, Thomas M Antonsen, Michelle Girvan, and Edward Ott. Modeling the network dynamics of pulse-coupled neurons. *Chaos: An Interdisciplinary Journal of Nonlinear Science*, 27(3):033102, 2017.

[13] Sarthak Chandra, David Hathcock, Kimberly Crain, Thomas M. Antonsen, Michelle Girvan, and Edward Ott. Modeling the network dynamics of pulse-coupled neurons. *Chaos: An Interdisciplinary Journal of Nonlinear Science*, 27(3):033102, March 2017.

[14] S. Coombes and M. R. Owen. Bumps, breathers, and waves in a neural network with wpike frequency adaptation. *Physical Review Letters*, 94(14):148102, apr 2005.

[15] Stephen Coombes. Waves, bumps, and patterns in neural field theories. *Biological cybernetics*, 93(2):91–108, 2005.

[16] Stephen Coombes and Áine Byrne. Next generation neural mass models. *arXiv preprint arXiv:1607.06251*, 2016.

[17] John R Cressman Jr, Ghanim Ullah, Jokubas Ziburkus, Steven J Schiff, and Ernest Barreto. The influence of sodium and potassium dynamics on excitability, seizures, and the stability of persistent states: I. single neuron dynamics. *Journal of computational neuroscience*, 26(2):159–170, 2009.

[18] Per Danzl, Robert Hansen, Guillaume Bonnet, and Jeff Moehlis. Partial phase synchronization of neural populations due to random poisson inputs. *Journal of computational neuroscience*, 25(1):141–157, 2008.

[19] Bard Ermentrout. *Simulating, analyzing, and animating dynamical systems: a guide to XPPAUT for researchers and students*, volume 14. Siam, 2002.

[20] Bard Ermentrout, Matthew Pascal, and Boris Gutkin. The effects of spike frequency adaptation and negative feedback on the synchronization of neural oscillators. *Neural Computation*, 13(6):1285–1310, 2001.

[21] G Bard Ermentrout, Bryce Beverlin II, and Theoden Netoff. Phase response curves to measure ion channel effects on neurons. In *Phase Response Curves in Neuroscience*, pages 207–236. Springer, 2012.

[22] G Bard Ermentrout, Stefanos E Folias, and Zachary P Kilpatrick. Spatiotemporal pattern formation in neural fields with linear adaptation. In *Neural Fields*, pages 119–151. Springer, 2014.

[23] G Bard Ermentrout, Roberto F Galán, and Nathaniel N Urban. Reliability, synchrony and noise. *Trends in neurosciences*, 31(8):428–434, 2008.

[24] G Bard Ermentrout, Jozsi Z Jalics, and Jonathan E Rubin. Stimulus-driven traveling solutions in continuum neuronal models with a general smooth firing rate function. *SIAM Journal on Applied Mathematics*, 70(8):3039–3064, 2010.

[25] G Bard Ermentrout and David H Terman. *Mathematical foundations of neuroscience*, volume 35. Springer Science & Business Media, 2010.

[26] G.Bard Ermentrout. n:m phase-locking of weakly coupled oscillators. *Journal of Mathematical Biology*, 12(3):327–342, 1981.

[27] George Bard Ermentrout and Nancy Kopell. Frequency plateaus in a chain of weakly coupled oscillators, i. *SIAM journal on Mathematical Analysis*, 15(2):215–237, 1984.

[28] Grégory Faye. Existence and stability of traveling pulses in a neural field equation with synaptic depression. *SIAM Journal on Applied Dynamical Systems*, 12(4):2032–2067, 2013.

[29] Stefanos E Folias. Nonlinear analysis of breathing pulses in a synaptically coupled neural network. *SIAM Journal on Applied Dynamical Systems*, 10(2):744–787, 2011.

[30] Stefanos E Folias. Traveling waves and breathers in an excitatory-inhibitory neural field. *Physical Review E*, 95(3):032210, 2017.

[31] Stefanos E Folias and Paul C. Bressloff. Breathing pulses in an excitatory neural network. *SIAM Journal on Applied Dynamical Systems*, 3(3):378–407, jan 2004.

[32] Stefanos E Folias and Paul C. Bressloff. Breathers in two-dimensional neural media. *Physical Review Letters*, 95(20):208107, nov 2005.

[33] Stefanos E Folias and Paul C. Bressloff. Stimulus-locked traveling waves and breathers in an excitatory neural network. *SIAM Journal on Applied Mathematics*, 65(6):2067–2092, January 2005.

[34] C. C. A. Fung and S. i Amari. Spontaneous motion on two-dimensional continuous attractors. *Neural Computation*, 27(3):507–547, mar 2015.

[35] C. C. Alan Fung, K. Y. Michael Wong, Hongzi Mao, and Si Wu. Fluctuation-response relation unifies dynamical behaviors in neural fields. *Physical Review E*, 92(2):022801, aug 2015.

[36] C. C. Alan Fung, K. Y. Michael Wong, He Wang, and Si Wu. Dynamical synapses enhance neural information processing: gracefulness, accuracy, and mobility. *Neural Computation*, 24(5):1147–1185, feb 2012.

[37] CC Alan Fung, KY Michael Wong, and S Wu. A moving bump in a continuous manifold: A comprehensive study of the tracking dynamics of continuous attractor neural networks. *Neural Computation*, 22(3):752–792, 2010.

[38] Roberto F Galán, G Bard Ermentrout, and Nathaniel N Urban. Optimal time scale for spike-time reliability: theory, simulations, and experiments. *Journal of neurophysiology*, 99(1):277–283, 2008.

[39] Natalia Gorelova, Jeremy K Seamans, and Charles R Yang. Mechanisms of dopamine activation of fast-spiking interneurons that exert inhibition in rat prefrontal cortex. *Journal of neurophysiology*, 88(6):3150–3166, 2002.

[40] Boris S Gutkin, G Bard Ermentrout, and Alex D Reyes. Phase-response curves give the responses of neurons to transient inputs. *Journal of neurophysiology*, 94(2):1623–1635, 2005.

[41] David Hansel and Haim Sompolinsky. 13 modeling feature selectivity in local cortical circuits. In Christof Koch and Idan Segev, editors, *Methods in Neuronal Modeling: From Synapses to Networks*, chapter 13, pages 499–567. Cambridge, MA, 1998.

[42] Frank C Hoppensteadt and Eugene M Izhikevich. *Weakly connected neural networks*, volume 126. Springer Science & Business Media, 2012.

[43] Vladimir Itskov, Carina Curto, Eva Pastalkova, and György Buzsáki. Cell assembly sequences arising from spike threshold adaptation keep track of time in the hippocampus. *The Journal of Neuroscience*, 31(8):2828–2834, 2011.

[44] Eugene M Izhikevich. *Dynamical systems in neuroscience*. MIT press, 2007.

[45] Ho Young Jeong and Boris Gutkin. Synchrony of neuronal oscillations controlled by gabaergic reversal potentials. *Neural Computation*, 19(3):706–729, 2007.

[46] Daniel Johnston and Samuel Miao-Sin Wu. *Foundations of cellular neurophysiology*. MIT press, 1994.

[47] James P Keener. *Principles of applied mathematics*. Addison-Wesley, 1988.

[48] Z. Kilpatrick and G. Faye. Pulse Bifurcations in Stochastic Neural Fields. *SIAM Journal on Applied Dynamical Systems*, 13(2):830–860, January 2014.

[49] Zachary P. Kilpatrick and Paul C. Bressloff. Spatially structured oscillations in a two-dimensional excitatory neuronal network with synaptic depression. *Journal of Computational Neuroscience*, 28(2):193–209, October 2009.

[50] Zachary P. Kilpatrick and Paul C. Bressloff. Effects of synaptic depression and adaptation on spatiotemporal dynamics of an excitatory neuronal network. *Physica D: Nonlinear Phenomena*, 239(9):547–560, May 2010.

[51] N. Kopell and L.N. Howard. Plane wave solutions to reaction diffusion equations. 52:291–328, 1973.

[52] Hiroshi Kori, Yoji Kawamura, Hiroya Nakao, Kensuke Arai, and Yoshiki Kuramoto. Collective-phase description of coupled oscillators with general network structure. *Physical Review E*, 80(3):036207, 2009.

[53] Y. Kuramoto. *Chemical Oscillations, Waves, and Turbulence*. Springer–Verlag, New York, 1984.

[54] Yoshiki Kuramoto and Ikuko Nishikawa. Statistical macrodynamics of large dynamical systems. case of a phase transition in oscillator communities. *Journal of Statistical Physics*, 49(3):569–605, Nov 1987.

[55] Wataru Kurebayashi, Sho Shirasaka, and Hiroya Nakao. Phase reduction method for strongly perturbed limit cycle oscillators. *Phys. Rev. Lett.*, 111:214101, Nov 2013.

[56] Wataru Kurebayashi, Sho Shirasaka, and Hiroya Nakao. A criterion for timescale decomposition of external inputs for generalized phase reduction of limit-cycle oscillators. *Nonlinear Theory and Its Applications, IEICE*, 6(2):171–180, 2015.

[57] C. Laing. Exact Neural Fields Incorporating Gap Junctions. *SIAM Journal on Applied Dynamical Systems*, 14(4):1899–1929, January 2015.

[58] Carlo R Laing. Derivation of a neural field model from a network of theta neurons. *Physical Review E*, 90(1):010901, 2014.

[59] Carlo R. Laing. The dynamics of networks of identical theta neurons. *The Journal of Mathematical Neuroscience*, 8(1):4, Feb 2018.

[60] Carlo R. Laing and André Longtin. Noise-induced stabilization of bumps in systems with long-range spatial coupling. *Physica D: Nonlinear Phenomena*, 160(3):149–172, December 2001.

[61] GJM Marée. Slow passage through a pitchfork bifurcation. *SIAM Journal on Applied Mathematics*, 56(3):889–918, 1996.

[62] David A McCormick. Cellular mechanisms underlying cholinergic and noradrenergic modulation of neuronal firing mode in the cat and guinea pig dorsal lateral geniculate nucleus. *The Journal of neuroscience*, 12(1):278–289, 1992.

[63] Ernest Montbrió, Diego Pazó, and Alex Roxin. Macroscopic Description for Networks of Spiking Neurons. *Physical Review X*, 5(2):021028, June 2015.

[64] Ken H Nagai and Hiroshi Kori. Noise-induced synchronization of a large population of globally coupled nonidentical oscillators. *Physical Review E*, 81(6):065202, 2010.

[65] Jakub Nowacki. XPPy, 2011.

[66] Edward Ott and Thomas M Antonsen. Low dimensional behavior of large systems of globally coupled oscillators. *Chaos: An Interdisciplinary Journal of Nonlinear Science*, 18(3):037113, 2008.

[67] Edward Ott and Thomas M. Antonsen. Long time evolution of phase oscillator systems. *Chaos: An Interdisciplinary Journal of Nonlinear Science*, 19(2):023117, May 2009.

[68] Youngmin Park and Bard Ermentrout. Weakly coupled oscillators in a slowly varying world. *Journal of computational neuroscience*, 40(3):269–281, 2016.

[69] Youngmin Park and G Bard Ermentrout. A multiple timescales approach to bridging spiking- and population-level dynamics. *Chaos, Submitted*, 2018.

[70] Youngmin Park and G Bard Ermentrout. Scalar reduction of a neural field model with spike frequency adaptation. *SIADS, In Press*, 2018.

[71] Youngmin Park, Stewart Heitmann, and G Bard Ermentrout. The utility of phase models in studying neural synchronization. *Computational Models of Brain and Behavior*, pages 493–504, 2017.

[72] Eva Pastalkova, Vladimir Itskov, Asohan Amarasingham, and György Buzsáki. Internally generated cell assembly sequences in the rat hippocampus. *Science*, 321(5894):1322–1327, 2008.

[73] Diego Pazó and Ernest Montbrió. Low-dimensional dynamics of populations of pulse-coupled oscillators. *Physical Review X*, 4(1):011009, 2014.

[74] Benjamin Pfeuty, Germán Mato, David Golomb, and David Hansel. Electrical synapses and synchrony: the role of intrinsic currents. *The Journal of neuroscience*, 23(15):6280–6294, 2003.

[75] Arkady Pikovsky, Michael Rosenblum, and Jürgen Kurths. *Synchronization: a universal concept in nonlinear sciences*, volume 12. Cambridge university press, 2003.

[76] D. Pinto and G. Bard Ermentrout. Spatially structured activity in synaptically coupled neuronal networks: I. Traveling fronts and pulses. *SIAM Journal on Applied Mathematics*, 62(1):206–225, jan 2001.

[77] Allen C Pipkin. *A course on integral equations*. Number 9. Springer Science & Business Media, 1991.

[78] D. Poll and Zachary P. Kilpatrick. Stochastic motion of bumps in planar neural fields. *SIAM Journal on Applied Mathematics*, 75(4):1553–1577, January 2015.

[79] Alfonso Renart, Rubén Moreno-Bote, Xiao-Jing Wang, and Néstor Parga. Mean-driven and fluctuation-driven persistent activity in recurrent networks. *Neural computation*, 19(1):1–46, 2007.

[80] Javier Roulet and Gabriel B. Mindlin. Average activity of excitatory and inhibitory neural populations. *Chaos: An Interdisciplinary Journal of Nonlinear Science*, 26(9):093104, September 2016.

[81] Jonathan J. Rubin, Jonathan E. Rubin, and G. Bard Ermentrout. Analysis of synchronization in a slowly changing environment: How slow coupling becomes fast weak coupling. *Phys. Rev. Lett.*, 110:204101, May 2013.

[82] Michael A Schwemmer and Timothy J Lewis. The theory of weakly coupled oscillators. In *Phase response curves in neuroscience*, pages 3–31. Springer, 2012.

[83] Michael A Schwemmer and Timothy J Lewis. The theory of weakly coupled oscillators. In *Phase Response Curves in Neuroscience*, pages 3–31. Springer, 2012.

[84] Arthur Sherman. Anti-phase, asymmetric and aperiodic oscillations in excitable cellsi. coupled bursters. *Bulletin of mathematical biology*, 56(5):811–835, 1994.

[85] Paul So, Bernard C Cotton, and Ernest Barreto. Synchronization in interacting populations of heterogeneous oscillators with time-varying coupling. *Chaos: An Interdisciplinary Journal of Nonlinear Science*, 18(3):037114, 2008.

[86] Klaus M Stiefel, Boris S Gutkin, and Terrence J Sejnowski. Cholinergic neuromodulation changes phase response curve shape and type in cortical pyramidal neurons. *PloS one*, 3(12):e3947–e3947, 2008.

[87] Klaus M Stiefel, Boris S Gutkin, and Terrence J Sejnowski. The effects of cholinergic neuromodulation on neuronal phase-response curves of modeled cortical neurons. *Journal of computational neuroscience*, 26(2):289–301, 2009.

[88] Jun-nosuke Teramae and Dan Tanaka. Robustness of the noise-induced phase synchronization in a general class of limit cycle oscillators. *Physical review letters*, 93(20):204103, 2004.

[89] RD Traub. Simulation of intrinsic bursting in ca3 hippocampal neurons. *Neuroscience*, 7(5):1233–1242, 1982.

[90] Xiao-Jing Wang. Synaptic reverberation underlying mnemonic persistent activity. *Trends in neurosciences*, 24(8):455–463, 2001.

[91] Xiao-Jing Wang and György Buzsáki. Gamma oscillation by synaptic inhibition in a hippocampal interneuronal network model. *The Journal of Neuroscience*, 16(20):6402–6413, 1996.

[92] Xiao-Jing Wang and György Buzsáki. Gamma oscillation by synaptic inhibition in a hippocampal interneuronal network model. *Journal of neuroscience*, 16(20):6402–6413, 1996.

[93] Shinya Watanabe and Steven H Strogatz. Integrability of a globally coupled oscillator array. *Physical review letters*, 70(16):2391, 1993.

[94] Shinya Watanabe and Steven H Strogatz. Constants of motion for superconducting josephson arrays. *Physica D: Nonlinear Phenomena*, 74(3-4):197–253, 1994.

[95] Hugh R Wilson and Jack D Cowan. Excitatory and inhibitory interactions in localized populations of model neurons. *Biophysical journal*, 12(1):1–24, 1972.

[96] Xiaohui Xie, Richard HR Hahnloser, and H Sebastian Seung. Double-ring network model of the head-direction system. *Physical Review E*, 66(4):041902, 2002.

[97] Lawrence Christopher York and Mark C. W. van Rossum. Recurrent networks with short term synaptic depression. *Journal of Computational Neuroscience*, 27(3):607, jul 2009.

[98] Wenhao Zhang and Si Wu. Neural information processing with feedback modulations. *Neural Computation*, 24(7):1695–1721, mar 2012.